Vibration from Underground Railways: Considering Piled Foundations and Twin Tunnels

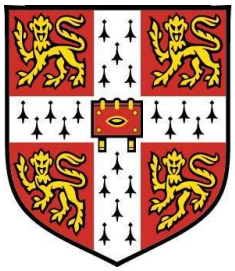

Kirsty Alison Kuo

King's College

University of Cambridge

A dissertation submitted for the degree of

Doctor of Philosophy

September 2010

To Matthew, Mum and Dad ...

Acknowledgements

I would like to thank Dr Hugh Hunt for providing me with the opportunity to undertake this project, and for his continual support and enthusiasm throughout the course of this research. He has provided me with many, varied opportunities to further my understanding of the field of dynamics and vibration, for which I am most grateful.

My sincere thanks goes to Dr Mohammed Hussein of Nottingham University for his assistance in understanding the Pipe-in-Pipe model, and his guidance on the formulation of the two-tunnel model. Mohammed patiently answered many questions, and provided insightful suggestions while reviewing aspects of this work. I would also like to express my appreciation to Dr James Talbot for the use of his boundary-element model for piles, and for the discussions we had on the direction of my work on piled foundations.

The collaborative efforts of the Structural Mechanics Group at Katholieke Universiteit Leuven, led by Professor Geert Degrande, have been instrumental in the validation of the pile models presented in this dissertation. In particular, I would like to acknowledge the modelling work done by Dr Stijn Francois and Mr Pieter Coulier. It has been a pleasure to work with them.

This research is primarily funded by the generous support of the General Sir John Monash Foundation of Australia. In particular I would like to thank past-CEO Mr Ken Crompton, present-CEO Dr Peter Binks, the Board of Directors and the sponsors who support these awards.

I would also like to thank King's College for their provision of a Studentship to supplement my funding. King's College has also provided a pleasant environment for me to live in, for which I am most grateful.

Finally, I would like to thank my husband Matthew, my best friend, with whom I am privileged to share my life. Thank you for your willingness to answer my geotechnical questions, discuss the directions of this research, edit my work and support me in the writing of this dissertation. But most of all, thank you for your love.

To God be the glory, as it is by Him and through Him that all things are accomplished.

I declare that, except for commonly understood and accepted ideas or where specific reference has been made to the work of others, this dissertation is the result of my own work and includes nothing which is the outcome of work done in collaboration. This dissertation is approximately 61,000 words in length and contains 89 figures.

Preface

Most engineering courses on vibration begin with a mass on a spring, and then move on to continuous systems such as strings, columns and membranes. These simple systems provide students with a good understanding of the fundamentals of vibration theory, and the physical behaviour of such systems is represented by using well-known equations.

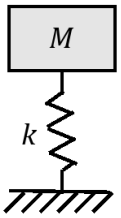

However, many vibration problems do not involve such simple systems. In the past, to solve these problems, engineers would turn to experimental investigations, or would construct simple models that could capture the essential physical behaviour and yet be solved using the available computational techniques. Nowadays, many engineers use commercial software packages that make use of powerful numerical methods such as finite-element or boundary-element methods as their primary tool in constructing models. The difficulty that may arise from the use of such software (that is specially designed to have a user-friendly interface) is that many practitioners lack an awareness of the limitations of these numerical models, and the uncertainty that may be present in the results is often poorly understood. For many complex systems there is no other method of calculating the vibration results, which means that critical engineering decisions may be based on essentially unvalidated results.

This dissertation aims to address this state of affairs by demonstrating that the vibration of a complex system can be accurately modelled using relatively simple techniques, and that such a model provides a complementary solution that can be used in conjunction with numerical formulations. The advantages of this approach are clear: reduced processing times allow for a quicker design process; the transparency of the solution minimises the occurrence of 'unknown' assumptions; and the use of simple models may even enable the modelling of some complex systems that are currently beyond modern numerical computational capabilities. These advantages, when augmented by the versatility and strength of numerical methods, provide a comprehensive framework for addressing vibration problems.

Abstract

Accurate predictions of ground-borne vibration levels in the vicinity of an underground railway are greatly sought after in modern urban centers. Yet the complexity involved in simulating the underground environment means that it is necessary to make simplifying assumptions about this system. One such commonly made assumption is to ignore the effects of nearby embedded structures such as piled foundations and neighbouring tunnels.

Through the formulation of computationally efficient mathematical models, this dissertation examines the dynamic behaviour of these two particular types of structures. The effect of the dynamic behaviour of these structures on the ground-borne vibration generated by an underground railway is considered.

The modelling of piled foundations begins with consideration of a single pile embedded in a linear, viscoelastic halfspace. Two approaches are pursued: the modification of an existing plane-strain pile model; and the development of a fully three-dimensional model formulated in the wavenumber domain. Methods for adapting models of infinite structures to simulate finite systems using mirror-imaging techniques are described. The interaction between two neighbouring piles is considered using the method of joining subsystems, and these results are extended to formulate models for pile groups. The mathematical model is validated against existing numerical solutions and is found to be both accurate and efficient. A building model and a model for the pile cap are developed, and are attached to the piled foundation. A case study is used to illustrate a procedure for assessing the vibration performance of pile groups subject to vibration generated by an underground railway.

The two-tunnel model uses the superposition of displacement fields to produce a fully coupled model of two infinitely long tunnels embedded in a homogeneous, viscoelastic fullspace. The significance of the interactions occurring between the two tunnels is quantified by calculating the insertion gains that result from the existence of a second tunnel. The results show that a high degree of inaccuracy exists in any underground-railway vibration prediction model that includes only one of the two tunnels present.

Contents

List of Figures

List of Tables

Chapter 1

Literature Review

On October 5, 2007, the £16 billion Crossrail Project was launched in London. This project will create a railway joining Maidenhead in the west with Essex in the east, and includes new twin tunnels passing under the central London area. These tunnels will pass underneath a number of vibration-sensitive sites, such as the Grand Central Sound Studios (an internationally renowned sound recording studio) and the Barbican Theatre. Of the 191 vibration-sensitive premises along the route, 101 are built on piled foundations, with the minimum pile-tunnel distance being less than 50m [163]. Both the occupants of these buildings and the railway developers are relying on engineers to predict the vibration levels resulting from the underground railway. Will it be possible for engineers to predict accurately the vibration levels in this railway, or in any other new or existing underground railway around the world? If not, can the prediction uncertainties and inaccuracies be quantified? The aim of this dissertation is to contribute answers to these questions.

This literature review begins with a general introduction to the problem of ground-borne vibration, including the major sources of ground-borne vibration and the ways in which both humans and structures respond to this excitation. The methods of reducing ground-borne vibration from underground railways are discussed, and several large-scale models of vibration from underground railways are introduced. This part of the literature review culminates with a description of the directions of this research. The later sections of the literature review examine in more detail the design and modelling of the piled-foundation and twin-tunnel structures that are the focus of this dissertation. To conclude, the primary objectives of this research are presented, and the subjects of the proceeding chapters are outlined.

1.1 The Problem of Ground-Borne Vibration

The problem of ground-borne vibration is generally not one of structural integrity, but rather one of environmental disturbance. This problem has become increasingly prevalent over the past century with increasing industrialisation, and as homes and offices are located in ever closer proximity to sources of ground-borne vibration. The transmission of ground-borne vibration through structural foundations and into buildings often results in the production of re-radiated noise. This is an undesirable and annoying effect for occupants, making ground-borne vibration a particularly important issue for urban developers. Furthermore, the day-to-day operation of vibration-sensitive premises, such as recording studios, concert halls, operating theatres and micro-manufacturing facilities, can be significantly affected by low levels of ground-borne vibration.

1.1.1 Sources of Ground-Borne Vibration

There are many sources of ground-borne vibration, including those below the ground, such as earthquakes and underground railways, and those at the surface, such as roads and construction activities. As this dissertation is primarily concerned with the transmission of vibration from the ground via structural foundations into buildings, sources of vibration within the building itself, such as air conditioners, banging doors and heavy footfalls, are not considered here.

The five primary sources of ground-borne vibration are presented here, with a brief discussion on the vibration levels produced by each.

Machine foundation vibration There are two types of machines that produce ground-borne vibration: those that create low-frequency, harmonically varying forces; and those that create impulsive forces. Harmonically varying forces result from rotating out-of-balance masses, which can be found in reciprocating engines, compressors and reciprocating presses. Impulsive loadings are produced by machinery such as guillotines, forging hammers and hydraulic presses. Some of these processes involve extremely large forces, and the vibration of the ground in the vicinity of such machinery is substantial as the majority of the impact energy is dissipated in the foundation and the underlying soil [132].

Whilst the level of vibration from machine foundations is not insignificant, this source of ground-borne vibration is usually not an issue of primary concern to the general public, as this kind of machinery is generally found in a fixed location within an industrial zone.

Construction activities Ground-borne vibration produced by construction activities can have an adverse effect on the environment and local residents, and in some cases can be of a magnitude large enough to result in damage to nearby property. There are five major sources of ground-borne vibration during construction: pile driving; compaction; tunnelling; excavation; and blasting. Of these activities, blasting produces the highest levels of vibration, and for this reason much research has been undertaken into this area and reliable prediction models for blasting exist [59]. Subsurface construction works (tunnelling, excavation and blasting) produce higher levels of ground-borne vibration than surface construction works.

Earthquakes Most earthquakes occur when the built-up shear stresses occurring along a geological fault exceed the frictional resistance across the fault. The two sides of the fault slip past each other, releasing large amounts of strain energy and generating pressure and shear waves. These waves propagate through the bedrock and the soil layers and along the ground surface, where damage is often sustained by foundations, buildings and other structures. The frequency range of interest in earthquake engineering is 0-10Hz.

Extensive research has been undertaken in earthquake engineering, driven by the catastrophic consequences (in terms of loss of life, structural damage and economic expense) of these events. Of particular importance in this area is the nonlinear behaviour of soils, which becomes significant when the shear strains exceed 10^{-4}, as is often the case during large-magnitude earthquakes [47]. Examples of nonlinear soil behaviour include slippage and gapping at soil-foundation interfaces, liquefaction of soils and hyperbolic stress-strain relationships. These effects have received much attention recently [37, 76, 105].

Roads The passage of vehicles over a road surface produces random, dynamic tyre forces due to the interaction between the rough road surface and the vehicle tyres. These dynamic forces are transmitted to the ground, resulting in ground-borne vibration. The passing of heavy goods vehicles is the principle source of vibration from road traffic [176].

The magnitude and frequency content of the vibration spectra produced by road traffic has been shown to be strongly dependent on the type of road surface [63] and the soil conditions [176]. Features such as speed humps and road cushions can also produce high levels of vibration that propagate into nearby buildings.

Railways The primary environmental impact from trains running both above and below the ground surface is ground-borne vibration. Rising fuel prices, urban congestion and population growth are all increasing the demand for the construction of rail networks within cities. The construction of these underground rail networks is bringing homes and offices into closer proximity to this vibration source than ever before.

Parametric excitation, an important mechanism of ground-borne vibration, occurs due to variation in the stiffness of the support system observed by the train. The most common example of this phenomenon is the passage of the wheel over the sleepers, resulting in the sleeper-passing frequency. Other examples include variations in the ballast stiffness and variations in the mechanical properties of the ground [56]. When the sleeper-passing frequency coincides with the total vehicle-on-track resonance, a maximum in the ground response is observed [28]. The passage of train bogies over sleepers can also result in longitudinal waves being formed in the surface profile of the track [55]. In this way, parametric excitation contributes to rail roughness, another mechanism of vibration generation.

Roughness or unevenness at the wheel-rail interface induces a relative displacement between the wheel and the rail, which can propagate through the rail, sleepers and ballast and into the ground as vibration. According to Nielsen [125], if an initial railhead irregularity is present in the system due to manufacturing or re-grinding of the rail, then the passage of the train over this roughness creates fluctuating creepages, contact forces, and contact patch dimensions. These fluctuations remove rail material due to wear, thus exacerbating the original roughness. The surface roughness observed by Thompson & Jones [168] has amplitudes from 1 to 50μm and wavelengths of 5-200mm, corresponding to a mid- to high- frequency range of vibration. The wheel contact length of 10-15mm acts as a filter on wavelengths shorter than the wheel contact length, thus high frequencies are strongly attenuated. High levels of roughness can result in nonlinearities, such as the loss of contact between the wheel and the rail, and the resulting impact upon re-connection.

There is another vibration mechanism that results from the interaction of the train with the rails: the wheel-passing frequency. This mechanism arises when successive axles of the train pass by a fixed observation point. An observer experiences a peak in the ground-borne vibration when a wheel is at the point closest to the observer; a trough occurs when the point closest to the observer is located between the two axles. This is a quasi-static effect as it can be modelled using the train static force (acting through the axles) moving along the track at the velocity of the train [65]. The wheel-passing frequency for a European Intercity train travelling at 200km/hr is in the range of 18-20Hz [6]. An experimental study by Auersch [6] shows that while the passage of

static axle loads is important in the localised region surrounding the track, this effect drops off rapidly with distance.

One of the least common mechanisms of ground-borne vibration from railways is the generation of a Mach cone, which occurs when the train moves forward at a speed greater than one of the wave speeds in the ground. The speeds of shear and Rayleigh waves (the two slowest-moving waves in the ground) are usually much higher than the fastest-moving trains. However, at a particular site near Gothenburg in Sweden the shear-wave speed in the soil (40ms^{-1}) is exceeded by the train speed of 55ms^{-1} and excessive vibration is experienced. Several investigations into this phenomenon have been conducted by Ekevid *et al.* [36], Kaynia *et al.* [91] and Madshus & Kaynia [110]. With the trends in railway-network development tending towards higher-speed trains, this mechanism of ground-borne vibration may become more of a concern in the future. As it currently rarely occurs, and then only in highly localised areas, the railway model used in this dissertation focuses on the other mechanisms of vibration generation from railways.

The peak vibrations generated by railways typically lie in the frequency range of 1-80Hz, the region comparable to the wheel/track resonance [56]. Analysis of the time history of acceleration measured in the ground when a train passes, shown in Figure 1.1, reveals the primary mechanisms by which ground-borne vibration is generated. The upper curve of Figure 1.1 shows that the vibration measured at a close distance to the track primarily originates from the wheel/rail contact area. The sleeper-passing frequency and the wheel-passing frequency are observed to occur in most of the train vibration spectra analysed by Heckl *et al.* [56].

Strong vibration also occurs when the wheel passes over a gap or other surface irregularity in the rail (such as track crossovers and turnouts) or when the wheel has a partially flat surface. In these circumstances the vibration amplitude increases with increasing train speed and with decreasing wheel radius [56].

1.1.2 Response of Buildings

The response of buildings to dynamic excitation depends on both the response characteristics of the buildings and foundations (natural frequencies, mode shapes, damping) and the spectral content of the excitation [73]. The existence of cracks in a building in the vicinity of a vibration source does not imply that this structural damage has resulted from the vibration source: cracking may be due to any number of factors, including settlement, material creep, natural ageing and occupational loads [73].

A feature of ground-borne vibration is the erratic way in which some buildings are

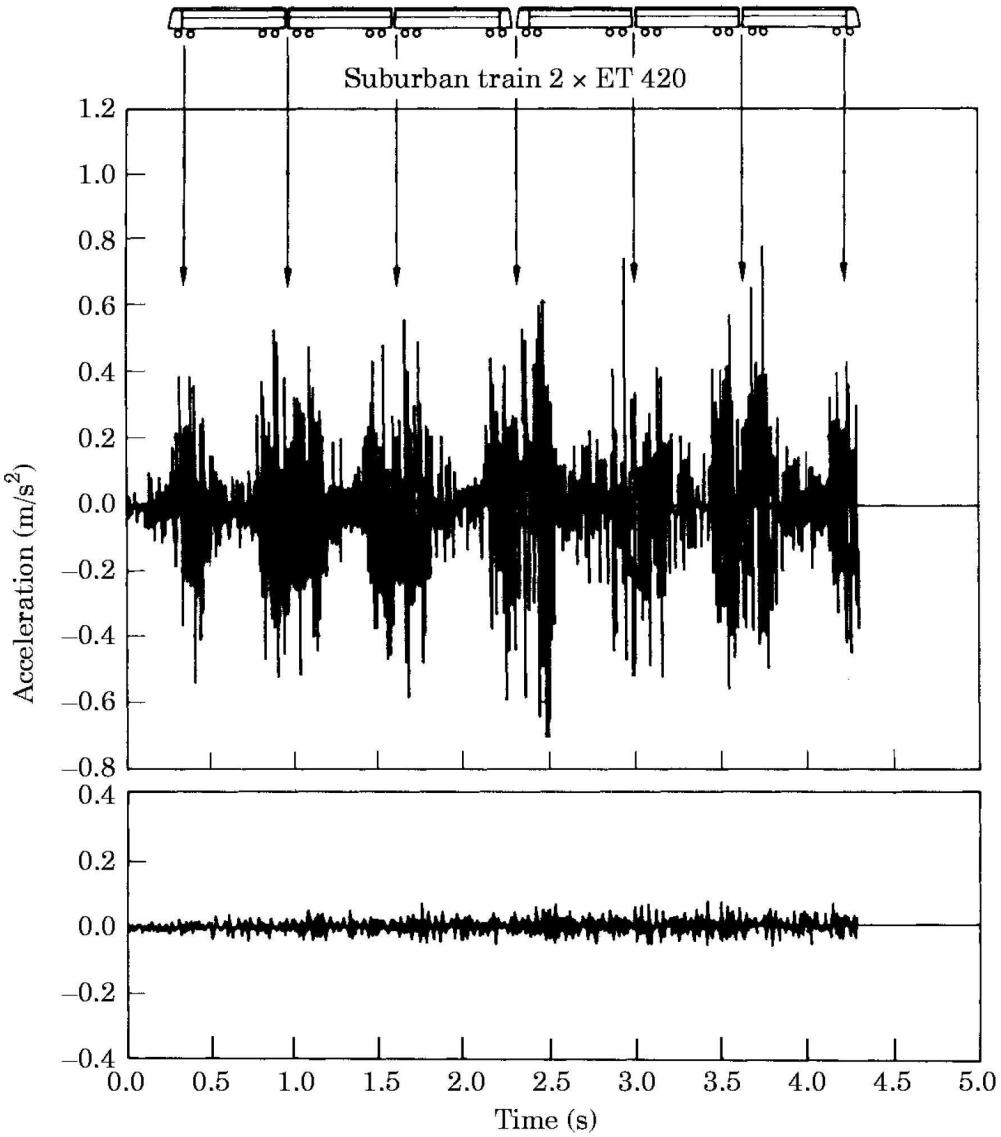

Fig. 1.1 The time history of the ground acceleration when a train passes at 120 km/hr (reproduced from Heckl *et al.* [56]). Upper curve: distance from the centre of the track is 3m; lower curve: distance from the centre of the track is 32m

affected by vibration, but neighbouring buildings are not. This can be explained by an observation: in order for a building/foundation mode to be excited, the relevant frequency must be present in the ground vibration, and the wavelength in the ground must be properly matched to the building/foundation dimensions [29]. The strains imposed in a building/foundation tend to be greater when the spectral content of the excitation is predominantly made up of lower frequencies [73].

The response of the building is also influenced by the geology of the area, the type and depth of the foundation of the building, the design and construction of the building, and even the arrangement of furniture within the building [29]. Generally, vibration with a high peak particle velocity acting on a building sited on hard ground induces the same magnitude of strain levels in the building as vibration of a lower peak particle velocity acting on a building sited on softer ground.

Watts & Krylov [177] observe that the amplitude and attenuation with distance of ground-borne, vehicle-induced vibration depends critically on the soil composition. In particular, it is the shear modulus of the ground that determines the magnitude of the vibration produced: a low shear modulus (soft soil) produces relatively large responses, whereas a high shear modulus (rock) produces little vibration. Watts & Krylov propose that soil layering would increase the magnitude of ground-borne vibration levels, as reflections from the layer interfaces would lead to lower rates of attenuation. However, in the discussion by Hood *et al.* [60] on the procedure developed for modelling the environmental impact of the Channel Tunnel Rail Link, the authors conclude from the available data for re-radiated noise that differences in soil layering do not have a major influence on the propagation of vibration.

Settlement or loss of bearing capacity may result when ground-borne vibration is transmitted through foundations on poor soils [73]. Factors influencing this phenomenon include: the particle size of the soil; soil uniformity; compaction; degree of saturation; internal stress state; peak multiaxial acceleration level; and duration of the vibration. In the extreme circumstance of high-magnitude excitation of a weak soil, the soil exhibits nonlinear behaviour and may undergo liquefaction [73].

The position of maximum vibration in a building is not always at the foundation: the response of the building may amplify the vibration such that the highest floor of the building has a greater magnitude of displacement than the foundation [73]. The lower floor levels are dominated by vertical vibration, whilst horizontal vibration becomes more significant at higher floor levels [109]. Due to the complex construction of a multi-storey building, the response of the building is difficult to predict beyond the most fundamental modes, so vibration measurement is usually the most economical method of determining a building's response.

Re-radiated noise occurs when ground-borne vibration excites building surfaces such as walls, floors and ceilings, and the vibration is transmitted to the air inside the building in the form of audible sound. A well-recognised example of high-frequency, re-radiated noise is the 'clinking' of wineglasses on a mantelpiece during an earthquake. However, re-radiated noise usually occurs at lower frequencies (between 16 and 250Hz), and is heard as a low, rumbling noise [60].

1.1.3 Human Response to Vibration and Re-radiated Noise

Numerous studies have been conducted into the response of humans to vibration and re-radiated noise. A study by Knall [93] shows that noise from road traffic, aircraft, industry and neighbours may cause more annoyance and disturbance to residents than railway noise. As this dissertation is concerned with the effects of underground railways, the following discussion will focus on railway noise alone.

The main concern of residents experiencing vibration and re-radiated noise from railways is the possibility of damage caused to the building. However, there are two orders of magnitude separating the threshold of human perception of vibration and the onset of building damage [59]. The most common, annoying aspects of railway noise and vibration are interruption of concentration, disturbance of sleep, and, in particular, interference with speech and communication [140]. The response of residents to vibration and re-radiated noise has been shown to depend not only on the level of the noise, but also on non-acoustic factors such as their attitude towards the railway, the neighbourhood environment and their sensitivity to noise [93].

There are more than a dozen indicators that have been proposed as measures of the annoyance of those subject to noise and vibration. One of the most widely-accepted indicators is the equivalent continuous sound pressure level L_{Aeq}, defined as

$$L_{Aeq} = 10 \log_{10} \left(\frac{1}{T} \int_0^T \frac{p_A^2}{p_0^2} dt \right) \tag{1.1}$$

where T is the time period, p_0 is the reference sound pressure of 20 μPa and p_A is the instantaneous sound pressure measured using an A-weighting frequency filter. The A-weighting filter is used on the sound pressure value to simulate the response of humans to pure sounds: in particular, humans are less responsive to sounds of low frequency, so the A-weighting filter reduces the measured sound pressure value. In a study by Crocker [26], L_{Aeq} is shown to correlate well with the psychological effects of noise. The World Health Organisation recommends that the equivalent continuous sound pressure level experienced outdoors during daytime should not exceed 55dB [26].

Howarth & Griffin [61], Vadillo *et al.* [171], Hood *et al.* [60] Öhrström [140], Knall [93] and Aasvang *et al.* [1] conduct studies into the effects of railway noise and vibration on humans. A summary of the relevant results is presented here.

Two experiments by Howarth & Griffin [61] show that human annoyance to railway-induced building vibration depends on both the frequency of train passes, and the magnitude of the vibration produced by the trains. The results suggest that neither the age nor the gender of subjects is a significant parameter.

A field study is conducted by Vadillo *et al.* [171] with the aim of determining an acceptable level of low-frequency, re-radiated noise within a residence. Residents exposed to maximum (1 second) levels below 32dB(A) do not complain about the presence of the train, even though they could sometimes feel vibration from the passing train. All residents exposed to maximum levels above 42dB(A) complain strongly about noise and vibration levels, with the vibration being the most annoying effect of the passing train. Varied responses are obtained when residents were exposed to maximum levels between 32-42dB(A).

A survey of 565 households on the perception of noise and vibration is conducted by Knall [93]. Seventy-eight percent of residents state that they were 'considerably' affected by noise, whereas only 57% are 'considerably' affected by vibration. Forty percent of residents identify damage to their property perceived to be due to the vibration caused by the railway. Knall [93] suggests that it is the proportion of train passes exceeding the perception threshold for vibration that has more affect on annoyance level than the frequency of train passes.

A survey of Swedish residents conducted by Öhrström [140] supports the finding by Vadillo *et al.* that the vibration, rather than the noise, is the more disturbing factor for the resident. Öhrström suggests a suitable environmental guideline for areas subject to both railway noise and railway vibration is a 10dB(A) lower noise level than those areas subject to only railway noise.

Aasvang [1] applies statistical analysis techniques to the results of a survey of residents living out of sight of railway traffic, to minimise the influence of air-borne noise on the results. Three percent of participants report sleep disturbance due to re-radiated railway noise, and the factors having the most effect on the annoyance of residents are their age, the noise level, the number of train passes, and the presence of sound-insulated windows in the dwelling. In general, Aasvang finds good agreement with the results of the study by Vadillo *et al.*. However, he attributes a slightly higher level of resident annoyance to the presence of trains during the night.

These studies highlight the difficulty in measuring the disturbance caused by railways and setting appropriate guidelines for acceptable levels of noise and vibration. Human

perception of noise and vibration is highly subjective, and in many cases people have difficulty in distinguishing the two. However, this disturbance remains an important issue for the modern urban environment.

1.2 Methods of Reducing Ground-Borne Vibration

The analysis of noise and vibration in buildings due to ground-borne vibration is an involved problem, as there are usually many possible vibration sources in the vicinity of a building. There are also an infinite number of transmission paths into the building, and a variety of mechanisms by which the vibrational energy is dissipated once inside the building. This means that there are a number of ways in which a ground-borne vibration problem can be addressed: isolation of the vibration source; disruption of the transmission path; and isolation of the building itself. After investigating these three categories of vibration-reducing techniques, some standard measures of vibration performance are explained.

1.2.1 Isolation of the Source

Isolation of the source (the railway) has the advantage of controlling the mechanism by which ground-borne vibration is generated, thereby reducing the incident vibration field for any nearby structures. The most common methods used to isolate the source involve targeting the mechanisms of ground-borne vibration generation in railways. Rail welding, rail grinding and wheel truing can be used to eliminate rail and wheel surface irregularities [166]. Slip-slide detectors on bogies reduce the occurrence of wheel flats [178], and the maintenance of the track/slab assembly prevents track settlement and deterioration of crossings [166]. Softening of the vehicle suspension stiffness and modification of the unsprung mass reduces vibration due to the bounce and wheel-hop modes [57]. Other methods of isolating the source aim to reduce the noise and vibration transmission into the ground. These include the use of rubber pads between the rails, base plates and sleepers [166], and floating slab track.

Floating slab track involves mounting the track/slab assembly on rubber bearings or steel springs. It is generally regarded as the most effective method of vibration isolation of the source for underground railways. Hussein [65] assesses the effectiveness of floating slab track using power-flow methods and shows that attenuation has a strong dependence on the floating-slab-track frequency and the excitation frequency. Other suggestions for isolation include increasing the tunnel depth, the use of extra heavy tunnel structures and resilient wheels [178].

1.2.2 Disruption of the Transmission Path

Some common vibration countermeasures that involve disruption of the transmission path include the construction of open trenches, in-filled trenches, wave-impeding blocks (WIBs) and pile rows. An example of an open trench is shown in Figure 1.2. These barriers diffract the surface waves radiated from the railway and reduce their amplitude.

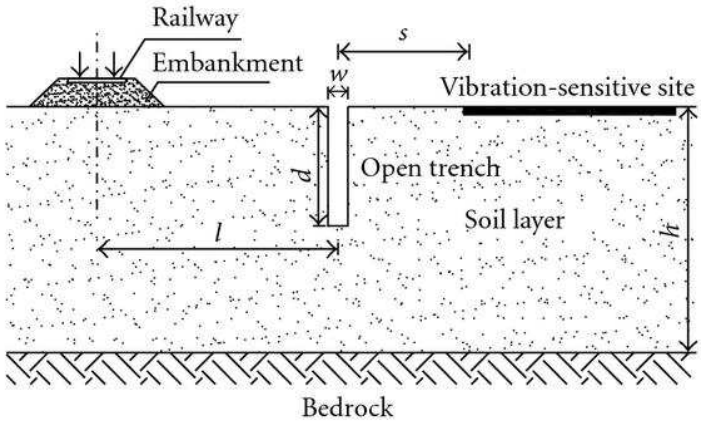

Fig. 1.2 An open trench located near a railway (reproduced from Di Mino *et al.* [33])

A study on the effectiveness of open trenches, in-filled trenches and a WIB in reducing rail-induced, ground-borne vibration is conducted by Hung *et al.* [62] using a 2.5D finite/infinite-element approach. Their findings show that open trenches are the most effective method of isolating the vibrations induced by the static and dynamic moving loads produced by trains. The WIB is seen to be effective only in isolating vibrations with wavelengths comparable to the dimensions of the WIB itself. Yang and Hung [188] determine the optimal parameter values for these three barriers in isolating the train-induced vibrations.

In order for a trench to achieve reasonable attenuation levels, the trench must have a depth of an order comparable to that of the surface wavelength. Due to soil stability and water-table level considerations, limits exist on the depth to which a trench can be excavated. Hence, the attenuation of ground-borne vibration by trenches is only effective for moderate- to high- frequency vibrations. The trench depth requirement prevents trenches from being used in practice for rail-induced, ground-borne vibration problems.

Pile rows have some distinct advantages over trenches for vibration isolation: there is no limit on the depth to which they can be driven; they can be arranged in any

possible geometry to create a wave barrier; they do not disturb the ground surface; and the design technology for foundation piles can be applied to the design of pile rows.

Liao and Sangrey [101] investigate the use of piles as isolation barriers for ground-borne vibration. They propose an isolation barrier consisting of a row of cylindrical piles, which scatter and diffract the propagating Rayleigh (R) waves. Their experiments using a shallow water tank show that the scattering of R waves by rows of piles is a feasible method of foundation isolation. The level of isolation achieved, however, is strongly dependent upon the soil-pile material properties; piles that are acoustically softer than the soil provide higher levels of attenuation.

Kattis *et al.* [83, 84] conduct further investigations into pile-row isolation barriers. A three-dimensional, boundary-element (BE) formulation in the frequency domain is used to model both the pile and the soil domains [84]. The vibration source is a vertical, harmonically varying force acting on the halfspace surface some distance from the pile row. They conclude that although piles and trenches screen waves in the same manner, trenches are more effective than piles as isolation barriers. The effectiveness of the pile row is dependent upon the spacing, length, depth and width of the piles, and independent of the cross-sectional shape of the piles. In a further paper by the same authors [83], the pile row is replaced by an effective trench to reduce the modelling complexity. Open trenches or piles are found to be more effective than concrete-filled trenches.

Other models of pile-row isolation barriers include those by Tsai *et al.* [170] and Gao *et al.* [46], who develop models using three-dimensional BE methods and Green's functions, respectively. Hildebrand [58] and Lane *et al.* [99] apply pile-row models to the lime cement columns used to mitigate problematic vibrations from surface railway tracks in Sweden. Two situations are examined: installation of the pile row directly beneath the track; and installation of the pile row some distance from the track. There is little difference between the two situations in the farfield; however, the pile row directly beneath the track provides better near-field vibration attenuation.

The installation of pile rows does not appear to be a commonly used solution to the problem of vibration from underground railways. This is primarily because the cost of installation of pile rows on the scale required for an urban rail network, such as the London Underground, would be prohibitive compared to the cost of more commonly used vibration-isolation techniques. To date, there is no evidence of research into the engineering of foundation piles for minimising vibration transmission into buildings.

1.2.3 Isolation of the Building

There are a number of methods that can be employed to reduce the vibration levels in buildings. Some of these methods can be used to mitigate vibration problems that arise post-construction. Damping treatments (such as free-layer damping and constrained-layer damping) can be applied to resonant floors or walls, and tuned vibration absorbers can be installed to attenuate specific resonant frequencies. Localised stiffening or mass addition can be used to move structural resonances away from the excitation frequency. Furniture designs can be selected so that they do not resonate at the excitation frequencies, and sensitive equipment can be moved near to the walls, where the vibration levels are likely to be lower than at the centre of the floor.

Other methods, such as base isolation or a box-in-box design, should be incorporated during the design stage of the building due to the considerable expense of retro-fitting. Base isolation involves the installation of steel springs or rubber bearings between the building and its foundation to isolate the building from the motion of the ground. The isolation system is defined by its isolation frequency, usually between 5 and 15 Hz, with a lower isolation frequency generally indicating more effective isolation. Cryer [27] investigates the effectiveness of base isolation using a two-dimensional, infinite building model. He concludes that the building vibration levels are strongly influenced by the natural frequency of the base-isolation system, yet are relatively insensitive to the damping in the isolation material. Talbot [166] develops a generic computational model of a two-dimensional, portal-frame model of a building coupled to a three-dimensional, boundary-element model of a piled foundation via isolation bearings. He agrees with the findings of Cryer, and also notes that modelling of piled foundations is crucial to predicting accurately the base-isolation efficiency.

The box-in-box technique provides a high level of vibration isolation to a particular part of a building, such as a concert hall, recording studio or cinema. It involves mounting a room on isolation bearings in order to isolate it from the rest of the building structure. No solid bridges, such as services, can exist between the internal room and the rest of the building structure. Two examples of recent use of the box-in-box technique are King's Place in London [145], and the Tokyo International Forum [87], both major concert venues.

1.2.4 Vibration-Performance Measures

In this dissertation, vibration-performance measures are required to assess the performance of various foundation designs. Transfer functions and dynamic impedance are often used to characterise the vibration performance of foundations [30, 116, 119, 128];

however, while these measures are useful for comparing the dynamic behaviour of models, they have little value in determining the levels of vibration attenuation provided by different foundation designs. There is no standard measure available for the comparison of foundation designs, so three methods are adopted from the assessment of base-isolation systems.

Insertion gain Insertion gain (IG) is a measure of the benefit gained by inserting a vibration neutraliser into the system of interest. For example, it is used to measure the attenuation achieved when an isolation bearing is installed into a building. It is a particularly useful measure for the engineer who wishes to evaluate the merits of alternative vibration-isolation techniques; however, it is not an easily measurable quantity in practice, due to the difficulties in conducting measurements both before and after installation of the vibration isolator. Insertion gain is usually expressed in decibels (dB), using

$$IG = 20 \log_{10} \left(\frac{x_{isol}(\omega)}{x_{unisol}(\omega)} \right), \tag{1.2}$$

where $x_{isol}(\omega)$ and $x_{unisol}(\omega)$ are the response of the system in the frequency (ω) domain in the isolated and unisolated condition, respectively. Due to the linear system assumption, the response may be expressed as a displacement, velocity or acceleration. Insertion gain can only be used for vibration in one direction; a different measure, namely power flow, is needed to remove the directional component of the vibration from the analysis.

Power flow Power-flow techniques can be applied to structures in order to identify the dominant vibration-transmission paths and the optimum position of a vibration neutraliser. Power-flow techniques are particularly useful in obtaining an overall assessment of the levels of vibration entering a structure as they remove the directional component of the vibration from the analysis.

Power-flow methods can be applied to various structures: Langley [100] analyses the power flows through a finite beam foundation and a grillage; and Talbot [166] calculates the power flows into a building with and without base isolation. Goyder and White [48, 49, 50] study the power flows through beam and plate foundations from isolated and unisolated machines.

For structures undergoing time-harmonic motion, the mean power flow $\bar{P}$ is expressed as the mean dissipative power, where for a structural element with one degree-of-freedom

$$\bar{P} = -\frac{1}{2} \Re(i\omega u F^{\star}). \tag{1.3}$$

The displacement of the element is u, and $F^\star$ is the complex conjugate of the force F acting on the element. For a structural element with more than one degree-of-freedom, the mean power flow is the sum of the power flows from each degree-of-freedom. For example, for an element with two translational and one rotational degree-of-freedom, the mean power flow is written as

$$\bar{P} = -\frac{1}{2}\Re(i\omega(uF^\star + vS^\star + \theta Q^\star)), \tag{1.4}$$

where u, v and θ are the generalised displacements, and $F^\star$, $S^\star$, and $Q^\star$ are the complex conjugates of the corresponding generalised forces.

Power-flow insertion gain is used by Talbot [166] as an effective means of assessing base-isolation performance. He proposes the power-flow insertion gain as a single measure of assessing isolation performance, as the total mean power flow entering a building (assuming no internal sources) drives all internal structural vibration and re-radiated noise. Power-flow insertion gain ($PFIG$) is defined as

$$PFIG = 10\log_{10}\left(\frac{\bar{P}_{isol}}{\bar{P}_{unisol}}\right), \tag{1.5}$$

where $\bar{P}_{isol}$ and $\bar{P}_{unisol}$ are the total mean power flows entering a building in the isolated and unisolated cases respectively.

RMS vibration level The final proposed measure of vibration levels provides a method of averaging the response over a range of frequencies. This is particularly useful for comparing structure designs, as the level of attenuation provided by a design is often highly dependent on frequency. The root mean square (RMS) or quadratic mean can be used to average the magnitude of a varying quantity. For underground railways, the varying quantity of interest is the velocity at a given point. The RMS velocity v_{RMS} is written as

$$v_{RMS} = \sqrt{\frac{1}{\omega_f - \omega_i}\int_{\omega_i}^{\omega_f} |v(\omega)|^2 \, d\omega}, \tag{1.6}$$

where $v(\omega)$ is the velocity at a given point as a function of frequency, and ω_i and ω_f are the lower and upper values of the frequency range to be included in the RMS average, respectively.

Other vibration-performance measures include peak particle velocity (PPV), vibration dose value (VDV), peak component particle velocity and dynamic magnification. Further details on these measures can be found in the relevant British Standard [74].

1.3 Modelling of Vibration from Underground Railways

The number of parameters involved in describing the underground environment makes the formulation of a comprehensive model of vibration from underground railways a virtually impossible task. For this reason, the modelling to-date either focuses on aspects of the vibration generation and propagation problems, for example wheel-rail interaction and Green's functions for vibration propagation in multi-layered soil, or on a simplified, large-scale underground environment. This section begins with an explanation of the way in which waves propagate through the soil. Next, an overview of some of the factors that are known to influence vibration from underground railways is presented, before the details of a number of the currently available large-scale models are examined. Particular attention is paid to the assumptions that are inherent in these models, and any work that has been done to quantify these assumptions.

1.3.1 Wave Propagation through the Soil

An understanding of the propagation of vibration through the soil is fundamental to modelling vibration generated by underground railways. The assumption of a homogeneous, isotropic, viscoelastic halfspace through which waves are propagating is used in many models, and is thus the system of interest.

A surface vibration source will generate three types of waves: Rayleigh waves, shear (S) waves and pressure (P) waves. Millar and Pursey [118] show that for a vertically oscillating circular disc on the surface of a homogeneous, isotropic, elastic halfspace the partition of energy is 67% Rayleigh waves, 26% S waves and 7% P waves. A buried vibration source generates S waves and P waves, and Rayleigh waves are generated when P waves or vertically polarised S waves are reflected at the free surface. The relative energy contribution of these Rayleigh waves is insignificant unless the vibration source is buried at a shallow depth [52].

The major features of the three wave types are summarised in Table 1.1 and illustrated in Figure 1.3. Stoneley and Love waves also exist, but arise only in layered media. The horizontal and vertical amplitude of the Rayleigh wave decays exponentially with the coordinate normal to the surface. In the farfield, the Rayleigh wave amplitude decays with distance along the free surface with a rate inversely proportional to the square root of the surface distance. The body waves in the medium (S and P waves) decay in amplitude at a rate inversely proportional to the spherical distance from the source.

As the wave propagates through the bulk medium, attenuation occurs due to two

Table 1.1 Major features of the three types of waves that propagate through a homogeneous halfspace

Wave Type	*Name*	*Speed*	*Region of travel*	*Particle motion relative to propagation direction*
Surface	Rayleigh	Slow	Along surface, to depth of one wavelength	Retrograde ellipse
Transverse body	Shear (S wave); Secondary; Distortional; Equivoluminal	Intermediate	Within bulk medium	Perpendicular; may be polarised in a particular direction
Longitudinal body	Pressure (P wave); Primary; Dilatational; Compression; Irrotational	Fast	Within bulk medium	Parallel

damping mechanisms: radiation (or geometric) damping; and material damping. Radiation damping is frequency independent, and results from the spreading of the wave energy over a larger area as the wavefront propagates away from a source. As Rayleigh waves are confined to the surface region, they are least affected by radiation damping. Material damping results from the frictional energy dissipation that occurs when a wave passes through the medium, creating cyclic stresses.

In the modelling of soil-structure interaction (SSI) in seismic engineering, it is commonly assumed that waves are attenuated by radiation damping, and not by material damping [4]. There is no agreement in seismic-engineering literature in relation to the importance of material damping: see Ambrosini [4] for further discussion. Experimental results of resonant column tests show that material damping in soils has a hysteretic nature [150]. Ambrosini [4] conducts an investigation into the effect of material damping on the seismic response of buildings using a lumped-parameter model. The correspondence principle is used to model hysteretic, frequency-independent material damping by replacing the shear modulus of elasticity of the soil with a corresponding complex term. The results show that material damping should be included in SSI models due to the effect it has on the displacement of the structure.

A hysteretic, frequency-independent type of material damping (similar to that used by Ambrosini) is commonly used in the dynamic analysis of foundations [127, 128, 129, 138]. The presence of viscoelastic damping behaviour is observed in the experimental work carried out by Hunt [63]. To account for the material damping, Hunt proposes a method in which all energy dissipation due to material damping in the soil is assumed

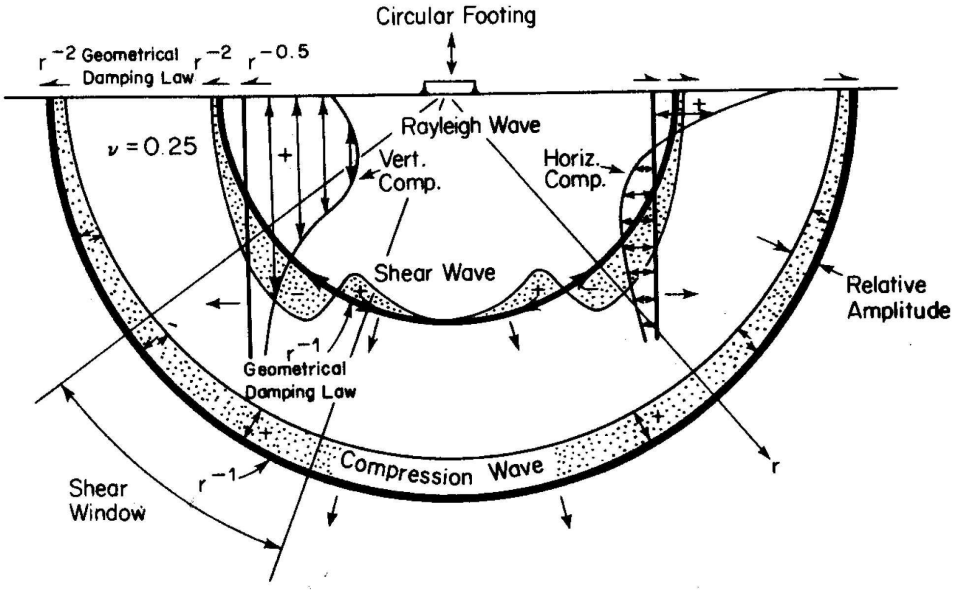

Fig. 1.3 Distribution of waves produced by the vibration of a circular footing on a homogeneous, isotropic, elastic halfspace (reproduced from Woods [186])

to occur through shear motion, described by the shear modulus G, with no losses in volumetric expansion, described by the bulk modulus K. This can be modelled using Biot's correspondence principle [13]:

$$G^* = G(1 + i\eta_G) \tag{1.7}$$

and

$$K^* = K, \tag{1.8}$$

where G^* is the complex shear modulus, K^* is the complex bulk modulus and η_G is the shear loss factor. The other soil parameters, such as Poisson's ratio, can be obtained using the standard elastic relations. This type of frequency-independent, hysteretic damping is used in many underground railway models, and will also be used in the soil models in this dissertation.

1.3.2 Factors that Influence Vibration from Underground Railways

A study by Kurzweil [98] identifies a number of factors that influence the magnitude and frequency of the ground-borne vibration produced by underground railways. These

include: train speed; axle load; carbody suspension; the presence of resilient wheels; the unsprung mass; wheel and rail conditions; the presence of resilient rail fasteners (including resiliently supported ties); the presence of floating slab track; ballast depth; the presence of ballast mats; and the tunnel construction. As mentioned in Section 1.1.2, soil layering can also affect the transmission of vibration from the underground railway to the ground surface.

1.3.3 Large-Scale Models of Vibration from Underground Railways

For more than one-hundred years researchers have been formulating models of train-induced vibration. The early models consider only discrete parts of the system, for example, Winkler's track model consists of a single infinite beam supported on an elastic foundation [179]. With the advent of modern computer technology, models considering multiple elements of the system have been developed. However, even with current modelling technology, simplifying assumptions are needed. These simplifications are often decided based on available computational power or engineering intuition, and in many cases the inaccuracy introduced by these simplifying assumptions remains unquantified.

In the past decade, the trend in the literature is towards the development of numerical models, such as finite-element models or coupled finite-element, boundary-element (FE-BE) models. Finite-element models of the soil require transmitting boundary conditions to correctly simulate wave propagation and prevent reflections at mesh boundaries. The approximate boundary conditions that may be used must be placed in the farfield, resulting in significant computational requirements, especially at high frequencies where fine meshes are required [160]. By coupling finite-element and boundary-element modelling methods together (FE-BE), limitations in the use of either method can be overcome. Boundary elements are well suited to the analysis of infinite media. However, when boundary elements are applied to thin structures such as tunnels both faces of the structure must be discretised, and numerical problems result. Hence a coupled approach, using finite elements for the tunnel and boundary elements for the soil, is preferred.

Although two-dimensional models offer reasonable qualitative results and computation times 1000-2000 times shorter than three-dimensional models [5], they are unsuitable for predicting underground-railway vibration as they can neither account for wave propagation along the track nor accurately simulate the radiation damping of the soil [51]. Three-dimensional modelling has hugely expensive computational requirements; hence the current trend is towards numerical methods that utilise the invariance in the tunnel's longitudinal-axis direction.

The proceeding section begins with an exposition of the Pipe-in-Pipe model, before introducing three numerical, underground-railway vibration models. The numerical models are: a coupled, periodic FE-BE model; a coupled, wavenumber (or two-and-a-half-dimensional) FE-BE model; and a finite/infinite-element model. These models are chosen on account of the thoroughness with which the vibration problem is treated and the efforts that are made to reduce computational demands. None of the models discussed here include piled foundations, and only the coupled, wavenumber FE-BE model considers twin tunnels.

The reader is also referred to the literature reviews by Forrest [41] and Hussein [65] for a detailed discussion of other models of vibration from underground and surface trains.

1.3.3.1 The Pipe-in-Pipe Model

The Pipe-in-Pipe (PiP) model is a well established tool for predicting vibration from underground railways. The primary advantage of PiP over other more detailed models, such as those using boundary-element methods, is the reduced processing time. In order to ensure that PiP is an effective tool that can be used in the field or in the design office, the processing time is kept below one minute for moderate computer specifications.

The Pipe-in-Pipe model has its origins in the work of Köpke [94] on the vibration of buried pipelines. In this work the inner cylinder, the pipeline itself, is modelled using thin-shell theory, while the outer cylinder of infinite outer diameter represents the surrounding soil. This model is first used for underground railways by Hunt and May [64], who calculate soil responses around a simply loaded, infinitely long railway tunnel.

Forrest [41] and Forrest & Hunt [42, 43] extend this model by incorporating floating slab track into the railway-tunnel model using periodic structure theory. In order to assess the performance of the floating slab track, a set of axles is coupled to the track, which is itself coupled to the tunnel via a single line of slab bearings. The roughness excitation of the moving train is simulated using a random, white-noise input under each axle mass.

The PiP software is developed by Hussein [65] and Hussein & Hunt [68, 69, 70], following work on a more comprehensive model of the train-track-tunnel system. Hussein [65] incorporates the response of a continuous slab subject to an oscillating moving load, and a discontinuous slab subject to both an oscillating moving load and a two degree-of-freedom model of a quarter of a train. He improves on the work of Forrest by considering both the radial and tangential loads transmitted to the tunnel wall from the track (Forrest considers only radial loads), and also considers a number of different

arrangements of the slab bearings.

The PiP model is validated against the coupled, periodic FE-BE approach developed by Gupta *et al.* [51]. Both models show agreement in the frequency-domain response of a tunnel embedded in a homogeneous fullspace. It is recognised that PiP is limited to certain scenarios by its inherent assumptions, which include a circular tunnel cross-section, isotropic and homogeneous soil properties and a linear soil response. An indication of the sensitivity of the PiP model to these assumptions can be found in the work of Gupta *et al.* [51]. They conduct a parametric study using both the PiP model and the coupled, periodic FE-BE approach. Parameters including soil shear modulus, soil material damping ratio, soil saturation, tunnel depth, tunnel structure and tunnel geometry are considered.

A later version of PiP incorporates the ElastoDynamics Toolbox (EDT) developed at the Katholieke Universiteit Leuven (KUL) [156]. This toolbox calculates the Green's functions for a variety of three-dimensional spaces, and using this toolbox, horizontal layers, rigid bedrock and a halfspace surface are incorporated into PiP [72]. The coupling of the EDT and the PiP model is carried out by using PiP to determine a set of fictitious forces acting in the soil, at the position of the tunnel, which simulate the vibration levels at the tunnel-soil interface. These fictitious forces are the input for the EDT, which calculates surface vibration levels by multiplying the fictitious forces and the Green's function of the halfspace. This formulation is based on the assumption that the tunnel nearfield vibration is not influenced by the free surface or a layer interface (that is, the tunnel is located sufficiently far from the free surface or from a layer interface). Use of the EDT increases the computation time of the PiP model, but the running time and computational requirements are still significantly less than those required by a coupled FE-BE approach.

An additional development is the use of an analytical solution by Tadeu *et al.* [164] for the Green's functions of a harmonic line load buried in a homogeneous, three-dimensional halfspace. This formulation is incorporated in the same way as the EDT, and results in a decreased running time when calculating the horizontal and longitudinal components of the response in a halfspace. Further research topics for the PiP model include the effect of inclined soil layers, twin-track tunnels, non-circular tunnels and curved tracks [10, 79].

1.3.3.2 A Coupled, Periodic Finite-Element-Boundary-Element (FE-BE) Model

The coupled, periodic FE-BE model presented here has been developed by KUL, in collaboration with École Centrale Paris, and the details of this model are found in Gupta *et al.* [51]. This model has its origins in a prediction model by Lombaert, Degrande & Cloteau [102, 103] for road-traffic-induced vibration. This model is adapted for rail vibration by Cloteau *et al.* [22, 23, 104].

The model is based on an assumption of periodicity in the longitudinal direction along the tunnel axis. Using this assumption, it is only necessary to model one periodic unit of the structure (the reference cell), which is repeated in the longitudinal direction using the Floquet transformation. The reference cell consists of two subdomains: the tunnel, modelled using a FE formulation, and the soil, modelled using BE methods. The Craig-Brampton substructuring method is used to separate the modes of the track and the tunnel, thus allowing alternative track configurations to be considered without requiring recomputation of the soil impedance. Validation of the coupled, periodic FE-BE model is carried out by comparison with the PiP model for the simple case of an invariant tunnel in a fullspace.

This model not only allows for alternative track configurations, but also affords freedom in the shape of the tunnel, the presence of rigid bedrock, and the layering of the halfspace. The computational requirements increase with the complexity of the surrounding soil structure, but by making use of periodicity the model still offers a significant improvement over fully three-dimensional tunnel models. Although this model has not yet been used to investigate twin tunnels, it is conceivable that the formulation could be extended to include an additional tunnel in the reference cell. However, from a computational point of view this may result in excessive runtimes.

The coupled, periodic FE-BE model gives accurate predictions of vibration from underground railways, and can be used to consider tunnels with a complex geometry and inhomogeneous soils. However, due to long computation times, it cannot easily be used as a design tool.

1.3.3.3 A Wavenumber FE-BE Model

Details of the wavenumber FE-BE model developed at the Institute of Sound and Vibration Research, Southampton, are provided by Sheng *et al.* [160, 161]. This method involves discretisation of a cross-sectional plane, with finite elements used for the tunnel/track structure and boundary elements used for the soil free surface and layers. The FE and BE domains are first coupled together, and then the global equations solved for

a discrete wavenumber. This process is repeated until the response has been obtained at a sufficient number of wavenumbers to allow calculation of the actual response using an inverse Fourier transformation.

The advantage of this method is that by making use of the longitudinal invariance the computation time is at most half of that needed for a fully three-dimensional model. One of the problems that does arise through the use of the wavenumber FE-BE model is the presence of singularities in the global boundary-element equation matrices for elements including a collocation node. This required the authors to devise an alternative integration method to the 10-point Gauss-Legendre quadrature scheme that is used for elements excluding the collocation point. Errors can also arise from the truncation of the ground surface and horizontal layers to form a BE model. This was overcome by the creation of 'edge elements' at the termination of the boundary.

Validation of the model is carried out in two stages: firstly, the BE model is validated against the response of a homogeneous halfspace subjected to an embedded, vertical point load, calculated using a semi-analytical method. Secondly, the coupled FE-BE model is validated against the response of an infinitely long tunnel embedded in a homogeneous halfspace, calculated using a model that is analytical in the wavenumber domain. In Sheng *et al.* [160] this wavenumber FE-BE model is used to compare the two tunnel designs shown in Figure 1.4: a large, single-bore, double-track tunnel; and a pair of single, twin-track tunnels. The two tunnels are taken as having the same depth-of-railhead, and one tunnel is subject to a unit vertical load. It is shown that the single tunnel generally produces significantly higher surface vibration levels. The scattering effect of the unloaded tunnel is seen to be significant at frequencies where the shear wavelengths are greater than half the distance between the two tunnels. The response of an underground railway with railpads is also computed by the same authors [161].

1.3.3.4 A Finite/Infinite-Element Model

The model for soil vibrations from underground railways developed by Yang and Hung [190] is based on a 2.5D finite/infinite-element approach formulated by the same authors [189]. This approach converts conventional plane-strain elements with two degrees-of-freedom (DOFs) per node to 2.5D finite elements by the addition of an extra DOF to account for the out-of-plane wave transmission. The near field is simulated using these 2.5D finite elements, while the farfield is simulated using infinite elements. An example mesh is shown in Figure 1.5.

The method is validated by comparison with the analytical solutions for a harmonic load moving at constant speed on a viscoelastic halfspace. Good agreement is observed

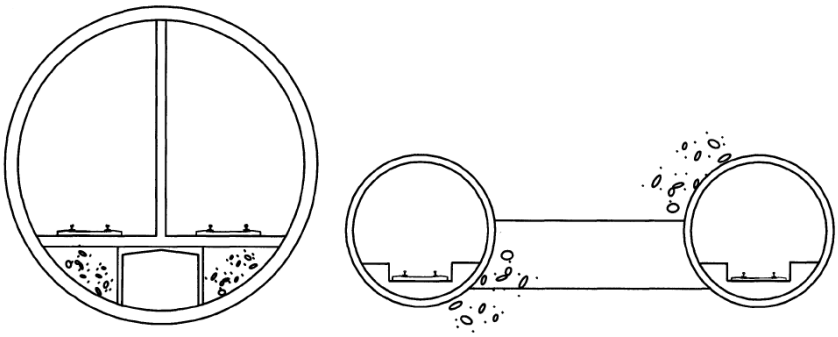

Fig. 1.4 The single-bore and twin-bore tunnel designs considered using the wavenumber FE-BE model (reproduced from Sheng *et al.* [161])

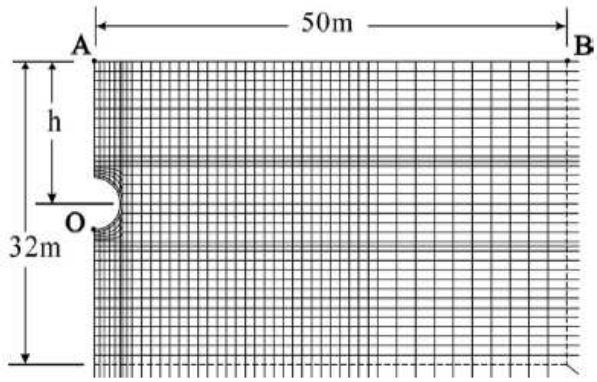

Fig. 1.5 The finite/infinite-element mesh for a half-space (reproduced from Yang & Hung [190])

in the subsonic, transonic and supersonic cases. The steady-state response of an elastic, infinite space and halfspace subject to a vertical, buried point load travelling at a constant, subsonic speed also agrees well with the theoretical solution.

A parametric study of a train moving through a tunnel embedded in a halfspace considers the effect of various train, soil and tunnel properties on the vibration of the ground surface. For dynamic moving loads, this study shows that the train speed does not influence the ground-surface velocity. The ground-surface vibration decreases with increasing soil stiffness and tunnel depth, but is not affected by the thickness of the tunnel lining.

1.4 Directions of the Research

The propagation of ground-borne vibration from underground railways can be disturbing and irritating to those working and living in the vicinity of a railway tunnel. While these vibrations may not be significant enough to result in structural damage, their effect on the health of occupants and the day-to-day operation of vibration-sensitive premises is recognised as an important environmental issue. There is therefore a strong demand for accurate, user-friendly models that can be used by railway and property designers to predict underground-railway vibration levels based on train, track, tunnel, soil and building parameters.

The number of parameters involved in describing the underground environment makes the formulation of a comprehensive model a virtually impossible task. For this reason, the modelling to date focuses either on aspects of the vibration generation and propagation problems, or on a simplified, large-scale underground environment. In considering the latter, the simplifications made in modelling the underground environment are often decided based on available computational power or engineering intuition. These simplifications can be classed into three broad categories: soil characteristics; train/track geometry; and embedded structures. In many cases the inaccuracy introduced by these simplifying assumptions remains unquantified. These inaccuracies are thought to be the primary reason why current predictive models for vibration from underground railways show significant variation from measurements of real systems.

The presence of embedded structures such as piled foundations and neighbouring tunnels are often ignored in predictive models. Yet the proximity of these structures to underground railways suggests that they could play a significant role in the transmission of ground-borne vibration. Questions remain unanswered as to the effect of these structures on the vibration levels in the soil. For example, how do the length, diameter, and number of piles affect the surface vibration levels? Does a neighbouring tunnel have any effect on the vibration levels in the farfield? This dissertation focuses on these two structure types. Through the formulation of accurate models of both piled foundations and twin tunnels, these questions are examined. A comprehensive model of piled foundations subject to vibration from underground railways is developed, and the inaccuracy introduced by disregarding the presence of a neighbouring tunnel is quantified.

The following sections of this literature review examine existing dynamic models for piled foundations and twin tunnels.

1.5 Piled-Foundation Design

The foundation of a building is *"that part of the structure in direct contact with the ground and which transmits the load of the structure to the ground"* (p.38, Tomlinson [169]). There are four major classes of foundation: pad foundations; strip foundations; raft foundations; and bearing piles. The type of foundation to be used is largely determined by the forces acting on the foundation and the environment within which the design is set. For example, bearing piles are commonly used to support structures that must resist uplift loads or lateral forces, or to support those structures which are sited over water. Bearing piles may also be required when shallow foundation designs (pad, strip or raft foundations) are insufficient in accommodating large static loads due to excessive settlements and/or bearing capacity failures. Within the category of bearing piles, there are two possible load-carrying pile designs: end-bearing (or point-bearing) piles; and friction (or cohesion/floating) piles. End-bearing piles are driven through the soft, upper layers of soil until they come to rest on firm material, such as limestone, slate or granite. The carrying capacity of such a pile is derived primarily from the penetration resistance of the material at the toe of the pile [2]. Friction piles penetrate soft soil layers, and transmit loads through the soil by skin friction.

The design of a foundation begins with a thorough site investigation. Information is collected on many aspects, including the site topography and geology, the location of buried services, the presence of chemical and biological contaminants, previous history and use of the site, availability and quality of local construction materials, and the ground-water and soil-strata records. While much of this information is obtained from a general reconnaissance of the site, detailed sub-surface information (such as bedrock and groundwater depths) is obtained though the drilling of boreholes.

The procedure for designing foundations is called the limit-state design procedure, and is given in Eurocode 7: Geotechnical Design [75]. In this code a number of limit states must not be exceeded. These include the ultimate limit state, the serviceability limit states, and the durability limit state. The ultimate limit state ensures avoidance of the risk of collapse or failure that would endanger people; the serviceability limit states ensure that the appearance or useful life of the structure is not damaged through deformations or deflections; and the durability limit state ensures that the structure and foundation can resist attack by substances in the ground or in the environment which could cause weakening or exceeding of the ultimate and serviceability limit states.

To achieve this, many design situations relating to the forces acting on the foundations and the surrounding environment are studied. Two such design situations are directly relevant to this dissertation: the movements and accelerations caused by earth-

quakes, explosions, vibrations and dynamic loads; and the effect of the new structure on existing structures or services. However, it is shown in Section 1.1 that vibration from underground railways seldom affects structural integrity, and is therefore not a primary consideration when designing a foundation using the limit-state design procedure. When piled foundations and underground railways are in close proximity, it is expected that the design of the piled foundation will have a significant influence on the transmission of ground-borne vibration into buildings. There is no evidence in the current foundation design codes that piled foundation designs are optimised for minimal vibration transmission.

1.6 Piled-Foundation Dynamics

The dynamic response of piled foundations has received much attention over the past 30 years, primarily from the research areas of seismic engineering, pile driving and machine-foundation design. This section consists of three parts: a review of single-pile models; a review of multiple-pile models; and a review of experimental investigations into pile dynamics.

1.6.1 Modelling Single-Pile Dynamics

The single pile is the fundamental unit for understanding the dynamic response of piled foundations. This section presents the main features of the most cited single-pile models in chronological order. Particular attention is given to the assumptions governing each model, and the procedures used to validate the models. As the earliest models of piles are extensions of models for embedded footings, this section begins with a brief description of some footing models.

The first dynamic foundation models are those for the dynamic response of footings resting on the ground, such as those developed by Luco & Westmann [108] and Veletsos & Wei [172]. These models are based on the steady-state response of a rigid disc resting on an elastic halfspace, formulated by Bycroft [16].

Models for embedded footings have been published by Beredugo & Novak [12] and Novak & Beredugo [134]. These models are based on an approximate analytical approach formulated by Baranov [9], which assumes that the soil overlying the footing base is composed of a series of infinitesimally thin, independent, horizontal layers. This means that wave energy can only be propagated in a horizontal direction (the plane-strain case), thus for vertical footing motion only shear waves can propagate from the footing.

It is this same approximate analytical approach that is used in Novak's landmark

paper on the dynamic response of a single pile [130], an early example of a model that includes radiation damping effects. The tip of the pile is embedded in rigid bedrock, and the soil around the pile is made up of an infinite number of infinitesimally thin, horizontal layers, perfectly bonded to the pile. The pile itself is modelled as an elastic column or Euler-Bernoulli beam, and the soil reactions are incorporated into the differential equation of the pile harmonic motion in the horizontal, vertical and rotational directions. The solution of this formulation shows that while piles can be used to eliminate or reduce permanent settlement in soil, they cannot eliminate vibration, and dynamic analysis is thus essential for piles subject to dynamic loadings.

Given this need for accurate models of pile dynamics, researchers set about solving the elastic-continuum problem to include wave propagation in all directions, rather than just the plane-strain case. Nogami and Novak [128] evaluate the vertical motion of an elastic soil layer overlying rigid bedrock, and use the result to incorporate the resistance of the soil to deformation into the differential equation of the pile harmonic motion in the vertical direction. By solving this equation they obtain the vibration characteristics of end-bearing piles, which are compared to Novak's model [130]. For slender piles, soft soils and frequencies higher than the first resonance of the layer, the plane-strain assumption models pile behaviour very well. Later papers by the same authors [129, 138] use the same method to evaluate the response of end-bearing piles in horizontal vibration. Comparison with Novak [130] again shows reasonable agreement for slender piles and higher frequencies.

Following the experimental results of Novak and Grigg [137] (see Section 1.6.3), Novak considers the vertical response of floating piles by assuming that the pile tip rests on a halfspace [131]. The reaction at the pile tip is obtained using Bycroft's solution for a circular disc resting on an elastic halfspace [16]. The results show that the tip condition is particularly important for weak soils, and that the agreement between this model and the experimental results of Novak and Grigg [137] improves when the pile is modelled as a floating pile rather than an end-bearing pile.

Novak and Aboul-Ella [133] create a pile model in horizontally layered media. The soil reactions are derived in Novak *et al.* [139] and result from the harmonic motion of a cylindrical body embedded in a viscoelastic continuum that is limited to the plane-strain case. The pile is modelled as a series of finite elements each with length equal to the thickness of the layer within which they are embedded. This theory is compared to the experimental results in Novak & Grigg [137], and gives good agreement. The results of this model are presented in a later paper [135] in the form of tables and charts of dimensionless stiffness constants.

Kuhlemeyer [96] is credited with the first rigorous, numerical solution to the single-

pile problem: an axisymmetric finite-element (FE) analysis of static and dynamic, laterally loaded, floating piles using energy-absorbing boundaries. This model is compared with Novak's model [130] and indicates that the Novak solution tends to overestimate the imaginary part of the compliance relative to that predicted by the FE solution. To assess the vertical vibration of floating piles, Kuhlemeyer formulates an analytical pile model that has an energy-absorbing boundary applied directly to the pile surface [97]. This is done by adopting the assumption for vertical motion used by Novak in [130]: that pure shear waves transmit all energy away from the pile through the soil. To satisfy this assumption, Kuhlemeyer uses the axisymmetric equations of motion presented by Waas [173] to solve the case of a rigid, infinitely long pile. This model is adapted to the case of a finite-length pile by the addition of a damper that simulates the propagation of a P wave in the soil away from the pile tip. This 'lumped mass (LM) model' shows less than 5% error when compared to Novak's model for floating piles [131]. Comparison of the LM model with the solution from the finite-element method that is used by Kuhlemeyer in [96] shows excellent agreement for a pile/soil Young's modulus ratio of 100, but poor agreement at high frequencies for higher ratios. Kuhlemeyer concludes that for wood or concrete piles either the LM model or Novak's model accurately represents vertically loaded, floating piles.

Flores-Berrones and Whitman [40] use a Winkler soil model to analyse the seismic response of an end-bearing pile with a mass attached at the pile head. Both material and geometric damping is neglected in this model.

Krishnan *et al.* [95] use a FE model to analyse the dynamic response of a laterally loaded, free-head, end-bearing pile embedded in a soil deposit with a linearly increasing Young's modulus. The finite-element formulation consists of a finite cylindrical region, discretised using toroidal finite elements, joined to a semi-infinite farfield that uses a 'consistent' boundary matrix to absorb the energy of outward spreading waves. A similar approach is used in Velez *et al.* [105] for the analysis of constrained-head, end-bearing piles.

Chow [20] uses the soil reactions calculated by Novak [130] to derive element matrices for a finite-element analysis of piles. Comparison with Novak's results [131, 133, 135] shows excellent agreement.

Sen *et al.* [157] present a boundary-element formulation for the dynamic response of single piles and pile groups. Green's functions for a periodic point force in an infinite solid, together with the mirror-image method for simulating a halfspace, are used to model the soil as a homogeneous, hysteretic, elastic halfspace. The pile is modelled as a beam/column structure with excitation at the pile head, and equilibrium and compatibility conditions are used to solve for the response. Comparison with Kuhlemeyer's work

[96, 97] shows good agreement in the real part of the response, but the model predicts a more damped system, possibly due to the energy-absorbing boundaries in Kuhlemeyer's model being less than 100% effective. Comparison with Kaynia and Kausel [89] (see Section 1.6.2) shows good agreement when the pile inertia is omitted: Sen *et al.* suggest that the pile inertia is not accounted for in the model by Kaynia and Kausel. Sen *et al.* [158] also develop a model for piles and pile groups in inhomogeneous soils using a similar method. The soil is modelled as a hysteretic, layered medium, using an explicit solution for Green's functions for dynamic loads in the interior of a layered stratum developed by Kausel [85]. The inhomogeneity in the soil is represented by Young's modulus increasing linearly with depth. Comparisons with static and dynamic solutions again show good agreement.

Wolf [180, 181] develops the Green's function for a cone model, based on the response of a loaded, rigid, massless, circular disk to a harmonically varying force. When this disc is resting on the surface of a homogeneous halfspace, the halfspace underneath the disc is modelled as a truncated, semi-infinite rod with a cross-sectional area varying as in a cone. The cone aspect ratio is determined by equating the static stiffness of the cone to that of a disc on a halfspace. Plane cross-sections are assumed to remain plane, and the outward propagation of waves from the disc through the infinite halfspace is enforced by allowing the waves to travel away from the disc only. To extend this model to a fullspace, a double cone is considered, where the waves can propagate both above and below the disc. Dynamic interaction factors are used to model the interaction between neighbouring piles, and comparison of the double-cone model with the solution for a 3x3 floating pile group by Kaynia and Kausel [89] shows very good agreement, particularly in the vertical direction. This approach is extended by Jaya and Prasad [77] to include a layered soil medium.

Three papers written by Rajapakse and Shah [151, 152, 153] derive the Green's functions for the harmonic motion of an elastic bar embedded in an elastic halfspace. A numerical solution scheme based on Lagrange's equations of motion and the discretisation technique is used to solve these equations. Impedance values are calculated for various bar properties, but no comparison with other models in the literature is offered.

Mamoon and Banerjee [115, 116] use a hybrid boundary-element formulation to obtain the response of single piles subject to incident seismic waves. The piles are represented by compressible beam/column elements and the soil by a hysteretic, viscoelastic halfspace. The Green's function that is used in this model is that for a dynamic point force in the interior of a semi-infinite solid, developed in Banerjee and Mamoon [8]. The incident wavefield consists of shear and pressure waves with amplitude constant with soil depth.

Nonlinear effects have been introduced into pile models in recent times. These include poroelastic soils [76, 106, 111, 175] and separation around the pile head [11, 37, 112]. These models use BE and FE formulations to provide an accurate illustration of the behaviour of piles during seismic excitation. Due to the computational expense of these models and their limited application to the linear conditions assumed in the case of vibration from underground railways, it is suggested that the reader refer to these papers for a detailed description of nonlinear methods.

Summary The linear models for single piles can be classified into three broad groups, listed here in order of increasing computation time, which generally corresponds to increasing solution accuracy. The 'dynamic Winkler foundation' approach determines the spring characteristics of the soil by considering outward propagating waves under horizontal plane-strain conditions. Analytical elastic-continuum-type formulations involve integration (direct or through boundary-element type discretisation) of the equations for displacements due to a subsurface point load, disc or other element acting within a halfspace. Dynamic finite-element formulations use axisymmetric or three-dimensional elements and special energy-absorbing boundaries to simulate the effect of outward spreading waves.

1.6.2 Modelling Pile-Group Dynamics

In most circumstances the spacing between the piles present in a pile group is small, and the pile-soil-pile interaction (PSPI) must be taken into account when considering the dynamic response of the pile group. This section considers the methods that have been employed to account for this interaction.

1.6.2.1 Inertial Interaction

In 1971, Poulos [146] introduced the concept of the superposition method for describing the static displacement of a pile group as a function of the static displacement of a single pile carrying the same load as a single pile in the group. This method superposes the interaction between two piles at a time, under the assumption that the presence of the other piles does not affect the motion of the two piles under consideration. The 'interaction factor' expresses the displacement of a pile as a function of the motion of the loaded, neighbouring pile.

Novak and Grigg [137] apply the interaction-factor method to the dynamic behaviour of pile groups, assuming that all piles carry the same pile-head load and that the dynamic behaviour of a pile group at low frequencies can be approximated using the inertial

interaction factors for static displacement. This theory is compared with experimental results, and predicts the general character of the response very well. Later studies by Sheta and Novak [162], Wolf and Von Arx [183] and Nogami [126] show a strong frequency-dependence of the (inertial) dynamic response, resulting in considerable differences between the dynamic and static group effects. As a result of this research, static interaction factors are seldom used for predicting the dynamic behaviour of pile groups. Instead, methods are developed for calculating frequency-dependent interaction factors.

Kaynia and Kausel [89] investigate the inertial interaction between piles in a group using a BE formulation based on the Green's functions for buried, dynamic barrel loads. The results show a strong frequency-dependence of the dynamic response, as a result of constructive and destructive interference taking place between various piles in the group. The results of the superposition method are compared with those obtained from a full three-dimensional analysis and are found to be in good agreement. In the static case the largest portion of the load is always carried by corner piles, while the piles closest to the centre carry the smallest portion. For the dynamic case, however, the forces carried by the piles at some frequencies increase towards the center of the group.

Nogami [127] develops an approach where a pile group is replaced by a single pile for calculation of the pile-head flexibility matrix. A Winkler model with the model parameters defined from a plane-strain condition is used to calculate the pile-head flexibility of a single, isolated pile. Using this result, the interactions between each pair of piles is approximated. Provided that both piles are identical and subjected to identical loads at the pile head, Nogami shows that the pile-head flexibility matrix for the two-pile group can be computed from that of the single, isolated pile.

Various numerical methods are used to model inertial pile-soil-pile interaction in pile groups. These include the computationally intensive method by Kaynia and Kausel [90] that involves the numerical evaluation of Green's functions for layered media, combined with an analytical solution for the dynamic response of piles. Other publications that use numerical methods to evaluate Green's functions include Roesset [155], Sen *et al.* [157], Waas and Hartmann [174] and Wolf and Von Arx [183]. A more recent model is a coupled BE (soil) - FE (pile) model by Padron *et al.* [142].

Approximate and closed-form procedures for calculating inertial interaction factors continue to be proposed, as they offer a more practical and less computationally intensive approach to this problem. Dobry and Gazetas [34] derive an approximate dynamic interaction factor for piles in a homogeneous halfspace using cylindrical wave-propagation equations. Mylonakes and Gazetas [121] use a dynamic Winkler foundation for the pile-soil interface. By considering the wavefield originating from a pile and being diffracted by a neighbouring pile, they obtain frequency-dependent interaction factors as closed-

form solutions. Cairo *et al.* [17, 18] calculate the interaction factors for vertically loaded pile groups embedded in layered soils using the closed-form stiffness matrices derived in Kausel and Roesset [86]. Soil flexibility matrices are summed, based on the simplifying assumption that the interaction forces are the same for all piles in a group. This is strictly only valid for pile groups axisymmetrically arranged in a ring and symmetrical groups consisting of two to four piles. However, this technique gives reasonable agreement with more rigorous theoretical solutions and with field test results of large-scale pile groups.

Talbot [166] uses a three-dimensional BE model of a single pile together with periodic structure theory to model an infinitely long row of piles. The single pile model uses a constant-element BE formulation and a four-element discretisation of the pile's circular circumference. Comparison with the static pile-head compliance results of Poulos and Davis [149] and the dynamic results of Kuhlemeyer [96, 97] and Sen *et al.* [157] show reasonable agreement. Due to computational limitations, Talbot avoids adding extra piles to the soil mesh and instead modifies the single-pile model to take the form of a repeating unit. An infinite number of these repeating units are joined to a single, central, loaded unit using periodic structure theory. In this way the PSPI is inherently accounted for. This model is validated by comparing the results of the single-pile model to a periodic model that has a single, central loaded pile joined to an infinite series of repeating soil units: good agreement is seen. Talbot connects the infinite row of piles to base-isolation and a portal frame model to investigate the response of a base-isolated building. He notes the importance of modelling both the building and the foundation, and shows that neglecting the inertial PSPI can lead to an overprediction of up to 7dB of the base-isolation efficiency.

1.6.2.2 Kinematic Interaction

Makris & Gazetas [114] apply the superposition method to the response of a pile group subject to seismic excitation. Using an approximate analytical approach based on a Winkler foundation and simple wave-spreading equations, they calculate the response of the piles to harmonic, vertically incident shear waves. The displacement of each pile is calculated as the sum of four components: the seismic displacement of the single pile; the kinematic interaction effects; the inertial displacement of the single pile (due to forces acting on the pile cap); and the inertial interaction effects. The interaction effects between the seismically loaded piles are observed to be very small, and the authors propose that such interaction can be neglected. A later paper by Makris & Badoni [113] considers the seismic response of a pile group to oblique-shear and Rayleigh waves.

Using a similar analytical approach to that used by Makris & Gazetas [114], the authors again conclude that the PSPI for seismically loaded piles is small and can be neglected. The analytical method developed in these papers is also used to evaluate soil-pile-bridge seismic interaction [122] and pile groups in layered soils [121].

Other methods for evaluating the response of seismically loaded pile groups include finite-element modelling [182, 184] and boundary-element modelling [92, 115, 116]. More recent models include: a FE model by Javan *et al.* [76] that incorporates nonlinear effects, such as elasto-plastic behaviour of soils and pore-water pressure gradients, in an earthquake-response analysis; a hidden variables model by Taherzadeh *et al.* [165]; and a FE model that uses a Winkler-type medium for the soil and elastodynamic Green's functions for calculating PSPI [32].

1.6.2.3 Pile and Railway Models

There are several examples of models that consider the interaction of railways and piled foundations. In all cases these models consider above-ground railways, and piled foundations that are either supporting the railway or are installed as vibration-reducing measures.

Ju [81] uses finite-element analysis to model a high-speed train travelling along a bridge that is located near a building, as shown in Figure 1.6. The bridge is mounted on piled piers, as shown in Figure 1.7, and three vibration-isolation measures are considered: a retaining wall; piled foundations; and soil improvement. The results show that of the three isolation measures, both the piled foundations and the soil improvement reduce the vertical vibration levels, but only the soil improvement reduces horizontal vibration levels.

A semi-analytical approach to the ground vibration induced by trains moving over elevated bridges is presented by Wu & Yang [187]. Figure 1.8(a) shows the elevated bridge system, and Figure 1.8(b) shows the simplified model. The piers and foundations are represented as rigid bodies, and the pile-soil system is represented by stiffness K_p and damping C_p coefficients, derived by assuming a frequency-independent pile response and static inertial interaction factors. The response of the soil is represented using the stiffness K_s and damping C_s coefficients, and only vertical vibration is considered.

Lu *et al.* [107] investigates the isolation of vibration due to moving loads, using pile rows embedded in a poroelastic halfspace. The influence of the pile on the poroelastic halfspace is modelled using Green's functions for a circular patch load, and the free-wavefield solution of the moving load is used to calculate the halfspace displacements in the absence of the pile. The pile itself is modelled as an elastic bar and is coupled to

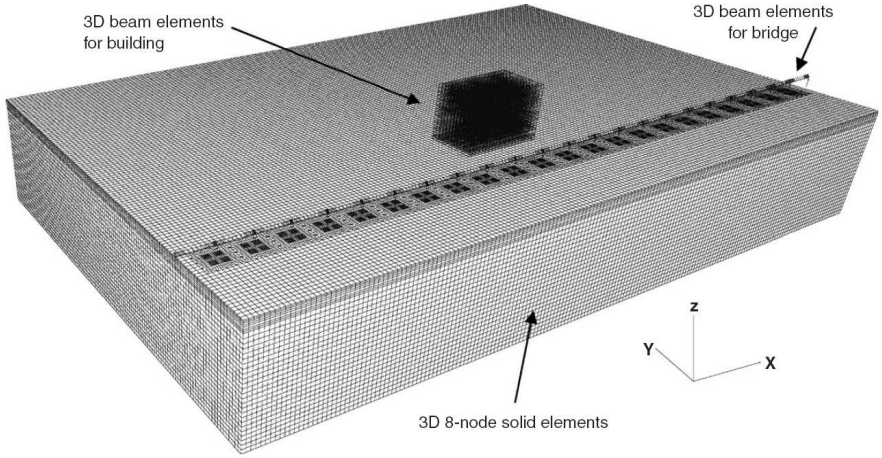

Fig. 1.6 The finite-element mesh (reproduced from Ju [81])

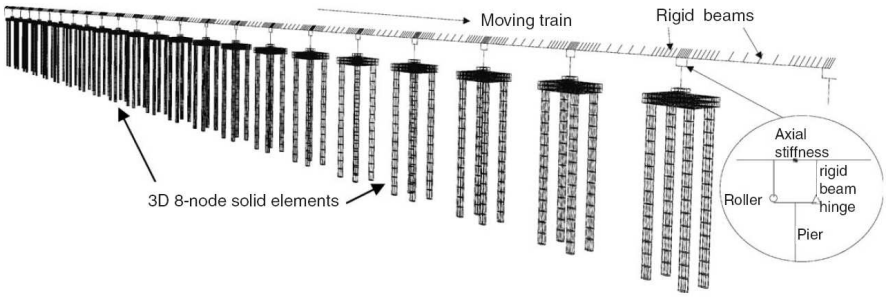

Fig. 1.7 The finite-element mesh of the bridge and foundations (reproduced from Ju [81])

the halfspace through the compatibility of vertical strains. The resulting equations are solved using numerical techniques. Reduction of the poroelastic medium to an elastic medium shows excellent agreement with the average vibration isolation calculated for a ten-pile row by Kattis *et al.* [83]. The authors conclude that longer pile lengths have a better vibration-isolation effect than shorter piles, and that better vibration isolation can be obtained with a smaller net spacing between neighbouring piles.

In concluding the discussion on the dynamic pile-group models, it is noted that in all the literature surveyed by the author of this dissertation, the pile cap, when included in the model, is modelled as a rigid body.

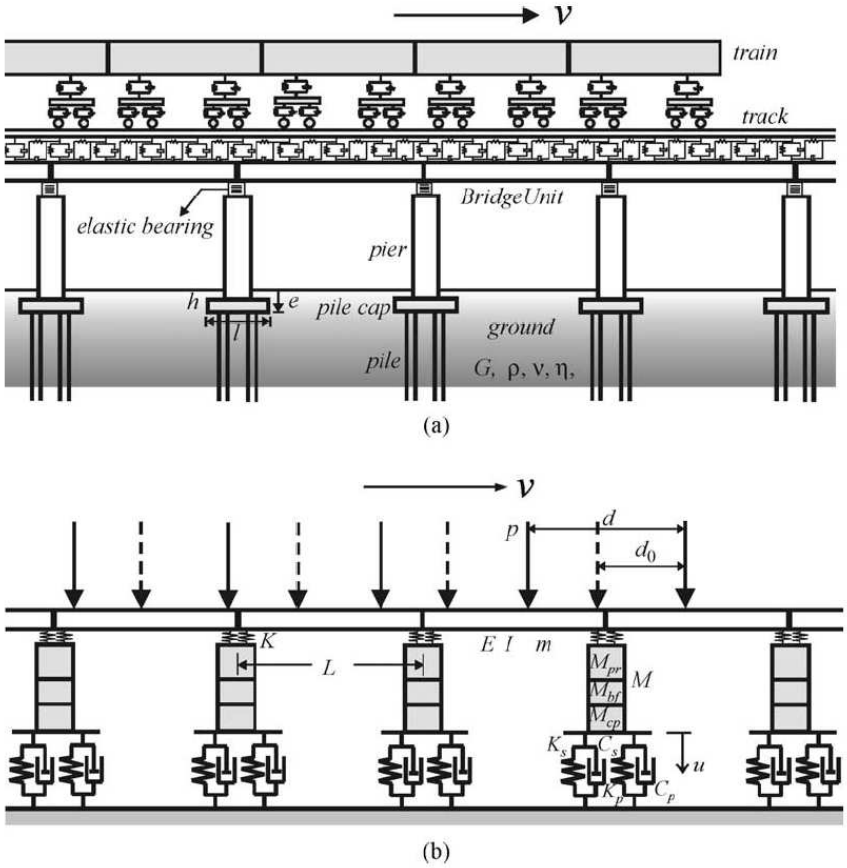

Fig. 1.8 The elevated bridge subject to a train of speed v: (a) schematic; (b) simplified model (reproduced from Wu & Yang [187])

1.6.3 Experimental Investigations into Pile Dynamics

Several experimental investigations into pile dynamics, on both a small and a full scale, have been undertaken. An overview of the experimental methods and findings are presented here.

Novak and Grigg [137] conduct dynamic experiments in the field with individual floating piles and pile groups. The size of the piles is limited to less than 10cm in diameter due to the force and frequency range of the mechanical oscillator attached to the pile head. Comparison of the results with Novak's theory for end-bearing piles [130] shows that the theory predicts the general character of the response very well for single piles. Experimental results also show that the response of the pile group cannot be obtained from the sum of the responses of individual piles, as the displacement of one pile contributes to the displacements of the other piles. The motion of the pile tip has a more profound effect on the vertical response of the pile than on the horizontal response of the pile.

El Sharnouby and Novak [38] conduct dynamic experiments in the field with a group of 102 closely-spaced piles. These piles are connected to a reinforced-concrete cap which is excited using a mechanical oscillator. As the piles are too small to drive into the ground, a large hole is dug and backfilled with a specially designed mixture around the piles. Comparison of the results with the static interaction factors by Poulos [146, 147, 148], the dynamic interaction factors by Kaynia and Kausel [89], and direct dynamic analysis by Waas and Hartman [174] is carried out by Novak and El Sharnouby in [136]. Whilst the static interaction factor provides a good estimate of the measured group stiffness in vertical vibration, the agreement is poor in horizontal vibration. With minor adjustments the dynamic interaction factors provide a reasonable estimate of the vertical and horizontal response, as does the direct dynamic analysis, although it has a tendency to overestimate the damping. The authors propose an equivalent pier concept, where the pile group is replaced by a single equivalent pier (a composite pile) with cross-sectional properties calculated in a way similar to reinforced concrete, as the piles act as 'reinforcement' in the bulk soil. This method shows the best agreement of those examined, but again has a tendency to overestimate the damping.

Han and Novak [53] conduct dynamic experiments on large-scale model piles subject to strong horizontal and vertical vibration, with the aim of evaluating the extent to which the linear theory assumption is applicable. A 3.38m pile is placed into a hole and backfilled using compacted sand before excitation of the order of up to 0.8-0.9g is applied to the pile head. Nonlinear behaviour is observed at large amplitude excitations; however, it is shown that a careful choice of soil parameters for a linear theoretical model can achieve good agreement between theory and experiment. Weakening of the soil around the pile occurs under repeated loadings, resulting in changes in the dynamic response of the pile. The presence of an interface between the backfill and the surrounding soil has little effect on the pile stiffness, but a profound effect on the radiation damping. Nevertheless, the effect of the changes in radiation damping is not as significant as the separation which occurs between the pile and the soil under repeated loadings.

Boominathan and Ayothiraman [14] simulate an elastic halfspace using a clay-filled steel basket in a logarithmic arc spiral shape. Model piles with various lengths are driven into the halfspace and subject to harmonic lateral vibrations with a magnitude of 7-30N and frequency from 2-50Hz. The short, rigid piles behave linearly, even at high magnitudes of the applied force, but the long, flexible piles behave linearly only at low magnitudes of the applied force. No comparison with theory is presented.

The same authors conduct lateral dynamic load tests on 33 different piles at petrochemical complexes in India. These piles are of various types: driven precast concrete; driven cast-in-situ concrete; and bored cast-in-situ concrete; ranging in length from 11m

to 30m. No consideration is given to group effects when the authors perform calculations for comparison with the experimental results. Good agreement between theory and experiment is observed in stiff clay and dense sand sites, however soft clay and loose sand sites offer poorer agreement. The relative contributions of soil nonlinearity and group effects to these results are not clear.

1.7 Twin-Tunnel Dynamics

Many underground railway lines around the world, including those in London, Copenhagen, Taipai, Bangkok and Washington D.C. consist of twin tunnels: one for the outbound direction; and one for the inbound direction. In most cases these tunnels are side-by-side, but occasionally, such as in the case of the Chungho Line in Taipai, the tunnels are piggy-back, with one on top of the other [15]. Whilst it is possible to incorporate both the inbound and outbound railway lines into one large tunnel, this results in a larger volume of excavated material and more involved construction techniques than those required for twin tunnels [54]. For these reasons, the twin-tunnel design is preferred.

The design of tunnels is an involved task, and there are several different approaches which can be used to calculate the static stresses and strains that arise during and post construction. The nonlinear behaviour of soil means that analytical and closed-form solutions cannot be considered as anything but elementary tools to aid in the understanding of tunnel behaviour. For this reason, bedded beam models, finite-element methods and finite-difference methods are the preferred methods of mathematical analysis. There are many examples of these types of models in the literature for static tunnel behaviour [3, 19, 21, 24, 82, 124, 143]. In recent decades observational methods, in which the design is influenced by observations made during tunnel construction, have become increasingly popular. One such method which is now often used is the New Austrian Tunnelling Method (NATM) [39]. NATM involves the use of sprayed concrete as an initial support to the excavation. The deformations and the load carried by this support are carefully monitored and the results are used to prescribe the excavation sequence and validate the design of the permanent lining, which is installed at a later date.

1.7.1 Modelling Twin-Tunnel Dynamics

As with piled foundations, the majority of models for the dynamic behaviour of twin tunnels are found in the field of earthquake engineering. The sole example of a twin-

tunnel model for underground railways is the wavenumber FE-BE model discussed in Section 1.3.3. For this reason, this section will focus solely on the dynamic models of twin tunnels (lined cavities) subject to seismic excitation. The reader is advised that many more models exist for the mutual interaction of twin voids or inclusions with wavefields.

The seismic modelling of twin-tunnel dynamics has its origins in the mutual interaction of multiple obstacles with wavefields, a topic which has been discussed in the literature for over a century and is of interest to many disciplines, including acoustics, electromagnetics and quantum mechanics. This problem is resolved using numerical or analytical methods. The numerical methods include the finite-difference method, the finite-element method and the boundary-element method, all of which can be used to analyse arbitrary-shaped tunnels. The analytical method is the wave function expansion method, described in [144], which expresses the total displacement wavefield as the superposition of the incident, reflected and diffracted wavefields. The seismic waves are assumed to be plane waves, and are expressed as potentials.

An early approximate analytical method was developed by Fotieva [45] for calculating the stresses acting on the twin-tunnel linings during an earthquake. This model was followed by the first model for twin tunnels subject to SH waves, developed by Balendra [7] using the wave function expansion method and the mirror-image technique.

Using a two-dimensional FE formulation, Okumura *et al.* [141] investigate the dynamic behaviour of twin tunnels and a single tunnel to incident SV waves. The degree of interaction between the tunnels is dependent on the tunnel separation distance and the shear-wave velocity of the soil, but not on the tunnel depth. When the tunnels are separated by a distance greater than twice the tunnel diameters, the interaction effects become negligible.

Moore and Guan [120] are the first to develop a three-dimensional, semi-analytical model of a pair of lined, cylindrical cavities subject to seismic excitation. In this model the response of each tunnel is considered separately, and then the method of successive reflections is applied to account for the interaction between them. This method of successive reflections involves repeated calculations of the response of a tunnel to the incident wave produced by the neighbouring tunnel until the solution converges. This method was first proposed by Thiruvenkatachar & Viswanathan [167] and is only suitable as an approximation for long-wavelength frequencies where the wavelength is large compared to the diameter of the cavity. This assumption is valid when considering seismic waves, which have a frequency range of 0-10Hz. However, the frequency range of railway vibration stretches up to 80Hz, making this kind of assumption unfeasible for underground-railway vibration. The halfspace surface is created using the mirror-image

method: a total of four tunnels in an infinite medium are modelled, as the twin tunnels and the incident wavefield are mirrored about the halfspace surface. The results are compared with the two-dimensional model of Balendra [7], and it is shown that there is a significant difference in the response of a three-dimensional model when compared to a two-dimensional model. The results from the two-dimensional model are generally more conservative. The response of the tunnels depends on the spacing of the tunnels, the incident angle of the seismic wave and the ratio of the stiffness of the tunnel lining to the soil. A comparison of a fullspace model with a halfspace model shows that the tunnel-halfspace interactions are negligible when the tunnel embedment depth is greater than the tunnel diameter.

A model for twin tunnels subject to incident, plane, SV waves is developed by Jianwen *et al.* [78], again using the wave function expansion method, which is referred to in this paper as the Fourier-Bessel series expansion method. The surface of the halfspace is simulated using a large, circular model, for which it is been shown that if the circle is large enough, the result converges to the exact solution of a halfspace. The model is verified by showing that the surface displacements tend towards those of the case of a single tunnel when the distance between the two tunnels approaches infinity. Results show that the interaction between the two tunnels significantly amplifies the surface displacements, and that the interaction between the two tunnels decreases with increasing separation distance, as is expected.

Another three-dimensional model is developed by Hasheminejad & Avazmohammadi [54], which is unique in that the soil medium is treated as a poroelastic medium using the Biot model and imperfect bonding can exist between the tunnel liner and the surrounding soil medium. The tunnels are modelled as parallel cylinders of arbitrary size, and the model can be extended to pipelines with the addition of fluid inside the tunnels. The resulting model represents the incident, plane, P and SV wavefields by scalar potentials, and requires "immense" computation times. Hence the calculated results for the stresses induced in the tunnel linings are limited to the frequency range of 0-3Hz.

1.7.2 Experimental Investigations into Twin-Tunnel Dynamics

One of the most extensive experimental investigations into the vibration of twin tunnels was commissioned in 2004 during the design of the GLC/NLC X-band linear collider [159]. This was a collaborative project to build a linear particle accelerator on a site in California (work on this project has now ceased). The collider construction consists of twin tunnels, one housing the beam and the other housing equipment, which includes vibration sources such as a klystron modulator and a water chiller. As beam stability is

essential to the operation of this collider, experimental and numerical investigations into the transmission and isolation of vibration from both the neighbouring tunnel and above-ground sources are conducted. The experimental investigation is conducted in twin tunnels of the Los Angeles Metro, chosen for their similarities in geometry and geology to the proposed design. This investigation involves measurement of the displacements of one tunnel due to impulsive excitation in the neighbouring tunnel. To confirm these results, simulations of the system are carried out using SASSI, a commercial program for solving dynamic soil-structure interaction problems. The lack of both further details about this model and the parameters used to calculate the transmissibility results makes any model comparisons impossible.

Another series of vibration measurements that include the effects of interaction between twin tunnels are those measured on the ground surface near the Bakerloo line in London by Degrande *et al.* [31]. Whilst such results are useful for comparison with large-scale predictive models of underground railway vibration, little information on the interaction between tunnels can be obtained from such measurements.

1.8 Conclusions

The propagation of ground-borne vibration from machine foundations, construction activities, earthquakes, roads and railways into nearby buildings can cause structural-integrity problems and environmental disturbance. Vibration from underground railways seldom causes structural damage, but is disturbing to occupants as it interferes with speech and communication, interrupts concentration, and disturbs sleep. Modifications to the vibration source, transmission path, and building design can reduce the level of vibration in the building. One such modification is the installation of pile rows to scatter and diffract the propagating waves.

During the design phase, the parameters for both piled foundations and railway tunnels are chosen to withstand the static stresses and strains produced during and post-excavation. These static stresses and strains are determined based on an understanding of the design loads and the existing ground conditions. Currently, however, little consideration is given to the design of foundations and twin tunnels to withstand dynamic stresses and strains, such as the low-frequency, small-strain incoming wave fields produced by underground railways. This raises the question: can the designs of such structures be optimised to eliminate the need for costly vibration-isolation measures, while at the same time ensuring structural integrity?

Experimental investigations into the dynamic response of various foundation and

tunnel geometries require measurements to be made before and after the construction of the embedded structures. This is time-consuming and expensive at both the large-scale and small-scale levels. Also, the experimental results are specific to the building, rail network and soil conditions, making it difficult to compare designs and draw general conclusions. This suggests that mathematical modelling is the most efficient method of investigating these types of structures.

Existing pile models account for the dynamic behaviour of a pile or a pile group in response to pile-head loadings, incident seismic waves or above-ground moving loads. No model exists for the dynamic response of a pile or a pile group in response to vibration from underground railways, and there is also little evidence in the literature of any type of dynamic model which accounts for the vibration interaction between neighbouring railway tunnels. This is because of the complexity of these problems, in particular the many factors that must be considered in the modelling of the generation and transmission of vibration from underground trains. A comprehensive model based on numerical techniques such as BE or FE methods is computationally expensive and beyond the capacity of the standard office desktop computer. For this reason, a more user-friendly approach is to seek semi-analytical solutions that have minimal computational requirements. These solutions provide property developers, railway designers and geotechnical engineers with the tools to evaluate various foundation and railway designs. This approach forms the fundamental modelling philosophy that underpins the research presented in this dissertation.

1.8.1 Objectives of the Research

The primary objective of this research is to develop computational models for the vibration response of piled foundations and neighbouring tunnels. These generic models accept a variety of material and geometric parameters, thereby supporting the modelling of specific case studies. In keeping with the philosophy of the Pipe-in-Pipe model, these models seek to capture the essential dynamic behaviour of the system whilst requiring minimal computation times. All computational modelling is undertaken with programs written specifically for this dissertation, using the Matlab technical computing software [117].

The models are formulated in the frequency domain, and all variables, unless otherwise stated, are defined in the frequency domain and represented using complex notation. All loadings are considered to be time-harmonic and steady-state.

The main applications of these piled-foundation and two-tunnel models are: to determine the effect of these embedded structures on ground-borne vibration; to evaluate

objectively the vibration performance of piled-foundation and twin-tunnel designs; and to establish the best design practice. In doing this, it is necessary to develop: an understanding of the soil-structure interaction associated with piles and tunnels, that is, how the presence of the structures alters the ground-borne wavefield; a comprehensive model of a piled foundations, including the interactions between neighbouring piles; and a comprehensive model of a two-tunnel system; as well as to determine appropriate methods of evaluating the vibration performance of piles and twin tunnels.

1.8.2 Outline of the Dissertation

This dissertation falls into three main sections: a single-pile model, multiple-pile models, and a two-tunnel model.

The subject of Chapter 2 is the systematic development and validation of a single-pile model. A simplified model considering only the plane-strain case is outlined and adapted for excitation from incident wavefields. A fully three-dimensional model is developed using an elastic continuum for the soil and a column or Euler-Bernoulli beam for the pile. These models are validated using an existing boundary-element model. Results are computed for the response, both at the pile head and in the farfield for pile-head loadings and incident wavefields. Conclusions are drawn regarding the accuracy and the suitability of each single-pile model.

The single-pile model is extended in Chapter 3 to consider pile groups and the attachment of buildings and pile caps. The method of joining subsystems is used to calculate pile-soil-pile interactions, and the results are compared to those obtained using a boundary-element model and the dynamic stiffness method. The pile groups are incorporated into the underground railway model and methods for simulating an attached building and a pile cap are outlined. The chapter concludes with a case study of two piled-foundation designs that have identical static bearing capacities but vary in their dynamic response.

Chapter 4 presents a unique model for two tunnels embedded in a homogeneous, viscoelastic soil. The vibration response of this two-tunnel system is calculated using the superposition of two displacement fields: one resulting from the tractions acting on the invert of a single tunnel, and the other resulting from the interactions between the two tunnels. By apportioning the displacement fields in this way, it is only ever necessary to consider a single-tunnel system. This chapter begins by outlining the single-tunnel model, and then describes how this model can be extended to account for the interactions between the tunnels. The results of the two-tunnel model are verified for model correctness by considering the symmetry of the displacement distributions

produced by a number of symmetric and antisymmetric force distributions. Vibration fields are analysed over a range of frequencies, tunnel orientations and tunnel geometries. To conclude, the significance of the interactions between two tunnels is quantified.

Based on the models presented in this dissertation, overall conclusions and recommendations for future work are presented in Chapter 5.

Chapter 2

Development of a Single-Pile Model

Numerical solutions of dynamic piled-foundation models, such as those based on the boundary-element method (BEM) or the finite-element method (FEM), generally offer robustness. However, these methods often have excessive formulation and computation times, making them unsuitable for evaluating design changes. For this reason, in this chapter a model is sought which captures the essential dynamic behaviour of the soil and foundation whilst requiring a minimal number of system parameters and an under-five-minute runtime. In formulating this model, simplifying assumptions regarding the linearity of the system are made.

The wavefield produced by an underground railway consists of low strain levels, for which it has been shown experimentally that the assumption of linear soil behaviour is justified [35]. Hence the models presented in this dissertation are based upon the treatment of the soil as a linear, elastic continuum. Nonlinear effects associated with high strain levels, such as slippage and gapping at soil-foundation interfaces, liquefaction of soils and hyperbolic stress-strain relationships, are not caused by the wavefield produced by the passage of trains through underground railways. Nonlinear effects resulting in long-term ground movements, such as consolidation, swelling, and rigid-body movement, are commonly observed to occur after tunnel excavation, especially in low-permeability soils [185]. These movements are a result of the pore pressures in the soil approaching a new equilibrium, and are therefore not considered in this study of harmonic forces. The soil in this dissertation is modelled as a homogeneous continuum, and the presence of soil layers and rigid bedrock is neglected. The absence of a firm substratum is consistent with the modelling of floating piles, and with the London geological formation.

Material damping is included in the piles, and the soil model includes both radiation and material damping. In both cases the material damping is included using a frequency-independent, hysteretic damping ratio.

The consideration of a single pile embedded in a halfspace is the first stage in the development of a comprehensive model for foundations subject to underground-railway vibration. In this chapter, two single-pile models are considered: a model for the plane-strain case and a fully three-dimensional model. Two types of loading are considered: an inertial loading resulting from a harmonic force applied at the pile head; and a kinematic loading resulting from an incident wavefield. Equations for both types of loadings are presented, and the models are validated by comparison with models derived using more complex numerical methods.

2.1 The Plane-Strain Case

When confronted with a complex three-dimensional system, in many cases a good approximation to the dynamic behaviour of the system is obtained with a two-dimensional model. This is the approach adopted by Novak [130, 134] in order to formulate an approximate solution for a single pile embedded in an elastic halfspace. In this section, Novak's model is extended to include underground-railway vibration. Novak's model assumes that the soil is made up of an infinite number of infinitesimally thin, independent, horizontal, elastic layers that extend to infinity. Compatibility between adjacent layers is only satisfied very far from the pile, and at the pile, where a perfect bond exists between the pile and the soil. This corresponds to the plane-strain case. The motion of the pile and the soil is limited to either the vertical or the horizontal plane, depending on the direction of excitation. This approach results in a closed-form solution for the dynamic soil reaction per unit length of the pile.

2.1.1 Novak's Model

The pile is modelled as a column in axial vibration or an Euler-Bernoulli beam in lateral vibration, and is embedded in the infinitesimal soil layers, as shown in Figure 2.1. The pile is subject to a time-harmonic varying force F acting at some distance z_1 from the pile head. This force can either act in the axial (z) direction, or the lateral (y) direction, causing displacements $u(z)$ or $w(z)$, respectively. The axial and lateral directions of motion are decoupled, therefore a force acting in the axial direction does not result in pile displacements in the lateral direction, and vice versa.

Using the approximate analytical approach formulated by Baranov [9], Novak derives the soil reactions for each layer. For axial vibration, the dynamic vertical soil reaction N_z can be written as

$$N_z = GS_z u(z), \tag{2.1}$$

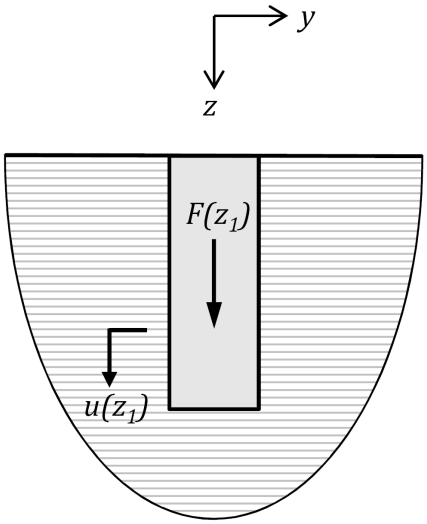

Fig. 2.1 Novak's plane-strain representation of a pile

where G is the soil shear modulus; $u(z)$ is the axial displacement of the pile at depth z;

$$S_z = 2\pi a_0 \frac{J_1(a_0)J_0(a_0) + Y_1(a_0)Y_0(a_0)}{J_0^2(a_0) + Y_0^2(a_0)} + \frac{4i}{J_0^2(a_0) + Y_0^2(a_0)}; \tag{2.2}$$

and a_0 is the dimensionless frequency parameter, given by

$$a_0 = a\omega\sqrt{\frac{\rho}{G}}. \tag{2.3}$$

$J_0(a_0)$ and $J_1(a_0)$ are Bessel functions of the first kind of order zero and one, respectively; $Y_0(a_0)$ and $Y_1(a_0)$ are Bessel functions of the second kind; ρ is the soil density; a is the pile radius; and ω is the angular frequency of interest.

For lateral vibration, the dynamic horizontal soil reaction N_y can be written as

$$N_y = GS_y w(z), \tag{2.4}$$

where the lateral displacement of the pile at height z is $w(z)$; and

$$S_y = 2\pi a_0 \frac{\frac{1}{\sqrt{q}} H_2^{(2)}(a_0)H_1^{(2)}(x_0) + H_1^{(2)}(x_0)H_1^{(2)}(a_0)}{H_0^{(2)}(a_0)H_2^{(2)}(x_0) + H_0^{(2)}(x_0)H_2^{(2)}(a_0)}. \tag{2.5}$$

$H_0^{(2)}(a_0)$ and $H_1^{(2)}(a_0)$ are Hankel functions of the second kind;

$$q = \frac{1-2\nu}{2(1-\nu)}; \tag{2.6}$$

ν is the Poisson's ratio of the soil; and

$$x_0 = \sqrt{q}a_0. \tag{2.7}$$

The pile end conditions are selected to model the essential dynamic behaviour of a floating pile: free end conditions are used in axial vibration, and also in lateral vibration when the piles are to be attached directly to the building. For the case of a piled raft foundation, the pile in lateral vibration is assumed to be constrained against rotation at the pile head. A discussion of the validity of this assumption can be found in Section 2.2.4. The dynamic soil reactions are directly incorporated into the differential equations of motion. For axial motion, pile behaviour is governed by the equation

$$m'\frac{\partial^2 u}{\partial t^2} - EA\frac{\partial^2 u}{\partial z^2} + N_z = 0, \tag{2.8}$$

and for lateral motion, pile behaviour is governed by the equation

$$m'\frac{\partial^2 w}{\partial t^2} + EI\frac{\partial^4 w}{\partial z^4} + N_y = 0. \tag{2.9}$$

The mass per unit length of the pile is m', A is the cross-sectional area, E is the Young's modulus, and I is the second moment of area. When a harmonic excitation F is applied in the z-direction at some point z_1 along the free-free column, the solution to Eq. 2.8 is

$$\frac{u(z)}{F} = \begin{cases} \dfrac{(-\cos\alpha z_1 - \sin\alpha z_1 \tan\alpha L)\cos\alpha z}{EA\alpha\tan\alpha L} & 0 \le z \le z_1 \\ \dfrac{-\cos\alpha z_1 \cos\alpha z}{EA\alpha\tan\alpha L} - \dfrac{\cos\alpha z_1 \sin\alpha z}{EA\alpha} & z_1 \le z \le L, \end{cases} \tag{2.10}$$

where L is the length of the pile, and

$$\alpha^2 = \frac{m'\omega^2 - GS_z}{EA}. \tag{2.11}$$

When a harmonic excitation F in the y-direction is applied at some point z_1 along

the beam, the solution to Eq. 2.9 is

$$\frac{w(z)}{F} = \begin{cases} A_1 e^{\beta z} + B_1 e^{i\beta z} + C_1 e^{-\beta z} + D_1 e^{-i\beta z} & 0 \le z \le z_1 \\ A_2 e^{\beta z} + B_2 e^{i\beta z} + C_2 e^{-\beta z} + D_2 e^{-i\beta z} & z_1 \le z \le L, \end{cases} \tag{2.12}$$

where

$$\beta^4 = \frac{m'\omega^2 - GS_y}{EI}. \tag{2.13}$$

The eight coefficients in Eq. 2.12 are determined by solution of the matrix equation, which results from substitution of the relevant boundary conditions. For a free-free beam, the boundary conditions are

$$\begin{aligned} w(z = z_1^-) - w(z = z_1^+) &= 0 \\ \left(\tfrac{\delta w}{\delta z}\right)_{z=z_1^-} - \left(\tfrac{\delta w}{\delta z}\right)_{z=z_1^+} &= 0 \\ \left(\tfrac{\delta^2 w}{\delta^2 z}\right)_{z=0} &= 0 \\ \left(\tfrac{\delta^3 w}{\delta^3 z}\right)_{z=0} &= 0 \\ \left(\tfrac{\delta^2 w}{\delta^2 z}\right)_{z=L} &= 0 \\ \left(\tfrac{\delta^3 w}{\delta^3 z}\right)_{z=L} &= 0 \\ \left(\tfrac{\delta^2 w}{\delta^2 z}\right)_{z=z_1^+} - \left(\tfrac{\delta^2 w}{\delta^2 z}\right)_{z=z_1^-} &= 0 \\ \left(\tfrac{\delta^3 w}{\delta^3 z}\right)_{z=z_1^+} - \left(\tfrac{\delta^3 w}{\delta^3 z}\right)_{z=z_1^-} &= \tfrac{1}{EI}, \end{aligned} \tag{2.14}$$

resulting in the equation

$$\begin{bmatrix} e^{\beta z_1} & e^{i\beta z_1} & e^{-\beta z_1} & e^{-i\beta z_1} & -e^{\beta z_1} & -e^{i\beta z_1} & -e^{-\beta z_1} & -e^{-i\beta z_1} \\ e^{\beta z_1} & ie^{i\beta z_1} & -e^{-\beta z_1} & -ie^{-i\beta z_1} & -e^{\beta z_1} & -ie^{i\beta z_1} & e^{-\beta z_1} & ie^{-i\beta z_1} \\ 1 & -1 & 1 & -1 & 0 & 0 & 0 & 0 \\ 1 & -i & -1 & i & 0 & 0 & 0 & 0 \\ 0 & 0 & 0 & 0 & e^{\beta L} & -e^{i\beta L} & e^{-\beta L} & -e^{-i\beta L} \\ 0 & 0 & 0 & 0 & e^{\beta L} & -ie^{i\beta L} & -e^{-\beta L} & ie^{-i\beta L} \\ e^{\beta z_1} & -e^{i\beta z_1} & e^{-\beta z_1} & -e^{-i\beta z_1} & -e^{\beta z_1} & e^{i\beta z_1} & -e^{-\beta z_1} & e^{-i\beta z_1} \\ e^{\beta z_1} & -ie^{i\beta z_1} & -e^{-\beta z_1} & ie^{-i\beta z_1} & -e^{\beta z_1} & ie^{i\beta z_1} & e^{-\beta z_1} & -ie^{-i\beta z_1} \end{bmatrix} \begin{Bmatrix} A_1 \\ B_1 \\ C_1 \\ D_1 \\ A_2 \\ B_2 \\ C_2 \\ D_2 \end{Bmatrix} = \begin{Bmatrix} 0 \\ 0 \\ 0 \\ 0 \\ 0 \\ 0 \\ 0 \\ \frac{-1}{\beta^3 EI} \end{Bmatrix}. \tag{2.15}$$

For a beam that is constrained against rotation at $z = 0$ and has a free end at $z = L$,

the boundary conditions are

$$\begin{aligned}
w(z=z_1^-) - w(z=z_1^+) &= 0 \\
\left(\tfrac{\delta w}{\delta z}\right)_{z=z_1^-} - \left(\tfrac{\delta w}{\delta z}\right)_{z=z_1^+} &= 0 \\
\left(\tfrac{\delta w}{\delta z}\right)_{z=0} &= 0 \\
\left(\tfrac{\delta^3 w}{\delta^3 z}\right)_{z=0} &= 0 \\
\left(\tfrac{\delta^2 w}{\delta^2 z}\right)_{z=L} &= 0 \\
\left(\tfrac{\delta^3 w}{\delta^3 z}\right)_{z=L} &= 0 \\
\left(\tfrac{\delta^2 w}{\delta^2 z}\right)_{z=z_1^+} - \left(\tfrac{\delta^2 w}{\delta^2 z}\right)_{z=z_1^-} &= 0 \\
\left(\tfrac{\delta^3 w}{\delta^3 z}\right)_{z=z_1^+} - \left(\tfrac{\delta^3 w}{\delta^3 z}\right)_{z=z_1^-} &= \tfrac{1}{EI},
\end{aligned} \tag{2.16}$$

resulting in the equation

$$\begin{bmatrix}
e^{\beta z_1} & e^{i\beta z_1} & e^{-\beta z_1} & e^{-i\beta z_1} & -e^{\beta z_1} & -e^{i\beta z_1} & -e^{-\beta z_1} & -e^{-i\beta z_1} \\
e^{\beta z_1} & ie^{i\beta z_1} & -e^{-\beta z_1} & -ie^{-i\beta z_1} & -e^{\beta z_1} & -ie^{i\beta z_1} & e^{-\beta z_1} & ie^{-i\beta z_1} \\
1 & i & -1 & -i & 0 & 0 & 0 & 0 \\
1 & -i & -1 & i & 0 & 0 & 0 & 0 \\
0 & 0 & 0 & 0 & e^{\beta L} & -e^{i\beta L} & e^{-\beta L} & -e^{-i\beta L} \\
0 & 0 & 0 & 0 & e^{\beta L} & -ie^{i\beta L} & -e^{-\beta L} & ie^{-i\beta L} \\
e^{\beta z_1} & -e^{i\beta z_1} & e^{-\beta z_1} & -e^{-i\beta z_1} & -e^{\beta z_1} & e^{i\beta z_1} & -e^{-\beta z_1} & e^{-i\beta z_1} \\
e^{\beta z_1} & -ie^{i\beta z_1} & -e^{-\beta z_1} & ie^{-i\beta z_1} & -e^{\beta z_1} & ie^{i\beta z_1} & e^{-\beta z_1} & -ie^{-i\beta z_1}
\end{bmatrix}
\begin{Bmatrix} A_1 \\ B_1 \\ C_1 \\ D_1 \\ A_2 \\ B_2 \\ C_2 \\ D_2 \end{Bmatrix}
=
\begin{Bmatrix} 0 \\ 0 \\ 0 \\ 0 \\ 0 \\ 0 \\ 0 \\ \frac{-1}{\beta^3 EI} \end{Bmatrix}. \tag{2.17}$$

The approximate farfield soil response due to the excitation of the pile results from application of the plane-strain assumption to the radiation of energy from the pile. For axial vibration, only cylindrical SV waves are emitted from the pile, and these waves propagate with the soil shear-wave speed c_s in the radial horizontal direction. All cylindrical waves emanate simultaneously from all points along the pile length and that the waves spread out in phase to form a cylindrical wave front. Based on this, the vertical soil displacement at a given depth $u_s(s,z)$ is expressed as a function of the vertical pile displacement at the same depth $u(z)$ by

$$u_s(s,z) = u(z)\sqrt{\frac{a}{s}} e^{-2\beta_s \omega \frac{s}{c_s}} e^{-i\omega \frac{s}{c_s}}, \tag{2.18}$$

where s is the radial distance from the pile to the point of interest and β_s is the hysteretic material damping ratio for shear waves in the soil.

For lateral vibration, cylindrical P waves are emitted from the pile, propagating with

the dilatational-wave velocity c_p in the transverse direction; and cylindrical SH waves are emitted from the pile, propagating with shear-wave velocity c_s perpendicular to the transverse direction of vibration. Based on this, the horizontal soil displacement at a given depth $w_s(s,z)$ is expressed as a function of the horizontal pile displacement at the same depth $w(z)$ by

$$w_s(s,z) = w(z)\left[\cos^2\phi\sqrt{\frac{a}{s}}e^{-2\beta_p\omega\frac{s}{c_p}}e^{-i\omega\frac{s}{c_p}} + \sin^2\phi\sqrt{\frac{a}{s}}e^{-2\beta_s\omega\frac{s}{c_s}}e^{-i\omega\frac{s}{c_s}}\right], \tag{2.19}$$

where ϕ is the angle between the applied lateral load and the line joining the pile to the point of interest, and β_p is the hysteretic material damping ratio for pressure waves in the soil. The accuracy of these equations is discussed in Section 2.3.2.

2.1.2 Novak's Model subject to an Incident Wavefield

Novak's model calculates the pile response for a specified set of inertial loadings. This model is now extended to incorporate excitation from an incident wavefield in order to calculate the vibration response of a single pile located near an underground railway.

The incident wavefield is represented by the vector of steady-state soil displacements $\mathbf{U}^{incident}$, calculated along the length of the pile using the PiP model. The PiP model used to calculate the displacements is the halfspace model that makes use of the Green's functions derived by Tadeu *et al.* [164].

The incident wavefield is calculated at a discrete number of points (nodes) along the pile, where the spacing between the nodes is small enough to capture the wave behaviour of the incident field. To fulfill the Nyquist criterion, the node spacing is half the shortest wavelength travelling through the soil, but for greater modelling accuracy five nodes per wavelength are used here. The cylindrical pile is discretised into N equally spaced segments along the pile length, as shown in Figure 2.2. At the top and bottom faces of each segment is a node where forces are applied to the pile and the displacements are calculated.

The incident wavefield is incorporated into the pile model using the method of joining subsystems, described in Appendix A. Referring to the variables used in this appendix and to Figure 2.3, subsystem A represents the PiP model and subsystem B represents the column/beam. The force input $x_1(t)$ takes the form of a white-noise unevenness input spectrum applied at the wheel-rail interface, and the displacement output $y_2(t)$ is calculated at each pile node. The governing equation for this system is Eq. A.8, which

can be written in the frequency domain in vectorised form as

$$\mathbf{Y}_2(\omega) = \left[\mathbf{I} + \mathbf{A}_{33}\mathbf{B}_{33}^{-1}\right]^{-1} \mathbf{U}^{incident}. \tag{2.20}$$

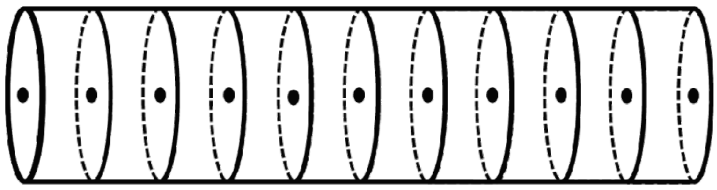

Fig. 2.2 Discretisation of the pile into N equally-spaced segments ($N = 10$ in this case), with $N + 1$ nodes for application of forces and displacements

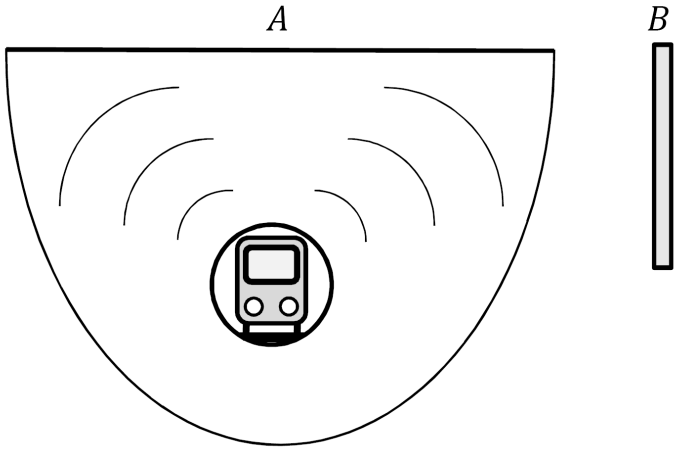

Fig. 2.3 The two separate subsystems that are joined together to obtain a pile-railway model

The frequency-response-function matrix $\mathbf{A}_{33}$ relates the displacement of the soil to the forces acting on the soil. Due to the lack of interaction between each soil layer, no cross-coupling terms can be calculated and hence this matrix is a diagonal matrix of order NxN. The diagonal terms are $\frac{1}{GS_zL/N}$ for axial vibration or $\frac{1}{GS_yL/N}$ for lateral vibration.

The frequency-response-function matrix $\mathbf{B}_{33}$ relates the displacement of the column/beam to the forces acting on the column/beam. The terms in this matrix are obtained by substituting the relevant node location z and force location z_1 into the standard equations for a finite column/beam. These equations are obtained by omitting

the soil reaction terms GS_z and GS_y from the definitions of α and β given in Eqs. 2.11 and 2.13.

2.2 A Three-Dimensional Model

The Novak model is a computationally efficient model of a single pile; however, it assumes plane-strain conditions and it uses simplifying assumptions to obtain equations for calculating soil displacements in the farfield. Later in this chapter it will be shown that the plane-strain assumption and the approximate wave-spreading equations presented in Section 2.1.1 do not provide an accurate means of accounting for soil behaviour. For this reason, and because no computationally efficient, three-dimensional model exists in the literature, a novel single-pile model is developed.

The PiP model consists of two cylinders: the outer cylinder representing the soil is modelled as an elastic continuum with an infinite outer radius and an inner radius equal to the outer radius of the tunnel. The tunnel is modelled as a thin-walled cylinder. This configuration is not solely applicable to a tunnel, but can also be used to represent other infinitely long embedded objects, such as pipelines. The PiP model is computationally efficient, three-dimensional, and has been shown to accurately model soil behaviour [51]. For these reasons, the novel single-pile model is obtained by adapting the PiP model of a tunnel embedded in a fullspace.

There are two major differences between the PiP model and a three-dimensional (3D), single-pile model. Firstly, the tunnel in the PiP model is modelled by a thin-walled cylinder with many cylindrical modes of deformation, as shown in Figure 2.4 and discussed further in Chapter 4. Piles, however, generally have a solid, circular cross-section. As the stiffness of the pile is far greater than that of the soil, the pile's displacement does not vary significantly across the cross-section of the pile. This means that it is only necessary to consider the $n = 0$ out-of-plane flexural mode for axial pile vibration and the $n = 1$ in-plane flexural mode for lateral pile vibration. The motion of the pile can therefore be represented by a column in axial vibration or an Euler-Bernoulli beam in lateral vibration. Whilst this model may neglect small amounts of cross-coupling between different vibration directions, it is expected that the overall behaviour of the pile can be sufficiently captured using these one-dimensional models for axial and lateral vibration. Secondly, the tunnel in the PiP model is infinitely long, whereas the pile has a finite length. If the PiP model is to be adapted for modelling a pile, methods for reducing an infinitely long model to a finite-length model must be formulated. These methods are detailed in Sections 2.2.3 & 2.2.4.

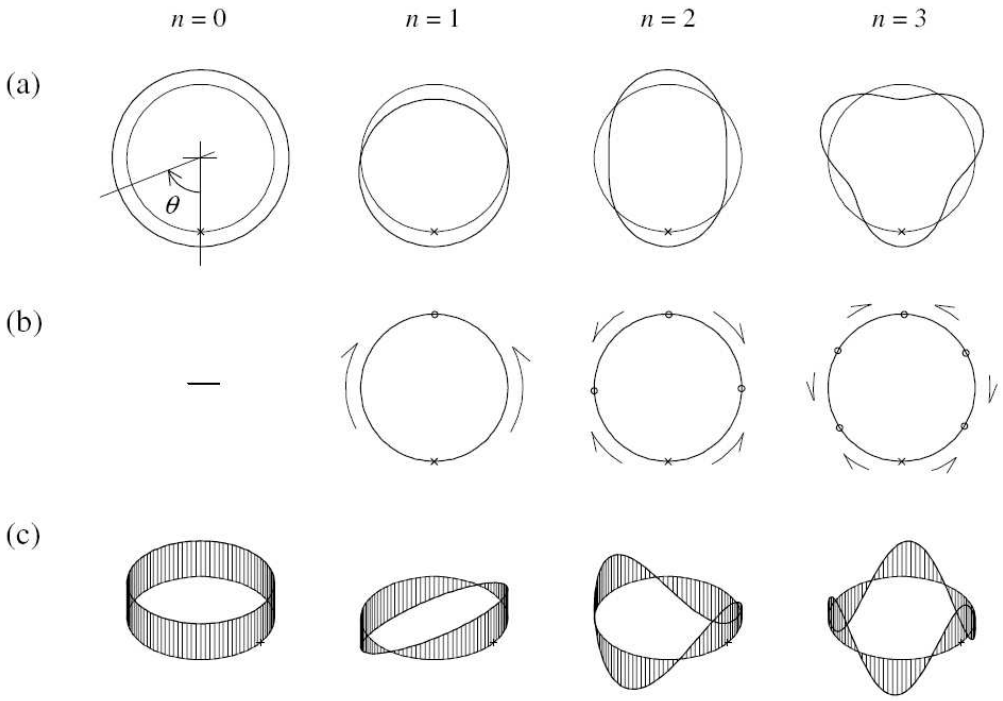

Fig. 2.4 Cylindrical modes of a thin-walled cylinder: (a) in-plane flexural ring modes, corresponding to radial deformations $\tilde{U}_r \cos n\theta$; (b) in-plane extensional ring modes, corresponding to tangential deformations $\tilde{U}_\theta \sin n\theta$; and (c) out-of-plane flexural ring modes, corresponding to longitudinal deformations $\tilde{U}_z \cos n\theta$. The crosses mark the point $\theta = 0$ on the undeformed ring, and the circles in (b) mark the additional nodal points on the ring's circumference (reproduced from Forrest [41])

In the proceeding sections, the PiP model is adapted to model an infinitely long pile embedded in soil and undergoing axial and lateral vibration. The full derivation of the relevant elastic-continuum equations is found in Forrest [41].

2.2.1 Axial Vibration of an Infinite Pile

Consider an infinite column of radius a, defined by right-handed cylindrical coordinates (r, θ, z), that is undergoing axial vibration and embedded in an infinite, elastic continuum. The displacement of the column at any given distance z along the column is invariant through the cross-section, thus the displacement of the column at any point is defined solely by the displacement in the z-direction: $\tilde{U}_z$. The tilde indicates that the variable is defined in the wavenumber (ξ) domain, and the capitalisation indicates that the variable is defined in the frequency domain. The pile displacements in the tangential and radial directions, $\tilde{U}_\theta$ and $\tilde{U}_r$, respectively, are zero (Poisson effects are

neglected). The column is assumed to be perfectly welded to the continuum at the column-continuum interface, so the displacement on the inner surface of the elastic continuum is also defined only by $\tilde{U}_z$. The elastic-continuum equations presented in Forrest [41] are used to obtain the stresses $\{\tilde{T}_{rr}, \tilde{T}_{r\theta}, \tilde{T}_{rz}\}^T$ acting at the outer surface of the column due to some arbitrary imposed displacement distribution $\tilde{U}_z$:

$$\left\{ \begin{array}{c} \tilde{T}_{rr} \\ \tilde{T}_{r\theta} \\ \tilde{T}_{rz} \end{array} \right\} = [\mathbf{T}_\infty]_{r=a} [\mathbf{U}_\infty]^{-1}_{r=a} \left\{ \begin{array}{c} 0 \\ 0 \\ 1 \end{array} \right\} \tilde{U}_z, \tag{2.21}$$

where the elements of the matrices $[\mathbf{T}_\infty]$ and $[\mathbf{U}_\infty]$ are given in Appendix B.

The magnitude of the stress in the $r\theta$ direction is zero, and the magnitude of the stress in the rr direction is negligible, therefore this stress is ignored. The force per unit length $\tilde{F}_{rz}$ arising from the stress $\tilde{T}_{rz}$ acting on the column in the axial (z) direction at the column-continuum interface is obtained by integrating over the column circumference:

$$\tilde{F}_{rz} = \int_0^{2\pi} \tilde{T}_{rz} a d\theta = 2\pi a \tilde{T}_{rz}. \tag{2.22}$$

The force per unit length acting on the column at the column-continuum interface $\tilde{F}_{rz}$ is now related to the displacement distribution imposed at the column-continuum interface $\tilde{U}_z$ by a function of ξ, the longitudinal wavenumber. This function of ξ represents the vertical stiffness per unit length of the elastic continuum, $K_z(\xi)$, and the relationship can be written as

$$\tilde{F}_{rz} = 2\pi a \left[\begin{array}{ccc} 0 & 0 & 1 \end{array} \right] [\mathbf{T}_\infty]_{r=a} [\mathbf{U}_\infty]^{-1}_{r=a} \left\{ \begin{array}{c} 0 \\ 0 \\ 1 \end{array} \right\} \tilde{U}_z = -K_z(\xi) \tilde{U}_z. \tag{2.23}$$

The elastic continuum (the soil) is represented by this stiffness function, which can be evaluated numerically using the above matrix equations. It should be noted that this stiffness function is not constant, but rather represents a function in the wavenumber domain. The soil should not be considered to be an equivalent elastic (Winkler) foundation, as this results in the nonhomogeneous column-on-elastic-foundation equation

$$-EA \frac{\partial^2 u_z}{\partial z^2} + k(z) u_z + m' \frac{\partial^2 u_z}{\partial t^2} = \delta(z), \tag{2.24}$$

where the term $\delta(z)$ represents a unit, harmonic excitation applied at $z = 0$. The Fourier transformation of this column-on-elastic-foundation equation requires a convolution as

both $k(z)$ and u_z are functions of z. The pile should instead be considered as being subject to a resulting force distribution $f_{rz}(z)$ imposed on the pile by the soil, where $f_{rz}(z)$ is the Fourier transformation pair of $\tilde{F}_{rz}(z)$. This force distribution has already been expressed and evaluated as a function of $\tilde{U}_z$ in the wavenumber domain (Eq. 2.23), thus avoiding the solving of a nonhomogeneous equation.

The force imposed by the soil on the pile is equal and opposite to the force imposed by the pile on the soil, and the displacement of the pile is equal to the displacement of the soil at the pile-soil interface. Using the standard equation for the axial vibration of an infinite column with Young's modulus E, cross-sectional area A and mass per unit length m', the equation of this system is

$$-EA\frac{\partial^2 u_z}{\partial z^2} + m'\frac{\partial^2 u_z}{\partial t^2} = \delta(z) + f_{rz}(z). \tag{2.25}$$

Application of the Fourier transformation, substitution of Eq. 2.23 and rearrangement of the resulting equation gives the displacement of the pile subject to a unit loading in the wavenumber domain as

$$\tilde{U}_z(\xi) = \frac{1}{EA\xi^2 + K_z(\xi) - m'\omega^2}. \tag{2.26}$$

The displacement of the pile in the space domain is obtained by application of an inverse Fourier transformation, defined here as

$$u_z(z) = \frac{1}{2\pi}\int_{-\infty}^{\infty} \tilde{U}_z(\xi) e^{i\xi z} d\xi. \tag{2.27}$$

The displacements $\left\{\tilde{U}_r, \tilde{U}_\theta, \tilde{U}_z\right\}^T_{r=R}$ at some radius R elsewhere in the soil can be calculated using

$$\left\{ \begin{array}{c} \tilde{U}_r \\ \tilde{U}_\theta \\ \tilde{U}_z \end{array} \right\}_{r=R} = [\mathbf{U}_\infty]_{r=R} [\mathbf{U}_\infty]^{-1}_{r=a} \left\{ \begin{array}{c} 0 \\ 0 \\ \tilde{U}_z \end{array} \right\}_{r=a}. \tag{2.28}$$

The displacements in space and time $\left\{ \begin{array}{ccc} u_r(z,t) & u_\theta(z,t) & u_z(z,t) \end{array} \right\}^T$ of a point in the soil are obtained by applying an inverse Fourier transformation to the wavenumber-domain displacements $\left\{\tilde{U}_r, \tilde{U}_\theta, \tilde{U}_z\right\}^T$. These displacements are given by

$$\left\{ \begin{array}{c} u_r(z,t) \\ u_\theta(z,t) \\ u_z(z,t) \end{array} \right\} = \frac{1}{2\pi}\int_{-\infty}^{\infty} \left\{ \begin{array}{c} \tilde{U}_r \\ 0 \\ \tilde{U}_z \end{array} \right\} e^{i\xi z} d\xi e^{i\omega t}. \tag{2.29}$$

2.2.2 Lateral Vibration of an Infinite Pile

Consider an infinite beam of radius a undergoing lateral vibration ($n = 1$) and embedded in an infinite, elastic continuum. The lateral displacement of the beam is invariant through the cross-section, thus the displacement of the beam is a function of the radial and tangential components of the displacement: $\tilde{U}_r \cos\theta$ and $\tilde{U}_\theta \sin\theta$, respectively. For some arbitrary imposed lateral displacement of the beam $\tilde{W}$ in the outwards radial direction at $\theta = 0$, it can be written that

$$\tilde{U}_r = -\tilde{U}_\theta = \tilde{W}. \tag{2.30}$$

There is no displacement in the $\tilde{U}_z$ direction, and the beam is assumed to be perfectly welded to the elastic continuum at the beam-continuum interface. The magnitudes of the stresses at the outer surface of the beam of radius a are

$$\left\{ \begin{array}{c} \tilde{T}_{rr} \\ \tilde{T}_{r\theta} \\ \tilde{T}_{rz} \end{array} \right\} = [\mathbf{T}_\infty]_{r=a} [\mathbf{U}_\infty]^{-1}_{r=a} \left\{ \begin{array}{c} 1 \\ -1 \\ 0 \end{array} \right\} \tilde{W}. \tag{2.31}$$

The magnitude of the stress in the rz direction is negligible. The stress in the lateral (y) direction $\tilde{T}_{ry}$ at a given value of θ is written as the vector summation of the stresses in the radial ($\tilde{T}_{rr} \cos\theta$) and tangential ($\tilde{T}_{r\theta} \sin\theta$) directions:

$$\tilde{T}_{ry} = \tilde{T}_{rr} \cos^2\theta - \tilde{T}_{r\theta} \sin^2\theta. \tag{2.32}$$

The force per unit length $\tilde{F}_{ry}$ arising from the lateral stress acting at the beam-continuum interface is obtained by integrating over the beam circumference:

$$\tilde{F}_{ry} = \int_0^{2\pi} (\tilde{T}_{rr} \cos^2\theta - \tilde{T}_{r\theta} \sin^2\theta) a d\theta = \pi a (\tilde{T}_{rr} - \tilde{T}_{r\theta}). \tag{2.33}$$

Thus the force per unit length acting on the beam at the beam-continuum interface $\tilde{F}_{ry}$ is related to the displacement distribution imposed at the beam-continuum interface $\tilde{W}$ by a function of ξ. This function of ξ represents the horizontal stiffness per unit length of the elastic continuum, $K_y(\xi)$, and is calculated from

$$\tilde{F}_{ry} = \pi a \left[\begin{array}{ccc} 1 & -1 & 0 \end{array} \right] [\mathbf{T}_\infty]_{r=a} [\mathbf{U}_\infty]^{-1}_{r=a} \left\{ \begin{array}{c} 1 \\ -1 \\ 0 \end{array} \right\} \tilde{W} = -K_y(\xi) \tilde{W}. \tag{2.34}$$

Following a similar procedure to that for the column, but now using the Euler-Bernoulli equation for the lateral vibration of an infinite beam with second moment of area I, the governing equation of this system is

$$EI\frac{\partial^4 w}{\partial z^4} + m'\frac{\partial^2 w}{\partial t^2} = \delta(z) + f_{ry}(z). \tag{2.35}$$

Application of the Fourier transformation, substitution of Eq. 2.34 and rearrangement of the resulting equation gives the displacement of the pile in the wavenumber domain as

$$\tilde{W}(\xi) = \frac{1}{EI\xi^4 + K_y(\xi) - m'\omega^2}. \tag{2.36}$$

The displacements $\left\{\tilde{U}_r, \tilde{U}_\theta, \tilde{U}_z\right\}^T_{r=R}$ at some radius R elsewhere in the soil can be calculated using

$$\left\{\begin{array}{c}\tilde{U}_r\\ \tilde{U}_\theta\\ \tilde{U}_z\end{array}\right\}_{r=R} = [\mathbf{U}_\infty]_{r=R}\,[\mathbf{U}_\infty]^{-1}_{r=a}\left\{\begin{array}{c}\tilde{W}\\ -\tilde{W}\\ 0\end{array}\right\}_{r=a}. \tag{2.37}$$

The displacements in space $\left\{\begin{array}{ccc} u_r(z,t) & u_\theta(z,t) & u_z(z,t)\end{array}\right\}^T$ are obtained by applying an inverse Fourier transformation to the wavenumber-domain displacements $\left\{\tilde{U}_r, \tilde{U}_\theta, \tilde{U}_z\right\}^T$. These displacements are given by

$$\left\{\begin{array}{c}u_r(z,t)\\ u_\theta(z,t)\\ u_z(z,t)\end{array}\right\} = \frac{1}{2\pi}\int_{-\infty}^{\infty}\left\{\begin{array}{c}\tilde{U}_r\cos\theta\\ \tilde{U}_\theta\sin\theta\\ \tilde{U}_z\cos\theta\end{array}\right\}e^{i\xi z}d\xi e^{i\omega t}. \tag{2.38}$$

2.2.3 Axial Vibration of a Finite Pile

The introduction of a boundary into an infinite system involves the simulation of end conditions, which can be achieved by applying scaled forces and moments to the system. For the case of a single pile undergoing axial vibration, the mirror-image method can be used to simulate zero-force and zero-displacement conditions, which correspond to free and fixed ends, respectively. The mirror-image method is illustrated using finite columns in Appendix C.

This section outlines the application of the mirror-image method to simulate the response of a single, finite-length pile using the superposition of axial forces on a single, infinite pile. It is noted in Section 2.2.1 that, when considered in the space domain, the model of an infinite pile undergoing axial vibration results in a nonhomogeneous

differential equation. The solving of this equation is avoided by considering the problem in the wavenumber domain. As the application of the mirror-image method to piles is best illustrated using equations of motion determined in the space domain, this section begins by ignoring the soil and considering only an infinite column undergoing axial vibration. It is later shown how this method can be extended to include the soil.

Before presenting the equations, an important stipulation regarding the mirror-image method must be made. Whilst it will be shown that exact solutions can be obtained using the mirror-image method on columns or beams, when this method is applied to systems with three-dimensional stress states, errors do arise. This is because the mirror-image method does not produce a stress field which completely satisfies the traction-free boundary conditions at the free surface. For example, when mirror-image vertical forces are applied, the vertical stress at the simulated free surface is zero due to symmetry, but there exists some residual shear stress at the simulated free surface, as the shear stresses do not cancel by symmetry. Similarly, when mirror-image lateral forces are applied, the shear stress at the simulated free surface is zero due to symmetry, but there exists some residual vertical stress at the simulated free surface [157]. Given that in this dissertation the systems to which the mirror-image method is being applied are assumed to be decoupled in the vertical and horizontal directions, it is estimated that the magnitude of the error introduced by using this method is small. However, it is recognised that this error may become significant when displacements perpendicular to the primary direction of excitation are calculated on the simulated free surface. The magnitude of this error is investigated in Section 2.3.

Consider the infinite column shown in Figure 2.5(a). This column is reduced to a harmonically excited, semi-infinite column by applying twice the force P to a mirror-image plane. The resulting semi-infinite system, shown in Figure 2.5(b), has the governing equation

$$Y_1(z) = \frac{-Pie^{-i\alpha z}}{EA\alpha}, \tag{2.39}$$

where

$$\alpha = +\sqrt{\frac{\rho\omega^2}{E}}. \tag{2.40}$$

The stress σ at a distance L from the free end of the semi-infinite column is defined as

$$\sigma = E\left(\frac{dY_1}{dz}\right)_{z=L} = \frac{-Pe^{-i\alpha L}}{A}. \tag{2.41}$$

In order to create a free end condition at $z = L$, and thus simulate a column of finite length L, it is necessary to apply an equal and opposite stress to the column at $z = L$. To do this, two equal forces P^* are applied to the infinite column at $z = -L$ and

$z = L$, respectively, as shown in Figure 2.5(c). These two forces simulate a semi-infinite column with a force P^* acting at $z = L$. The governing equation for this system, shown in Figure 2.5(d), is

$$Y_2(z) = \frac{-P^* i \left(e^{i\alpha z} + e^{-i\alpha z}\right)}{EA\alpha \left(e^{i\alpha L} - e^{-i\alpha L}\right)}, \tag{2.42}$$

and the stress produced by this force at $z = L$ is

$$\sigma = E \left(\frac{dY_2}{dz}\right)_{z=L} = \frac{P^*}{A}. \tag{2.43}$$

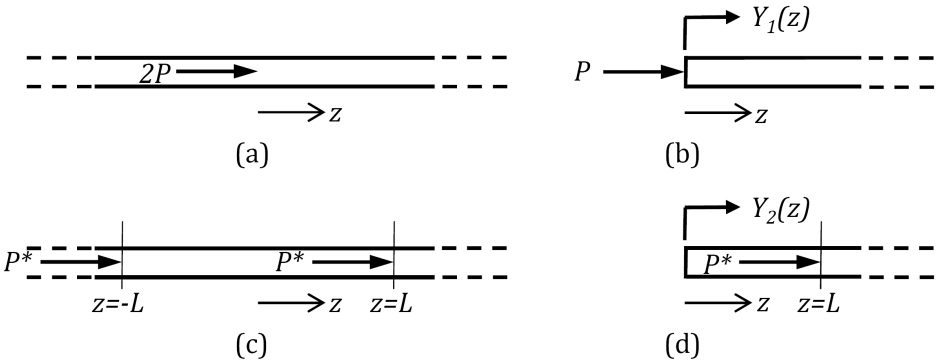

Fig. 2.5 (a) Infinite column with load $2P$ at $z = 0$; (b) semi-infinite column with end loading P; (c) infinite column with load P^* at $z = -L$ and $z = L$; and (d) semi-infinite column with load P^* at $z = L$

In order for this stress to be the equal and opposite of that produced by the original load P (Eq. 2.41), the force equilibrium statement

$$P^* = Pe^{-i\alpha L} \tag{2.44}$$

must be fulfilled.

Superposing the displacements due to the original load, Y_1, and the displacements due to the loads acting at $z = L$ and $z = -L$, Y_2, gives the response

$$Y_1(z) + Y_2(z) = \frac{-Pi \left(e^{-i\alpha 2L} e^{i\alpha z} + e^{-i\alpha z}\right)}{EA\alpha \left(1 - e^{-i\alpha 2L}\right)}, \tag{2.45}$$

which is the governing equation for a free-free finite column of length L subject to excitation P at $z = 0$. This demonstrates the application of the mirror-image method to infinite systems in order to simulate the response of a finite system.

Extension of this procedure to the infinite cylinder-soil system results in the approximate axial driving-point response of a finite pile. The procedure is outlined below.

1. Calculate the response of the column-soil system using Eq. 2.26, when twice the unit force is applied to the column at $z = 0$.

2. Use Eq. 2.29 to transform this response into the space domain, then calculate the force $EA\frac{du}{dz}$ at $z = L$.

3. Apply scaled mirror-image forces $P_x^* = -EA\left(\frac{du}{dz}\right)_{z=L}$ to the column at $z = L$ and $z = -L$, both acting in the same direction, and calculate the response of the column-soil system in the z-domain using Eq. 2.26 & 2.29.

4. Superimpose the displacement response calculated in Step 2 and the displacement response from the mirror-image forces.

2.2.4 Lateral Vibration of a Finite Pile

An end condition for an Euler-Bernoulli beam undergoing lateral vibration requires the specification of two boundary conditions. For example, a free end is characterised by zero shear force and zero moment acting on the end; a pinned end is characterised by zero displacement of the end and zero moment acting on the end; and a fixed end is characterised by zero displacement and zero rotation of the end. There are four parameters of interest for Euler-Bernoulli beams undergoing lateral vibration: displacement w, rotation $\frac{dw}{dz}$, moment $-EI\frac{d^2w}{dz^2}$, and shear force $-EI\frac{d^3w}{dz^3}$. The sign convention used here defines the positive direction of the shearing force as acting upwards on the left of the elemental section, and the positive direction of the moment on the left of the elemental section as acting clockwise. Figures 2.6 & 2.7 show the variation of these four parameters for two cases: a shear force is applied to an infinite beam; and a moment is applied to an infinite beam.

When using the mirror-image method, only two of the four parameters can be set to known values at any given position. To demonstrate this, consider the infinite beam shown in Figure 2.8(a), where a shear force P applied at $z = L$ has been mirror imaged about the $z = 0$ plane. As both forces are acting in the same direction, the parameters that are odd functions (rotation and shear force) will sum to zero at $z = 0$, whereas the parameters that are even functions (displacement and moment) will not sum to zero at $z = 0$. Now consider the infinite beam shown in Figure 2.8(b), where the forces are acting in opposite directions. In this case the even functions will sum to zero at $z = 0$ whereas the odd functions will not sum to zero at $z = 0$. When moments acting in the

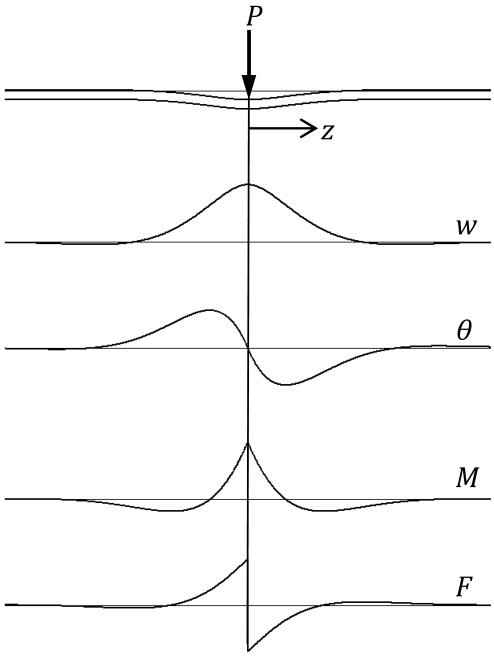

Fig. 2.6 Infinite beam loaded with force P. Shown from top to bottom: schematic of the loaded beam; displacement w; rotation $\theta = \frac{dw}{dz}$; moment $M = -EI\frac{d^2w}{dz^2}$; and shear force $F = -EI\frac{d^3w}{dz^3}$

same direction are applied to the infinite beam, the parameters that are odd functions (displacement and moment) will sum to zero at $z = 0$, whereas the even functions (rotation and shear force) will not sum to zero at $z = 0$. When these moments act in opposite directions, the rotation and shear force will sum to zero at $z = 0$, whereas the displacement and moment will not.

Two important observations result from this. Firstly, the creation of a free or fixed end on an infinite beam requires the application of both mirror-image shear forces and moments. Secondly, in order to ensure a parameter is equal to zero at the mirror-image plane, the sign of one, and only one, of the mirror-image shear forces must be opposite to the sign of one of the mirror-image moments. For example, to produce zero rotation at $z = 0$, both the shear forces must act in the same direction, whereas the moments must act in opposite directions.

This section outlines a procedure for simulating a finite beam with known force P applied at one end, and a free end at $z = L$, from an infinite beam. The infinite beam is reduced to a semi-infinite beam with shear force P and zero rotation at the end by

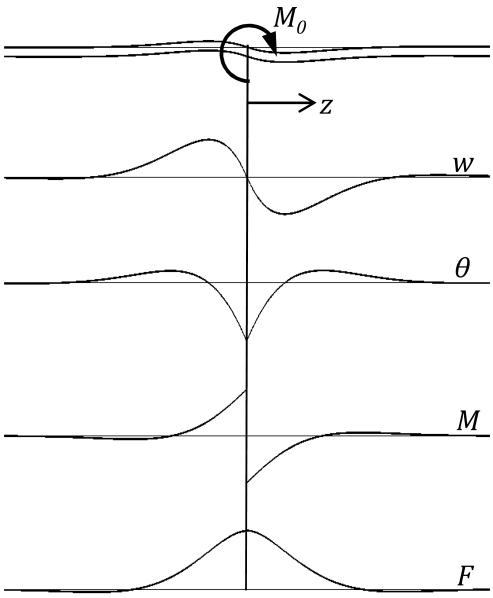

Fig. 2.7 Infinite beam loaded with moment M_0. Shown from top to bottom: schematic of the loaded beam; displacement w; rotation $\theta = \frac{dw}{dz}$; moment $M = -EI\frac{d^2w}{dz^2}$; and shear force $F = -EI\frac{d^3w}{dz^3}$

applying a shear force $2P$ at $z = 0$. The loaded infinite beam is shown in Figure 2.9(a). The equation of motion for this Euler-Bernoulli beam has a general solution of the form

$$\frac{W_1(z)}{P} = A_1 e^{\beta z} + B_1 e^{i\beta z} + C_1 e^{-\beta z} + D_1 e^{-i\beta z} \qquad 0 \leq z \tag{2.46}$$

where

$$\beta = +\sqrt[4]{\frac{m'\omega^2}{EI}}. \tag{2.47}$$

The terms $e^{\beta z}$ and $e^{i\beta z}$ represent waves travelling from $z = \infty$ towards $z = 0$, hence $A_1 = B_1 = 0$. Substitution of the two boundary conditions

$$\begin{array}{rcl} \left(\frac{\delta W_1(z)}{\delta z}\right)_{z=0} & = & 0 \\ \left(\frac{\delta^3 W_1(z)}{\delta^3 z}\right)_{z=0} & = & \frac{P}{EI} \end{array} \tag{2.48}$$

results in the equation

$$W_1(z) = \frac{-P\left(ie^{-i\beta z} + e^{-\beta z}\right)}{2EI\beta^3}. \tag{2.49}$$

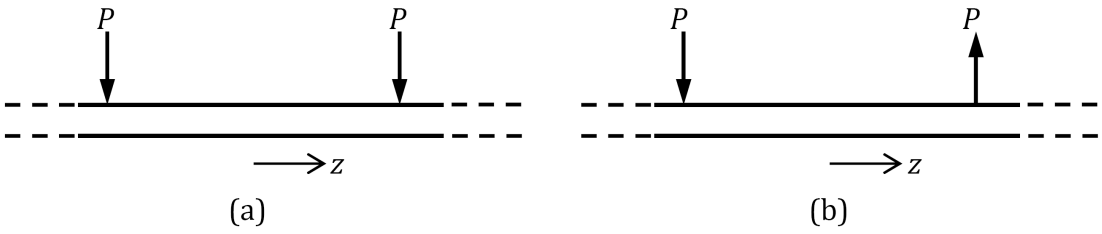

Fig. 2.8 (a) Infinite beam loaded with mirror-image forces P acting in the same direction; and (b) infinite beam loaded with mirror-image forces P acting in opposite directions

This is also the equation of motion as for the system shown in Figure 2.9(b). In producing the load P at the end of the semi-infinite beam, the beam is constrained to have zero rotation at the end, meaning that this end is not by definition 'free'. To allow free rotation of this end, it is necessary to apply a moment at $z = 0$. This moment would produce an additional force acting at the end. Thus, to obtain a free end, the magnitude of the forces and moments applied to the infinite beam must be suitably scaled to produce a net force of P and a net moment of zero acting on the end of the semi-infinite beam. This method is straightforward to implement when considering a simple, continuous system such as the Euler-Bernoulli beam. However, when the displacements of a more complex system are being evaluated at discrete points, as is the case for the three-dimensional pile model, the calculation of the second and third derivatives corresponding to the moment and force, respectively, introduces a high level of numerical error in the area of the applied loadings. For this reason, a force (and no moment) is applied to the infinite beam at $z = 0$ such that there is no rotation at $z = 0$. This is a reasonable assumption as many piled foundations have the piles rigidly connected to a pile cap. This connection impedes pile-head rotation due to the large mass of the pile cap. The neglecting of the rotational component of motion is further justified by the results of Talbot's model [166]. For an infinite pile row connected to an infinite building, the rotational motion represents the smallest contribution to the mean power flowing into the building of the three components of motion (vertical, horizontal and rotational) that are considered. The size of this contribution generally varies between $\pm 5\%$.

To create a free end at $z = L$, it is first necessary to determine the moment and the force acting at $z = L$ on the semi-infinite beam. These are obtained by differentiating the equation of motion, Eq. 2.49. The moment is written as

$$-EI\left(\frac{d^2W}{dz^2}\right)_{z=L} = \frac{P\left(-ie^{-i\beta L} + e^{-\beta L}\right)}{2\beta}, \tag{2.50}$$

and the shear force is written as

$$-EI\left(\frac{d^3W}{dz^3}\right)_{z=L} = \frac{P\left(-e^{-i\beta L} - e^{-\beta L}\right)}{2}. \tag{2.51}$$

Mirror-image moments and forces are then applied to the infinite beam to create zero net moment and zero net force at $z = L$. The direction of the forces and moments are chosen to preserve the zero-rotation condition at $z = 0$, and to ensure that no additional force is applied at $z = 0$. Thus both the forces act in the same direction, and the moments act in opposite directions, as shown in Figure 2.9(c). The equation of motion for this system is

$$\begin{aligned} W_2(z) = &\frac{-F\left(ie^{-i\beta(z+L)} + e^{-\beta(z+L)} + ie^{i\beta(z-L)} + e^{\beta(z-L)}\right)}{4EI\beta^3} \\ &+ \frac{M\left(e^{-i\beta(z+L)} - e^{-\beta(z+L)} + e^{i\beta(z-L)} - e^{\beta(z-L)}\right)}{4EI\beta^2}. \end{aligned} \tag{2.52}$$

Setting the forces and moments at $z = L$ to be equal and opposite to those on the semi-infinite beam (Eq. 2.50 & 2.51) results in

$$\begin{aligned} \frac{P\left(ie^{-i\beta L} - e^{-\beta L}\right)}{2\beta} = &\frac{F\left(-ie^{-i\beta 2L} + e^{-\beta 2L} - i + 1\right)}{4\beta} \\ &- \frac{M\left(e^{-i\beta L} + e^{-\beta L} + 2\right)}{4} \end{aligned} \tag{2.53}$$

and

$$\begin{aligned} \frac{P\left(e^{-i\beta L} + e^{-\beta L}\right)}{2} = &\frac{F\left(-e^{-i\beta 2L} - e^{-\beta 2L} + 2\right)}{4} \\ &- \frac{M\beta\left(-ie^{-i\beta 2L} - e^{-\beta 2L} + i + 1\right)}{4}. \end{aligned} \tag{2.54}$$

These two equations are solved simultaneously to determine values for F and M. Substitution of these values into Eq. 2.52 gives the equation of motion for the system shown in Figure 2.9(d), which, when summed with the equation of motion for the semi-infinite beam shown in Figure 2.9(b), gives the equation of motion of the finite beam shown in Figure 2.9(e).

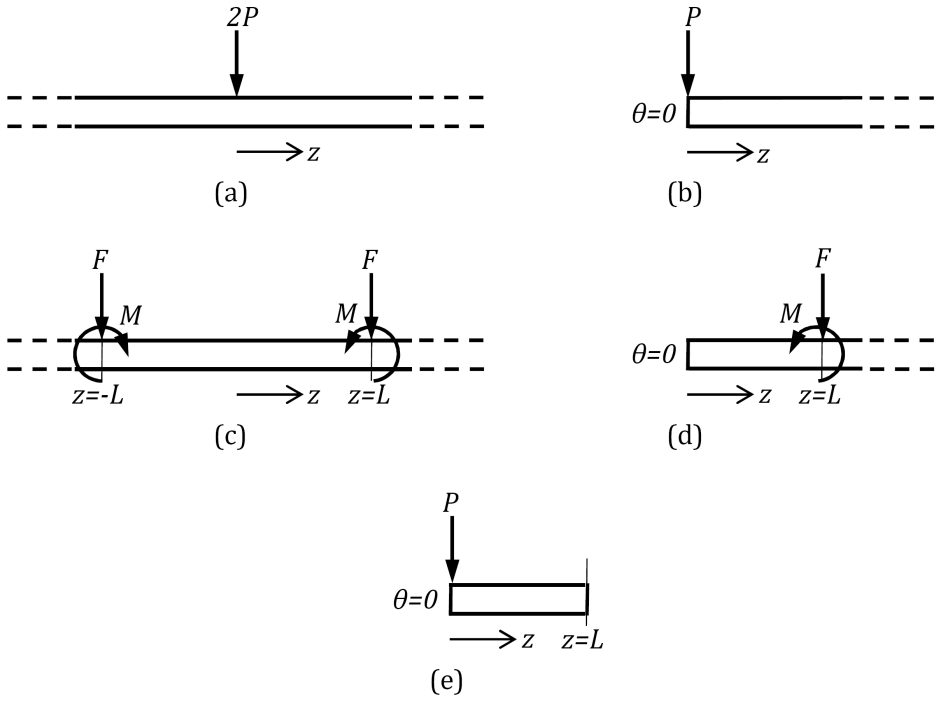

Fig. 2.9 (a) Infinite beam loaded with force $2P$ at $z = 0$; (b) semi-infinite beam loaded with force P and rotation-constrained at $z = 0$; (c) infinite beam loaded with forces F and moments M at $z = -L$ and $z = L$; (d) semi-infinite beam loaded with force F and moment M at $z = L$; and (e) finite beam loaded with force P and rotation-constrained at $z = 0$

Extension of this procedure to the infinite beam-soil system results in the approximate lateral driving-point response of a finite pile. The procedure is outlined below.

1. Apply twice the unit force to the infinite beam, and calculate the response of the beam-soil system using Equation 2.36.

2. Transform this response into the space domain using Equation 2.38, and calculate the moment $-EI\frac{d^2w}{dz^2}$ and shear force $-EI\frac{d^3w}{dz^3}$ distributions along the beam. Obtain the shear force and moment at $z = L$.

3. Apply unit, mirror-image forces acting in the same direction at $z = L$ and $z = -L$ to the beam, and calculate the response of the beam-soil system in the space domain using Eq. 2.36 and the inverse Fourier transformation.

4. Calculate the response of the beam-soil system in the space domain to unit, mirror-image moments acting in opposite directions at $z = L$ and $z = -L$. Note that it

is not necessary to apply the moments directly to the beam, as it can be observed from Figures 2.6 & 2.7 that the response of the system to a unit moment is the derivative of the response of the system (in the space domain) to a unit force.

5. Calculate the resulting moment and force at $z = L$ due to the mirror-image forces, and calculate the resulting moment and force at $z = L$ due to the mirror-image moments. Scale the mirror-image moments and forces such that the net moment and the net force produced at $z = L$ are equal and opposite to those moments and forces obtained in Step 2.

6. Superimpose the displacement responses due to the unit force from Step 1, and the mirror-image forces and moments from Step 5.

2.2.5 Incident Wavefields

As with Novak's model, the incident wavefield generated by the PiP model is incorporated into the three-dimensional model using the method of joining subsystems. However, as the three-dimensional model represents an infinite system discretised in the wavenumber domain, the coupling equation for this system (Eq. A.8) is written in vectorised form in the wavenumber domain, rather than the space domain, as

$$\tilde{\mathbf{Y}}_2(\omega) = \left[\mathbf{I} + \tilde{\mathbf{A}}_{33}\tilde{\mathbf{B}}_{33}^{-1}\right]^{-1} \tilde{\mathbf{U}}^{incident}. \tag{2.55}$$

The frequency-response-function matrix $\tilde{\mathbf{A}}_{33}$ relates the displacements at the cylindrical void to the forces acting on the cylindrical void. This has already been determined in the form of the vertical or horizontal soil stiffness of the elastic continuum. Hence in axial vibration

$$\tilde{\mathbf{A}}_{33} = \frac{1}{K_z(\xi)}, \tag{2.56}$$

and in lateral vibration

$$\tilde{\mathbf{A}}_{33} = \frac{1}{K_y(\xi)}. \tag{2.57}$$

The frequency-response-function matrix $\tilde{\mathbf{B}}_{33}$ relates the displacement of the column/beam to the forces acting on the column/beam. This is given by the equation for an infinite column in the wavenumber domain, written as

$$\tilde{\mathbf{B}}_{33} = \frac{1}{EA\xi^2 - m'\omega^2}; \tag{2.58}$$

or an infinite beam in the wavenumber domain, written as

$$\tilde{\mathbf{B}}_{33} = \frac{1}{EI\xi^4 - m'\omega^2}. \tag{2.59}$$

The incident wavefield, $\tilde{\mathbf{U}}^{incident}$, is required in the wavenumber domain, however the output from the PiP model is given at a series of discrete points in the space domain. The transformation from the space domain to the wavenumber domain involves a discrete Fourier transformation, calculated numerically at a sufficiently large number of discrete points to capture all of the displacement response. The number of discrete points required in the PiP model for conversion from the wavenumber domain to the space domain without any loss of dynamic behaviour is $N = 2048$. The calculation of the incident wavefield at every one of 1024 points along the length of the semi-infinite pile represents a considerable computational investment, limiting the efficiency of the formulation. Hence it is preferable to calculate the incident wavefield at a sufficient number of points in the space domain to represent accurately the wavefield whilst maintaining computational efficiency. Due to the damping influence of the soil, it is expected that those points at a considerable distance from the finite-pile region will have little influence on the response of the finite pile. For this reason, the response of the finite pile subjected to an incident wavefield can be determined using a reduced number of points in the space domain. This is discussed further in Section 2.3.3.

Substitution of the frequency-response-function matrices and the incident wavefield into Eq. 2.55 determines the displacement of the semi-infinite pile subject to an incident wavefield. The mirror-image method in Sections 2.2.3 & 2.2.4 is then used to convert the semi-infinite pile to a finite pile.

2.3 Validation and Comparison of Models

The single-pile model is an idealised system; therefore, validation of the numerical models derived above cannot easily be achieved by comparison with experimental results. Instead, the numerical models that are derived in this chapter are compared with the output of a more complex numerical method, namely a boundary-element method. The frequency range of interest for underground-railway vibration is 1-80Hz; therefore results will be presented for this frequency range. For models which include only piles and no railway, the results are presented in terms of dimensionless frequency: $a_0 = \frac{\omega a}{c_s}$.

The model presented for comparison is a boundary-element model (BEM) developed by Talbot [166] and furthered by Coulier [25]. This model incorporates the vertical,

horizontal and rotational motion of a single, floating pile embedded in a homogeneous, isotropic, linear-elastic halfspace. The halfspace is modelled using a constant-element BE formulation, and a four-element (square) or eight-element (octagonal) discretisation of the pile's circular circumference. A steady-state, time-harmonic loading is applied to the pile head. The pile is modelled as a column in axial vibration, or a Timoshenko beam in lateral vibration. Each node has three fully-coupled, orthogonal, displacement degrees-of-freedom: two lateral degrees-of-freedom and one vertical degree-of-freedom. The discretisations used in the BEM represent the pile as having either a solid, square cross-section, with the length of the diagonal being equal to the diameter $2a$ of the pile, or a solid, octagonal cross-section, with diameter $2a$.

The three-dimensional model is discretised in the longitudinal direction using 2048 points at a spacing of 0.25m. This is the same number of points and the same spacing as is used in the PiP model. This spacing produces at least five nodes per wavelength at 200Hz, and the number of points is sufficient to capture all of the features of the displacement response in the soil. The parameters used to calculate the results in Sections 2.3.1 & 2.3.2 are given in Table 2.1. The pile is made of concrete, and the soil parameters are representative of London clay. The material damping ratios are included in the wave speeds, such that the complex shear wave speed c_s^* is given by $c_s^* = c_s(1 + i2\beta_s)$, and the complex pressure wave speed c_p^* is given by $c_p^* = c_p(1 + i2\beta_p)$.

Table 2.1 Pile and soil parameters used for calculating the results of the single-pile models

Pile Properties	*Symbol*	*Value*
Density	ρ	2800kgm^{-3}
Young's Modulus	E	40GPa
Poisson's Ratio	ν	0.30
Length	L	20m
Radius	a	$\frac{1}{2\sqrt{2}}$m
Hysteretic Material Damping Ratio (Shear Wave)	β_s	0.05
Hysteretic Material Damping Ratio (Pressure Wave)	β_p	0.05
Soil Properties	*Symbol*	*Value*
Density	ρ	2250kgm^{-3}
Shear Modulus	G	90MPa
Poisson's Ratio	ν	0.40
Shear Wave Speed	c_s	200ms^{-1}
Pressure Wave Speed	c_p	490ms^{-1}
Hysteretic Material Damping Ratio (Shear Wave)	β_s	0.03
Hysteretic Material Damping Ratio (Pressure Wave)	β_p	0.03

2.3.1 The Infinite Pile

The validation of the three-dimensional model begins with consideration of the infinitely long pile in axial or lateral vibration. The equations for the infinite pile, presented in Sections 2.2.1 and 2.2.2, are compared to a modified version of the BEM. To simulate an infinitely long pile, the free surface has been removed from the BEM and the pile has been extended to a length that is sufficient to model the behaviour of the infinite pile. Further details of this work are presented in Coulier [25]. Two sets of results using the BEM are calculated: a pile of length $L = 40$m with an octagonal cross-section; and a pile of length $L = 100$m with a square cross-section.

The response of the infinite pile as a function of non-dimensional frequency $a_0 = \frac{\omega a}{c_s}$ is presented in Figures 2.10 and 2.11. The frequency range shown in these figures corresponds to 0-80Hz. In both of these figures the magnitude and the phase for the driving-point response are calculated. The response of the infinitely long pile in both axial and lateral vibration varies smoothly with frequency. No resonant peaks are observed in the response, as is expected for an infinitely long structure with a rigid cross section.

The phase of the driving-point response of a pile will approach zero as the frequency tends to zero, as the static driving-point response is purely real. A phase artefact, due to the use of the correspondence principle for material damping, exists in the models near zero frequency. The phase of the response approaches a number close to, but not equal to, zero.

The agreement between the three-dimensional model and the BEM improves when the length of the BE pile increases and when the pile's circular cross-section is represented by an octagon rather than a square. It is expected that the addition of more boundary elements around the pile circumference would further improve the agreement between the two models.

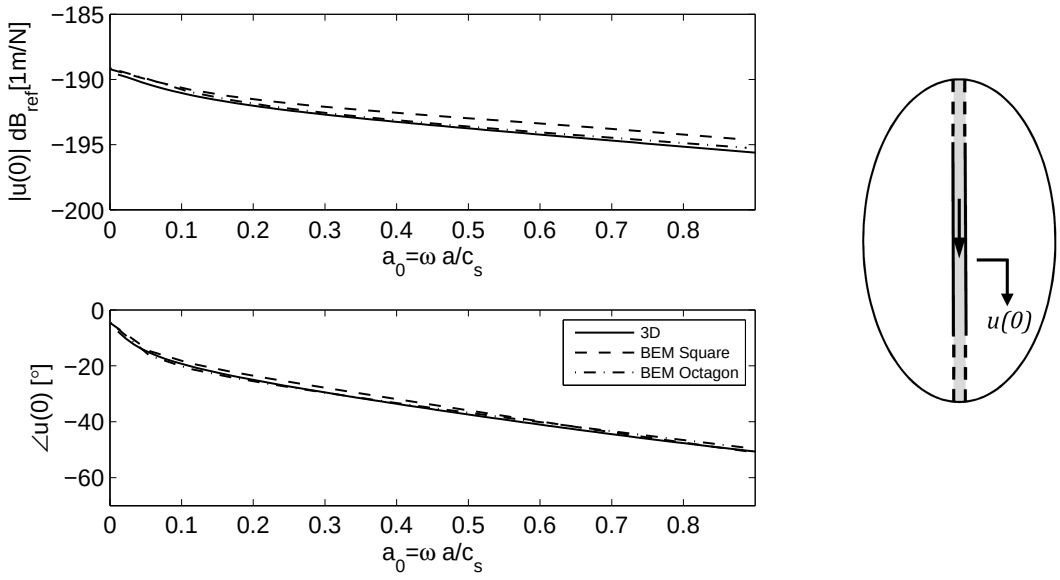

Fig. 2.10 The magnitude and phase of the axial driving-point response of an infinite pile

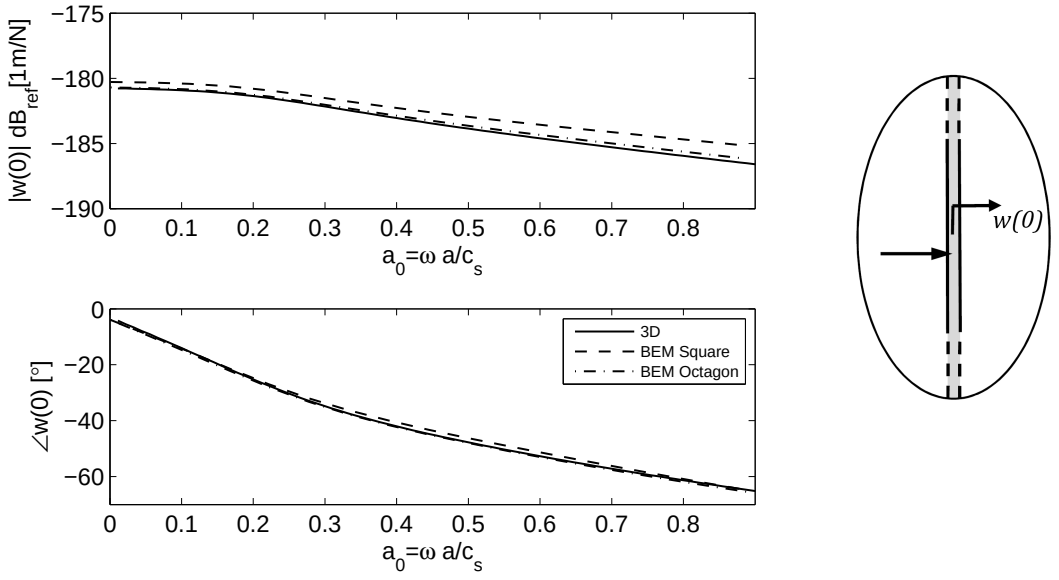

Fig. 2.11 The magnitude and phase of the lateral driving-point response of an infinite pile

2.3.2 The Finite Pile

The response of a finite pile as a function of frequency is presented in Figures 2.12 and 2.13. In these figures, the results for Novak's model, the three-dimensional model and the BEM with square and octagonal cross-sections are presented.

The response of the finite pile in both axial and lateral vibration varies smoothly with frequency. A column with the same dimensions, material properties and boundary conditions of the finite pile has the first two natural frequencies at 0Hz and 94.5Hz. A beam with the same dimensions, material properties and boundary conditions of the finite pile has the first seven natural frequencies at 0Hz, 1.5Hz, 8.0Hz, 19.8Hz, 36.9Hz, 59.2Hz and 86.8Hz. None of these beam or column resonances are observed, which implies that the soil has a strong damping effect on the pile.

In both axial and lateral vibration, the phase of the driving-point response calculated using Novak's model does not approach zero as the frequency tends to zero. This is because the soil reactions are poorly-defined at very low frequencies. A phase artefact due to the material damping coefficient is again observed in the 3D and BE models at very low frequencies.

In axial vibration, the agreement between the four models is very good, with less than 2dB and 10° variation existing over the frequency range of 80Hz. The agreement between the three-dimensional model and the BEM improves when the pile's circular cross-section is represented by an octagon rather than a square.

In lateral vibration, there is very good agreement (2dB, 5° variation) between the three-dimensional model and the BEM over the frequency range of 0-80Hz. Again, the octagonal cross-section BEM provides better agreement than the square cross-section BEM.

For the lateral driving-point response, Novak's model shows poor agreement with the three-dimensional model and the BEM. The variation between Novak's model and the other models ranges between 10dB at low frequencies to 4dB at higher frequencies. The Novak model consistently overestimates the response of the pile in lateral vibration. In particular, the imaginary part of the compliance has been overestimated, as is also observed by Kuhlemeyer [96]. This error in Novak's model is due to the inaccuracy introduced by the plane-strain assumption. Plane-strain conditions imply that the pile is infinitely long in the z-direction, which is a reasonable assumption when the longest wavelength in the pile is short compared to the displacement variation along the length of the finite pile. To investigate the accuracy of the plane-strain assumption, Figures 2.14 & 2.15 show the real part of the displacement of the pile as a function of distance along the pile, and dimensionless frequency a_0 for axial and lateral vibration, respectively. The

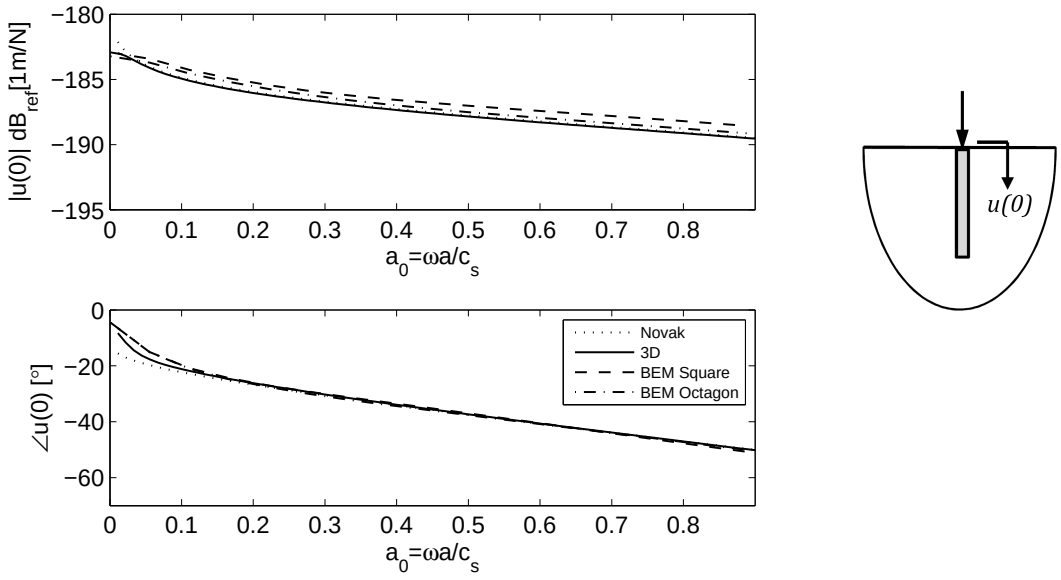

Fig. 2.12 The axial response of a pile subject to a unit harmonic excitation in the z-direction

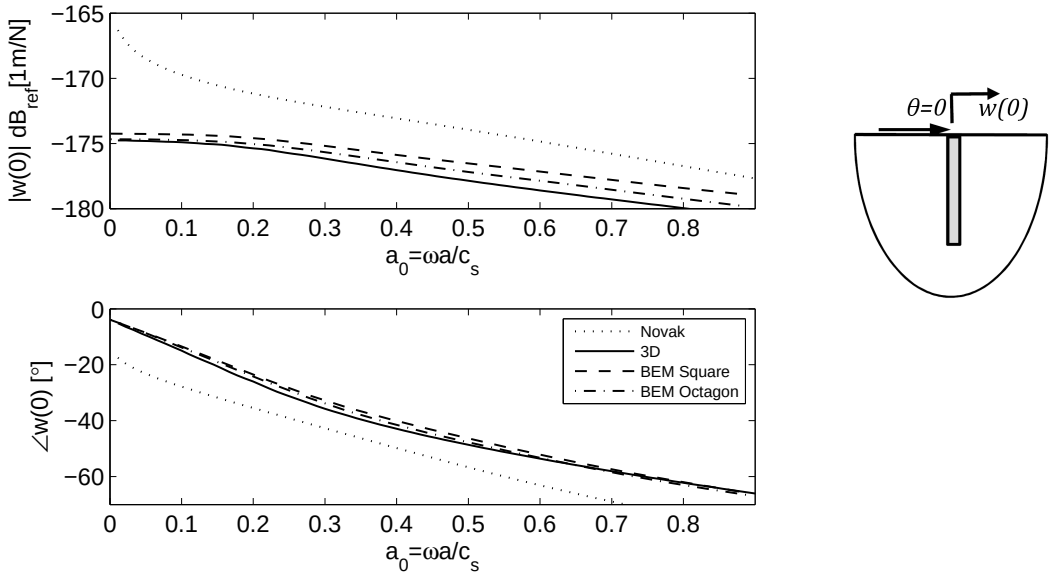

Fig. 2.13 The lateral response of a pile (with zero rotation at the pile head) subject to a unit harmonic excitation in the w-direction

displacements are normalised with respect to the real part of the pile-head displacement, and the shading scale on the right of these figures indicates this normalised coefficient. A coefficient of one represents a real displacement equal to the real pile-head displacement. The results shown in these figures are generated using the 3D model.

Figures 2.14 & 2.15 show a fundamental difference in the behaviour of piles in axial and in lateral vibration. In axial vibration, at any given frequency, the displacement of the pile is seen to be relatively invariant with length, with the displacement magnitude decaying along the length of the pile. As the displacement variation along the length of the pile is small, the plane-strain assumption is valid. Hence good agreement is seen between the models in Figure 2.12 at every frequency except the lowest frequencies ($a_0 < 0.03$) within this range. In lateral vibration, the pile exhibits more localised deformations, with a steep decline in displacement magnitude near the pile head, and with displacement oscillations along the length of the pile. Within the frequency range of 1-80Hz, the longest wavelength in the pile is larger than the rate of displacement variation; hence the plane-strain assumption provides a poor representation of pile behaviour. At higher frequencies, the wavelength decreases and the plane-strain assumption models the lateral pile behaviour more accurately. This is observed when the lateral driving-point response is calculated at frequencies above 400Hz using the Novak and 3D models: the variation between the two models is less than 1dB. The displacement behaviour of the piles in axial and lateral vibration is explained by considering the geometry of the pile. The pile is a slender cylinder, which is stiffer in axial compression than in lateral bending.

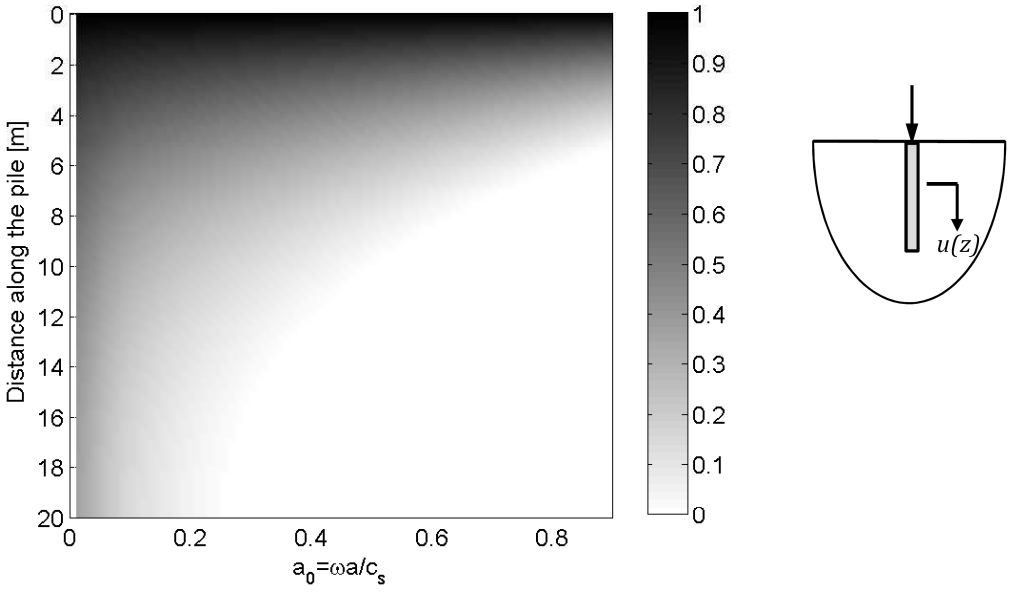

Fig. 2.14 The normalised, real, axial displacement of a pile $\frac{u(z)}{u(0)}$ as a function of pile length and dimensionless frequency

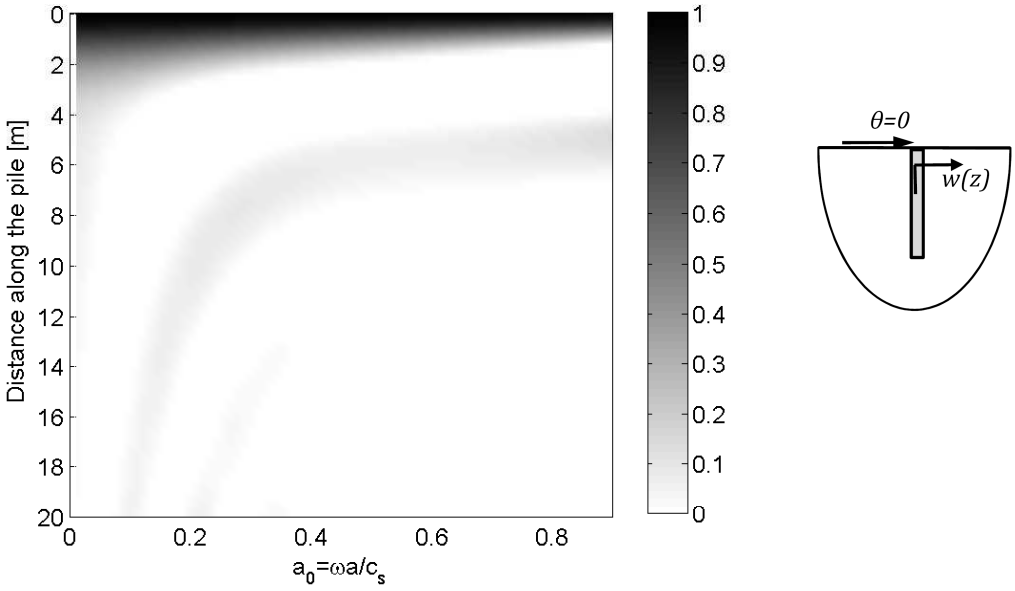

Fig. 2.15 The normalised, real, lateral displacement of a pile $\frac{w(z)}{w(0)}$ as a function of pile length and dimensionless frequency

2.3.2.1 The Farfield Response

To further investigate the response of a single pile to pile-head excitation, the farfield response is calculated on the free surface at distances of 5m, 10m and 20m from the pile. Results at other depths are not available for comparison because the discretisation of the soil in the BE model only allows displacements to be calculated at the free surface and along the pile-soil interface. Figures 2.16 to 2.19 show the real and imaginary parts of the vertical and horizontal displacements as a function of frequency when the pile is excited by a vertical or horizontal pile-head load. The results of the Novak, the three-dimensional and the BE models are shown.

For the case of the vertical farfield response when a vertical force is applied to the pile head (Figure 2.16), all three models show good agreement in both the real and imaginary part over the designated frequency range.

Novak's model assumes that only SV waves propagate from a pile in axial vibration, and only P and SH waves propagate from a pile in lateral vibration. These assumptions imply that farfield displacements are only produced in the direction of the pile's vibration. Hence, as is seen in Figures 2.17 and 2.18 for Novak's model, the horizontal farfield response is zero when a vertical force is applied to the pile head, and the vertical farfield response is zero when a horizontal force is applied to the pile head.

The three-dimensional model shows only moderate agreement with the BEM in Figures 2.17 and 2.18. The observed deviations are due to the error present in the three-dimensional model, resulting from the use of the mirror-image method. This error is discussed in Section 2.2.3, and is believed to be the primary cause of the deviation encountered in these figures. This error only occurs in the farfield, and not on the pile itself. The overall inaccuracy introduced into the calculated farfield displacements by the use of the mirror-image method, when considering a pile subject to an incident wavefield, is expected to be moderately small. This is because the farfield response in any given direction is dominated by the displacements generated by the response of the pile in that same direction, and not by the cross-coupling effects.

Novak's model shows large deviations from the other models in Figure 2.19, which shows the horizontal farfield response when a horizontal force is applied to the pile head. This is due to two sources of error: firstly, the inaccuracy due to the plane-strain assumption; and secondly, the inaccuracies present in the wave-spreading equation (Eq. 2.19), due to the assumption that only P and SH waves are propagated in the farfield.

For all response directions, the agreement between the three-dimensional model and the BEM is good at low non-dimensional frequencies ($a_0 < 0.2$), but as the non-dimensional frequency increases, greater deviations are observed. This may be due to:

the deviation in the lateral driving-point response observed in Figures 2.12 & 2.13; error introduced by use of the mirror-image method; and/or the constant-element discretisation used in the BEM.

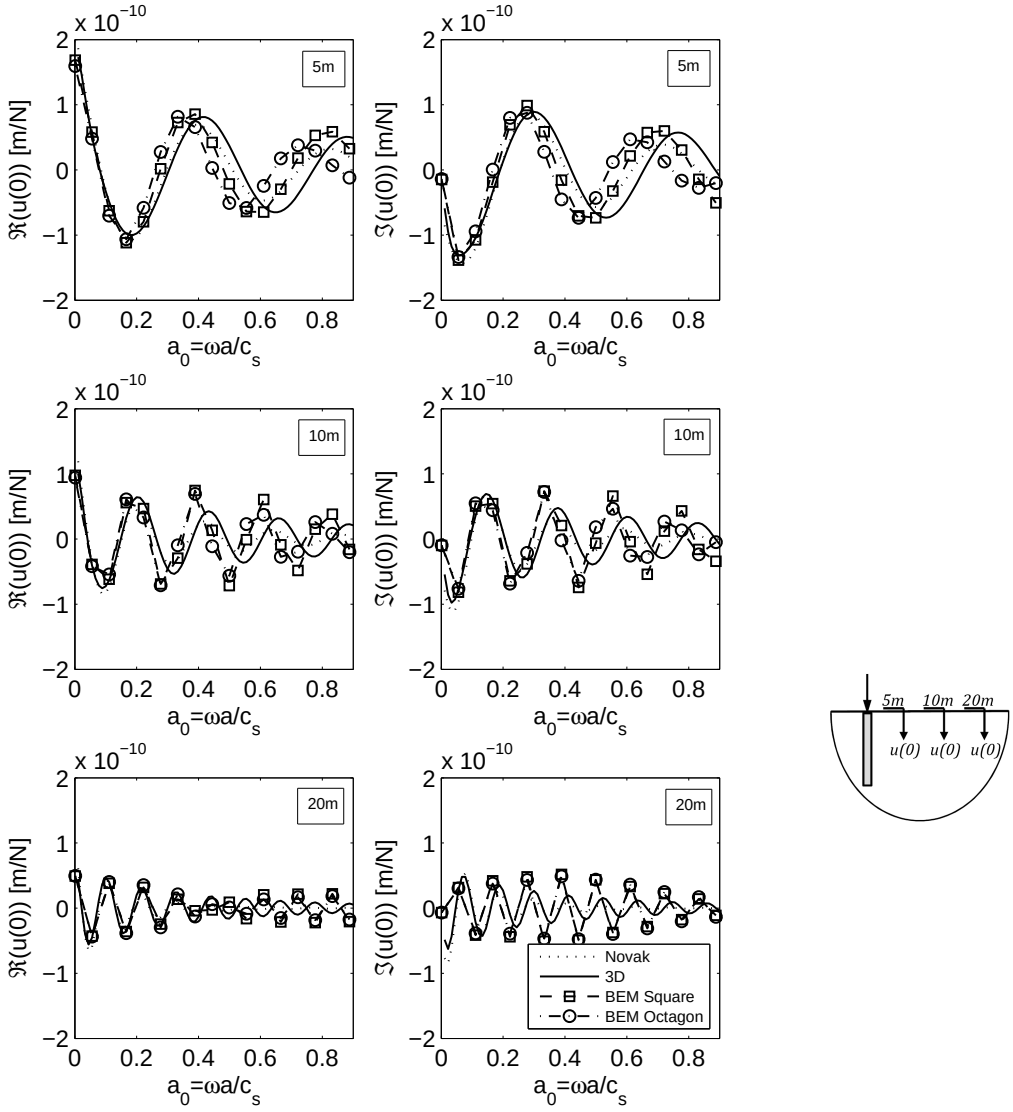

Fig. 2.16 Real (left) and imaginary (right) parts of the vertical farfield displacements on the surface of the halfspace ($z = 0m$) at distance 5m (top); 10m (middle); and 20m (bottom) from a pile undergoing excitation in the z-direction

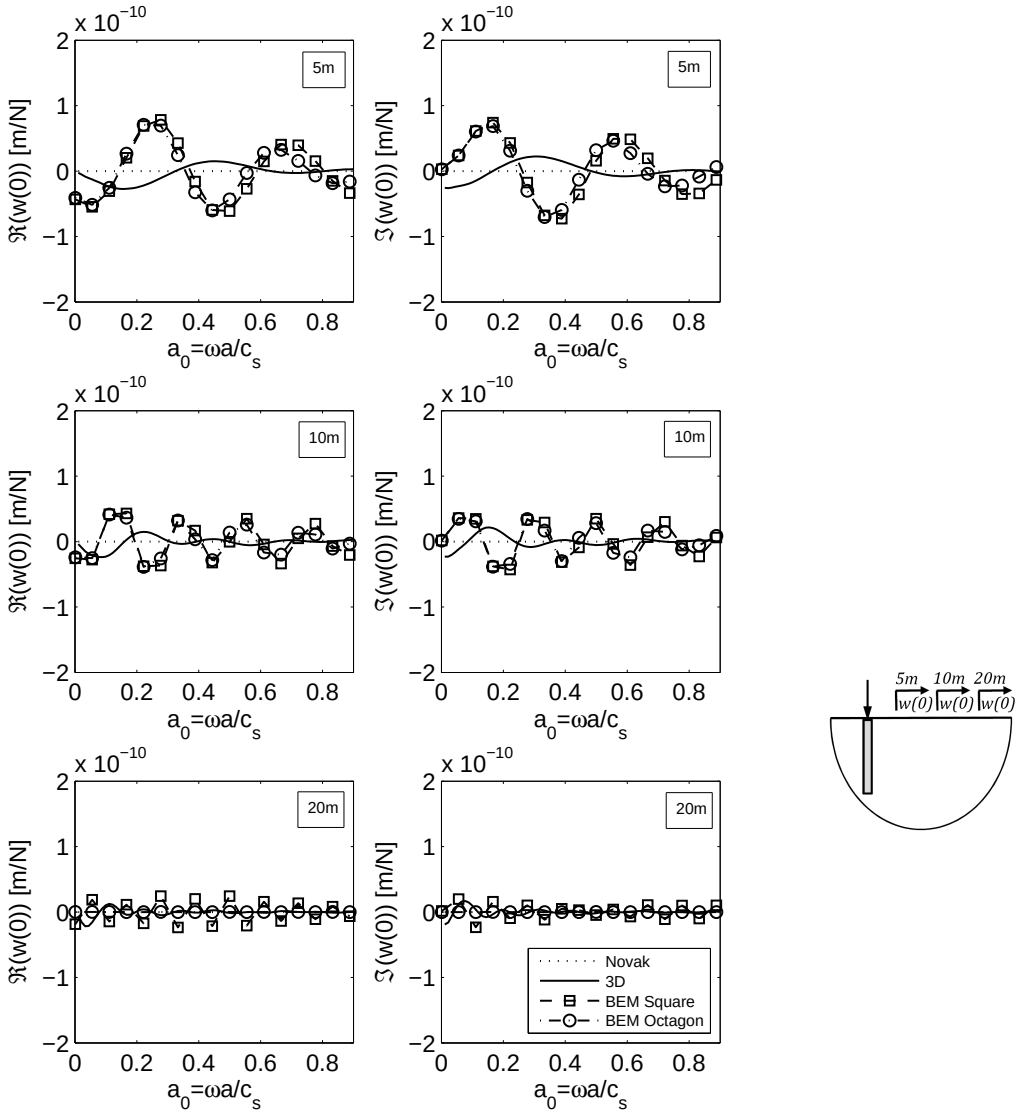

Fig. 2.17 Real (left) and imaginary (right) parts of the horizontal farfield displacements on the surface of the halfspace ($z = 0m$) at distance 5m (top); 10m (middle); and 20m (bottom) from a pile undergoing excitation in the z-direction

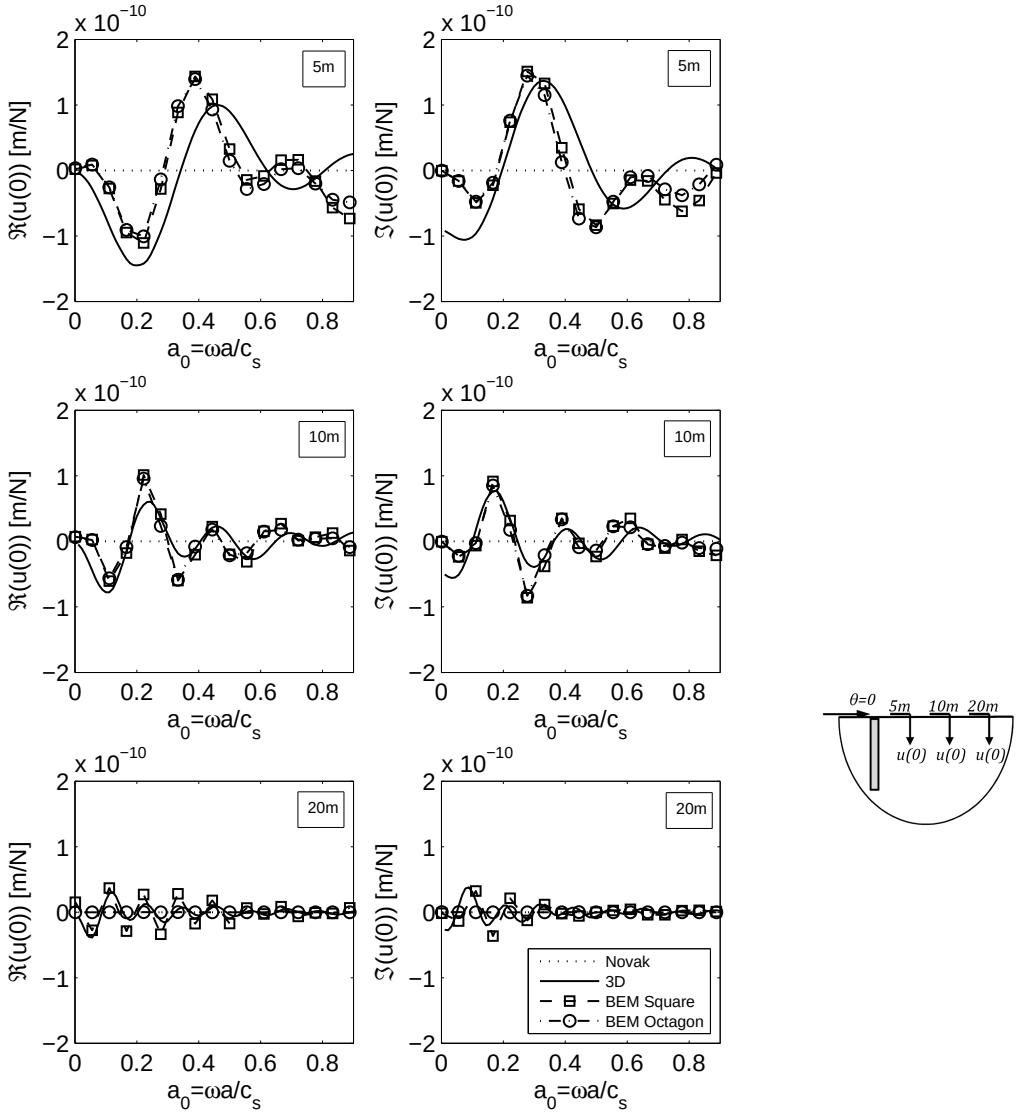

Fig. 2.18 Real (left) and imaginary (right) parts of the vertical farfield displacements on the surface of the halfspace ($z = 0m$) at distance 5m (top); 10m (middle); and 20m (bottom) from a pile undergoing excitation in the w-direction

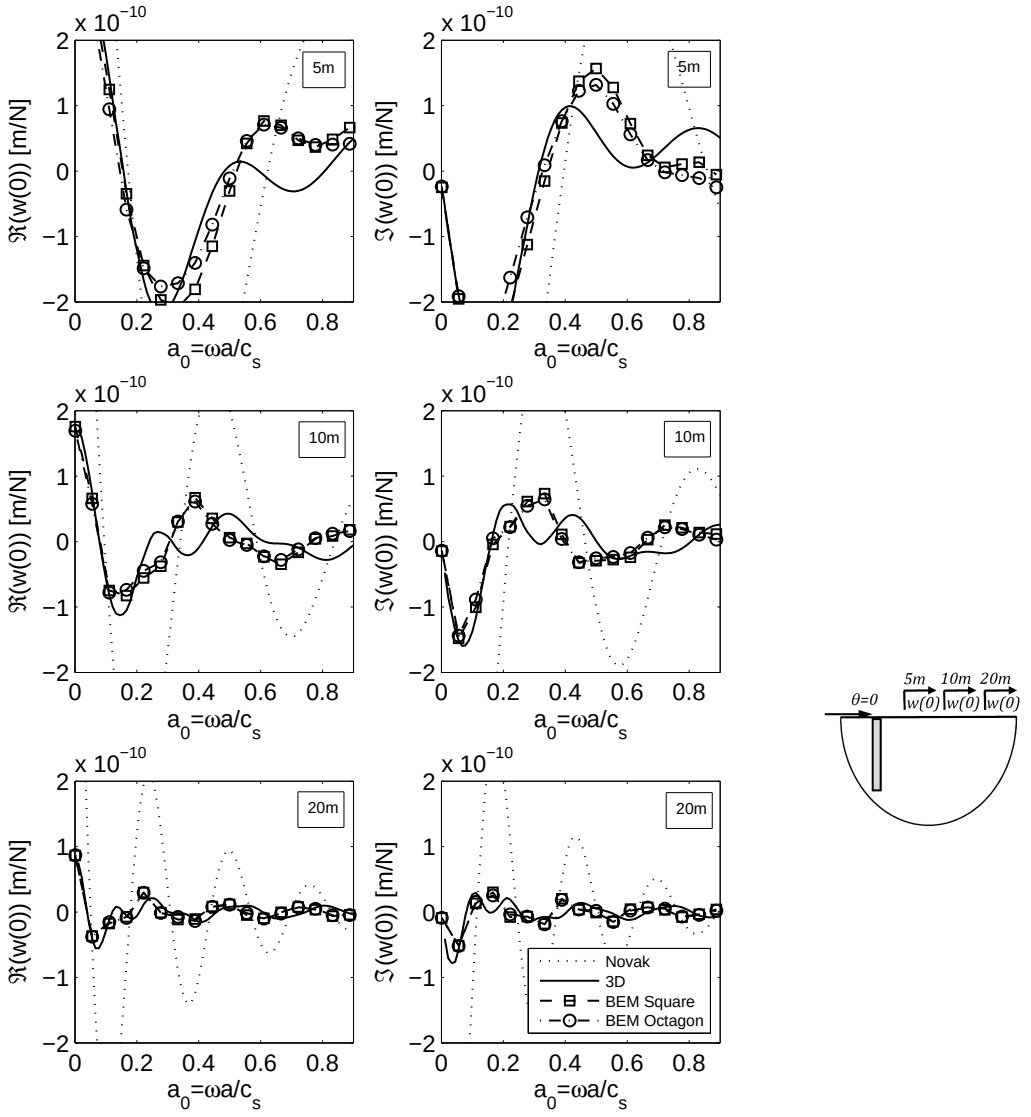

Fig. 2.19 Real (left) and imaginary (right) parts of the horizontal farfield displacements on the surface of the halfspace ($z = 0m$) at distance 5m (top); 10m (middle); and 20m (bottom) from a pile undergoing excitation in the w-direction

2.3.2.2 Power Flow in a Single Pile

By analysing the power flow in a single pile, it is possible to determine the critical positions where energy enters and exits the pile, thus allowing the design of effective vibration-isolation systems. Power-flow methods also provide a useful check for undamped vibration models, as the mean power input must equal the mean power output at any frequency.

For the Novak and the three-dimensional models, the displacements and forces are calculated at a series of equally spaced nodes along the central pile axis. Applying the mean power-flow equation to these nodes calculates the power flowing through the pile cross-section. The mean power flow through the pile skin is thus given as the difference in the mean power flows of two adjacent nodes. For the BEM, nodes exist on each of the pile-skin faces, and hence application of the mean power-flow equation to one of these nodes calculates the mean power flow through the pile-skin face.

For any undamped structure, the total mean power flow around the system boundary must be equal to zero in order to satisfy conservation of energy requirements. For the driving-point response of a single pile subject to a unit force, the mean input power flow P_{in} is represented by the imaginary part of the driving-point response, and the mean output power flow P_{out} is calculated by summing the mean power flow contributions over all remaining nodes. Figures 2.20 and 2.21 show the mean input and output power flows for the axial and lateral pile-head excitation of a single pile with no material damping. Results are calculated for all three models.

As is expected for the undamped pile, these plots show that for all three models the mean input power flow is equal to the mean output power flow over a range of frequencies. For axial pile-head excitation, very little deviation is seen between the three models over the frequency range. For lateral pile-head excitation, the Novak model consistently overpredicts the power flows, but there is good agreement in the three-dimensional and BE models. This overprediction is due to the inability of the Novak model to accurately model pile behaviour in lateral vibration, as is observed in Figure 2.13, the lateral driving-point response.

Figures 2.22 and 2.23 show the power outflow through the skin of a damped pile undergoing axial and lateral excitation, respectively, and calculated using the 3D model. These two plots reveal some trends in the behaviour of piles under axial and lateral loadings. It can be seen that the power entering the pile by an axial loading is dissipated along the whole length of the pile, with the maximum power outflow (15%) occurring near the point of application of the load, and the magnitude of power outflow decreasing with distance along the pile. The rate of decrease of the power outflow with distance

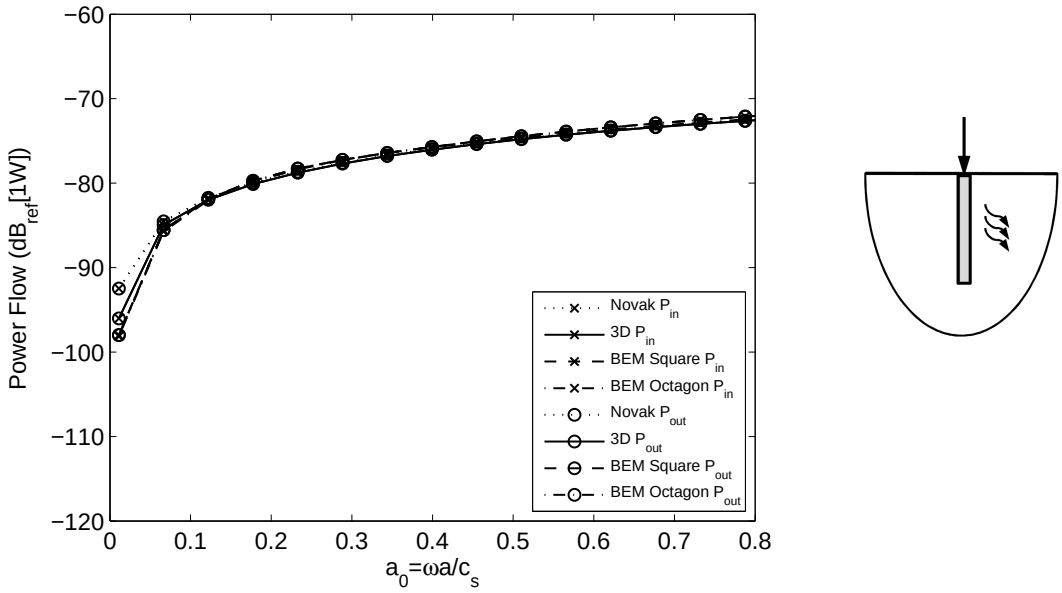

Fig. 2.20 Net power flow through a single pile subject to axial pile-head excitation, plotted as a function of dimensionless frequency

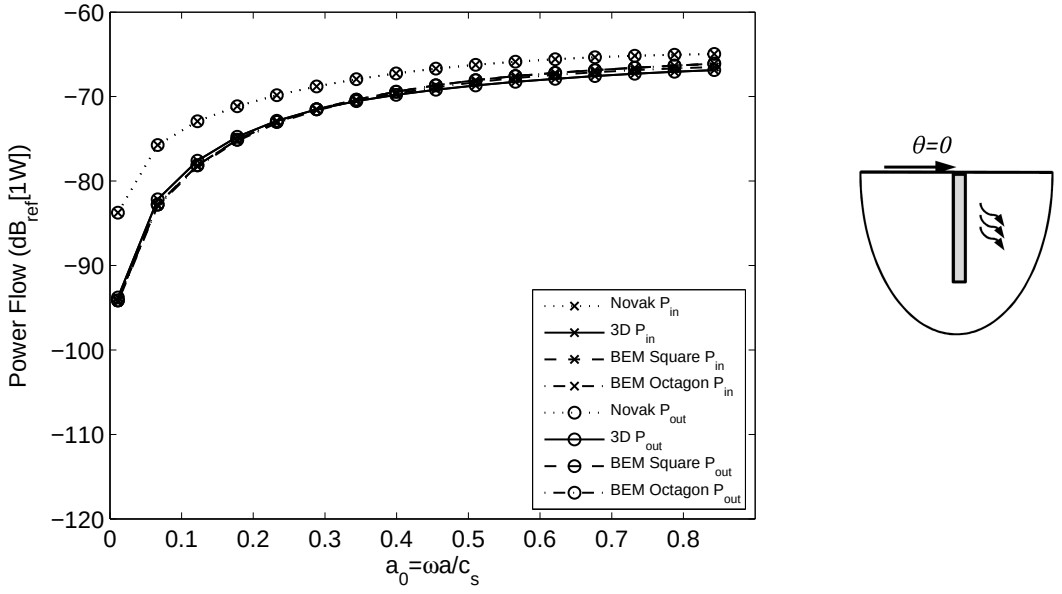

Fig. 2.21 Net power flow through a single pile subject to lateral pile-head excitation, plotted as a function of dimensionless frequency

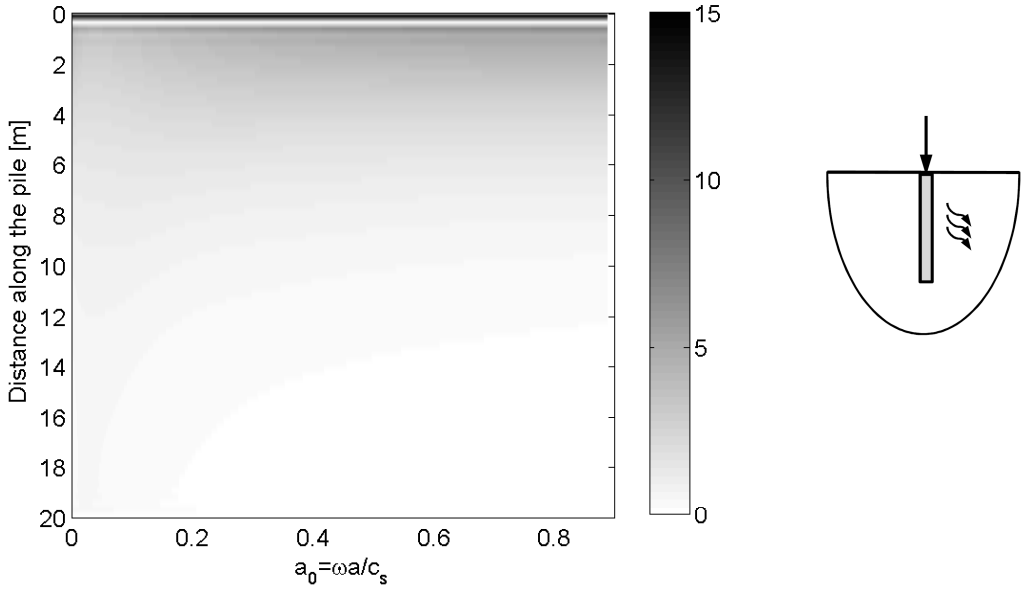

Fig. 2.22 Power flow as a percentage of the total power output [%] through the skin of a single pile subject to axial pile-head excitation, plotted as a function of dimensionless frequency

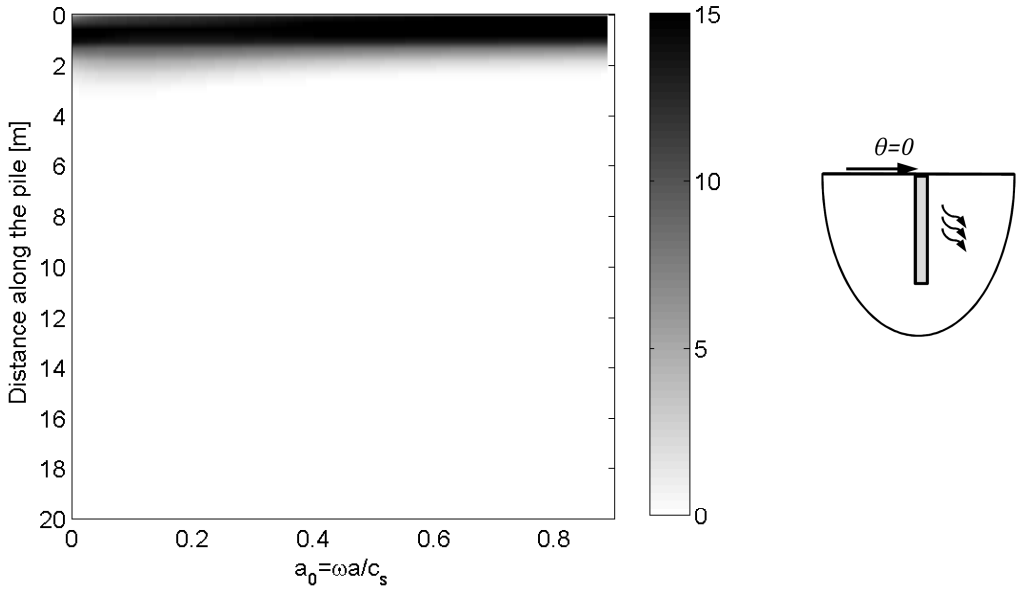

Fig. 2.23 Power flow as a percentage of the total power output [%] through the skin of a single pile subject to lateral pile-head excitation, plotted as a function of dimensionless frequency

along the pile is seen to be dependent on frequency. This is in contrast with Figure 2.23, where it can be seen that the power entering the pile by a lateral loading is dissipated in a highly localised region near the point of application of the load. Very little power outflow occurs along the remaining length of the pile, and this behaviour is independent of frequency. These power-flow distributions are expected, as the stiffness of a slender cylinder like a pile is higher in compression than bending. This means that quasi-uniform displacements and shear stresses will be produced along the length of a pile undergoing axial excitation, whereas a pile undergoing lateral excitation will exhibit more localised deformation and stresses.

2.3.3 The Pile subject to an Incident Wavefield

The validation and comparison of the single-pile model concludes by considering the pile-head response of a single pile embedded near an underground railway. The computation of these results involves the use of the PiP model, and the methods for calculating the response of a single pile subject to an incident wavefield. The parameters used to calculate these results are the PiP model default parameters, which are partially reproduced in Table 2.2. Train, rail, railpad and slab parameters can be found in Jones *et al.* [80].

Before calculating these results, it is first necessary to examine the convergence of the three-dimensional model. As mentioned in Section 2.2.5, the use of 1024 points to represent the incident wavefield along the longitudinal pile axis is a considerable computational expense. For this reason, a solution with reasonable accuracy that makes use of fewer points in the longitudinal direction is sought. The convergence process is illustrated in Figure 2.24, which shows the graph of the real and imaginary parts of the pile-head response of a single pile subject to an incident wavefield. Both the axial and lateral responses are shown, and the 20m-long pile is located 10m from the longitudinal axis of the tunnel. These figures show the results for a frequency range of 1-80Hz.

From Figure 2.24 it can be seen that the dynamic behaviour of the pile is modelled with comparable accuracy to the solution obtained using 1024 points by using just 121 points. The distance covered by these points corresponds to 1.5 pile lengths. The solution obtained using 81 points, which covers a distance equal to the length of the pile, shows considerable deviation from the 1024-point solution. Thus when using the three-dimensional model to represent a pile subject to an incident wavefield, it is recommended that the wavefield be represented by a series of points stretching over a distance of 1.5 pile lengths. For very short piles ($L \leq 5$m) this guideline is insufficient, and further convergence testing is required to maintain sufficiently accurate results.

Table 2.2 Pile, soil and tunnel parameters used for calculating the results of the incident-wavefield models

Pile Properties	*Symbol*	*Value*
Density	ρ	2500kgm^{-3}
Young's Modulus	E	30GPa
Poisson's Ratio	ν	0.25
Length	L	$20m$
Radius	a	$\frac{1}{2\sqrt{2}}$m
Hysteretic Material Damping Ratio (Shear Wave)	β_s	0.00
Hysteretic Material Damping Ratio (Pressure Wave)	β_p	0.00
Soil Properties	*Symbol*	*Value*
Density	ρ	2000kgm^{-3}
Shear Modulus	G	191MPa
Poisson's Ratio	ν	0.44
Shear Wave Speed	c_S	309ms^{-1}
Pressure Wave Speed	c_P	944.1ms^{-1}
Hysteretic Material Damping Ratio (Shear Wave)	β_S	0.03
Hysteretic Material Damping Ratio (Pressure Wave)	β_P	0.03
Tunnel Properties	*Symbol*	*Value*
Density	ρ	2500kgm^{-3}
Shear Modulus	G	19.2GPa
Poisson's Ratio	ν	0.30
Hysteretic Material Damping Ratio (Shear Wave)	β_S	0.00
Hysteretic Material Damping Ratio (Pressure Wave)	β_P	0.00
Depth		25m

Figures 2.25 & 2.26 present the pile-head response, in the axial and lateral directions, respectively, for a single, 20m-long pile located 10m from the longitudinal axis of the tunnel and subject to an incident wavefield. The greenfield displacements (when no piles are present) are also shown in these figures. The Novak model shows considerable deviation from the BE and 3D models for the axial response. Whilst the shape of the Novak-model response approximately matches these two models, this deviation ranges up to 20dB in localised regions. The agreement between the Novak model and the BE and 3D models is good for the lateral response.

Very good agreement is observed between the BEM and the 3D model for both the axial and lateral response. Over the entire frequency range, the maximum deviation that occurs is 5dB in axial vibration and 2.5dB in lateral vibration. In axial vibration, the 3D model generally provides a more conservative estimate than the BEM for the amount of vibration attenuation achieved. The phase of all three models agrees well in

both axial and lateral vibration.

Figures 2.28 & 2.30 show the real part of the displacement of a pile, calculated using the 3D model, as a function of the distance along the pile and frequency for axial and lateral vibration, respectively. For comparison, the real part of the greenfield displacements (when no piles are present) are shown in Figures 2.27 & 2.29. The shading scale on the right of these figures indicates the magnitude of the real displacements.

From these figures it is observed that the addition of a pile has a much greater effect on the axial vibration levels than the lateral vibration levels, although the greenfield vibration levels for these two directions of vibration are of similar orders of magnitude. As seen in Figure 2.25, the addition of a pile attenuates the greenfield axial vibration levels, with the amount of attenuation increasing with increasing frequency. The wavelength of the shear wave is equal to the length of the pile at 15Hz. The maximum attenuation is seen to occur at frequencies where the wavelength of the shear wave is shorter than, or of a similar order to, the length of the pile. This finding correlates with diffraction theory, which predicts that the most pronounced changes to a wavefield occur when the wavefield encounters objects which have a size of the order of the wavelength of the field. The stiffening effect of the pile results in the attenuation of the greenfield vibrations. The pile is not completely rigid, as the deformed shape of the pile shows some similarity to the greenfield soil displacements.

In lateral vibration, the addition of the pile is seen to increase the vibration level at higher frequencies marginally. The flexibility of the pile in lateral vibration results in negligible deviation of the deformed shape of the pile from the greenfield soil displacements.

To further qualify the behaviour of piles in axial and lateral vibration, Figures 2.31 to 2.38 present the real part of the greenfield displacements and the real part of the pile displacements, calculated using the 3D model, as a function of the distance along the pile and frequency. The location of the pile remains the same as the pile length is varied from 5m to 60m. From these figures it is concluded that the generalised behaviour of the pile is not dependent upon the pile length.

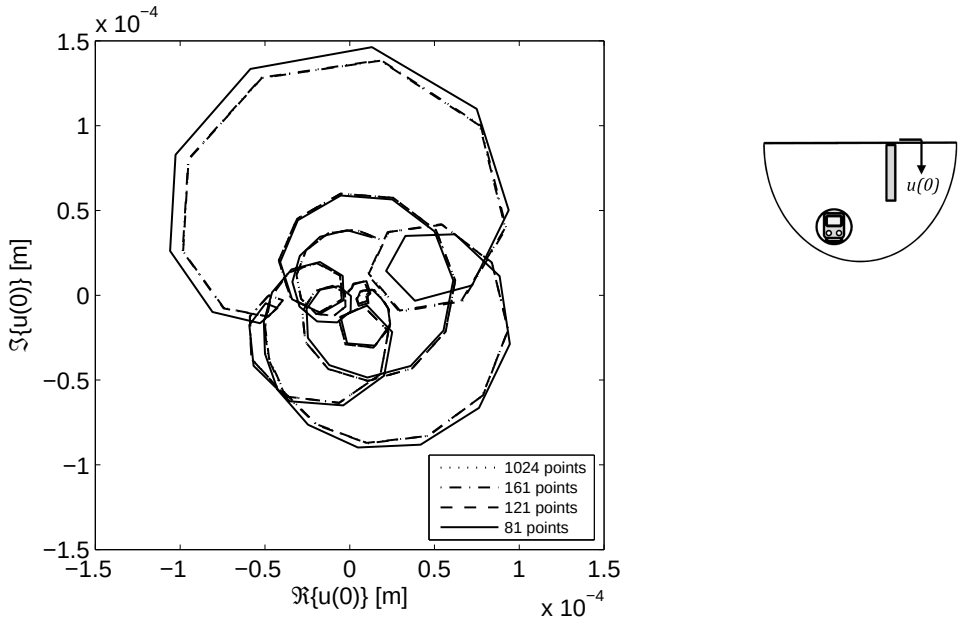

(a)

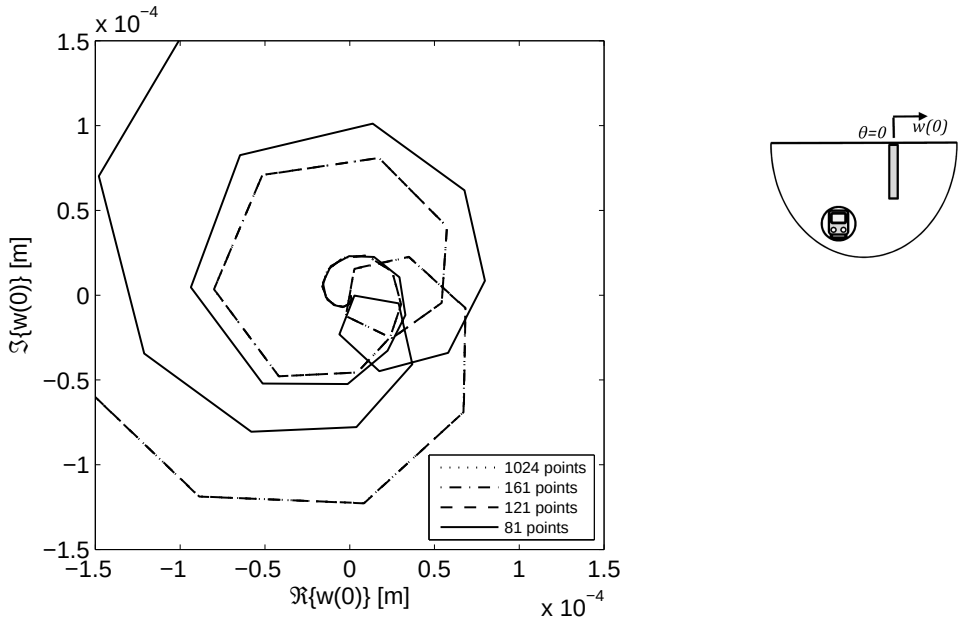

(b)

Fig. 2.24 (a) Axial, and (b) lateral pile-head response of a single pile subject to an incident wavefield consisting of varying numbers of input points

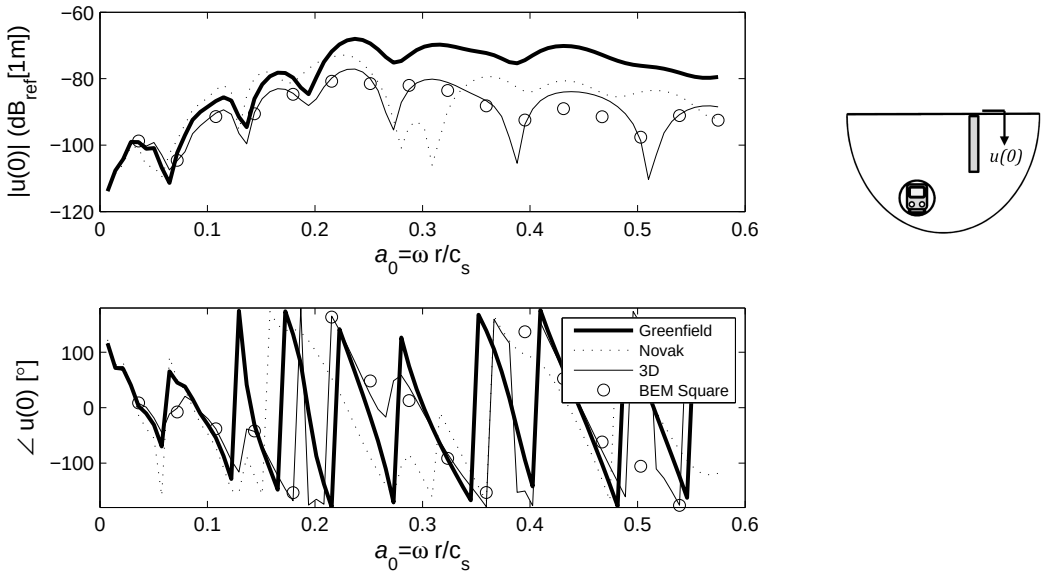

Fig. 2.25 The vertical response of a single pile subject to an incident wavefield generated using the PiP software

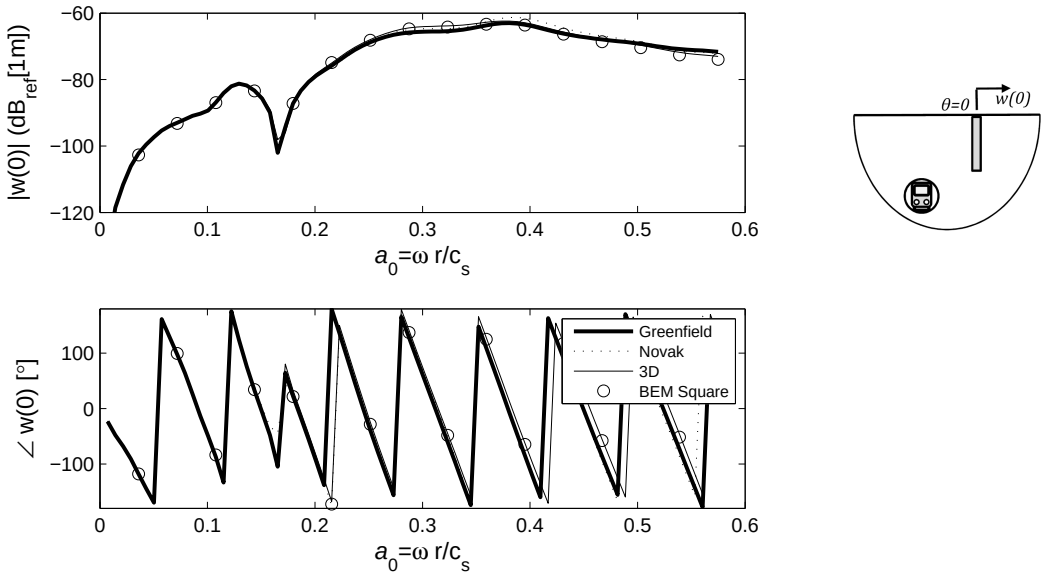

Fig. 2.26 The horizontal response of a single pile subject to an incident wavefield generated using the PiP software

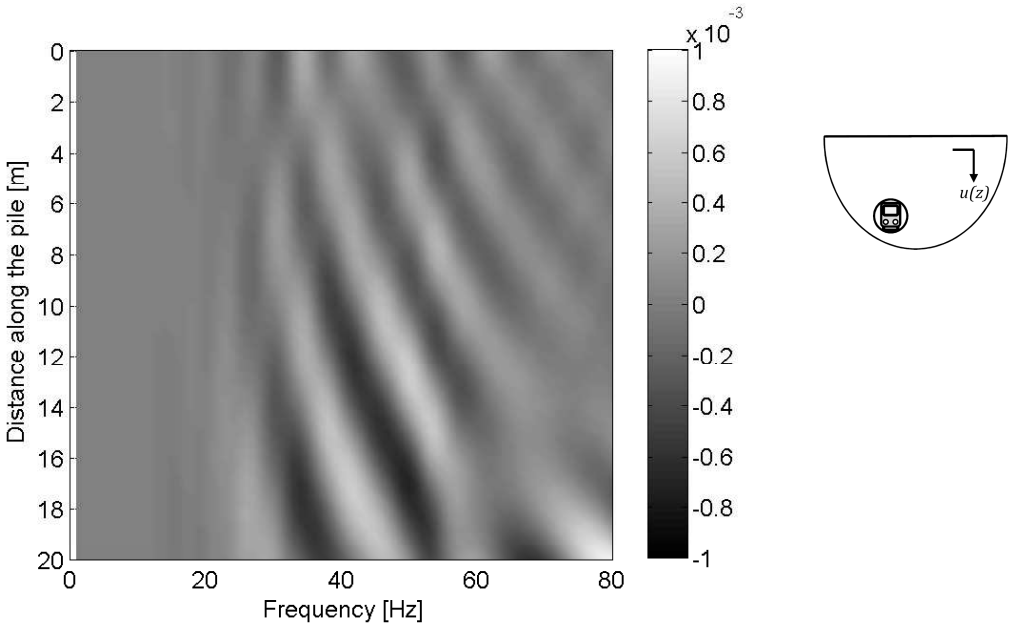

Fig. 2.27 The real axial displacement [m] of the incident wavefield as a function of pile length $L = 20$m and frequency

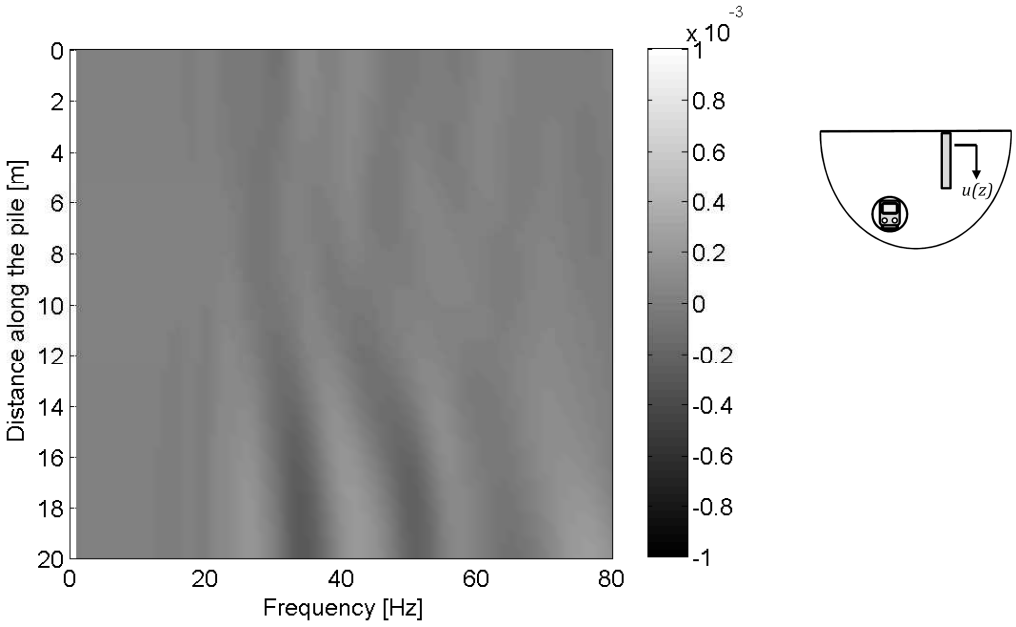

Fig. 2.28 The real axial displacement [m] of a pile subject to the incident wavefield as a function of pile length $L = 20$m and frequency

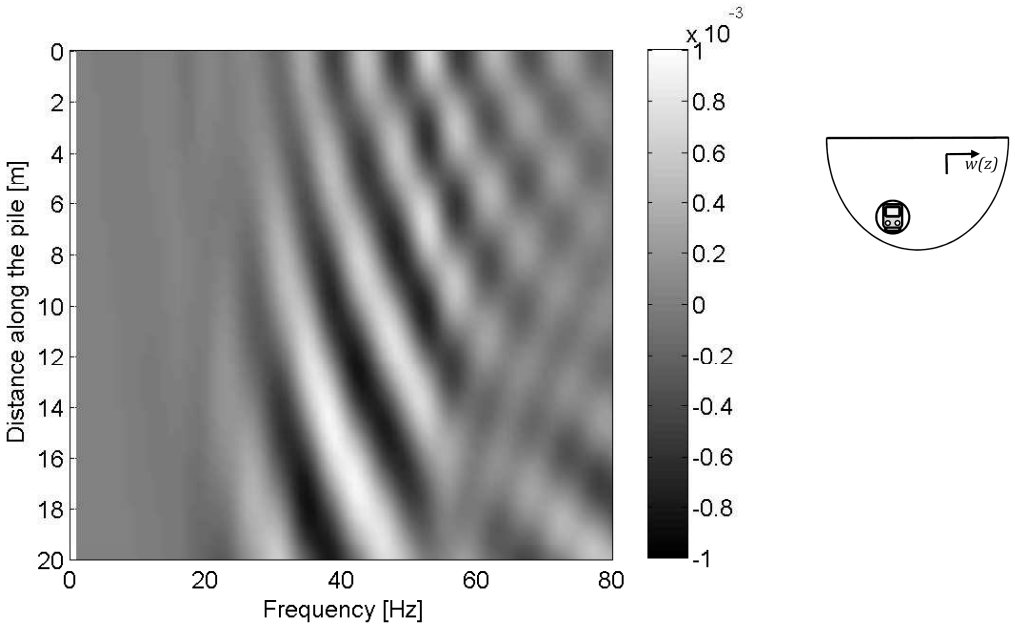

Fig. 2.29 The real lateral displacement [m] of the incident wavefield as a function of pile length $L = 20$m and frequency

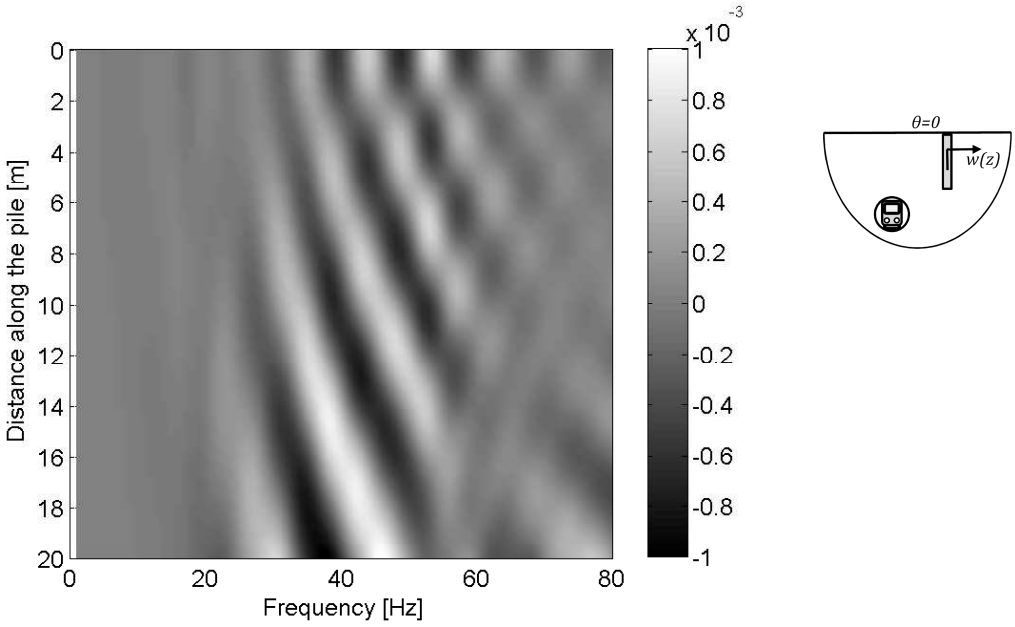

Fig. 2.30 The real lateral displacement [m] of a pile subject to the incident wavefield as a function of pile length $L = 20$m and frequency

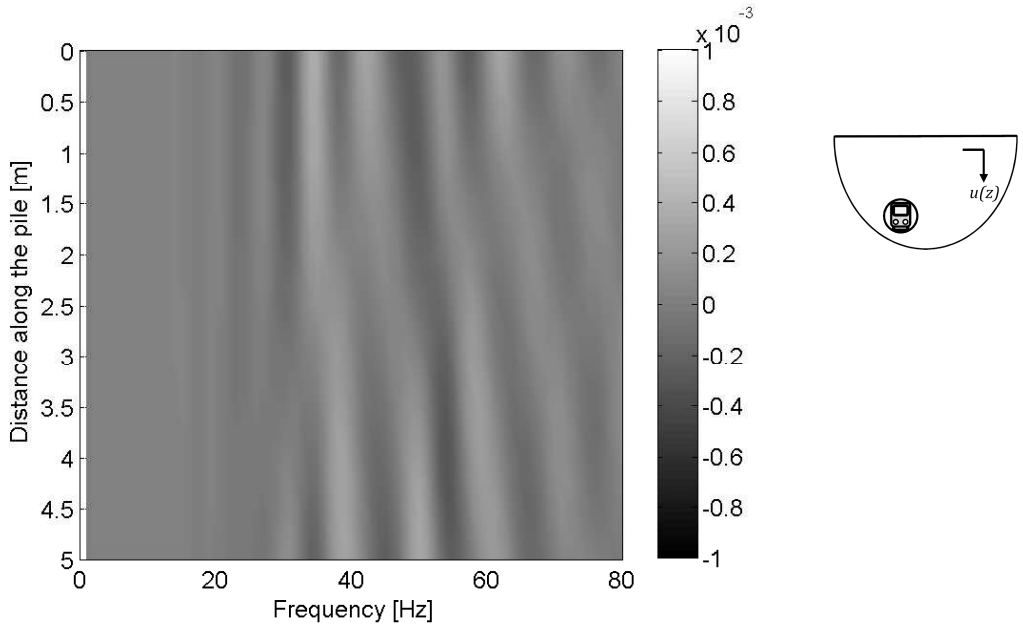

Fig. 2.31 The real axial displacement [m] of the incident wavefield as a function of pile length $L = 5$m and frequency

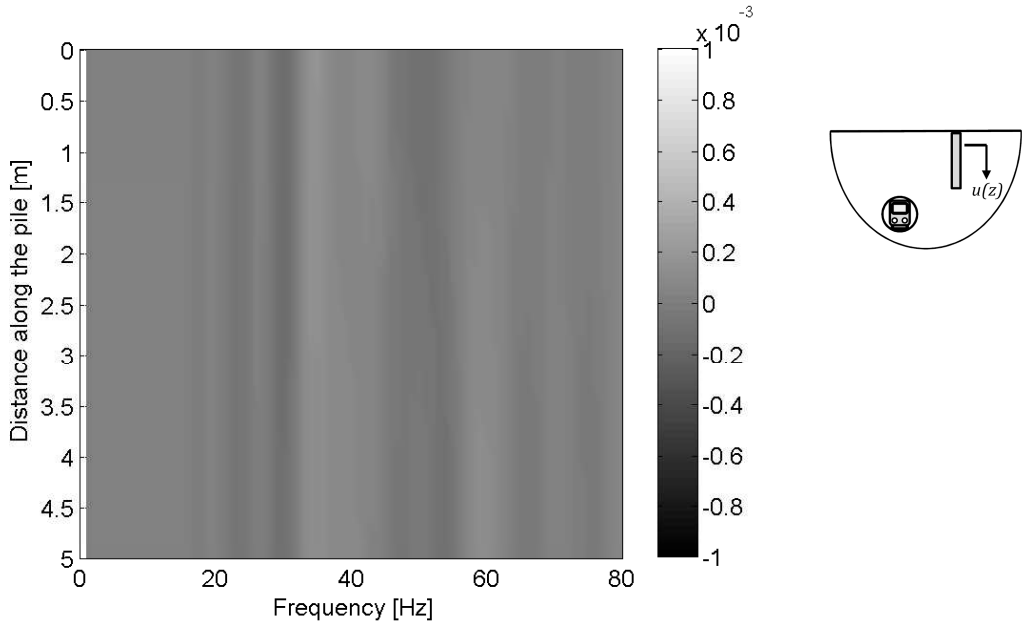

Fig. 2.32 The real axial displacement [m] of a pile subject to the incident wavefield as a function of pile length $L = 5$m and frequency

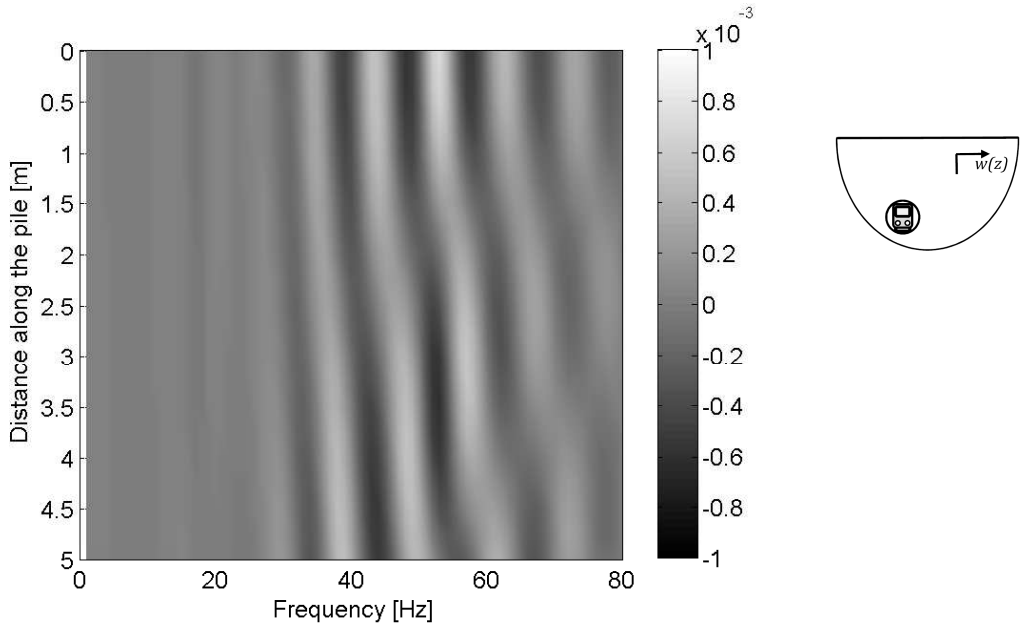

Fig. 2.33 The real lateral displacement [m] of the incident wavefield as a function of pile length $L = 5$m and frequency

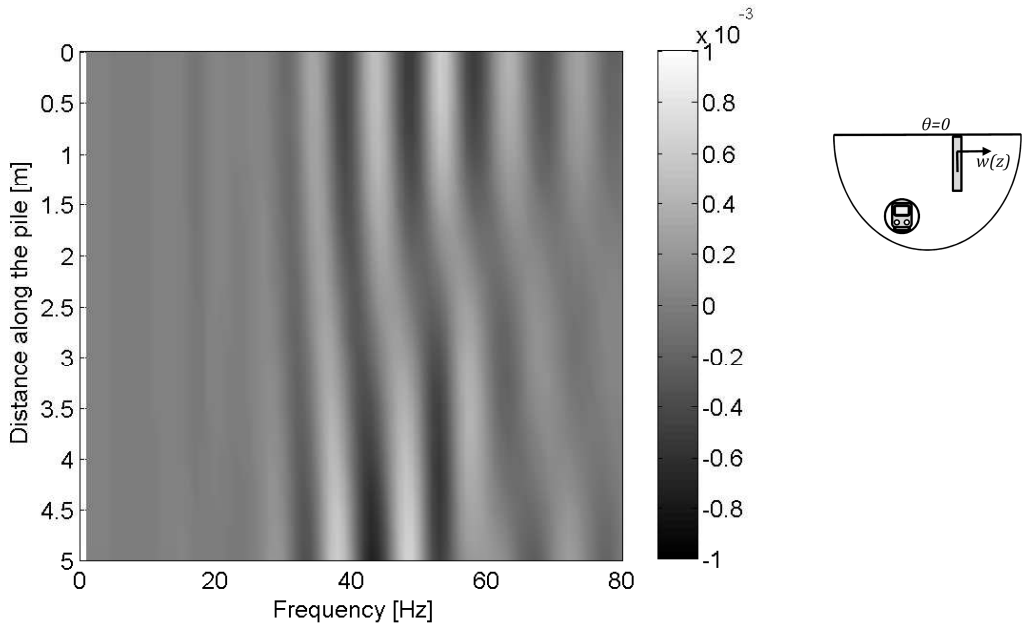

Fig. 2.34 The real lateral displacement [m] of a pile subject to the incident wavefield as a function of pile length $L = 5$m and frequency

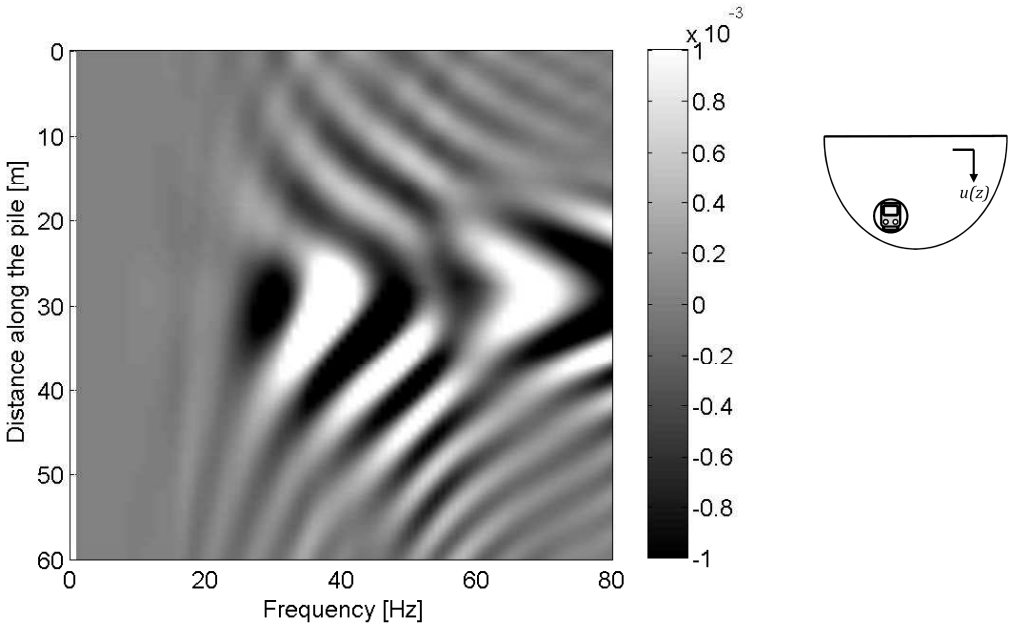

Fig. 2.35 The real axial displacement [m] of the incident wavefield as a function of pile length $L = 60$m and frequency

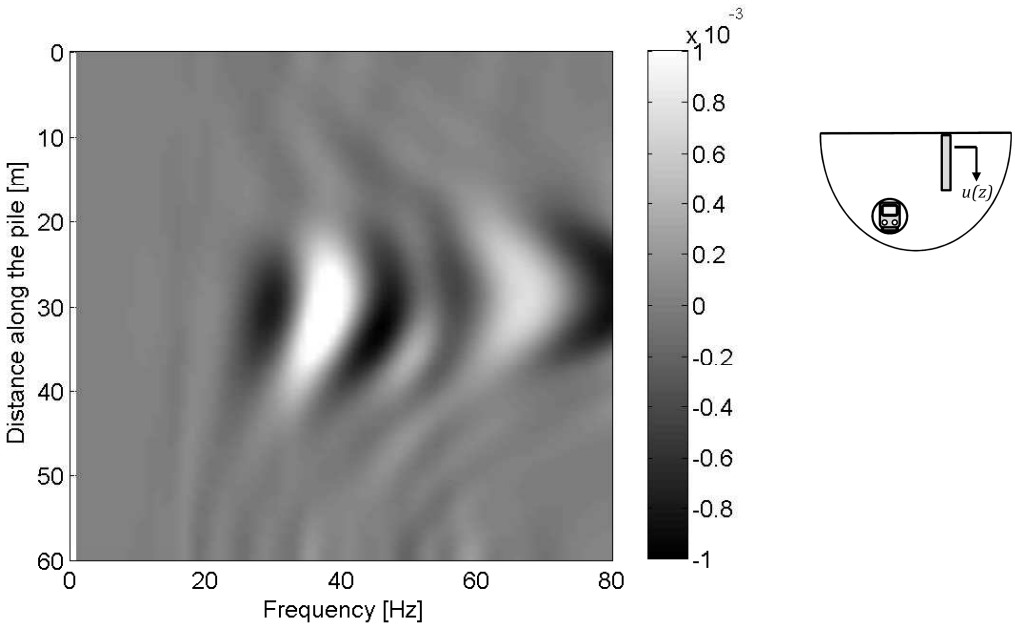

Fig. 2.36 The real axial displacement [m] of a pile subject to the incident wavefield as a function of pile length $L = 60$m and frequency

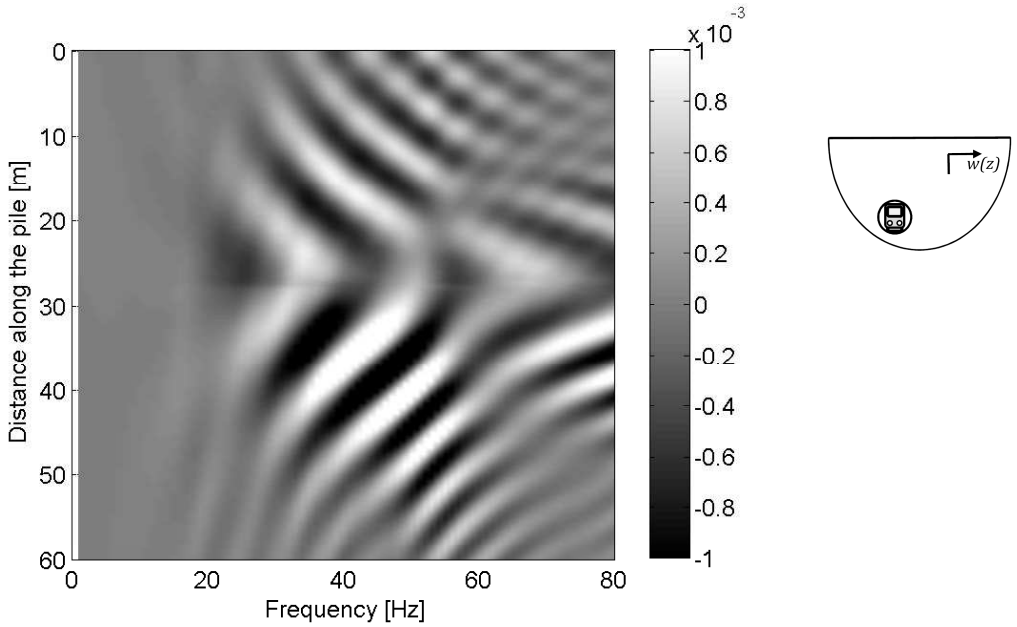

Fig. 2.37 The real lateral displacement [m] of the incident wavefield as a function of pile length $L = 60$m and frequency

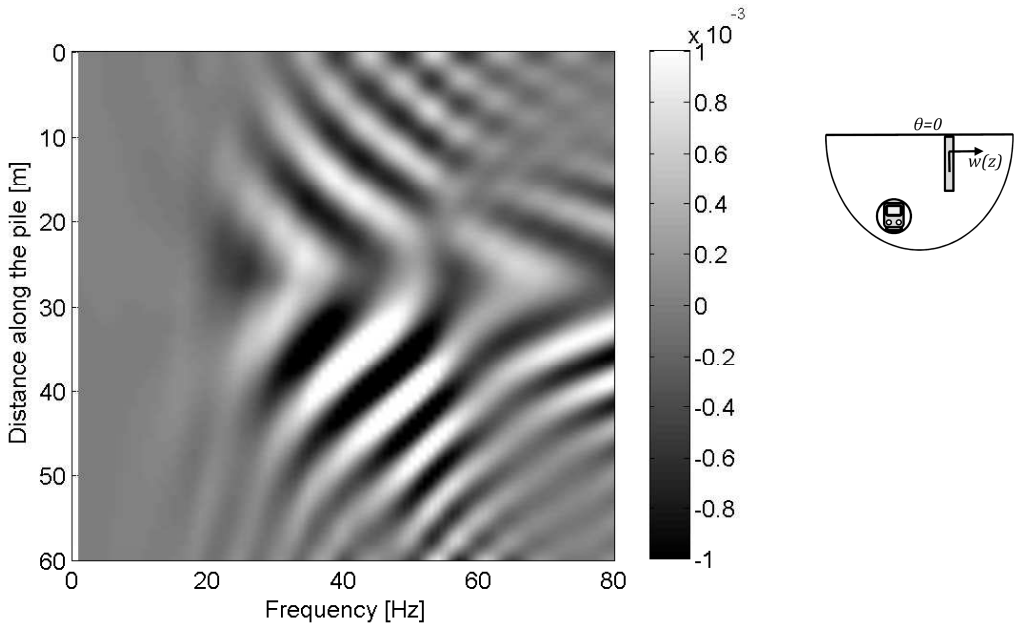

Fig. 2.38 The real lateral displacement [m] of a pile subject to the incident wavefield as a function of pile length $L = 60$m and frequency

2.3.3.1 Power Flow through a Pile subject to an Incident Wavefield

Figure 2.39 shows the mean power flow through the skin of the single pile subject to an incident wavefield, plotted as a function of frequency. Both the power flows attributed to the axial and the lateral directions are included. The power flows due to displacements and forces in the longitudinal direction of the tunnel are not considered as they are insignificant. The sign convention used here denotes power outflows as positive.

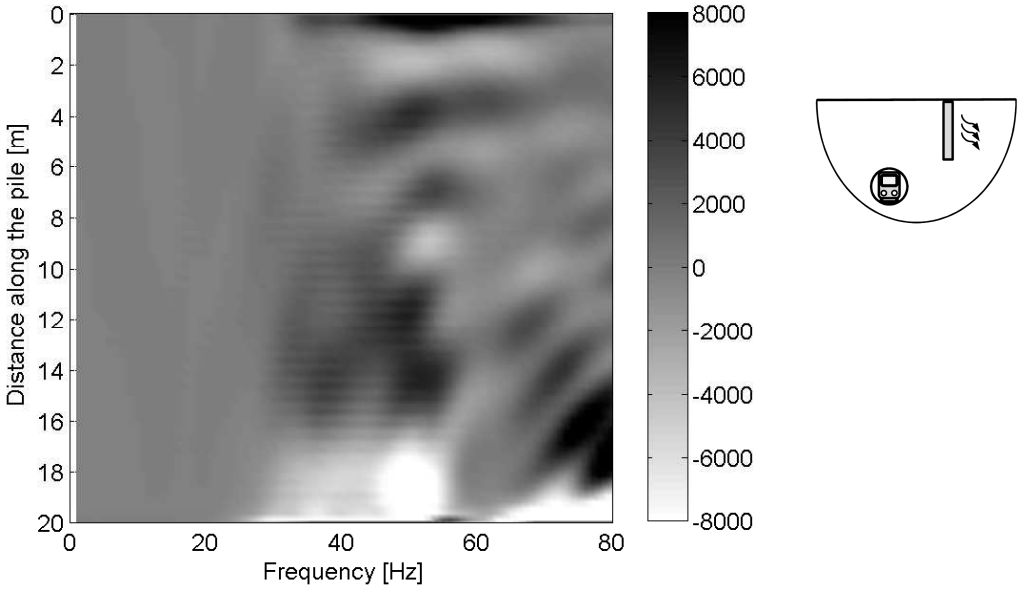

Fig. 2.39 The net power flow [W/m] through a single pile subject to an incident wavefield generated using the PiP software

The magnitude of the power flows are small at frequencies less than 25Hz, resulting in relatively uniform shading in this region. This is due to the displacements and forces along the length of the pile being several orders of magnitude smaller in this frequency range than at higher frequencies. These small displacements can be seen, for example, in the pile-head response in Figures 2.25 & 2.26.

At frequencies higher than 25Hz, the regions of maximum power flow are localised and highly dependent on frequency. As a broad generalisation, for this pile geometry the power enters the pile in the pile-tip region and is dissipated along the length of the pile. The power flows due to the separate axial and lateral vibration directions are shown in Figures 2.40 & 2.41, respectively. The lateral power flows are again observed to exhibit more localised behaviour than the axial power flows. The relative contributions of the two vibration directions to the net power flow are of similar magnitude: neither the axial or lateral vibration directions dominate the net power flow from a pile.

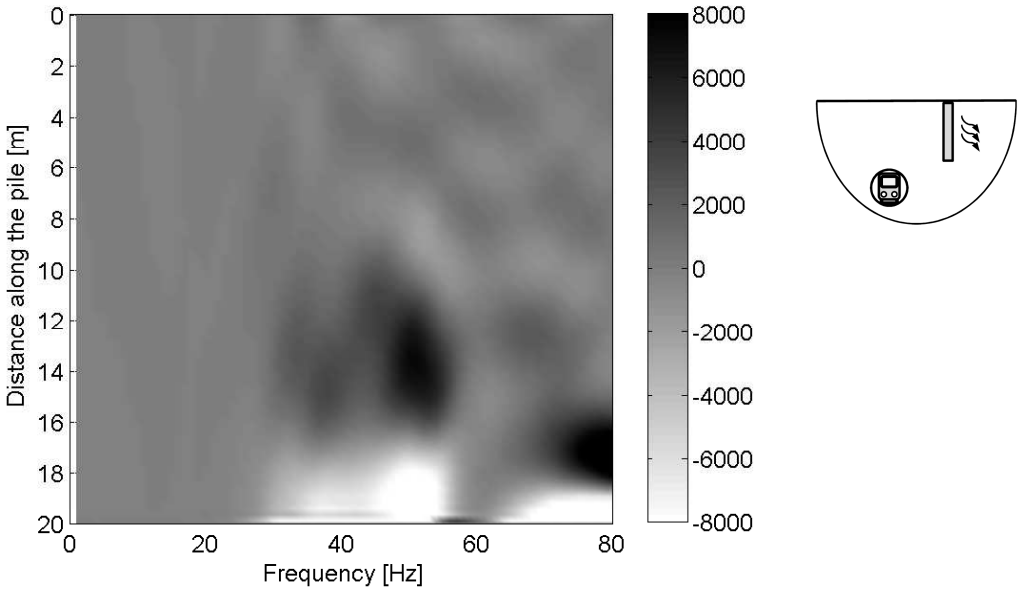

Fig. 2.40 The power flow [W/m] due to axial vibration for a single pile subject to an incident wavefield generated using the PiP software

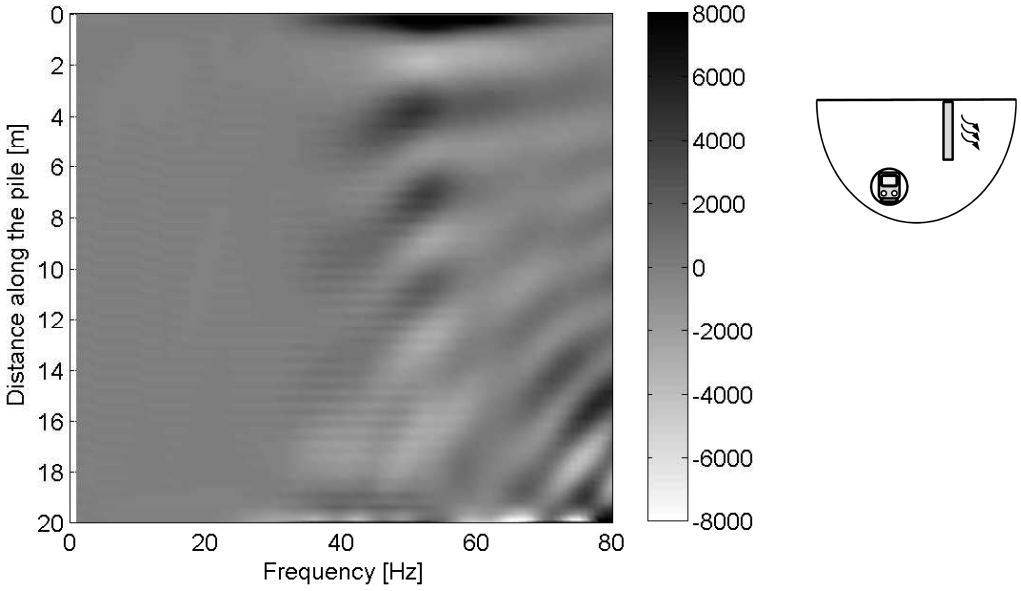

Fig. 2.41 The power flow [W/m] due to lateral vibration for a single pile subject to an incident wavefield generated using the PiP software

2.4 Conclusions

In this chapter, two computationally efficient pile models are developed. The well-known Novak model for the plane-strain case is adapted to calculate farfield displacements and incorporate incident wavefields; and the formulation of a novel, three-dimensional model is outlined. Comparison with existing published models shows that the three-dimensional model is a good representation of purely axial or lateral pile behaviour, and the plane-strain assumption renders the Novak model ineffective in certain situations. The most notable of these are the lateral, pile-head, driving-point response, the farfield displacements and the response of a pile to an incident wavefield. The use of the mirror-image method in the three-dimensional model to reduce the infinitely long pile to a finite pile results in some error in calculating the farfield displacements, due to failure of the boundary conditions at the free surface. The overall inaccuracy introduced into the farfield displacements due to this error is expected to be moderately small.

Analysis of the displacement of a single pile subject to a pile-head load highlights the differences in axial and lateral vibration behaviour; the pile is stiffer in compression than bending, resulting in an axial displacement distribution that is relatively invariant with length, and a lateral displacement distribution that shows localised variation with length. This behaviour dominates the response of a single pile to an incident wavefield generated by an underground railway. The axial stiffness of the pile results in a significant reduction of the greenfield axial vibrations at frequencies above those where the wavelength of the shear wave is equal to the length of the pile. The lateral flexibility of the pile results in the pile deforming with the incident wavefield, and therefore the greenfield lateral vibration levels are not significantly altered. Comparison with a boundary-element model verifies the accuracy and efficiency of the three-dimensional model.

The next chapter extends the single-pile models to consider the interaction between neighbouring piles and the response of a pile-building model.

Chapter 3

Multiple-Pile Models

The application of a single-pile model to real-life situations is limited, as structural foundations generally consist of pile groups. The response of a pile group cannot simply be represented as the sum of the responses of a number of single piles, because the vibration of one pile will influence the vibration of surrounding piles. This effect is known as pile-soil-pile interaction (PSPI), and the level of interaction between piles becomes more significant as the distance separating the piles decreases.

It is possible to calculate the response of a pile group by creating a fully-coupled model which includes each pile and therefore inherently accounts for the interactions between them. Examples of this include models by Kaynia [88] and Coulier [25]. The difficulty with this approach is that it requires the formulation of a new model for every new pile-group arrangement, and the number of elements required when using BE or FE models quickly exceeds available computational capacities. For this reason, many researchers prefer to consider the response of a single pile within a pile group to be the sum of two components: the response of the single pile considered individually; and the response of the single pile due to interactions with neighbouring piles, the PSPI.

The PSPI component of the response of the single pile consists of two components: direct fields; and reflected fields. The number of reflections from neighbouring piles required to model system behaviour accurately is dependent upon the damping properties of the medium and the pile spacing. As soil is a highly-damped medium, it is proposed that it is sufficient to include only those fields propagated directly from neighbouring piles in the PSPI component. These direct fields are calculated without regard for intermediate piles. This is known as the 'superposition method', because it is proposed by Poulos [149] that the PSPI component of the response of a pile within a pile group can be well-estimated by superposing the effect of each neighbouring pile. Whilst this method is only strictly valid for linear systems, it is also used by researchers for moder-

ately nonlinear systems in the field of earthquake engineering [122]. The superposition method is used to calculate PSPI in pile groups subject to inertial and/or kinematic loadings. Experimental measurements and comparisons with fully-coupled models show that the use of the superposition method is valid for inertial loadings, with the accuracy of this method improving as the pile-spacing increases, as is expected [88].

To calculate the overall response of a pile group it is necessary to know the response of one pile due to the excitation of a neighbouring pile. For pile groups subject to inertial loadings (loads acting on the pile heads), this information is contained within the inertial interaction factor α, which is defined by Kaynia [88] as

$$\alpha = \frac{\text{additional dynamic head deflection of pile 2 caused by pile 1}}{\text{static head deflection of pile 1 (considered individually)}}. \tag{3.1}$$

This interaction factor is calculated by applying a point force to the pile head of pile 1, determining the pile-head response of pile 2 due to the excitation of pile 1, and then dividing this response by the static response of a single pile (considered individually) subject to the same point force applied to the pile head.

For kinematic loadings (loads produced by an incident wavefield), the interaction between two neighbouring piles is proportional to the difference between the displacement of the loaded pile and the freefield excitation. This is due to the fact that the response of a pile group subject to an incident wavefield can be written as the superposition of the response of every individual pile to the incident wavefield and the PSPI, which occurs in the absence of the incident wavefield. For example, in Section 2.3.3 it is shown that a pile subject to an incident wavefield generated from an underground railway is flexible in the lateral direction, with the displacement of the loaded pile closely following the displacement of the incident wavefield. The interaction between this pile and a neighbouring pile is negligible, as the PSPI resulting from the difference between the displacement of the loaded pile and the incident wavefield is negligible. There is no definition of an interaction factor for kinematic loadings, as the pile displacement is strongly dependent upon the nature of the incident field.

This chapter adopts the superposition method for calculating PSPI, and a method for calculating the interaction between two neighbouring piles is presented in Section 3.1. This method is based upon the method of joining subsystems. The interaction factors generated using the two-pile model are validated against results published for two existing two-pile models. The models are then extended to consider pile groups subject to vibration from underground railways. This chapter concludes with the development of a model of a piled building, and a case study to demonstrate how this model can be used to evaluate the response of a building to vibration from underground railways.

3.1 Modelling Two Finite-Length Piles

Following a similar method to that used to couple a single pile to an incident wavefield, the method of joining subsystems is used to couple a second pile to the existing single-pile model. The two subsystems are illustrated in Figure 3.1: subsystem A is represented by a loaded, finite-length pile, and subsystem B is represented by a column or an Euler-Bernoulli beam to be coupled at a distance s from the pile in subsystem A. The displacement output $Y_2(\omega)$ is to be calculated at each node along the length of the pile represented by subsystem B. The incident wavefield, $\mathbf{U}^{incident}$, represents the soil displacements at distance s from the pile in subsystem A. The governing equation of the coupled system in the space domain is

$$\mathbf{Y}_2(\omega) = \left[\mathbf{I} + \mathbf{A}_{33}\mathbf{B}_{33}^{-1}\right]^{-1} \mathbf{U}^{incident}. \tag{3.2}$$

The equivalent equation formulated in the wavenumber domain is

$$\tilde{\mathbf{Y}}_2(\omega) = \left[\mathbf{I} + \tilde{\mathbf{A}}_{33}\tilde{\mathbf{B}}_{33}^{-1}\right]^{-1} \tilde{\mathbf{U}}^{incident}. \tag{3.3}$$

The matrices $\mathbf{A}_{33}$, $\mathbf{B}_{33}$, $\tilde{\mathbf{A}}_{33}$ and $\tilde{\mathbf{B}}_{33}$ are the same as those used in Sections 2.1.2 and 2.2.5 for the Novak model and the three-dimensional model, respectively.

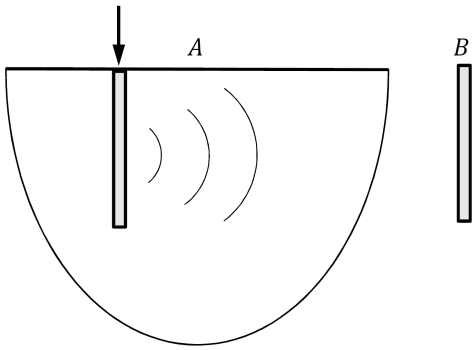

Fig. 3.1 The two separate subsystems which are joined together to form a two-pile system

When calculating the response of a single pile subjected to an incident wavefield, the incident wavefield is calculated using the PiP model. When calculating the interaction between two neighbouring piles, the incident wavefield is produced by the loaded, single pile. The methods for calculating the incident wavefield using the Novak model and the three-dimensional model are detailed below.

Novak's model For the Novak model, this incident wavefield is obtained by propagating the displacement response of the loaded single pile. The displacement propagation is achieved using the wave-spreading equations given in Equations 2.18 & 2.19.

The three-dimensional model The three-dimensional model requires the incident wavefield, $\tilde{\mathbf{U}}^{incident}$, to be calculated at some distance s from the pile axis in the wavenumber domain. This can be accomplished using the wave-spreading equations given in Eqs. 2.28 & 2.37. These equations determine the displacements in the wavenumber domain, at some radius R from the wavenumber-domain displacements at the soil-pile interface.

As subsystem A represents a single, loaded, finite pile embedded in a halfspace, the displacements of the single pile that are to be transformed into the wavenumber domain are those obtained after the mirror-image method has been applied to the single pile. However, it should be noted that it is not just those displacements along the length of the finite pile that are transformed into the wavenumber domain. The infinite limits of the Fourier transformation require the input of those displacements along the whole length of the infinite pile. To illustrate this, Figure 3.2(a) shows the two 'infinite' subsystems which are joined together. The equivalent 'finite' representation of these subsystems for the case of axial vibration is shown in Figure 3.2(b). The finite pile in subsystem A is represented in Figure 3.2(b) as an infinite pile that has been cut at $z = L$. This is a more accurate representation of the physical system, as the mirror-image method does not remove the lower portion of the pile when a free end is created. This representation is also effective in conveying the notion that displacements are known along the length of this 'infinite' pile even though the pile is essentially modelled as being finite in length.

Thus the method used to simulate a finite-length, two-pile model is:

1. Create a finite pile and calculate the displacements along the pile. For inertial excitation, use the method detailed in Section 2.2.3 for axial vibration, or Section 2.2.4 for lateral vibration. For a kinematic loading, calculate the displacement of the pile subject to the incident wavefield using the method in Section 2.2.5. Propagate the pile displacements to the location of pile 2 by substituting $R = s$ into Equations 2.28 & 2.37.

2. Attach pile 2 using the method of joining subsystems. The displacements propagated from pile 1 represent those produced in a halfspace, therefore pile 2, although represented by the equation for an infinite column/beam, will represent a semi-infinite pile embedded in a halfspace when it has been coupled to subsystem A.

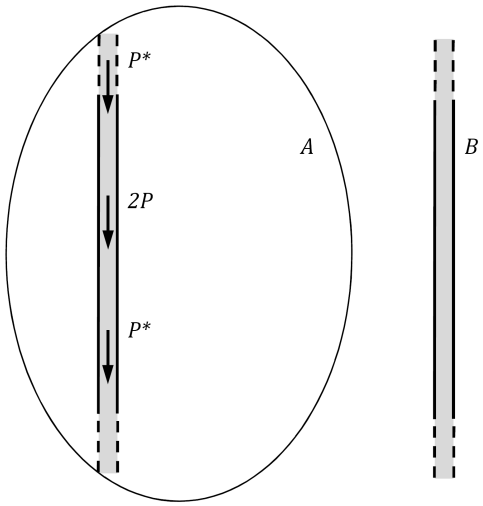

(a) Subsystem A is represented by the infinite pile with applied axial excitation and scaled mirror-image forces; subsystem B is represented by an infinite column

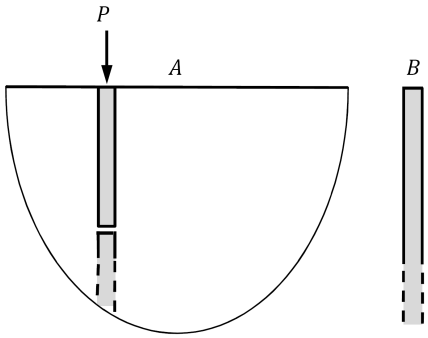

(b) The equivalent subsystem representation: subsystem A consists of a finite pile with applied axial pile-head excitation; subsystem B consists of a semi-infinite column

Fig. 3.2 The two separate subsystems used for the three-dimensional model (with applied axial forces) which are joined together to form a two-pile system

3. Convert semi-infinite pile 2 to a finite pile using the mirror-image method detailed in Section 2.2.3 for axial vibration, or Section 2.2.4 for lateral vibration.

It is expected that the application of the mirror-image forces and moments in Step 3 will result in the radiation of some additional displacement to pile 1, and thus introduce some inaccuracies into the model. However, the magnitude of these inaccuracies is expected to be small, and to decrease with increasing pile separation distance.

3.2 Validation of the Two-Pile Model

The inertial interaction factors calculated using the Novak and the three-dimensional models are presented in this section. Three different pile-separation distances are used: $s = 4a$, $s = 10a$, and $s = 20a$. The results are compared with those obtained by Kaynia using a dynamic stiffness matrix (DSM) formulation [88], and those obtained by Coulier using an extended form of Talbot's boundary-element model [25].

The Kaynia model assumes that the soil medium is a viscoelastic halfspace, the piles are made of a linear, elastic material, and the piles are perfectly bonded to the soil. The pile is discretised into segments, and the force distributions at the pile-soil interface are modelled using piecewise-constant barrel loads and circular loads. Displacements at

the pile-head are obtained by assembling the appropriate stiffness matrices and using numerical integration to evaluate the load equations.

The Coulier model is an extension of the BE model introduced in Section 2.3. In accounting for the response of two piles rather than the response of a single pile, the transfer-function matrix now relates the tractions acting on each of the piles and the free surface to the displacements of each of the piles and the free surface. In this way, the model inherently accounts for pile-soil-pile interactions. Both the Kaynia model and the Coulier model are coupled source-receiver models.

The parameters used to obtain the results are presented in Table 3.1. Figure 3.3 shows the real and imaginary parts of the inertial interaction factors for the axial response of the pile, and Figures 3.4 & 3.5 show the real and imaginary parts of the inertial interaction factors for the lateral response of the pile when the force is aligned at 0° and 90°, respectively, from the line joining the two piles. The results are plotted as a function of dimensionless frequency $a_0 = \frac{\omega a}{c_s}$, which corresponds to a frequency range of approximately 0-80Hz. The inertial interaction factors calculated using the Kaynia model are for piles with a free end condition at the pile head, whereas the inertial interaction factors calculated using the Novak, 3D and BE models are for piles with the pile head constrained against rotation. The end condition of the pile head has little effect on the results shown in these figures as the inertial interaction factors are calculated using displacements that are normalised against the pile-head displacement of a single pile.

Table 3.1 Pile and soil parameters used for calculating the results of the two-pile models

Pile Properties	*Symbol*	*Value*
Density	ρ	2500kgm^{-3}
Young's Modulus	E	30GPa
Poisson's Ratio	ν	0.25
Length	L	10.5m
Radius	a	0.35m
Hysteretic Material Damping Ratio (Shear Wave)	β_S	0.00
Hysteretic Material Damping Ratio (Pressure Wave)	β_P	0.00
Soil Properties	*Symbol*	*Value*
Density	ρ	1750kgm^{-3}
Young's Modulus	E	30MPa
Poisson's Ratio	ν	0.4
Hysteretic Material Damping Ratio (Shear Wave)	β_S	0.025
Hysteretic Material Damping Ratio (Pressure Wave)	β_P	0.025

For both the axial and the lateral interaction factors, the Novak model generally provides a conservative result when compared to the other models. This is due to inaccuracy in the static value of the response of a single pile (seen in Figures 2.12 & 2.13) and the approximate nature of the wave-spreading equations. The gradient of the real part of the Novak interaction factors changes significantly as $a_0 \rightarrow 0$, similar to the behaviour observed in the pile-head driving-point response in Figure 2.13. This trend is also observed in the imaginary part in the case of lateral vibration. Compared with the three-dimensional model, the Novak model does not accurately represent inertial pile-soil-pile interactions.

The three-dimensional model generally compares well with the results obtained using the DSM formulation and the BE method. As the distance between the two piles increases, there is no significant change in the amount of variation observed between the models, two of which represent coupled source-receiver models (DSM, BEM), and two of which represent uncoupled source-receiver models (Novak, 3D). This implies that there is no great inaccuracy introduced into the Novak model or the three-dimensional model at these separation distances through the use of the method of joining subsystems. Nevertheless, the inherent accuracy of the method of using interaction factors to model pile-soil-pile interactions in a pile group increases as the pile-separation distance increases.

The magnitude of the deviation between the DSM formulation, the BEM and the three-dimensional model is of a similar scale. Yet to compute the same set of results, the three-dimensional model requires a runtime of less than one second, compared to minutes or hours for the DSM formulation or the BEM. This represents a significant improvement in the modelling of pile-soil-pile interactions.

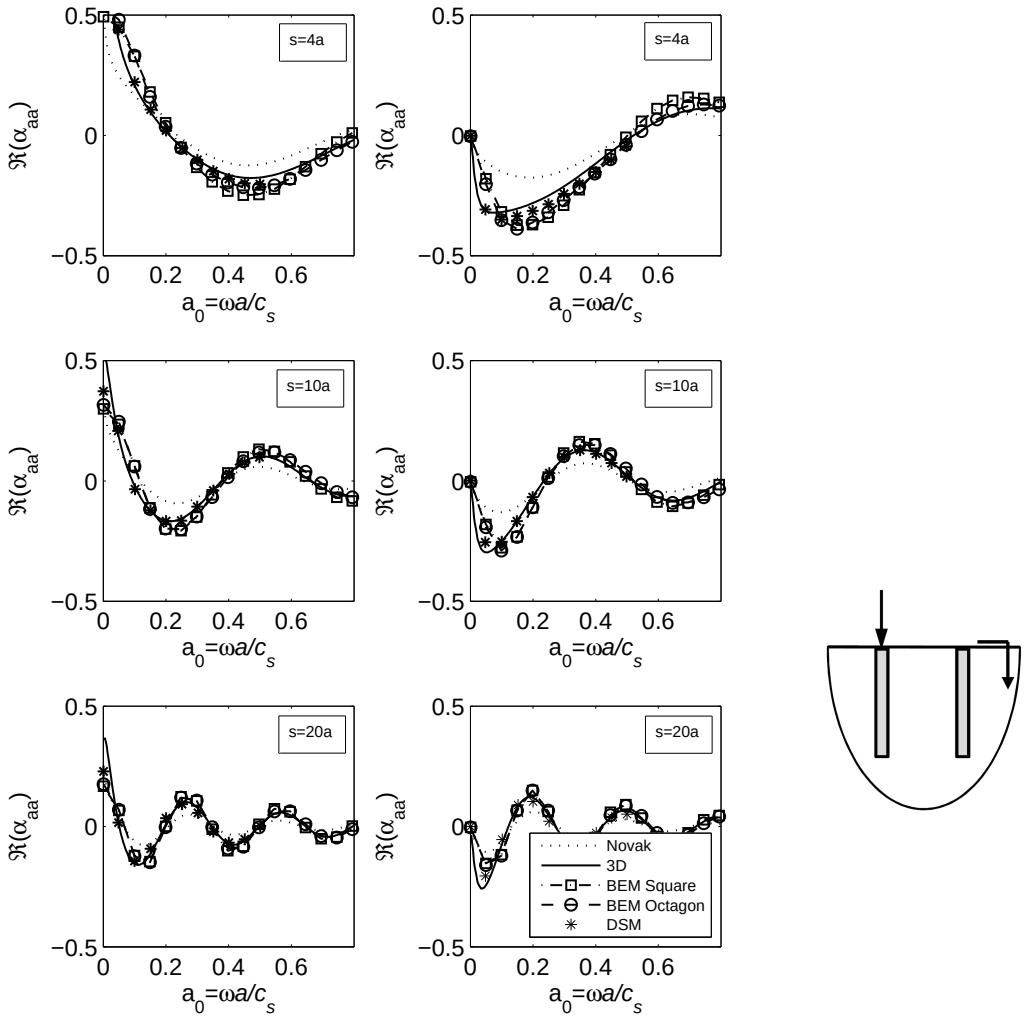

Fig. 3.3 Real part (left), and imaginary part (right) of the axial response of a finite pile at horizontal distances $s = 4a$ (top), $s = 10a$ (middle) and $s = 20a$ (bottom) from a finite single pile undergoing harmonic axial excitation

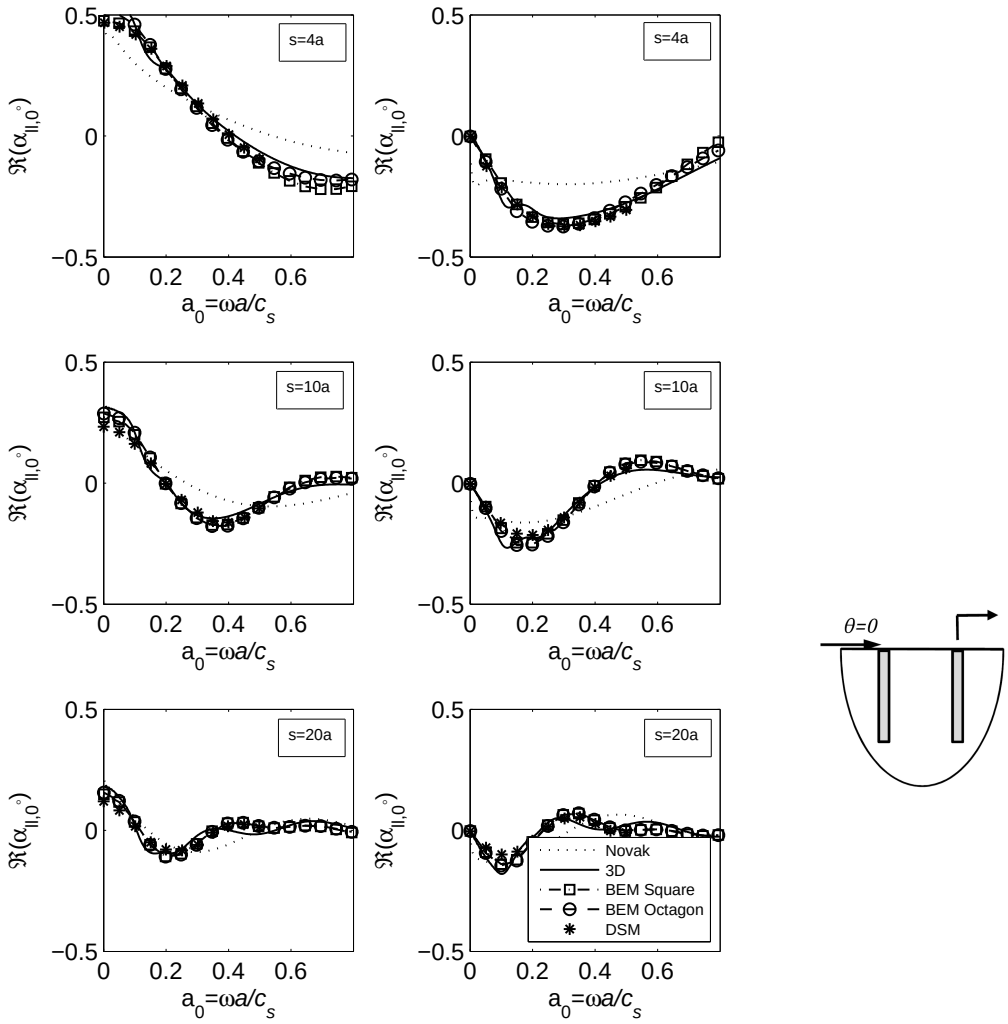

Fig. 3.4 Real part (left), and imaginary part (right) of the lateral response at 0° of a finite pile at horizontal distances $s = 4a$ (top), $s = 10a$ (middle) and $s = 20a$ (bottom) from a finite single pile undergoing harmonic lateral excitation

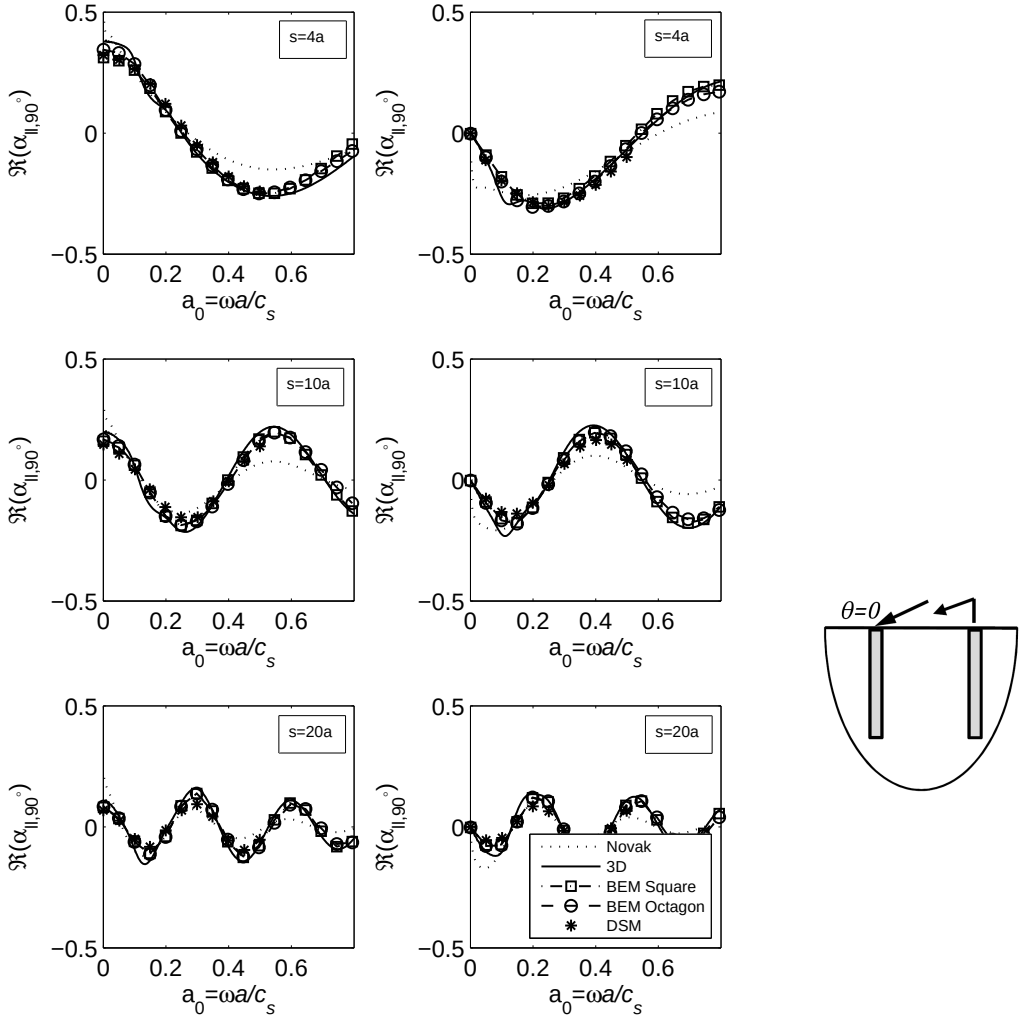

Fig. 3.5 Real part (left), and imaginary part (right) of the lateral response at 90° of a finite pile at horizontal distances $s = 4a$ (top), $s = 10a$ (middle) and $s = 20a$ (bottom) from a finite single pile undergoing harmonic lateral excitation

3.3 Modelling a Pile Group subject to an Incident Wavefield

In this section, the superposition method is used to consider the response of a pile group subject to an incident wavefield generated by an underground railway. The method for calculating the response of a pile group to incident excitation is given below.

1. Calculate the response of each individual, finite pile to the incident wavefield using the method outlined in Sections 2.1.2 & 2.2.5.

2. Calculate the difference between the displacement of the pile and the displacement of the incident wavefield. If using the 3D model, transform this difference in displacement into the wavenumber domain. Propagate the result to the location of a neighbouring pile and use the method of joining subsystems to attach a second pile, as detailed in Section 3.1. Repeat this procedure for every pair of piles to obtain the kinematic interactions in the pile group.

3. Apply the method of superposition to calculate the response of the pile group. This involves summing the contributions from Steps 1 & 2 for each pile within the pile group.

To compare the results of the Novak and 3D models to the BE method, two pile configurations are used: a four-pile row and a two-pile row. The number and length of the piles give both pile-row configurations approximately the same static bearing capacity. The four-pile configuration represents the current limit on the number of piles that are included in the BE model, as the inclusion of additional piles would require extensive algebraic formulations. This illustrates the primary advantage of using the superposition method: the inclusion of additional piles is a simple procedure, and there is no upper limit on the number of piles that can be accounted for.

The parameters used to calculate the response of the two pile configurations are given in Table 2.2. The two pile-group designs are given in Table 3.2, and the results are shown in Figures 3.6 to 3.11. The results are calculated using both the Novak and the 3D models, and are compared with the results of the BE model. Additional results calculated using the 3D model without accounting for the interactions between piles (3D no PSPI) are also shown in these figures. All models are subject to the same incident wavefield from the underground railway.

From these figures it can be seen that there is generally good agreement between the Novak, 3D and BE models over the given frequency range. For the axial response of both the four-pile group and the two-pile group, good agreement between all models is

Table 3.2 Pile-group parameters used for calculating the results of the pile-group models

Four-Pile-Group Properties	*Symbol*	*Value*
Length	L	5m
Separation Distance	s	1.5m
Two-Pile-Group Properties	*Symbol*	*Value*
Length	L	10m
Separation Distance	s	3.0m

observed at frequencies less than 30Hz. Above this frequency, deviations of up to 10dB are observed. For the lateral response, the agreement between the 3D and BEM is good, with the Novak model deviating by up to 3dB at frequencies above 50Hz.

Little deviation is observed between the 3D model that includes PSPI and the 3D model that does not include PSPI. In some cases, such as in Figure 3.8 at 60-80Hz, the 3D model that does not include PSPI shows better agreement with the BEM. From this it is concluded that the superposition method does not provide a comprehensive representation of the interactions occurring in this pile group. Further investigation is required to determine whether the superposition-method error is specific to this group of (closely-spaced) piles, or whether this error applies to all pile groups subject to vibration from an underground railway. One known source of error in the superposition method applicable to all pile groups is a shadowing effect resulting from wave scattering of intermediate piles, described by Coulier [25].

The kinematic interaction effects in these pile groups subject to an incident wavefield generated by an underground railway are small. A similar observation is made by Makris & Gazetas [114] during their investigation into the lateral response of pile groups to vertically propagating seismic S waves, and Makris & Badoni [113] during their investigation into the seismic response of pile groups to Rayleigh and obliquely incident SH waves.

In order to compare the dynamic response of the two different pile-group configurations, a suitable measure for the vibration response of the foundation must be identified. The use of displacement magnitudes in Figures 3.6 to 3.11 does not provide a clear indication of which foundation configuration transmits the greatest amount of vibrational energy into a building. For this reason, the foundation model is extended in Section 3.4 to consider the addition of a simplified building model to the piled foundation, and power-flow techniques are used to evaluate two foundation configurations.

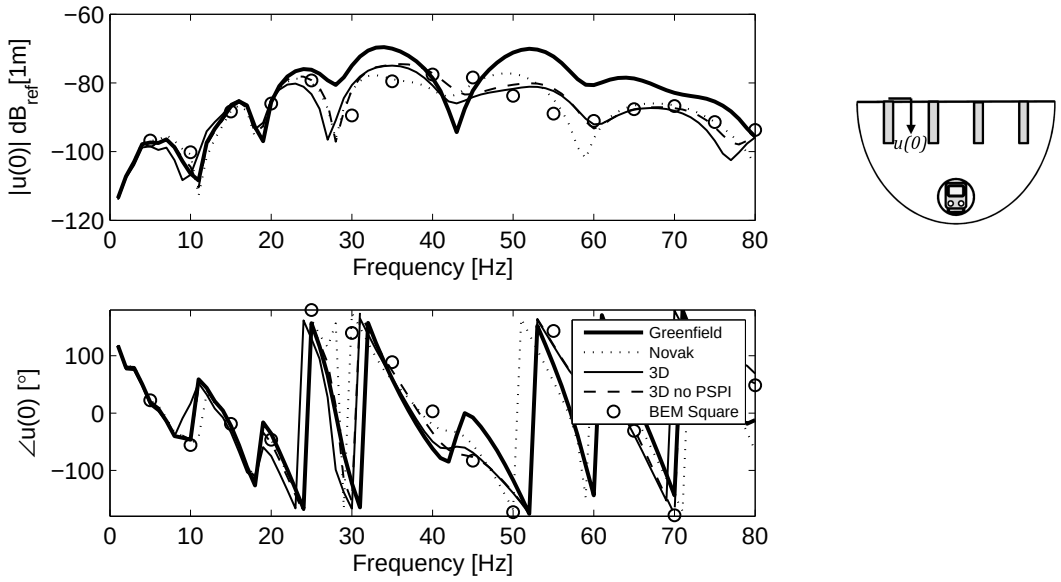

Fig. 3.6 The vertical response of an outer pile in a four-pile row subject to an incident wavefield generated using the PiP software

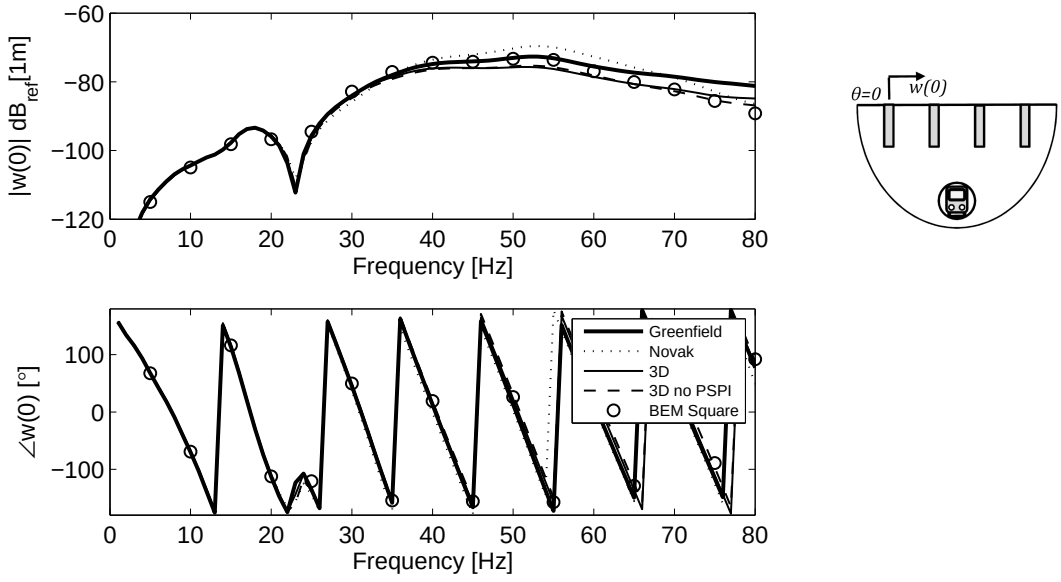

Fig. 3.7 The horizontal response of an outer pile in a four-pile row subject to an incident wavefield generated using the PiP software

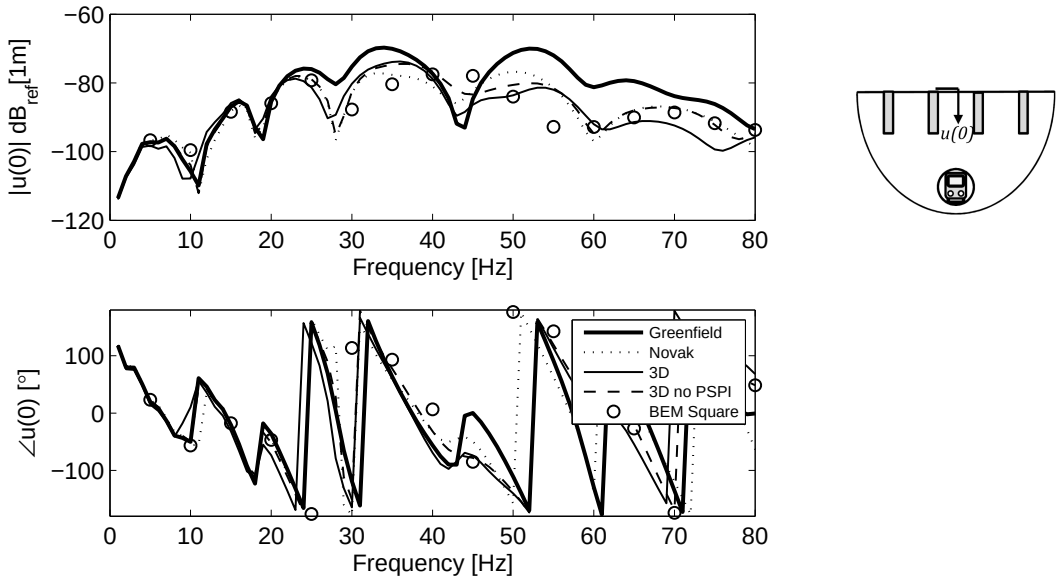

Fig. 3.8 The vertical response of an inner pile in a four-pile row subject to an incident wavefield generated using the PiP software

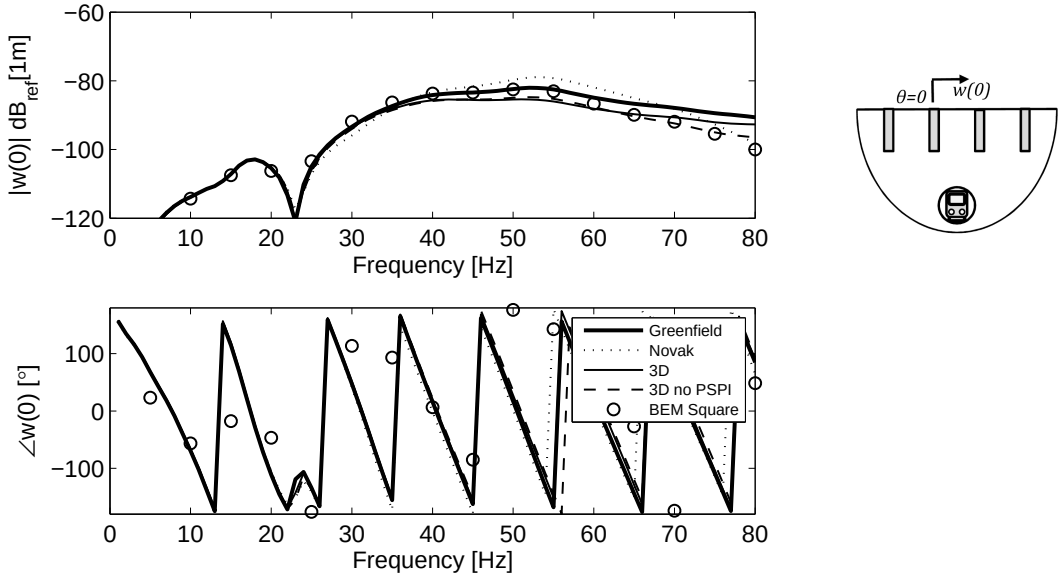

Fig. 3.9 The horizontal response of an inner pile in a four-pile row subject to an incident wavefield generated using the PiP software

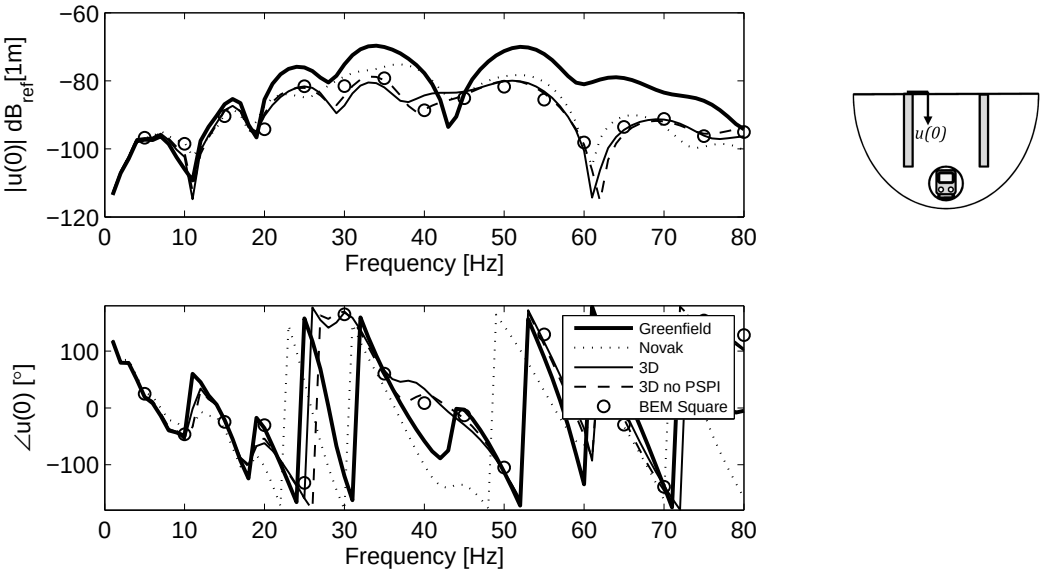

Fig. 3.10 The vertical response of a pile in a two-pile row subject to an incident wavefield generated using the PiP software

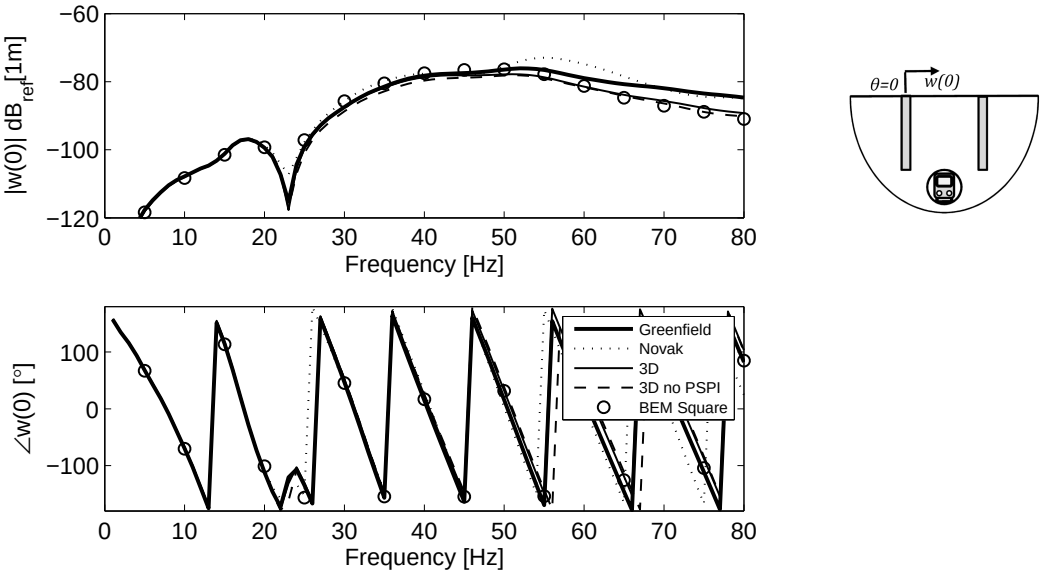

Fig. 3.11 The horizontal response of a pile in a two-pile row subject to an incident wavefield generated using the PiP software

3.4 Modelling a Piled Building subject to an Incident Wavefield

When considering dynamic models of buildings, a range of approaches is possible. Cryer [27] provides an overview of these approaches, which vary in complexity from the simple analytical model of a mass on a spring to more complex numerical methods and statistical energy analysis. In keeping with the design tool philosophy that underpins this dissertation, the building model introduced in this section is that of a semi-infinite column or a semi-infinite Euler beam. This model is chosen for a number of reasons. Firstly, the use of an analytical model is expected to offer both efficient computation times and reasonable accuracy. Secondly, the infinite column or beam is a generic model that improves on the simple, analytical, mass-on-a-spring model by accounting for the essential compression and bending behaviour of a tall building. Finally, the infinite column or beam provides a good representation of the dissipative nature of a building, as vibrational energy is radiated away from the foundation, and the resonances associated with finite models are avoided.

In this section, the attachment of the building, in the form of a semi-infinite column or beam, to the pile head is presented. It is also shown how a finite beam or column can be used to represent the pile cap, joining the pile heads and the building.

3.4.1 Modelling a Building

It is a straightforward exercise to show that the mechanical driving-point impedance of a semi-infinite column Z_u is given by

$$Z_u = \frac{F}{i\omega U_0} = \sqrt{m'EA} \tag{3.4}$$

where U_0 is the axial driving-point displacement, F is the axial force, m' is the mass per unit length, E is Young's Modulus and A is the cross-sectional area of the column. This relationship is obtained by substituting $z = 0$ into Eq. 2.39.

For a semi-infinite beam, both shear forces T and bending moments M can produce bending waves in the beam, thus both must be taken into account when considering beam behaviour. The lateral driving-point velocity $\dot{W}_0$ can be written as

$$\dot{W}_0 = i\omega W_0 = \frac{1}{Z_b}T + \frac{1}{W_b'}M \tag{3.5}$$

and the rotational driving-point velocity $\dot{\theta}_0$ can be written as

$$\dot{\theta}_0 = i\omega\theta_0 = \frac{1}{W_b'}T + \frac{1}{W_b}M. \tag{3.6}$$

The shear force impedance Z_b is given by

$$Z_b = \frac{1}{2}m'c_B(1+i), \tag{3.7}$$

the bending moment impedance W_b is given by

$$W_b = \frac{1}{2}m'c_B\frac{1-i}{\omega\sqrt{\frac{m'}{EI}}}, \tag{3.8}$$

and the coupled shear-bending impedance W_b' is given by

$$W_b' = -\sqrt{EIm'}. \tag{3.9}$$

The bending-wave velocity in the beam is c_B, where

$$c_B = \frac{\sqrt{\omega}}{\left(\frac{m'}{EI}\right)^{1/4}} \tag{3.10}$$

and I is the second moment of area.

Applying the constraint of zero rotation at the pile head ($\theta_0 = 0$) to Equation 3.6, then substituting the resulting expression into Equation 3.5 gives the relationship between the lateral driving-point velocity and the shear force, written as

$$\dot{W}_0 = i\omega W_0 = \frac{1}{Z_w}T = \left(\frac{1}{Z_b} - \frac{W_b}{(W_b')^2}\right)T. \tag{3.11}$$

Now that the relationships between the driving-point displacement of the semi-infinite column/beam and the force acting on the end of the semi-infinite column/beam are determined, the building model is attached to the pile heads. For the case of axial vibration of the pile, a semi-infinite column is attached to the pile head, and for the case of lateral vibration of the pile, a semi-infinite beam is attached to the pile head. Referring to Figure 3.12, which shows two identical piles undergoing axial vibration, the relationship between the driving-point displacements of the semi-infinite columns (U_{b1}, U_{b2}) and the forces acting on the ends of the semi-infinite columns (F_{p1}, F_{p2}) can be

written as

$$\begin{Bmatrix} U_{b1} \\ U_{b2} \end{Bmatrix} = \begin{bmatrix} \frac{1}{i\omega Z_u} & 0 \\ 0 & \frac{1}{i\omega Z_u} \end{bmatrix} \begin{Bmatrix} -F_{p1} \\ -F_{p2} \end{Bmatrix}. \tag{3.12}$$

The equation for the displacement of the pile heads is given by

$$\begin{Bmatrix} U_{b1} \\ U_{b2} \end{Bmatrix} = \begin{bmatrix} H_{11} & H_{12} \\ H_{12} & H_{11} \end{bmatrix} \begin{Bmatrix} F_{p1} \\ F_{p2} \end{Bmatrix} + \begin{Bmatrix} U_{p1} \\ U_{p2} \end{Bmatrix}, \tag{3.13}$$

where U_{p1} and U_{p2} are the displacements at pile heads 1 & 2, respectively, for the piled foundation subject to vibration from an underground railway; H_{11} is the driving-point response of a single pile; and H_{12} is the pile-head displacement of pile 1 when a unit force is applied to the pile head of pile 2.

Rearrangement of these two equations results in the governing equation for the piled building model:

$$\begin{Bmatrix} U_{b1} \\ U_{b2} \end{Bmatrix} = \left[[\mathbf{I}] + \begin{bmatrix} H_{11} & H_{12} \\ H_{12} & H_{11} \end{bmatrix} \begin{bmatrix} \frac{1}{i\omega Z_u} & 0 \\ 0 & \frac{1}{i\omega Z_u} \end{bmatrix}^{-1} \right]^{-1} \begin{Bmatrix} U_{p1} \\ U_{p2} \end{Bmatrix}, \tag{3.14}$$

where [**I**] is the identity matrix. This equation can be extended to account for more than two piles, and non-identical piles.

Using a similar method, the equation for lateral vibration of two identical piles is given by

$$\begin{Bmatrix} W_{b1} \\ W_{b2} \end{Bmatrix} = \left[[\mathbf{I}] + \begin{bmatrix} H_{11} & H_{12} \\ H_{12} & H_{11} \end{bmatrix} \begin{bmatrix} \frac{1}{i\omega Z_w} & 0 \\ 0 & \frac{1}{i\omega Z_w} \end{bmatrix}^{-1} \right]^{-1} \begin{Bmatrix} W_{p1} \\ W_{p2} \end{Bmatrix} \tag{3.15}$$

where the variables W_{b1}, W_{b2}, H_{11}, H_{12}, W_{p1} & W_{p2} are the lateral analogues of those variables defined in Equation 3.14.

3.4.2 Modelling a Pile Cap

The pile cap generally takes the form of a large concrete slab joining the pile heads. In seismic models the pile cap is considered as a rigid body, an assumption that is only valid at very low frequencies. For vibration from underground railways, a more accurate simulation of the pile cap is achieved by considering pile-cap deformations. For a simple pile row in axial or lateral vibration, the pile cap is modelled as a finite Euler beam or column, respectively. The pile cap is a structure with free-free boundary conditions, subject to external forces from the pile heads and, if a building is attached, external forces from the semi-infinite columns or beams. The standard linear theory for finite

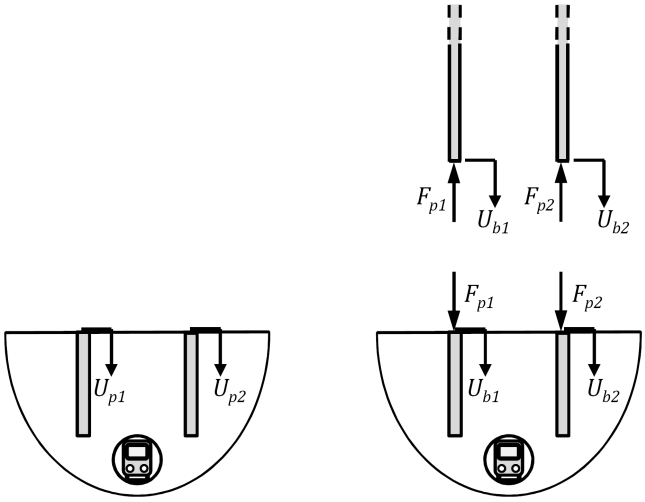

Fig. 3.12 The definition of pile-head displacements for (a) a piled foundation; and (b) a piled building

beams or columns can be used to generate transfer-function matrices relating forces acting on the pile cap to displacements at the pile-head locations. For example, the dynamic behaviour of the finite free-free Euler beam, which is used to model a pile cap attached to a pile row undergoing axial vibration, is given by Equations 2.12 & 2.15. Similarly, the dynamic behaviour of the finite free-free column, which is used to model a pile cap attached to a pile row undergoing lateral vibration, is given by Equation 2.10.

The method of joining subsystems is used to attach the pile cap to the piled foundation by replacing the building-impedance matrix in Equations 3.14 & 3.15 with the pile-cap transfer matrix. For the case where the pile cap is subject to external forces from both the pile heads and the semi-infinite columns or beams, the standard linear theory for finite beams or columns is used to relate the net force acting on the pile cap to displacements at the pile-head locations. For the two-pile configuration shown in Figure 3.13, the transfer matrix [**W**] of the beam representing the pile cap is given by

$$\begin{Bmatrix} U_{b1} \\ U_{b2} \end{Bmatrix} = [\mathbf{W}] \begin{Bmatrix} -F_{p1} - F_{d1} \\ -F_{p2} - F_{d2} \end{Bmatrix}. \tag{3.16}$$

From Section 3.4.1, the transfer function of the building model is given by

$$\begin{Bmatrix} U_{b1} \\ U_{b2} \end{Bmatrix} = \begin{bmatrix} \frac{1}{i\omega Z_u} & 0 \\ 0 & \frac{1}{i\omega Z_u} \end{bmatrix} \begin{Bmatrix} F_{d1} \\ F_{d2} \end{Bmatrix}, \tag{3.17}$$

and the transfer matrix of the piled foundation is

$$\begin{Bmatrix} U_{b1} \\ U_{b2} \end{Bmatrix} = \begin{bmatrix} H_{11} & H_{12} \\ H_{12} & H_{11} \end{bmatrix} \begin{Bmatrix} F_{p1} \\ F_{p2} \end{Bmatrix} + \begin{Bmatrix} U_{p1} \\ U_{p2} \end{Bmatrix}. \tag{3.18}$$

Rearrangement of these Equations 3.16, 3.17 & 3.18 results in the governing equation for the piled raft foundation with attached building shown in Figure 3.13. This equation is written as

$$\begin{Bmatrix} U_{b1} \\ U_{b2} \end{Bmatrix} = \left[[\mathbf{I}] + \begin{bmatrix} H_{11} & H_{12} \\ H_{12} & H_{11} \end{bmatrix} \left[[\mathbf{W}]^{-1} + \begin{bmatrix} \frac{1}{i\omega Z_w} & 0 \\ 0 & \frac{1}{i\omega Z_w} \end{bmatrix}^{-1} \right] \right]^{-1} \begin{Bmatrix} U_{p1} \\ U_{p2} \end{Bmatrix}, \tag{3.19}$$

and can be re-written in generalised matrix form as

$$\mathbf{U}_b = \left[[\mathbf{I}] + [\mathbf{H}] \left[[\mathbf{W}]^{-1} + [\mathbf{Z}]^{-1} \right] \right]^{-1} \mathbf{U}_p. \tag{3.20}$$

A similar equation can be written for piles in lateral vibration.

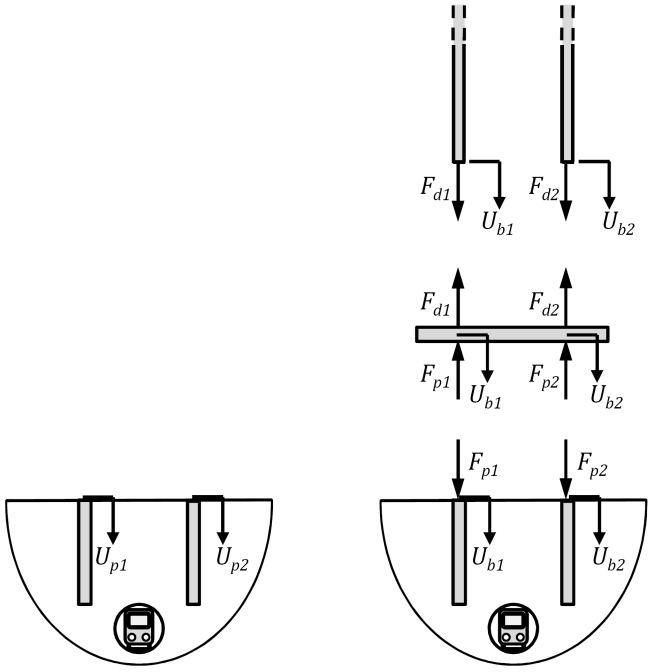

Fig. 3.13 The definition of pile-head displacements for (a) a piled foundation; and (b) a piled raft foundation with attached building

For a three-dimensional pile-group arrangement, the pile cap is best represented by a rectangular, isotropic plate joining each of the pile heads. Whilst the differential

equation of motion for such a plate is well-known, no analytical solution exists for the free-free-free-free boundary condition. A finite-element approach would be required to determine the numerical solution [123]. The pile cap is instead simulated using two layers of beams/columns: one layer joins the pile heads lying in the plane perpendicular to the tunnel's longitudinal axis, and the other layer joins the pile heads lying in the plane parallel to the tunnel's longitudinal axis. The pile cap for a sixteen-pile group is shown in Figure 3.14.

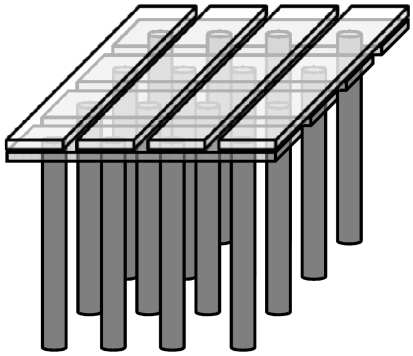

Fig. 3.14 The pile-cap model, consisting of two layers of beams/columns

The second layer of beams/columns are incorporated into the pile cap model using a similar analysis to that detailed earlier in this section. The governing equation, written in the same generalised form as Equation 3.20, is

$$\mathbf{U}_b = \left[[\mathbf{I}] + [\mathbf{H}]\left[[\mathbf{W}_1]^{-1} + [\mathbf{W}_2]^{-1} + [\mathbf{Z}]^{-1}\right]\right]^{-1}\mathbf{U}_p, \tag{3.21}$$

where $[\mathbf{W}_1]$ and $[\mathbf{W}_2]$ are the transfer matrices for the two layers of beams/columns.

3.4.3 Results for the Piled Building

In this section, the building and pile-cap models are attached to the four-pile row considered in Section 3.3. The pile cap has dimensions 5.5x2x0.3m and is made of concrete with material properties equal to those of the piles. The infinite columns/beams representing the building have the same material properties and radii as the piles. The results for the piled building (referred to as '3D Piled Building') are calculated using the 3D model and are presented in Figures 3.15 to 3.18. Also presented in these figures are the pile-head displacements of the foundation with no building or pile cap attached (referred

to as '3D Piles'), and the displacements of the piled building when the kinematic-PSPI components have been neglected (referred to as '3D Piled Building no k-PSPI').

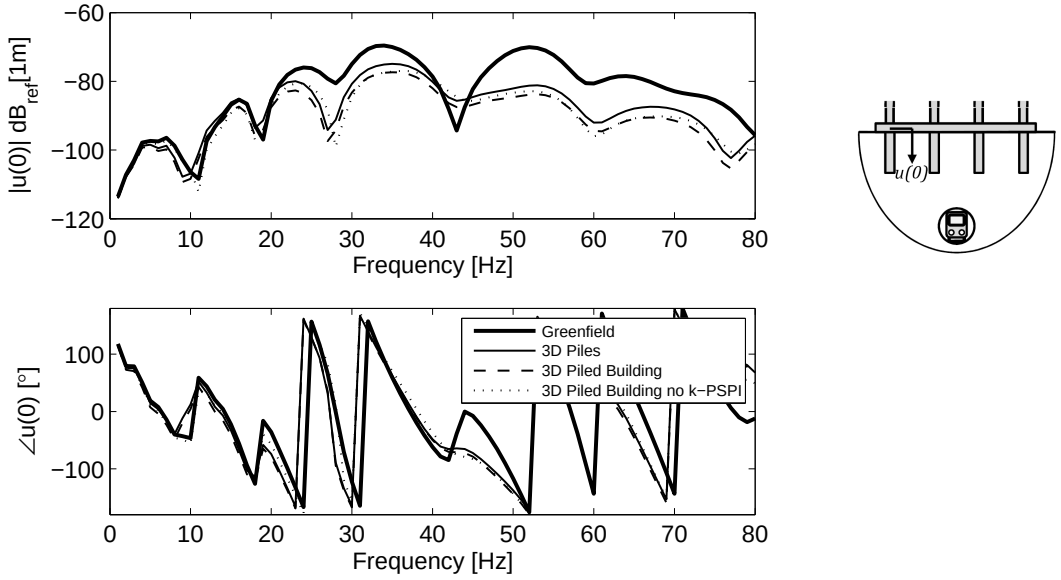

Fig. 3.15 The vertical response of an outer pile in a four-pile row attached to a pile cap and building, and subject to an incident wavefield generated using the PiP software

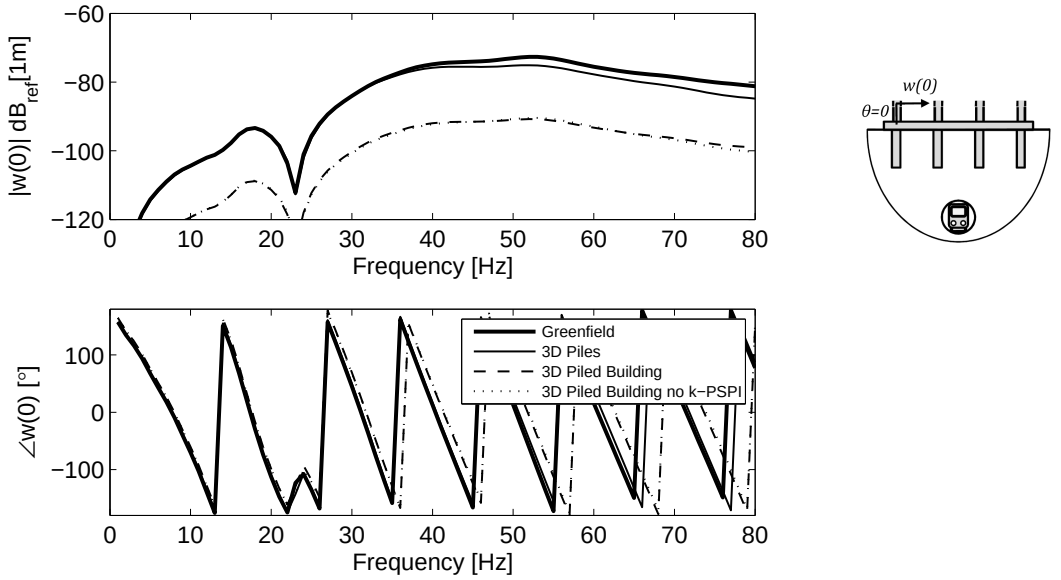

Fig. 3.16 The horizontal response of an outer pile in a four-pile row attached to a pile cap and building, and subject to an incident wavefield generated using the PiP software

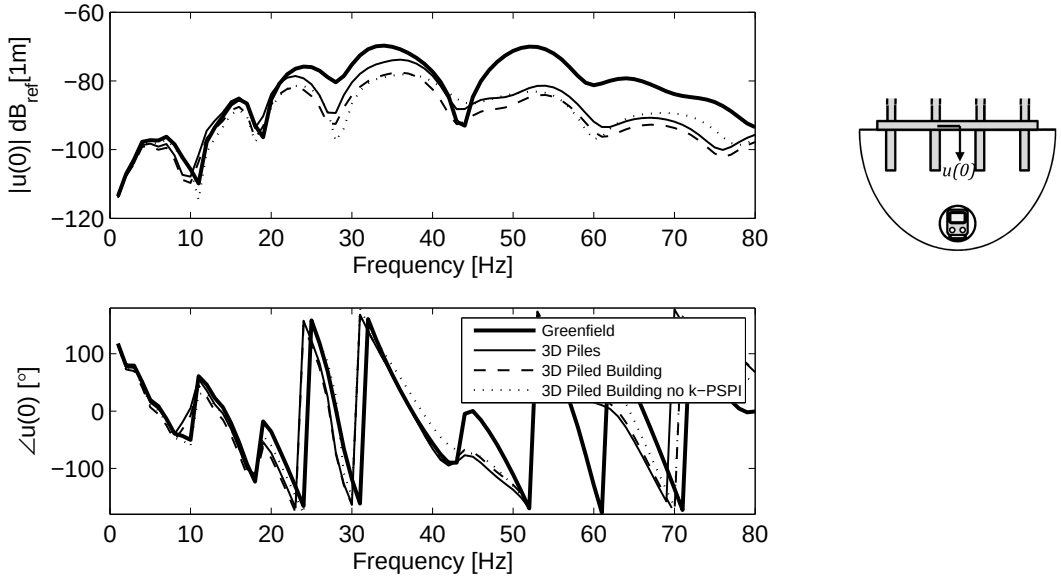

Fig. 3.17 The vertical response of an inner pile in a four-pile row attached to a pile cap and building, and subject to an incident wavefield generated using the PiP software

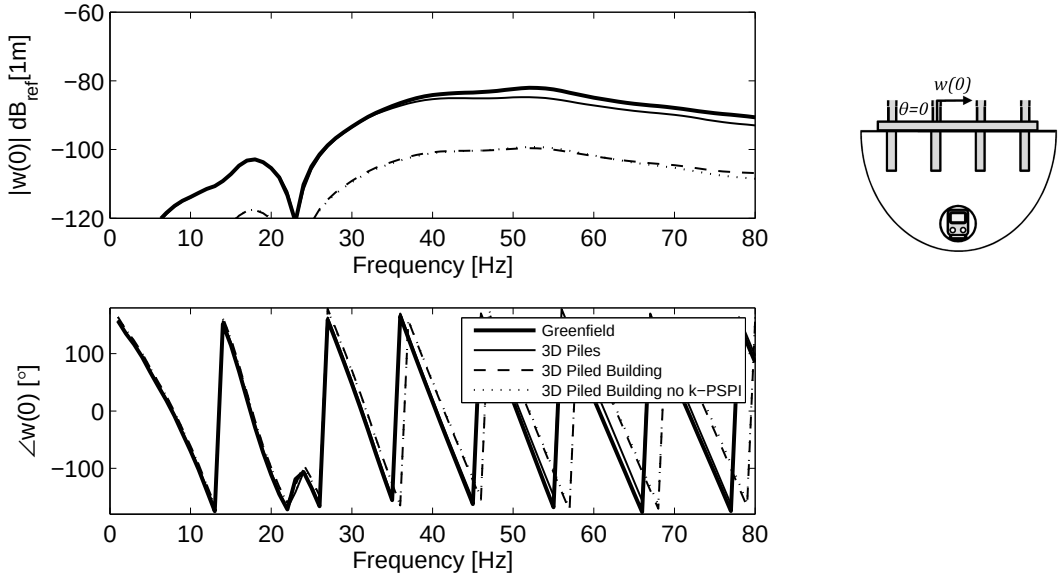

Fig. 3.18 The horizontal response of an inner pile in a four-pile row attached to a pile cap and building, and subject to an incident wavefield generated using the PiP software

From these figures it is apparent that for this pile group the addition of a pile cap and a building has a significant constraining effect on the horizontal pile-head response, resulting in frequency-independent attenuation of approximately 15dB. This is because the antisymmetric nature of the horizontal incident wavefield generated by the underground railway results in antisymmetric, horizontal, pile-row displacements which are resisted by the stiffness of the pile cap. This constraining effect would not be as pronounced if the pile group were not located directly above the tunnel, as the displacements of all the piles in such a group would be in the same direction, resulting in horizontal rigid-body motion of the pile cap. The addition of a pile cap and a building has a less-pronounced effect on the vertical pile-head response. This is because the vertical incident wavefield generated by the underground railway results in symmetric, vertical, pile-row displacements, and the pile cap is thus excited in vertical rigid-body motion. The effect of neglecting the kinematic PSPI is again observed to be small.

3.5 Case Study: Evaluating Two Foundation Designs

A virtual case study is now presented in which the dynamic response of two friction-pile foundation designs is evaluated. The foundation designs are chosen to resist the total static load of a generic five-storey building.

For a given ground condition, the number and size of piles in a pile-group foundation is largely determined by the total static load from the building (Q) to be resisted by the foundation. It is beyond the scope of this dissertation to include a discussion of the many other factors which can govern the design of piled foundations. The interested reader is referred to design handbooks such as Tomlinson [169] and Eurocode 7 [75] for further details on pile design. Each of the N piles in the pile group provides resistance in the form of shaft capacity Q_s and base capacity Q_b, where the total load from the building is given as

$$Q = N(Q_s + Q_b). \tag{3.22}$$

The shaft capacity is proportional to the shaft area of the pile, written as

$$Q_s = 2\pi a L \bar{q}_s, \tag{3.23}$$

and the base capacity is likewise proportional to the base area of the pile, written as

$$Q_b = \pi a^2 \bar{q}_b. \tag{3.24}$$

The pile radius is a, L is the pile length, and $\bar{q}_s$ and $\bar{q}_b$ depend on the soil conditions. In this study typical values for clay are used: 12.5kPa and 87.5kPa, respectively.

Using these formulae, two foundation designs are proposed for a generic, five-storey building with a net load of 4000kN: a nine-pile group, and a sixteen-pile group. Dimensions are given in Figure 3.19, and a safety factor of 2 is applied. The material parameters for the pile cap and the building models are the same as for those of the piles. Apart from those parameters specified in Figure 3.19, all other parameters are given in Table 2.2. The centre of each pile group is located 10m from the longitudinal axis of the railway tunnel, and the tunnel axis is located 20m below the ground surface. A semi-infinite beam or column is attached to the pile cap at each of the pile-head locations to simulate a building.

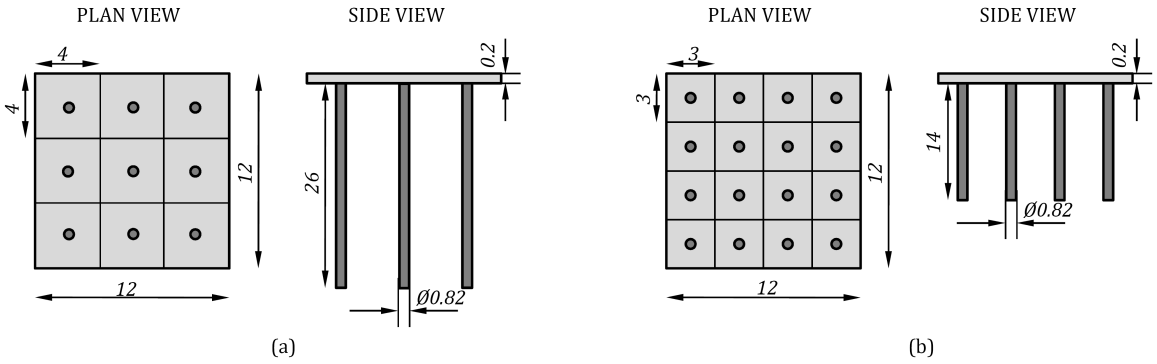

Fig. 3.19 Foundation dimensions for two pile-group designs: (a) a nine-pile group; and (b) a sixteen-pile group. All dimensions are given in [m]. Not to scale

The results of this modelling are presented in Figure 3.20 in terms of the net power flow entering the building. From this figure it can be seen that the sixteen-pile group results in greater vibrational-energy transmission into the building, of the order of 6dB over the frequency range of 40-60Hz. Considering the simplifying assumptions that are involved in producing this result, 6dB represents a small margin. From a geotechnical perspective, the preferred pile design of those that meet the design criteria is generally that which involves the fewest piles. This case study shows that no significant advantage in terms of vibration attenuation has been attained by using a foundation with a greater number of piles. Thus, the designer can recommend the nine-pile foundation.

For both the nine-pile and sixteen-pile foundation designs, the horizontal component dominates the power flow into the building. This is in contrast with the response of the four-pile row examined in Section 3.4.3; for this pile row the vertical component dominates the pile-group response. This illustrates the variability that is present in the response of pile groups to underground-railway vibration, and highlights the need for

models to include an accurate representation of the incident wavefield.

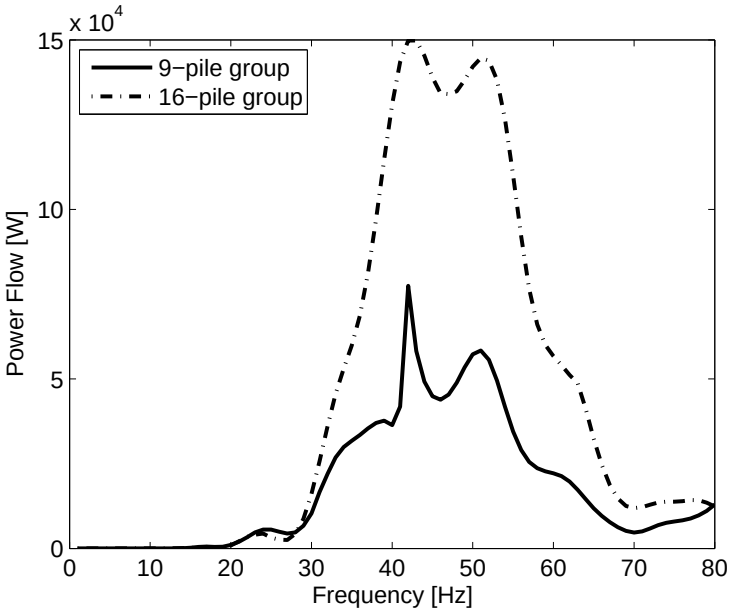

Fig. 3.20 The power flows entering a building for the two pile-group configurations

The power flow is frequency-dependent, and for design situations in which a number of foundation designs have comparable levels of power flow, the designer is recommended to use RMS power flow as a means of removing the frequency component from the power-flow results.

3.6 Conclusions

In this chapter, the Novak and the three-dimensional single-pile models developed in Chapter 2 are extended to consider the pile-soil-pile interaction (PSPI) occurring between two piles. The inertial interaction factors calculated using the two-pile formulation are validated by comparison with results obtained using the dynamic stiffness matrix method and the boundary-element method. The agreement is excellent for the three-dimensional model, but the Novak model consistently underpredicts the PSPI. The superposition method is used to calculate the PSPI in pile groups, and a row of piles subject to vibration from an underground railway is analysed. The results from this pile row show that the kinematic interaction occurring between the piles represents only a small proportion of the total pile-group response, and that the superposition method may not provide an accurate representation of the interactions occurring in this closely-spaced pile group.

Methods are proposed for modelling a building as a collection of semi-infinite columns or beams, and for modelling a pile cap as a series of finite columns or beams. The method of joining subsystems is used to attach the pile cap and the building to the piled foundation. To conclude this chapter, a case study of two piled foundations with equal static bearing capacity is presented. By using power-flow techniques to calculate the vibrational energy entering the building, it is demonstrated that the nine-pile group provides better vibration attenuation than the sixteen-pile group.

This concludes the study of piled foundations subject to underground-railway vibration. The next chapter considers the effects of neighbouring tunnels.

Chapter 4

A Two-Tunnel Model

Many underground railway lines around the world, including those in London, Copenhagen, Taipei, Bangkok and Washington D.C. consist of two tunnels of identical construction, known as 'twin tunnels': one for the outbound direction; and one for the inbound direction. In most cases these tunnels are located side by side, but occasionally, such as in the case of the Chungho Line in Taipei, the tunnels are piggy-back, with one on top of the other [15]. Twin tunnels also exist at intermediate orientations. Numerical models and scale models of twin tunnels exist in the literature [3, 21, 24, 82, 124, 143] for the purposes of determining the static stresses and strains produced during and post- excavation. To date, the only evidence in the literature of a dynamic model which accounts for the vibration interaction between neighbouring tunnels is the wavenumber FE-BE model [160] discussed in Section 1.3.3.3. This model compares the response of a large, single-bore, double-track tunnel with the response of a pair of single, twin-track tunnels embedded in an elastic halfspace.

This chapter describes the formulation of a novel solution for two parallel tunnels of circular cross-section embedded in a homogeneous, elastic soil. This two-tunnel system can be used to represent both a twin-tunnel railway line, and a single tunnel with buried services located nearby. The two-tunnel model is an extension of the single-tunnel (PiP) model developed by Forrest & Hunt [43, 44] and furthered by Hussein & Hunt [70, 71]. Whilst various single-tunnel models exist, this model is unique in that it is a 2.5D model, and therefore more accurate than a simple 2D approach. Furthermore, it does not require the excessive computation times associated with FE and BE approaches. For example, the runtime of the single-tunnel model on a personal computer of moderate specifications is less than one minute. To run the equivalent scenario using a coupled FE-BE model takes 17 hours using one processor of a high-performance cluster [66]. This short process runtime is achieved through the modelling of the tunnel lining as

an infinitely long, thin-walled cylinder and the modelling of the soil as an infinite, elastic medium. The thin-walled cylinder is modelled using a simplification of Volmir's linear equations for a general, thin shell, and the soil is modelled as an infinite, elastic continuum in cylindrical coordinates with an inner radius equal to the radius of the thin-walled cylinder, and an outer radius of infinity. Both the stresses and the displacements of the tunnel and the soil are described using two sets of Fourier series components: one for symmetric contributions; and one for antisymmetric contributions, for a limited number of modeshapes. This single-tunnel model is an efficient and accurate method for calculating vibration from underground railways [51]. Methods exist for adapting this model to obtain vibration predictions in a homogeneous or layered halfspace without a significant loss of computational efficiency [67]. These same methods can be applied to the two-tunnel model described here.

This chapter is divided into three sections. The single-tunnel model is presented in Section 4.1 to provide an introduction to the modelling of two tunnels, presented in Section 4.2. Section 4.3 contains the results and discussion of the two-tunnel model, and the conclusions are presented in Section 4.4.

4.1 Modelling a Single Tunnel

The purpose of this section is to present the analytical background of the dynamic single-tunnel model developed by Forrest & Hunt [43, 44] and furthered by Hussein & Hunt [70, 71]. This model consists of the tunnel, represented by a thin-walled cylinder made of linear, elastic, homogeneous, isotropic material. The soil is modelled as a three-dimensional, homogeneous, isotropic, elastic solid in the form of a thick-walled cylinder with an infinite outer radius. This model is invariant in the longitudinal direction, thus allowing the formulation of equations in the longitudinal-wavenumber (ξ) domain, as well as in the frequency domain. The modelling of Forrest & Hunt and Hussein & Hunt also allows for components such as floating slab track, rail pads and rails to be added to the model. The analytical details of these components are not included here, as it is the tunnel-soil model that is central to the content of this chapter. Instead, in this chapter the dynamic train forces act directly on the tunnel invert. Any force that is applied to the circular tunnel invert is periodic, and can thus be represented using a Fourier series involving the linear sum of sine and cosine components. These sine and cosine components give rise to two types of loading conditions: those which are distributed symmetrically about one of the tunnel's axes of symmetry in the cross-sectional plane, and those which are distributed antisymmetrically about the same axis of symmetry.

These two loading conditions are referred to here as the 'symmetric' and 'antisymmetric' loading cases, respectively. As both the tunnel and the soil are axisymmetric, the symmetry of the loading condition also extends to the displacements and stresses in the soil. For example, a sinusoidal force acting on the tunnel invert will result in a sinusoidal distribution of soil displacements. This feature allows for separate computation of the soil displacements due to each of the two loading conditions, resulting in a significant reduction in the computation times. The total soil displacements are then expressed as the sum of the displacements due to each of these two loading conditions.

Consider the tunnel, represented by the thin-walled cylinder shown in Figure 4.1, which is undergoing modal displacements $\left\{\tilde{U}_{rn}, \tilde{U}_{\theta n}, \tilde{U}_{zn}\right\}^T$ at the mean radius (R) of the cylinder in the radial, tangential and longitudinal directions, respectively. These displacements are the result of applied loads per unit area $\left\{\tilde{Q}_{rn}, \tilde{Q}_{\theta n}, \tilde{Q}_{zn}\right\}^T$ acting on the thin-walled cylinder in the radial, tangential and longitudinal directions, respectively. As the tunnel is represented as an infinitely-long, cylindrical shell, both the loading and the displacement of the tunnel can be written as a linear combination of components which are harmonic in time t and space z. The space-harmonic variation of the loading and the displacement is captured by defining the components in the longitudinal-wavenumber domain, represented by the term $e^{i\xi z}$. The time-harmonic variation of the loading and the displacement is captured by defining the components in the frequency domain, represented by the term $e^{i\omega t}$. The subscript n represents the modenumber, and the tilde on the uppercase coefficients indicates that they are in the longitudinal-wavenumber domain. The uppercase coefficient indicates that the variable is defined in the frequency domain.

The symmetric, harmonic, displacement components are of the form

$$\begin{aligned} u_r(z,t) &= \tilde{U}^1_{rn} \cos n\theta e^{i(\omega t+\xi z)} \\ u_\theta(z,t) &= \tilde{U}^1_{\theta n} \sin n\theta e^{i(\omega t+\xi z)} \\ u_z(z,t) &= \tilde{U}^1_{zn} \cos n\theta e^{i(\omega t+\xi z)}, \end{aligned} \tag{4.1}$$

where the superscript 1 represents the symmetric case.

The antisymmetric, harmonic, displacement components are of the form

$$\begin{aligned} u_r(z,t) &= \tilde{U}^2_{rn} \sin n\theta e^{i(\omega t+\xi z)} \\ u_\theta(z,t) &= \tilde{U}^2_{\theta n} \cos n\theta e^{i(\omega t+\xi z)} \\ u_z(z,t) &= \tilde{U}^2_{zn} \sin n\theta e^{i(\omega t+\xi z)}, \end{aligned} \tag{4.2}$$

where the superscript 2 represents the antisymmetric case.

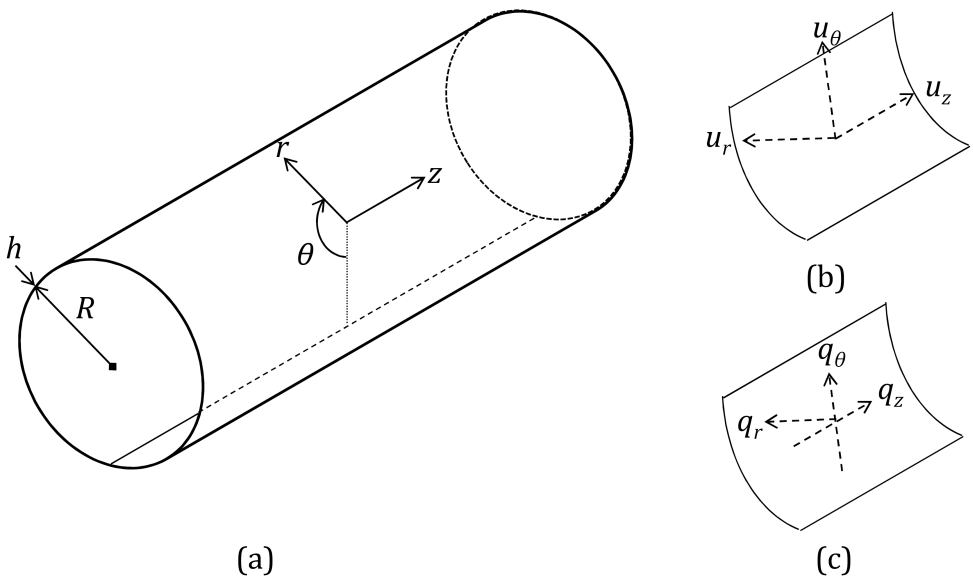

Fig. 4.1 The coordinate system used for the infinitely long, thin-walled cylinder showing: (a) the cylindrical coordinate system; (b) the corresponding displacement components; and (c) the corresponding traction components

Similarly, the symmetric, harmonic loading components are of the form

$$\begin{aligned} q_r(z,t) &= \tilde{Q}^1_{rn} \cos n\theta e^{i(\omega t+\xi z)} \\ q_\theta(z,t) &= \tilde{Q}^1_{\theta n} \sin n\theta e^{i(\omega t+\xi z)} \\ q_z(z,t) &= \tilde{Q}^1_{zn} \cos n\theta e^{i(\omega t+\xi z)}, \end{aligned} \tag{4.3}$$

and the antisymmetric, harmonic loading components are of the form

$$\begin{aligned} q_r(z,t) &= \tilde{Q}^2_{rn} \sin n\theta e^{i(\omega t+\xi z)} \\ q_\theta(z,t) &= \tilde{Q}^2_{\theta n} \cos n\theta e^{i(\omega t+\xi z)} \\ q_z(z,t) &= \tilde{Q}^2_{zn} \sin n\theta e^{i(\omega t+\xi z)}. \end{aligned} \tag{4.4}$$

As this is a thin-walled cylinder, the stresses and the displacements are assumed to be unchanging through the thickness of the cylinder. The expression for the motion of this cylinder is derived using a simplification of Volmir's linear equations for a general

thin shell [43, 44], and is written as

$$\begin{Bmatrix} \tilde{U}_{rn} \\ \tilde{U}_{\theta n} \\ \tilde{U}_{zn} \end{Bmatrix} = [\mathbf{A}_E]^{-1}_{r=R} \begin{Bmatrix} \tilde{Q}_{rn} \\ \tilde{Q}_{\theta n} \\ \tilde{Q}_{zn} \end{Bmatrix}, \tag{4.5}$$

where the elements of the matrix $[\mathbf{A}_E]$ are given in Appendix B. The signs of the elements in the matrix $[\mathbf{A}_E]$ are determined by the symmetry of the loading condition, and hence this equation, together with the equations below, must be replicated using the appropriate matrix elements in order to calculate the displacements arising from both the symmetric and antisymmetric loading conditions.

A similar expression can be obtained for the soil, represented by a thick-walled cylinder with inner radius R and infinite outer radius. This expression relates the modal displacements of the inner surface of the soil cylinder $\left\{\tilde{U}_{rn}, \tilde{U}_{\theta n}, \tilde{U}_{zn}\right\}^T$ to the tractions acting on the inner surface of the soil cylinder $\left\{\tilde{T}_{rn}, \tilde{T}_{\theta n}, \tilde{T}_{zn}\right\}^T$. This expression is obtained by solving the wave equation describing motion within an elastic medium, the derivation for which can be found in Forrest & Hunt [43, 44]. The expression for the motion of the thick-walled cylinder is given by

$$\begin{Bmatrix} \tilde{U}_{rn} \\ \tilde{U}_{\theta n} \\ \tilde{U}_{zn} \end{Bmatrix} = [\mathbf{U}]_{r=R} [\mathbf{T}_r]^{-1}_{r=R} \begin{Bmatrix} \tilde{T}_{rn} \\ \tilde{T}_{\theta n} \\ \tilde{T}_{zn} \end{Bmatrix}, \tag{4.6}$$

where $[\mathbf{T}_r]$ is the top half of the 6x3 matrix $[\mathbf{T}]$, and the elements of the matrices $[\mathbf{U}]$ and $[\mathbf{T}]$ are given in Appendix B.

More generally, it can be written that at a radius R_f in the thick-walled cylinder the soil displacements are given by

$$\begin{Bmatrix} \tilde{U}_{rn} \\ \tilde{U}_{\theta n} \\ \tilde{U}_{zn} \end{Bmatrix}_{r=R_f} = [\mathbf{U}]_{r=Rf} \begin{Bmatrix} B \\ B_r \\ B_z \end{Bmatrix}, \tag{4.7}$$

and the six components of the stress tensor are given by

$$\left\{\begin{matrix}\tilde{T}_{rrn}\\ \tilde{T}_{r\theta n}\\ \tilde{T}_{rzn}\\ \tilde{T}_{\theta\theta n}\\ \tilde{T}_{\theta zn}\\ \tilde{T}_{zzn}\end{matrix}\right\}_{r=R_f} = [\mathbf{T}]_{r=R_f}\left\{\begin{matrix}B\\ B_r\\ B_z\end{matrix}\right\}. \tag{4.8}$$

where $\{B, B_r, B_z\}^T$ is a coefficient vector determined from boundary conditions.

There are three boundary conditions: the tractions on the inside of the uncoupled tunnel are equal to the tractions $\left\{\tilde{P}_{rn}, \tilde{P}_{\theta n}, \tilde{P}_{zn}\right\}^T$ resulting from the applied train loads; the displacements at the interface of the tunnel and the soil continuum are compatible; and the tractions acting on the outside of the tunnel are equal and opposite to the tractions acting on the inside of the soil cavity. These boundary conditions are used to couple the thin-walled cylinder to the soil. The modal displacement components $\left\{\tilde{U}_{rn}, \tilde{U}_{\theta n}, \tilde{U}_{zn}\right\}^T_{r=R}$ at the tunnel-soil interface of the coupled system are then given by

$$\left\{\begin{matrix}\tilde{U}_{rn}\\ \tilde{U}_{\theta n}\\ \tilde{U}_{zn}\end{matrix}\right\}_{r=R} = [\mathbf{U}]_{r=R}\left\{\begin{matrix}B\\ B_r\\ B_z\end{matrix}\right\}, \tag{4.9}$$

where

$$\left\{\begin{matrix}B\\ B_r\\ B_z\end{matrix}\right\} = \left([\mathbf{A}_E]_{r=R}[\mathbf{U}]_{r=R} + [\mathbf{T}_r]_{r=R}\right)^{-1}\left\{\begin{matrix}P_{rn}\\ P_{\theta n}\\ P_{zn}\end{matrix}\right\}. \tag{4.10}$$

The displacements in space and time $\{u_r(z,t), u_\theta(z,t), u_z(z,t)\}^T$ are obtained by applying an inverse Fourier transformation to the wavenumber-domain displacements $\left\{\tilde{U}_{rn}, \tilde{U}_{\theta n}, \tilde{U}_{zn}\right\}^T$. For the symmetric loading case

$$\left\{\begin{matrix}u_r(z,t)\\ u_\theta(z,t)\\ u_z(z,t)\end{matrix}\right\} = \frac{1}{2\pi}\int_{-\infty}^{\infty}\sum_{n=0}^{\infty}\left\{\begin{matrix}\tilde{U}_{rn}\cos n\theta\\ \tilde{U}_{\theta n}\sin n\theta\\ \tilde{U}_{zn}\cos n\theta\end{matrix}\right\} e^{i\xi z} d\xi e^{i\omega t}, \tag{4.11}$$

and for the antisymmetric loading case

$$\begin{Bmatrix} u_r(z,t) \\ u_\theta(z,t) \\ u_z(z,t) \end{Bmatrix} = \frac{1}{2\pi} \int_{-\infty}^{\infty} \sum_{n=0}^{\infty} \begin{Bmatrix} \tilde{U}_{rn} \sin n\theta \\ \tilde{U}_{\theta n} \cos n\theta \\ \tilde{U}_{zn} \sin n\theta \end{Bmatrix} e^{i\xi z} d\xi e^{i\omega t}. \tag{4.12}$$

When the above method is implemented in a mathematical routine, the wavenumber integral in these expressions, and all those in the following sections that contain the wavenumber integral, are evaluated numerically using the inverse Discrete Fourier transformation. The number and spacing of the discrete wavenumbers are selected to ensure that the Nyquist criterion is satisfied and the maximum wavenumber is large enough to capture all the broad wavenumber information.

4.2 Modelling Two Tunnels

Consider two tunnels with circular cross-sections, of mean radius R_1 and R_2 and thickness h_1 and h_2, respectively. The tunnels are separated by a distance c, with tunnel 2 located at an angle α from tunnel 1. Each tunnel has its own set of material parameters such as density and Young's modulus. In the case of twin tunnels, $R_1 = R_2$, $h_1 = h_2$ and only one set of material parameters is needed to define both tunnels. Two right-handed, cylindrical coordinate systems, centred on each tunnel, are defined: (r, θ, z), oriented clockwise on tunnel 1; and (s, ϕ, z), oriented clockwise on tunnel 2. This configuration is illustrated in Figure 4.2.

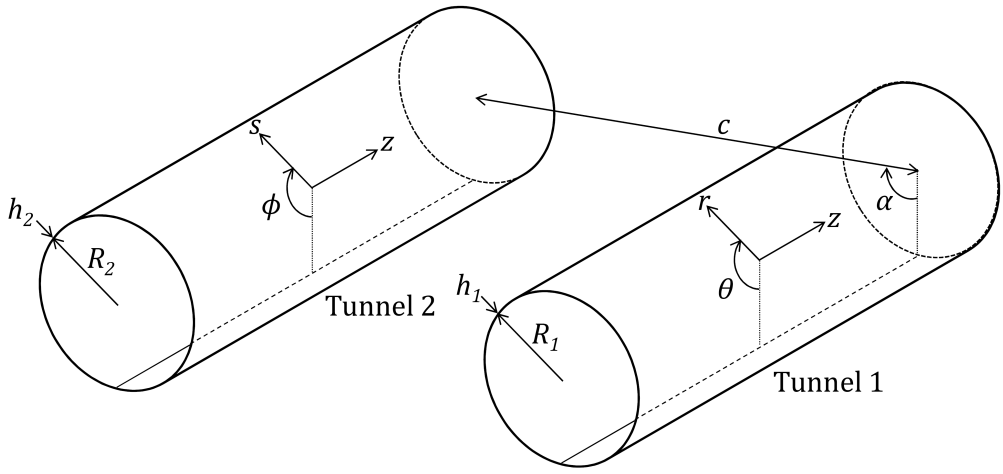

Fig. 4.2 The two tunnels and their associated coordinate systems

4.2.1 Dynamic Train Forces

Each of the tunnels is subject to a set of known, dynamic train forces acting directly on the tunnel invert. These known, dynamic train forces result in traction vectors $\tilde{\mathbf{P}}_1$ and $\tilde{\mathbf{P}}_2$, where the subscript indicates that the traction vectors act on the inverts of tunnel 1 and tunnel 2, respectively. The traction vectors have three components, acting in the directions of the coordinate axes. Using Fourier decomposition, these traction components can be expressed as a combination of two loading cases: symmetric; and antisymmetric, denoted by the superscripts 1 and 2 respectively, and also a combination of N modeshapes, where the subscript n is used to denote the n^{th} modeshape. Thus the known traction vectors acting on the inside of tunnel 1 are $\tilde{\mathbf{P}}^1_{1n}$ and $\tilde{\mathbf{P}}^2_{1n}$, and can be written as

$$\begin{aligned}\tilde{\mathbf{P}}^1_{1n} &= \sum_{n=0}^{N} \begin{Bmatrix} \tilde{P}^1_{rn} \cos n\theta \\ \tilde{P}^1_{\theta n} \sin n\theta \\ \tilde{P}^1_{zn} \cos n\theta \end{Bmatrix} e^{i(\omega t + \xi z)} \\ \tilde{\mathbf{P}}^2_{1n} &= \sum_{n=0}^{N} \begin{Bmatrix} \tilde{P}^2_{rn} \sin n\theta \\ \tilde{P}^2_{\theta n} \cos n\theta \\ \tilde{P}^2_{zn} \sin n\theta \end{Bmatrix} e^{i(\omega t + \xi z)}.\end{aligned} \tag{4.13}$$

Similarly, the known traction vectors acting on the inside of tunnel 2 are $\tilde{\mathbf{P}}^1_{2n}$ and $\tilde{\mathbf{P}}^2_{2n}$, and can be written as

$$\begin{aligned}\tilde{\mathbf{P}}^1_{2n} &= \sum_{n=0}^{N} \begin{Bmatrix} \tilde{P}^1_{sn} \cos n\phi \\ \tilde{P}^1_{\phi n} \sin n\phi \\ \tilde{P}^1_{zn} \cos n\phi \end{Bmatrix} e^{i(\omega t + \xi z)} \\ \tilde{\mathbf{P}}^2_{2n} &= \sum_{n=0}^{N} \begin{Bmatrix} \tilde{P}^2_{sn} \sin n\phi \\ \tilde{P}^2_{\phi n} \cos n\phi \\ \tilde{P}^2_{zn} \sin n\phi \end{Bmatrix} e^{i(\omega t + \xi z)}.\end{aligned} \tag{4.14}$$

To illustrate how a known dynamic load can be written in this form, consider a unit, harmonic point load acting on the invert of tunnel 1 at $\theta = \frac{\pi}{2}$, $z = 0$ in the radial direction, as shown in Figure 4.3.

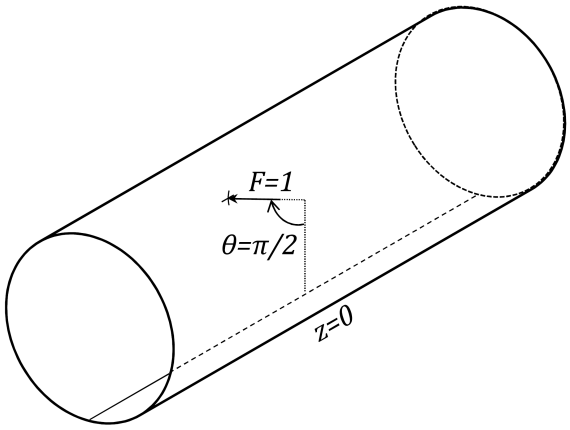

Fig. 4.3 A unit, harmonic point load acting on the invert of tunnel 1 in the radial direction

The traction vector produced by this force can be written in the space and frequency domains as

$$\begin{Bmatrix} P_r \\ P_\theta \\ P_z \end{Bmatrix} = \begin{Bmatrix} \frac{\delta(\theta-\frac{\pi}{2})\delta(z)}{R_1} e^{i\omega t} \\ 0 \\ 0 \end{Bmatrix}, \tag{4.15}$$

where $\delta(\theta - \frac{\pi}{2})$ and $\delta(z)$ are Dirac delta functions. The traction components produced by this point load must be decomposed into a function of the N space-harmonic components. This is done by considering the circumferential variation of the load, which is represented by the term $\delta(\theta - \frac{\pi}{2})$. This term can be expressed as a linear combination of symmetric and antisymmetric ring modes by means of Fourier series decomposition:

$$\begin{aligned}
\delta(\theta - \tfrac{\pi}{2}) &= a_0 + \sum_{n=1}^{\infty} \left(a_n \cos n\theta + b_n \sin n\theta\right), \\
\text{with } a_0 &= \tfrac{1}{2\pi} \int_{-\pi}^{\pi} \delta(\theta - \tfrac{\pi}{2}) d\theta = \tfrac{1}{2\pi}; \\
a_n &= \tfrac{1}{\pi} \int_{-\pi}^{\pi} \delta(\theta - \tfrac{\pi}{2}) \cos n\theta d\theta = \begin{cases} 0 & n \text{ is odd} \\ \frac{(-1)^{\frac{n}{2}}}{\pi} & n \text{ is even;} \end{cases} \\
\text{and } b_n &= \tfrac{1}{\pi} \int_{-\pi}^{\pi} \delta(\theta - \tfrac{\pi}{2}) \sin n\theta d\theta = \begin{cases} \frac{(-1)^{\frac{n-1}{2}}}{\pi} & n \text{ is odd} \\ 0 & n \text{ is even.} \end{cases}
\end{aligned} \tag{4.16}$$

The longitudinal variation of the load is then represented by the term $\delta(z)$, which

can be expressed in the wavenumber domain using the Fourier transformation

$$\int_{-\infty}^{\infty} \delta(z) e^{-i\xi z} dz = 1 \text{ for all } \xi. \tag{4.17}$$

The definition of the Fourier transformation used here puts the factor $\frac{1}{2\pi}$ in the inverse transformation.

Substituting the expressions for the circumferential and longitudinal variation of the load into Equation 4.15 results in

$$\begin{aligned} P_r &= \tfrac{1}{2\pi} \int_{-\infty}^{\infty} \left(\tfrac{1}{2\pi R_1} + \tfrac{1}{\pi R_1} \sum_{n=2,4,6,\ldots}^{\infty} (-1)^{\frac{n}{2}} \cos n\theta + \ldots \right. \\ &\quad \left. \ldots \tfrac{1}{\pi R_1} \sum_{n=1,3,5,\ldots}^{\infty} (-1)^{\frac{n-1}{2}} \sin n\theta \right) e^{i\xi z} d\xi e^{i\omega t}; \\ P_\theta &= 0; \\ \text{and } P_z &= 0. \end{aligned} \tag{4.18}$$

Hence the traction vector $\tilde{\mathbf{P}}_1$ resulting from the unit point load can be written in the form of Equation 4.13, where

$$\begin{aligned} \begin{Bmatrix} \tilde{P}^1_{rn} \\ \tilde{P}^1_{\theta n} \\ \tilde{P}^1_{zn} \end{Bmatrix} &= \left\{ \begin{Bmatrix} \frac{1}{2\pi R_1} & n = 0 \\ 0 & n = 1, 3, 5, \ldots \\ \frac{1}{\pi R_1}(-1)^{\frac{n}{2}} & n = 2, 4, 6, \ldots \end{Bmatrix} \right\}, \\ & \qquad \begin{matrix} 0 \\ 0 \end{matrix} \\ \text{and } \begin{Bmatrix} \tilde{P}^2_{rn} \\ \tilde{P}^2_{\theta n} \\ \tilde{P}^2_{zn} \end{Bmatrix} &= \left\{ \begin{Bmatrix} 0 & n \text{ is even} \\ \frac{1}{\pi R_1}(-1)^{\frac{n-1}{2}} & n \text{ is odd} \end{Bmatrix} \right\}. \\ & \qquad \begin{matrix} 0 \\ 0 \end{matrix} \end{aligned} \tag{4.19}$$

4.2.2 Dynamic Cavity Forces

Using the equations for a thin-walled cylinder, the net applied load per unit area acting on each of the two tunnels can be expressed as a function of the tunnel displacements: $\tilde{\mathbf{U}}_{1-tt}$ and $\tilde{\mathbf{U}}_{2-tt}$ for tunnel 1 and tunnel 2, respectively. The net applied load per unit area acting on each of the two tunnels is equal to the difference between the tractions resulting from the dynamic train forces, $\tilde{\mathbf{P}}_1$ and $\tilde{\mathbf{P}}_2$, and the tractions resulting from the dynamic cavity forces, $\tilde{\mathbf{Q}}_1$ and $\tilde{\mathbf{Q}}_2$. This is illustrated in Figure 4.4. The equations for the two tunnels are

$$\begin{aligned}
\tilde{\mathbf{P}}^1_{1n} - \tilde{\mathbf{Q}}^1_{1n} &= [\mathbf{A}_E]_{r=R_1}\, \tilde{\mathbf{U}}^1_{1n-tt} \\
\tilde{\mathbf{P}}^2_{1n} - \tilde{\mathbf{Q}}^2_{1n} &= [\mathbf{A}_E]_{r=R_1}\, \tilde{\mathbf{U}}^2_{1n-tt} \\
\tilde{\mathbf{P}}^1_{2n} - \tilde{\mathbf{Q}}^1_{2n} &= [\mathbf{A}_E]_{r=R_2}\, \tilde{\mathbf{U}}^1_{2n-tt} \\
\tilde{\mathbf{P}}^2_{2n} - \tilde{\mathbf{Q}}^2_{2n} &= [\mathbf{A}_E]_{r=R_2}\, \tilde{\mathbf{U}}^2_{2n-tt}.
\end{aligned} \tag{4.20}$$

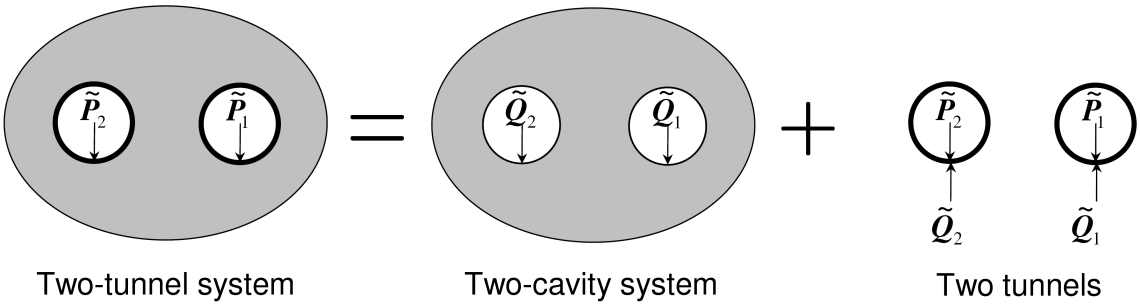

Fig. 4.4 A free-body diagram showing the tractions resulting from the dynamic train forces, $\tilde{\mathbf{P}}_1$ and $\tilde{\mathbf{P}}_2$, and the traction resulting from the dynamic cavity forces, $\tilde{\mathbf{Q}}_1$ and $\tilde{\mathbf{Q}}_2$. The net applied load per unit area acting on each of the two tunnels is equal to the difference between the tractions resulting from the dynamic train forces and the tractions resulting from the dynamic cavity forces

4.2.3 Superposition of Displacement Fields

The vibration response of the two-cavity system can be written as the superposition of two displacement fields. One displacement field is the result of forces acting on a single cavity (similar to a direct field), while the other displacement field is the result of the interactions between the two cavities (similar to a scattered field). Hence, the tractions resulting from the dynamic cavity forces are written as the sum of two contri-

butions: those traction vectors acting on a single cavity, $\tilde{\mathbf{F}}_1$ and $\tilde{\mathbf{F}}_2$; and those traction vectors representing the motion induced by the neighbouring cavity, $\tilde{\mathbf{G}}_1$ and $\tilde{\mathbf{G}}_2$. This is illustrated in Figure 4.5, and expressed in

$$\begin{aligned}
\tilde{\mathbf{Q}}^1_{1n} &= \tilde{\mathbf{F}}^1_{1n} + \tilde{\mathbf{G}}^1_{1n} \\
\tilde{\mathbf{Q}}^2_{1n} &= \tilde{\mathbf{F}}^2_{1n} + \tilde{\mathbf{G}}^2_{1n} \\
\tilde{\mathbf{Q}}^1_{2n} &= \tilde{\mathbf{F}}^1_{2n} + \tilde{\mathbf{G}}^1_{2n} \\
\tilde{\mathbf{Q}}^2_{2n} &= \tilde{\mathbf{F}}^2_{2n} + \tilde{\mathbf{G}}^2_{2n}.
\end{aligned} \tag{4.21}$$

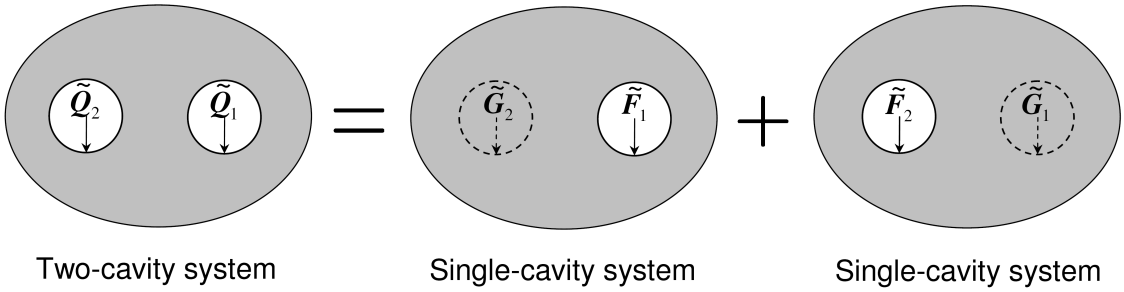

Fig. 4.5 The tractions resulting from the dynamic cavity forces, $\tilde{\mathbf{Q}}_1$ and $\tilde{\mathbf{Q}}_2$, are written as the sum of two contributions: those traction vectors acting on a single cavity, $\tilde{\mathbf{F}}_1$ and $\tilde{\mathbf{F}}_2$; and those traction vectors representing the motion induced by the neighbouring cavity, $\tilde{\mathbf{G}}_1$ and $\tilde{\mathbf{G}}_2$

These traction vectors include components for every coordinate direction, every mode-number n, every wavenumber ξ, and every frequency. To solve these equations, the interaction terms $\tilde{\mathbf{G}}_1$ and $\tilde{\mathbf{G}}_2$ are expressed in terms of the variables $\tilde{\mathbf{F}}_1$ and $\tilde{\mathbf{F}}_2$. This is done by writing the traction vectors representing the motion induced by the neighbouring cavity as a function of the traction vectors acting directly on the neighbouring cavity. To calculate the traction vectors representing the motion induced by the neighbouring cavity, the equations for a single-cavity model are used to determine the stresses around the virtual surface of the neighbouring cavity. Thus to calculate $\tilde{\mathbf{G}}_2$, the traction vector $\tilde{\mathbf{F}}_1$ is applied to cavity 1, and the soil-continuum equations are used to calculate the resulting stresses around the virtual surface of cavity 2. The soil-continuum equations are then used to transform these stresses into the equivalent traction vector ($\tilde{\mathbf{G}}_2$) acting on cavity 2. The advantage of this method is that by apportioning the known traction vectors in this way, it is only ever necessary to consider a single-cavity system at any time. The traction vector $\tilde{\mathbf{G}}_1$ is likewise calculated by applying $\tilde{\mathbf{F}}_2$ to cavity 2, using the

soil-continuum equations to calculate the resulting stresses around the virtual surface of cavity 1, and then transforming these stresses into the equivalent traction vector ($\tilde{\mathbf{G}}_1$) acting on cavity 1. The details of this method are presented in Section 4.2.4.

4.2.4 Calculating Stresses around a Virtual Surface

It should be noted that the following formulation is for the calculation of the traction vector $\tilde{\mathbf{G}}_2$ resulting from the traction vector $\tilde{\mathbf{F}}_1$ that is applied to cavity 1. To obtain the traction vector $\tilde{\mathbf{G}}_1$, the same formulation can be used by substituting $\tilde{\mathbf{F}}_2$ for $\tilde{\mathbf{F}}_1$.

The equations of the soil continuum are used to calculate the stresses resulting from the traction vector $\tilde{\mathbf{F}}_1$ at a point on the virtual surface of cavity 2, for each modenumber n. The stresses are calculated at a radial distance R_f from cavity 1, which corresponds to a radial distance R_2 from cavity 2, using

$$\begin{Bmatrix} \tilde{T}^1_{rrn} \\ \tilde{T}^1_{r\theta n} \\ \tilde{T}^1_{rzn} \\ \tilde{T}^1_{\theta\theta n} \\ \tilde{T}^1_{\theta zn} \\ \tilde{T}^1_{zzn} \end{Bmatrix}_{r=R_f} = [\mathbf{T}]_{r=R_f} [\mathbf{T}_r]^{-1}_{r=R_1} \begin{Bmatrix} \tilde{F}^1_{rn} \\ \tilde{F}^1_{\theta n} \\ \tilde{F}^1_{zn} \end{Bmatrix}. \tag{4.22}$$

The total stresses at the point $(R_f, \Theta_f, 0)$, which corresponds to the point $(R_2, \Phi_f, 0)$ on cavity 2, is calculated by combining the stress contributions from each modenumber:

$$\begin{Bmatrix} \tilde{T}_{rr} \\ \tilde{T}_{r\theta} \\ \tilde{T}_{rz} \\ \tilde{T}_{\theta\theta} \\ \tilde{T}_{\theta z} \\ \tilde{T}_{zz} \end{Bmatrix}_{(R_f,\Theta_f,0)} = \sum_{n=0}^{N} \begin{Bmatrix} \tilde{T}^1_{rrn} \cos n\Theta_f \\ \tilde{T}^1_{r\theta n} \sin n\Theta_f \\ \tilde{T}^1_{rzn} \cos n\Theta_f \\ \tilde{T}^1_{\theta\theta n} \cos n\Theta_f \\ \tilde{T}^1_{\theta zn} \sin n\Theta_f \\ \tilde{T}^1_{zzn} \cos n\Theta_f \end{Bmatrix}. \tag{4.23}$$

The stresses that are calculated using Equation 4.23 are defined in the (r, θ, z) directions, and are now converted to the (s, ϕ, z) directions to obtain compatibility with the cavity 2 coordinate system. The equations for converting stresses between the (r, θ, z) and (s, ϕ, z) coordinate systems are obtained by considering vector geometry, and are

written as

$$\begin{aligned}
\tilde{T}_{ss} &= -\tilde{T}_{rr}\sin^2(\Psi) + \tilde{T}_{r\theta}\sin(\Psi)\cos(\Psi) - \tilde{T}_{\theta\theta}\cos^2(\Psi) \\
\tilde{T}_{s\phi} &= -\tilde{T}_{rr}\sin(\Psi)\cos(\Psi) + \tilde{T}_{r\theta}(\cos^2(\Psi) - \sin^2(\Psi)) + \tilde{T}_{\theta\theta}\sin(\Psi)\cos(\Psi) \\
\tilde{T}_{sz} &= -\tilde{T}_{rz}\sin(\Psi) + \tilde{T}_{\theta z}\cos(\Psi),
\end{aligned} \tag{4.24}$$

where $\Psi = \Phi_f - \Theta_f - \frac{3\pi}{2}$.

These equations are assembled into a 3x6 transformation matrix, denoted [**A**], such that

$$\begin{Bmatrix} \tilde{T}_{ss} \\ \tilde{T}_{s\phi} \\ \tilde{T}_{sz} \end{Bmatrix}_{(R_2,\Phi_f,0)} = [\mathbf{A}] \begin{Bmatrix} \tilde{T}_{rr} \\ \tilde{T}_{r\theta} \\ \tilde{T}_{rz} \\ \tilde{T}_{\theta\theta} \\ \tilde{T}_{\theta z} \\ \tilde{T}_{zz} \end{Bmatrix}_{(R_f,\Theta_f,0)}, \tag{4.25}$$

where [**A**] is given by

$$[\mathbf{A}] = \begin{bmatrix} -\sin^2(\Psi) & 2\sin(\Psi)\cos(\Psi) & 0 & -\cos^2(\Psi) & 0 & 0 \\ -\sin(\Psi)\cos(\Psi) & \cos^2(\Psi) - \sin^2(\Psi) & 0 & \sin(\Psi)\cos(\Psi) & 0 & 0 \\ 0 & 0 & -\sin(\Psi) & 0 & \cos(\Psi) & 0 \end{bmatrix}. \tag{4.26}$$

At this stage, the stresses in the (s, ϕ, z) directions are calculated as a function of $\tilde{\mathbf{F}}_1^1$ at a single point $(R_2, \Phi_f, 0)$ on the virtual surface of cavity 2. It is necessary to calculate these stresses at a series of M evenly spaced points around the virtual surface of cavity 2. This is achieved by substituting into Equations 4.22-4.25 the radial distance R_f, which varies between limits $\langle c - R_2, c + R_2 \rangle$, and the angles Θ_f and Φ_f, which vary accordingly. Once the series of M stresses are determined, Fourier decomposition is used to partition the stresses into those contributions due to the symmetric and antisymmetric loading cases, and the n modenumbers. These stress contributions represent the stress state that is induced by the action of the traction vector $\tilde{\mathbf{G}}_2$ on a real cavity. Hence the components of the traction vector $\tilde{\mathbf{G}}_2$ due to $\tilde{\mathbf{F}}_1^1$ are given by

$$\begin{aligned}
\begin{Bmatrix} \tilde{G}^1_{sn} \\ \tilde{G}^2_{\phi n} \\ \tilde{G}^1_{zn} \end{Bmatrix}_{n=0} &= \frac{1}{2\pi}\int_{-\pi}^{\pi} \begin{Bmatrix} \tilde{T}_{ss} \\ \tilde{T}_{s\phi} \\ \tilde{T}_{sz} \end{Bmatrix} d\phi = \frac{1}{2\pi}\sum_{m=1}^{M} \begin{Bmatrix} \tilde{T}_{ss}(m) \\ \tilde{T}_{s\phi}(m) \\ \tilde{T}_{sz}(m) \end{Bmatrix} \Delta\phi \\
\begin{Bmatrix} \tilde{G}^1_{sn} \\ \tilde{G}^2_{\phi n} \\ \tilde{G}^1_{zn} \end{Bmatrix}_{n\geq 1} &= \frac{1}{\pi}\int_{-\pi}^{\pi} \begin{Bmatrix} \tilde{T}_{ss} \\ \tilde{T}_{s\phi} \\ \tilde{T}_{sz} \end{Bmatrix} \cos n\phi d\phi = \frac{1}{\pi}\sum_{m=1}^{M} \begin{Bmatrix} \tilde{T}_{ss}(m) \\ \tilde{T}_{s\phi}(m) \\ \tilde{T}_{sz}(m) \end{Bmatrix} \cos n\phi \Delta\phi,
\end{aligned} \tag{4.27}$$

and

$$\begin{Bmatrix} \tilde{G}^2_{sn} \\ \tilde{G}^1_{\phi n} \\ \tilde{G}^2_{zn} \end{Bmatrix} = \frac{1}{\pi} \int_{-\pi}^{\pi} \begin{Bmatrix} \tilde{T}_{ss} \\ \tilde{T}_{s\phi} \\ \tilde{T}_{sz} \end{Bmatrix} \sin n\phi d\phi$$
$$= \frac{1}{\pi} \sum_{m=1}^{M} \begin{Bmatrix} \tilde{T}_{ss}(m) \\ \tilde{T}_{s\phi}(m) \\ \tilde{T}_{sz}(m) \end{Bmatrix} \sin n\phi \Delta\phi. \tag{4.28}$$

As the integrals in Equations 4.27 & 4.28 are evaluated using Riemann sums, the stresses need to be calculated at a sufficient number of M points to achieve a close approximation to the integral. The required number of points is determined in Section 4.3. Repeating Equations 4.22 to 4.28 for the antisymmetric loading case determines the components of the traction vector $\tilde{\mathbf{G}}_2$ due to the traction vector $\tilde{\mathbf{F}}_1$.

The end-result of the series of equations presented in this section is that the traction vectors $\tilde{\mathbf{G}}^1_{2n}$ and $\tilde{\mathbf{G}}^2_{2n}$ are expressed as linear functions of the traction vectors $\tilde{\mathbf{F}}^1_{1n}$ and $\tilde{\mathbf{F}}^2_{1n}$: $f_3(\tilde{\mathbf{F}}^1_{1n}, \tilde{\mathbf{F}}^2_{1n})$; and $f_4(\tilde{\mathbf{F}}^1_{1n}, \tilde{\mathbf{F}}^2_{1n})$, respectively. Using the same procedure, the traction vectors $\tilde{\mathbf{G}}^1_{1n}$ and $\tilde{\mathbf{G}}^2_{1n}$ are expressed as linear functions of the traction vectors $\tilde{\mathbf{F}}^1_{2n}$ and $\tilde{\mathbf{F}}^2_{2n}$: $f_1(\tilde{\mathbf{F}}^1_{2n}, \tilde{\mathbf{F}}^2_{2n})$; and $f_2(\tilde{\mathbf{F}}^1_{2n}, \tilde{\mathbf{F}}^2_{2n})$, respectively. Hence Equation 4.21 is now be written as a series of simultaneous equations:

$$\begin{aligned} \tilde{\mathbf{Q}}^1_{1n} &= \tilde{\mathbf{F}}^1_{1n} + f_1(\tilde{\mathbf{F}}^1_{2n}, \tilde{\mathbf{F}}^2_{2n}) \\ \tilde{\mathbf{Q}}^2_{1n} &= \tilde{\mathbf{F}}^2_{1n} + f_2(\tilde{\mathbf{F}}^1_{2n}, \tilde{\mathbf{F}}^2_{2n}) \\ \tilde{\mathbf{Q}}^1_{2n} &= \tilde{\mathbf{F}}^1_{2n} + f_3(\tilde{\mathbf{F}}^1_{1n}, \tilde{\mathbf{F}}^2_{1n}) \\ \tilde{\mathbf{Q}}^2_{2n} &= \tilde{\mathbf{F}}^2_{2n} + f_4(\tilde{\mathbf{F}}^1_{1n}, \tilde{\mathbf{F}}^2_{1n}). \end{aligned} \tag{4.29}$$

4.2.5 Solving the System of Equations

Combining Equation 4.29 with the expression for the dynamic cavity forces in Equation 4.20 gives

$$\begin{aligned} \tilde{\mathbf{P}}^1_{1n} &= [\mathbf{A}_E]_{r=R_1} \tilde{\mathbf{U}}^1_{1n-tt} + \tilde{\mathbf{F}}^1_{1n} + f_1(\tilde{\mathbf{F}}^1_{2n}, \tilde{\mathbf{F}}^2_{2n}) \\ \tilde{\mathbf{P}}^2_{1n} &= [\mathbf{A}_E]_{r=R_1} \tilde{\mathbf{U}}^2_{1n-tt} + \tilde{\mathbf{F}}^2_{1n} + f_2(\tilde{\mathbf{F}}^1_{2n}, \tilde{\mathbf{F}}^2_{2n}) \\ \tilde{\mathbf{P}}^1_{2n} &= [\mathbf{A}_E]_{r=R_2} \tilde{\mathbf{U}}^1_{2n-tt} + \tilde{\mathbf{F}}^1_{2n} + f_3(\tilde{\mathbf{F}}^1_{1n}, \tilde{\mathbf{F}}^2_{1n}) \\ \tilde{\mathbf{P}}^2_{2n} &= [\mathbf{A}_E]_{r=R_2} \tilde{\mathbf{U}}^2_{2n-tt} + \tilde{\mathbf{F}}^2_{2n} + f_4(\tilde{\mathbf{F}}^1_{1n}, \tilde{\mathbf{F}}^2_{1n}). \end{aligned} \tag{4.30}$$

In order to solve these equations, it is necessary to express the displacements of the two tunnels, $\tilde{\mathbf{U}}_{1-tt}$ and $\tilde{\mathbf{U}}_{2-tt}$, as a function of the traction vectors acting on a single cavity, $\tilde{\mathbf{F}}_1$ and $\tilde{\mathbf{F}}_2$.

The displacements of the two-tunnel system are equal to the displacements of the two-cavity system, $\tilde{\mathbf{U}}_{1-cc}$ and $\tilde{\mathbf{U}}_{2-cc}$, and equal to the displacements of the two tunnels,

$\tilde{\mathbf{U}}_{1-tt}$ and $\tilde{\mathbf{U}}_{2-tt}$, by compatibility of displacements. This is illustrated in Figure 4.6, and expressed in

$$\begin{aligned} \tilde{\mathbf{U}}^1_{1n-tt} &= \tilde{\mathbf{U}}^1_{1n-cc} \\ \tilde{\mathbf{U}}^2_{1n-tt} &= \tilde{\mathbf{U}}^2_{1n-cc} \\ \tilde{\mathbf{U}}^1_{2n-tt} &= \tilde{\mathbf{U}}^1_{2n-cc} \\ \tilde{\mathbf{U}}^2_{2n-tt} &= \tilde{\mathbf{U}}^2_{2n-cc}. \end{aligned} \tag{4.31}$$

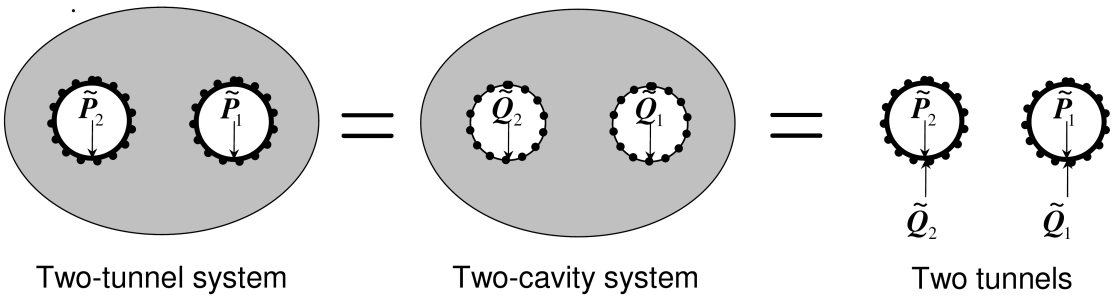

Fig. 4.6 The displacements of the two-tunnel system are equal to the displacements of the two-cavity system and equal to the displacements of the two tunnels, by compatibility of displacements

As in Section 4.2.3, the principle of superposition can be used to write the displacements of the two-cavity system as the sum of those displacements resulting from the traction vectors $\tilde{\mathbf{F}}_1$ and $\tilde{\mathbf{F}}_2$ acting on a single cavity, and those displacements resulting from the interactions between the two cavities. This is illustrated in Figure 4.7, and expressed in

$$\begin{aligned} \tilde{\mathbf{U}}_{1-cc} &= \tilde{\mathbf{U}}_{1-sc} + \tilde{\mathbf{U}}_{1-nc} \\ \tilde{\mathbf{U}}_{2-cc} &= \tilde{\mathbf{U}}_{2-sc} + \tilde{\mathbf{U}}_{2-nc}, \end{aligned} \tag{4.32}$$

where $\tilde{\mathbf{U}}_{1-sc}$ and $\tilde{\mathbf{U}}_{2-sc}$ are the displacements resulting from traction vectors acting on a single cavity, and $\tilde{\mathbf{U}}_{1-nc}$ and $\tilde{\mathbf{U}}_{2-nc}$ are the displacements resulting from the interactions between the two cavities.

Considering the displacements of cavity 2, the displacement contribution $\tilde{\mathbf{U}}_{2-sc}$ is calculated by applying traction vector $\tilde{\mathbf{F}}_2$ to a single cavity model:

$$\begin{Bmatrix} \tilde{U}_{sn} \\ \tilde{U}_{\phi n} \\ \tilde{U}_{zn} \end{Bmatrix}_{2-sc} = [\mathbf{U}]_{r=R_2} [\mathbf{T}_r]^{-1}_{r=R_2} \begin{Bmatrix} \tilde{F}_{sn} \\ \tilde{F}_{\phi n} \\ \tilde{F}_{zn} \end{Bmatrix}. \tag{4.33}$$

The displacement contribution representing the motion induced by the neighbouring

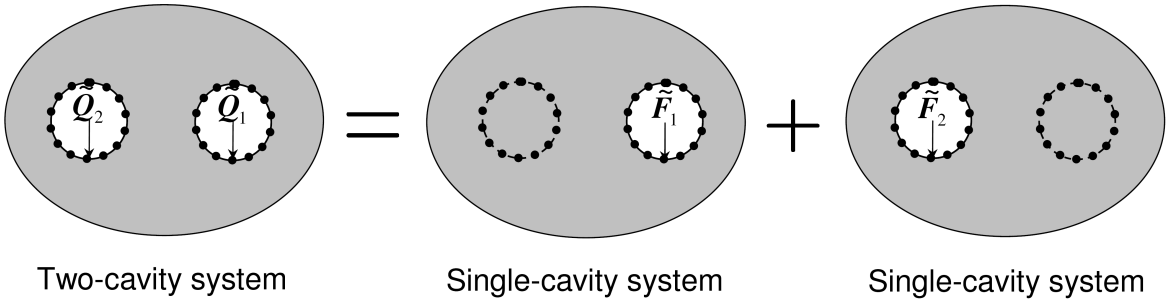

Fig. 4.7 The displacements of the two-cavity system are written as the sum of two contributions: those displacements resulting from the loads acting on a single cavity; and those displacements resulting from the interactions between the two cavities

cavity, $\tilde{\mathbf{U}}_{2-nc}$, is obtained by calculating the displacements on the virtual surface of cavity 2 that result from the application of the traction vector $\tilde{\mathbf{F}}_1$ on cavity 1. Following a similar procedure to that detailed in Section 4.2.4 for calculating the stresses around a virtual surface, the displacements around the virtual surface are calculated at a radial distance R_f from cavity 1, which corresponds to a radial distance R_2 from cavity 2, using

$$\begin{Bmatrix} \tilde{U}^1_{rn} \\ \tilde{U}^1_{\theta n} \\ \tilde{U}^1_{zn} \end{Bmatrix}_{r=R_f} = [\mathbf{U}]_{r=R_f} [\mathbf{T}_r]^{-1}_{r=R_1} \begin{Bmatrix} \tilde{F}^1_{rn} \\ \tilde{F}^1_{\theta n} \\ \tilde{F}^1_{zn} \end{Bmatrix}. \tag{4.34}$$

The total displacement at the point $(R_f, \Theta_f, 0)$, which corresponds to the point $(R_2, \Phi_f, 0)$ on cavity 2, is calculated by combining the displacement contributions from each mode-enumber:

$$\begin{Bmatrix} \tilde{U}_r \\ \tilde{U}_\theta \\ \tilde{U}_z \end{Bmatrix}_{(R_f,\Theta_f,0)} = \sum_{n=0}^{N} \begin{Bmatrix} \tilde{U}^1_{rn} \cos n\Theta_f \\ \tilde{U}^1_{\theta n} \sin n\Theta_f \\ \tilde{U}^1_{zn} \cos n\Theta_f \end{Bmatrix}. \tag{4.35}$$

The displacements are now converted to the (s, ϕ, z) directions to obtain compatibility with the cavity 2 coordinate system. The equations for converting displacements between the (r, θ, z) and (s, ϕ, z) coordinate systems are obtained by considering vector geometry, and are assembled into a 3x3 transformation matrix, denoted $[\mathbf{A}]$, such that

$$\begin{Bmatrix} \tilde{U}_s \\ \tilde{U}_\phi \\ \tilde{U}_z \end{Bmatrix}_{(R_2,\Phi_f,0)} = [\mathbf{A}] \begin{Bmatrix} \tilde{U}_r \\ \tilde{U}_\theta \\ \tilde{U}_z \end{Bmatrix}_{(R_f,\Theta_f,0)}, \tag{4.36}$$

where $[\mathbf{A}]$ is given by

$$[\mathbf{A}] = \begin{bmatrix} \cos(\Theta_f - \Phi_f)) & -\sin(\Theta_f - \Phi_f) & 0 \\ \sin(\Theta_f - \Phi_f) & \cos(\Theta_f - \Phi_f) & 0 \\ 0 & 0 & 1 \end{bmatrix}. \tag{4.37}$$

After calculating the displacements at a series of M evenly spaced points around the virtual surface of cavity 2, following the same procedure as in Section 4.2.4, Fourier decomposition is used to partition the displacements into those contributions due to the symmetric and antisymmetric loading cases, and the n modenumbers. These displacement contributions represent the displacements resulting from the interactions between the two cavities due to $\tilde{\mathbf{F}}_1^1$, $\tilde{\mathbf{U}}_{2-nc}$, and are given by

$$\begin{aligned} \begin{Bmatrix} \tilde{U}^1_{sn} \\ \tilde{U}^2_{\phi n} \\ \tilde{U}^1_{zn} \end{Bmatrix}_{2(n=0)-nc} &= \frac{1}{2\pi} \int_{-\pi}^{\pi} \begin{Bmatrix} \tilde{U}_s \\ \tilde{U}_\phi \\ \tilde{U}_z \end{Bmatrix} d\phi = \frac{1}{2\pi} \sum_{m=1}^{M} \begin{Bmatrix} \tilde{U}_s(m) \\ \tilde{U}_\phi(m) \\ \tilde{U}_z(m) \end{Bmatrix} \Delta\phi \\ \begin{Bmatrix} \tilde{U}^1_{sn} \\ \tilde{U}^2_{\phi n} \\ \tilde{U}^1_{zn} \end{Bmatrix}_{2(n\geq 1)-nc} &= \frac{1}{\pi} \int_{-\pi}^{\pi} \begin{Bmatrix} \tilde{U}_s \\ \tilde{U}_\phi \\ \tilde{U}_z \end{Bmatrix} \cos n\phi d\phi = \frac{1}{\pi} \sum_{m=1}^{M} \begin{Bmatrix} \tilde{U}_s(m) \\ \tilde{U}_\phi(m) \\ \tilde{U}_z(m) \end{Bmatrix} \cos n\phi \Delta\phi, \end{aligned} \tag{4.38}$$

and

$$\begin{aligned} \begin{Bmatrix} \tilde{U}^2_{sn} \\ \tilde{U}^1_{\phi n} \\ \tilde{U}^2_{zn} \end{Bmatrix}_{2-nc} &= \frac{1}{\pi} \int_{-\pi}^{\pi} \begin{Bmatrix} \tilde{U}_s \\ \tilde{U}_\phi \\ \tilde{U}_z \end{Bmatrix} \sin n\phi d\phi \\ &= \frac{1}{\pi} \sum_{m=1}^{M} \begin{Bmatrix} \tilde{U}_s(m) \\ \tilde{U}_\phi(m) \\ \tilde{U}_z(m) \end{Bmatrix} \sin n\phi \Delta\phi. \end{aligned} \tag{4.39}$$

Repeating Equations 4.34 to 4.39 for the antisymmetric loading case determines the components of $\tilde{\mathbf{U}}_{2-nc}$ due to $\tilde{\mathbf{F}}_1^2$.

The displacements on cavity 2 resulting from the interactions between the two cavities are now expressed as linear functions of the traction vectors $\tilde{\mathbf{F}}_{1n}^1$ and $\tilde{\mathbf{F}}_{1n}^2$: $g_3(\tilde{\mathbf{F}}_{1n}^1, \tilde{\mathbf{F}}_{1n}^2)$; and $g_4(\tilde{\mathbf{F}}_{1n}^1, \tilde{\mathbf{F}}_{1n}^2)$, respectively. Using the same procedure, the displacements on cavity 1 resulting from the interactions between the two cavities are expressed as linear functions of the traction vectors $\tilde{\mathbf{F}}_{2n}^1$ and $\tilde{\mathbf{F}}_{2n}^2$: $g_1(\tilde{\mathbf{F}}_{2n}^1, \tilde{\mathbf{F}}_{2n}^2)$; and $g_2(\tilde{\mathbf{F}}_{2n}^1, \tilde{\mathbf{F}}_{2n}^2)$, respectively. Hence the displacements of the two tunnels are represented by a series of

equations:

$$\begin{aligned}
\tilde{\mathbf{U}}^1_{1n-tt} &= [\mathbf{U}]_{r=R_1}[\mathbf{T}_r]^{-1}_{r=R_1}\tilde{\mathbf{F}}^1_{1n} + g_1(\tilde{\mathbf{F}}^1_{2n}, \tilde{\mathbf{F}}^2_{2n}) \\
\tilde{\mathbf{U}}^2_{1n-tt} &= [\mathbf{U}]_{r=R_1}[\mathbf{T}_r]^{-1}_{r=R_1}\tilde{\mathbf{F}}^2_{1n} + g_2(\tilde{\mathbf{F}}^1_{2n}, \tilde{\mathbf{F}}^2_{2n}) \\
\tilde{\mathbf{U}}^1_{2n-tt} &= [\mathbf{U}]_{r=R_2}[\mathbf{T}_r]^{-1}_{r=R_2}\tilde{\mathbf{F}}^1_{2n} + g_3(\tilde{\mathbf{F}}^1_{1n}, \tilde{\mathbf{F}}^2_{1n}) \\
\tilde{\mathbf{U}}^2_{2n-tt} &= [\mathbf{U}]_{r=R_2}[\mathbf{T}_r]^{-1}_{r=R_2}\tilde{\mathbf{F}}^2_{2n} + g_3(\tilde{\mathbf{F}}^1_{1n}, \tilde{\mathbf{F}}^2_{1n}).
\end{aligned} \tag{4.40}$$

Substituting this into Equation 4.30 results in

$$\begin{aligned}
\tilde{\mathbf{P}}^1_{1n} &= [\mathbf{A}_E]_{r=R_1}\left([\mathbf{U}]_{r=R_1}[\mathbf{T}_r]^{-1}_{r=R_1}\tilde{\mathbf{F}}^1_{1n} + g_1\left(\tilde{\mathbf{F}}^1_{2n}, \tilde{\mathbf{F}}^2_{2n}\right)\right) + \tilde{\mathbf{F}}^1_{1n} + f_1(\tilde{\mathbf{F}}^1_{2n}, \tilde{\mathbf{F}}^2_{2n}) \\
\tilde{\mathbf{P}}^2_{1n} &= [\mathbf{A}_E]_{r=R_1}\left([\mathbf{U}]_{r=R_1}[\mathbf{T}_r]^{-1}_{r=R_1}\tilde{\mathbf{F}}^2_{1n} + g_2\left(\tilde{\mathbf{F}}^1_{2n}, \tilde{\mathbf{F}}^2_{2n}\right)\right) + \tilde{\mathbf{F}}^2_{1n} + f_2(\tilde{\mathbf{F}}^1_{2n}, \tilde{\mathbf{F}}^2_{2n}) \\
\tilde{\mathbf{P}}^1_{2n} &= [\mathbf{A}_E]_{r=R_2}\left([\mathbf{U}]_{r=R_2}[\mathbf{T}_r]^{-1}_{r=R_2}\tilde{\mathbf{F}}^1_{2n} + g_3\left(\tilde{\mathbf{F}}^1_{1n}, \tilde{\mathbf{F}}^2_{1n}\right)\right) + \tilde{\mathbf{F}}^1_{2n} + f_3(\tilde{\mathbf{F}}^1_{1n}, \tilde{\mathbf{F}}^2_{1n}) \\
\tilde{\mathbf{P}}^2_{2n} &= [\mathbf{A}_E]_{r=R_2}\left([\mathbf{U}]_{r=R_2}[\mathbf{T}_r]^{-1}_{r=R_2}\tilde{\mathbf{F}}^2_{2n} + g_4\left(\tilde{\mathbf{F}}^1_{1n}, \tilde{\mathbf{F}}^2_{1n}\right)\right) + \tilde{\mathbf{F}}^2_{2n} + f_4(\tilde{\mathbf{F}}^1_{1n}, \tilde{\mathbf{F}}^2_{1n}).
\end{aligned} \tag{4.41}$$

The solution of these simultaneous equations is found using the blockwise inversion technique. This solution represents the traction vectors $\tilde{\mathbf{F}}_1$ and $\tilde{\mathbf{F}}_2$ applied to the single-cavity models in order to replicate the displacement field produced by the known traction vectors $\tilde{\mathbf{P}}_1$ and $\tilde{\mathbf{P}}_2$, which are applied to the two-tunnel model. The displacement field of the two-tunnel model is thus the superposition of the displacement field produced by the traction vector $\tilde{\mathbf{F}}_1$ acting on cavity 1 in a single-cavity model, and the displacement field produced by the traction vector $\tilde{\mathbf{F}}_2$ acting on cavity 2 in a single-cavity model.

4.3 Results and Discussion

The above equations are implemented in Matlab, and the displacement fields are presented in terms of the vertical or horizontal displacements, always in terms of $\mathrm{dB_{ref}}$[1m]. Unless otherwise specified, the tunnel and soil parameters used to calculate the results are shown in Table 4.1.

It is necessary to determine the number of circular modenumbers (N) and points around the virtual cavity surface (M) required to capture the dynamic behaviour of the system. Figure 4.8 shows the vertical and horizontal displacements calculated at $s = 6$m and $-90° < \phi < 90°$ for twin, side-by-side tunnels at a frequency of 100Hz. The excitation is a unit, harmonic, radial point load applied to the invert of the right-hand tunnel. Results are calculated for the first 9, 10, 11, 12 and 13 circular modenumbers, with $M = 200$. Convergence is achieved by using the first 13 modenumbers.

Using the value $N = 13$, the number of points around the virtual tunnel surface is varied by multiples of N. In order to satisfy the Nyquist criterion, M must be at least double the value of N. Increasing the number of points beyond $N = 4M$ results in no

Table 4.1 Parameter values used for the two-tunnel model

Tunnel Properties	*Symbol*	*Value*
Density	ρ	2500kgm^{-3}
Young's Modulus	E	50GPa
Poisson's Ratio	ν	0.30
Tunnel Separation Distance	c	10m
Tunnel Separation Angle	α	$\frac{\pi}{2}$
Radius	$R_1 = R_2$	3m
Thickness	$h_1 = h_2$	0.25m
Soil Properties	*Symbol*	*Value*
Lamé's First Parameter	λ	360MPa
Lamé's Second Parameter	μ	90MPa
Density	ρ	2250kgm^{-3}
Shear Modulus Damping Ratio	η_G	0.06

change in the displacements, hence $N = 13$ and $M = 52$ are used to calculate the results presented in this section.

The correctness of the numerical implementation of the above equations can be verified by considering a number of loading cases that are known to produce symmetric results. These are calculated for twin tunnels at an arbitrary frequency of 60Hz and are shown in Figures 4.9 to 4.11. The arrows shown in these figures, and those following, indicate a unit, harmonic point load acting in the indicated direction at the point of intersection with the tunnel invert. The displacement field is calculated over a 30mx30m area located in the plane of these loads. Figure 4.9 shows the vertical displacement field for two radial point loads acting on the tunnel base, and as expected, the displacement field is symmetric about $x = -5$. Figure 4.10 shows the horizontal displacement field for two tangential point loads acting on the tunnel base. This displacement field is symmetric about $x = -5$ and has zero horizontal displacements along this line. Figure 4.11 shows the horizontal displacement field for two radial point loads acting on the tunnel wall. As expected, this displacement field is symmetric about $x = -5$ and $y = 0$, and has zero horizontal displacements along the line $x = -5$. Due to the nature of the shading function used to produce these figures, very slight, localised shading variations may be observed when inspecting the symmetry of each plot. However, this does not compromise the overall symmetry of the plots, nor challenge the correctness of the numerical implementation.

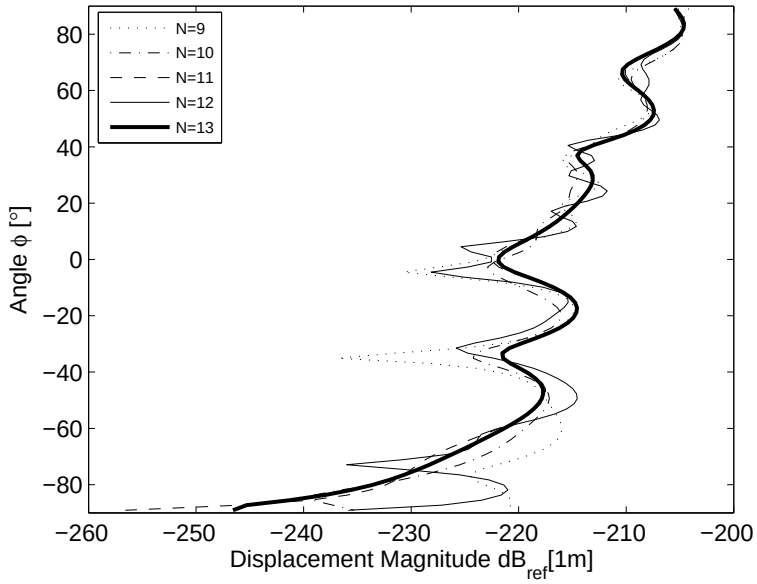

(a) 100Hz vertical displacement

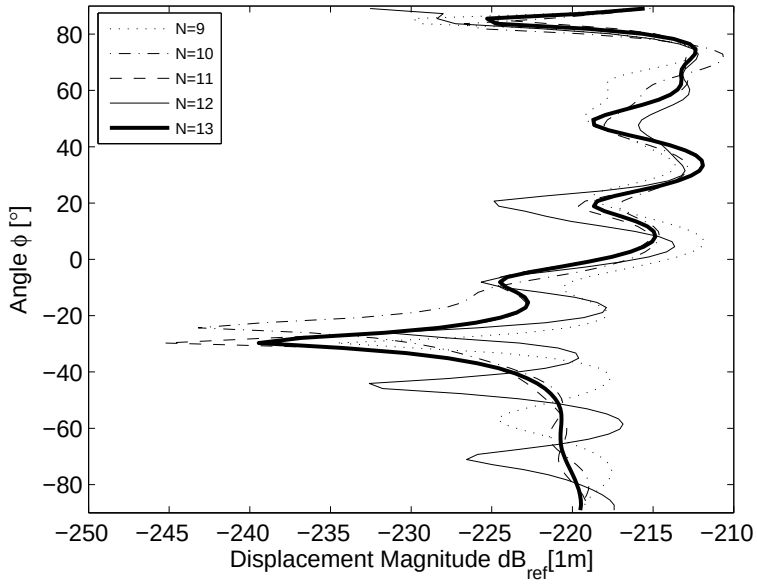

(b) 100Hz horizontal displacement

Fig. 4.8 Convergence plot showing: (a) the vertical; and (b) the horizontal, displacements at 100Hz at $s = 6$m in a twin-tunnel system

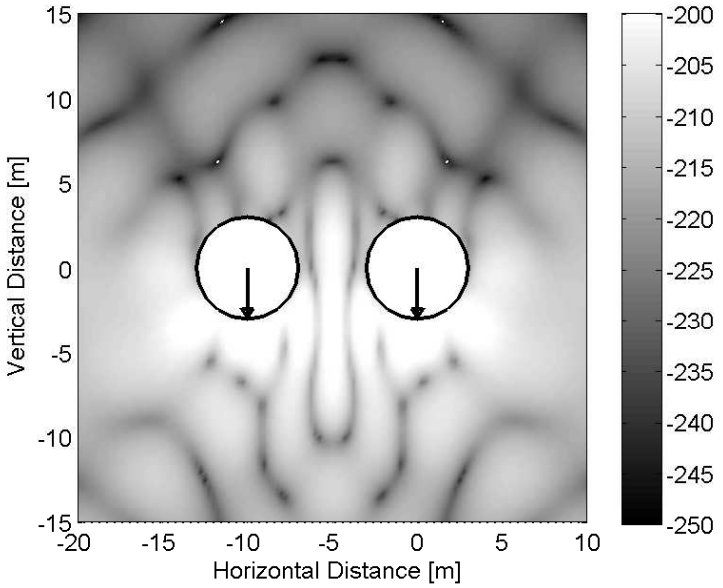

Fig. 4.9 A symmetric loading distribution: vertical displacements (dB_{ref}[1m]) resulting from two radial point loads acting on the tunnel base

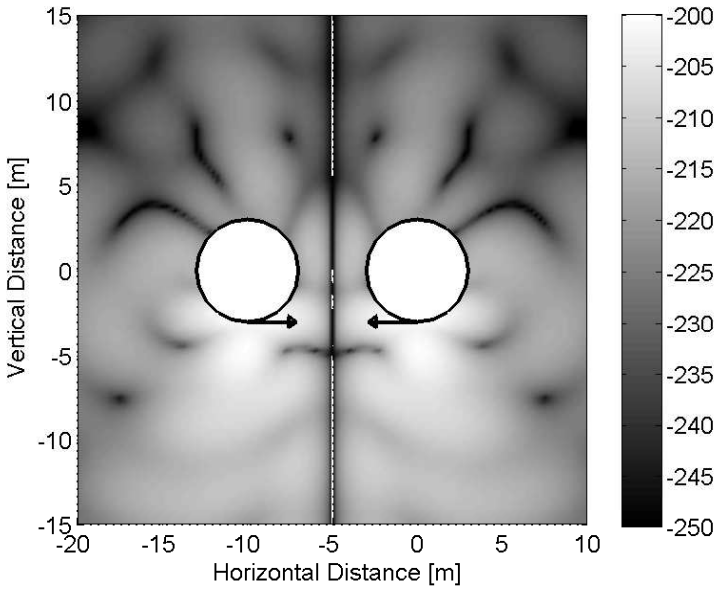

Fig. 4.10 A symmetric loading distribution: horizontal displacements (dB_{ref}[1m]) resulting from two tangential point loads acting on the tunnel base

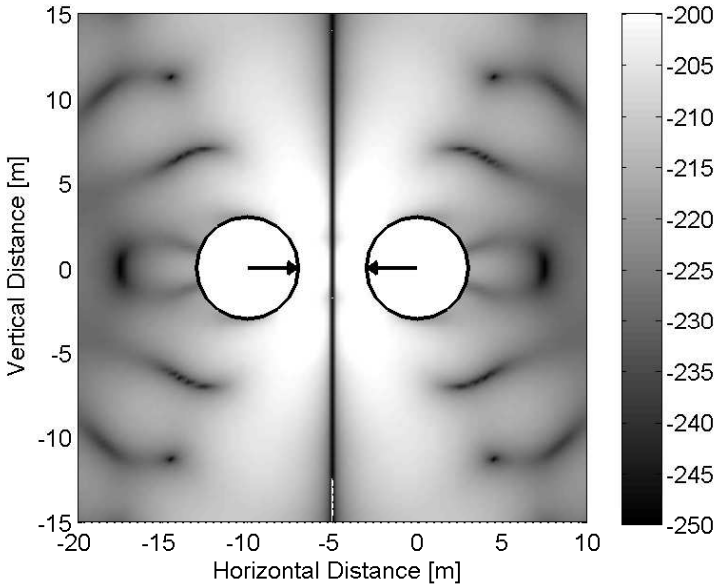

Fig. 4.11 A symmetric loading distribution: horizontal displacements ($dB_{ref}[1m]$) resulting from two radial point loads acting on the tunnel wall

The main aim of this modelling is to quantify the inaccuracy that exists in vibration-prediction models that include only one of the two tunnels present. This inaccuracy is expressed here in terms of insertion gain. Originally used for assessing vibration-isolation performance, insertion gain is used here to represent the ratio of the vibration response of a two-tunnel model to that of a single-tunnel model. In this way the insertion gain essentially represents the change in the vibration response, expressed in dB, at any given location when a two-tunnel model is employed. The procedure for calculating the insertion gain is illustrated in Figures 4.12 to 4.14, and this measure can be seen to be particularly useful at locating regions which are susceptible to inaccuracies resulting from a single-tunnel assumption. For the case shown in Figure 4.14, the region above the right-hand tunnel predicts twin-tunnel vibration levels in the order of 20dB greater than those predicted by the single-tunnel model. A shadow region to the left of the left-hand tunnel is also observed.

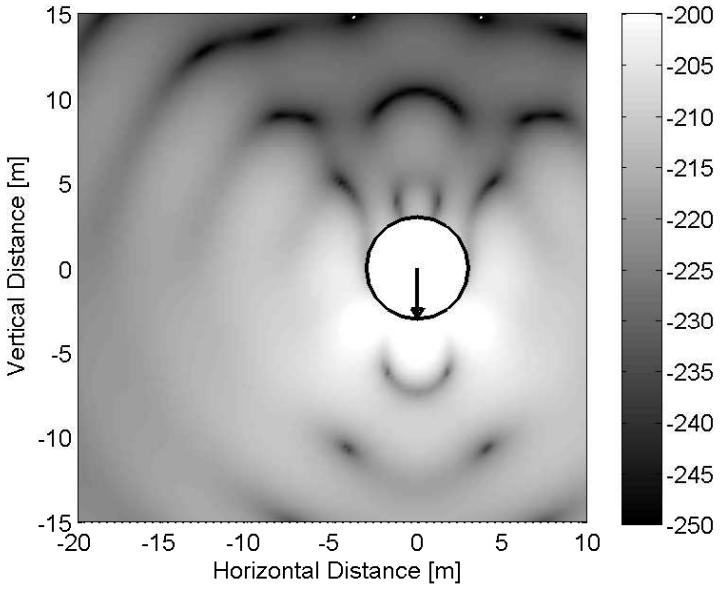

Fig. 4.12 The vertical displacement field (dB_{ref}[1m]) produced at 60Hz by a unit, vertical point force applied to a tunnel invert, calculated using a single-tunnel model

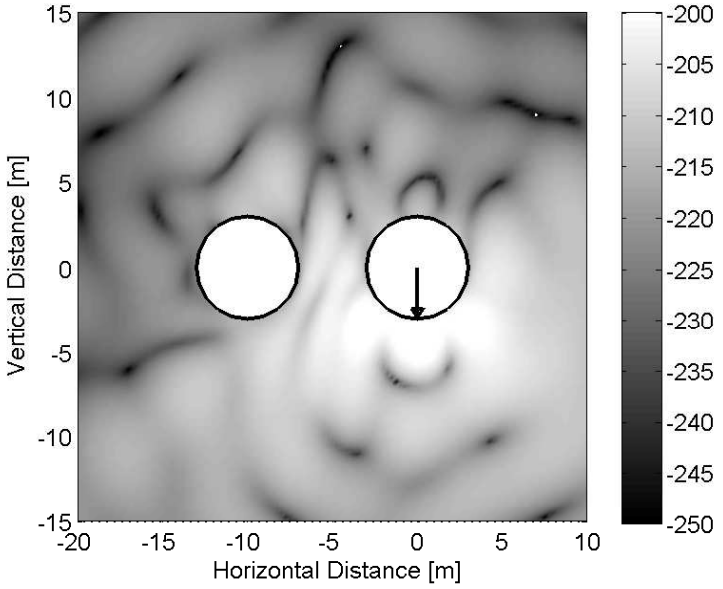

Fig. 4.13 The vertical displacement field (dB_{ref}[1m]) produced at 60Hz by a unit, vertical point force applied to a tunnel invert, calculated using a twin-tunnel model

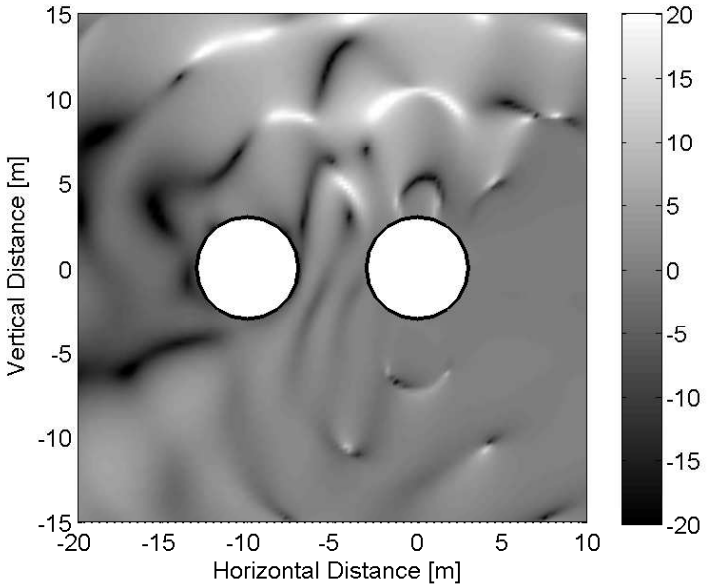

Fig. 4.14 The insertion gain (dB) represents the difference between the vertical displacement fields produced at 60Hz by the single-tunnel model and the twin-tunnel model

4.3.1 Insertion-Gain Results

As vibration predictions are commonly made at the ground surface, it is useful to focus this discussion on the region directly above the twin tunnels. The two-tunnel model presented in this chapter is that for a fullspace, and this model can be used as the basis of a two-tunnel model in a layered or homogeneous halfspace. The layered or homogeneous halfspace is incorporated using the fictitious-force method detailed in Hussein *et al.* [67]. Previous investigations into underground-railway models have shown that when the tunnel is at a depth of two tunnel diameters or more, the vibrations calculated at an equivalent surface location using a fullspace model are approximately 6dB less than those calculated using a halfspace model [80]. It is also acknowledged that soil inhomogeneities, such as layering, permeability, and the presence of bedrock, can have a significant influence on the accuracy of vibration predictions. For this reason, the results presented here are not purported to be accurate vibration predictions, but rather a quantification of one type of inaccuracy that can be present in vibration predictions.

In the following figures, the vibration response as a function of frequency, tunnel orientation and tunnel thickness is investigated. In each case, a unit, harmonic point load is applied radially to the base of tunnel 1. This loading can be easily extended to represent a line load by the use of superposition. Tunnel 1 represents the right-hand

tunnel in the case of side-by-side tunnels, or the lower tunnel in the case of piggy-back tunnels. One of the defining characteristics of the two-tunnel model is the absence of the cylindrical symmetry of the single-tunnel model. For a single-tunnel model, a symmetric loading condition gives rise to purely symmetric soil displacements and stress distributions, and an antisymmetric loading condition gives rise to purely antisymmetric soil displacements and stress distributions. This is not the case for the two-tunnel model. Due to the symmetry of the loading of the single-tunnel model, seen in Figure 4.12, a line of zero horizontal displacements is produced at $x = 0$ for this model. This means that any insertion-gain results for the two-tunnel model presented in terms of horizontal displacements show a line of infinite insertion gain at $x = 0$. For this reason, the insertion gains are presented not only for vertical and horizontal displacements, but also for displacement magnitudes. To obtain the displacement-magnitude insertion gain, the maximum value of the displacement magnitude is calculated for both the two-tunnel model and the single-tunnel model using the method detailed in Appendix D. The displacement-magnitude insertion gain, although not commonly used to characterise displacement fields, is useful here as it provides a clearer indication of the vibration hot-spots than either the vertical or horizontal displacements.

Figure 4.15 presents the insertion gain for the two most commonly used twin-tunnel orientations: side-by-side; and piggy-back, as a function of frequency and horizontal position along a horizontal line located 15m above the centre of tunnel 1. In both cases a unit, harmonic point load has been applied radially to the base of tunnel 1. For the side-by-side tunnels, the insertion gain is seen to be highly dependent on both frequency and measurement position. There is no apparent trend in the distribution, which is due to the scattering effect of the second tunnel. For the piggy-back tunnels, it can be seen that the maximum-negative insertion gains occur in the region stretching directly above the tunnel invert. At low frequencies, the maximum insertion gains occur in a series of bands centred on $x = 0$. This series of bands transitions into a more irregular pattern at around 80Hz: the frequency at which the wavelength of the pressure wave is equal to the tunnel diameter. This suggests that at low frequencies very little diffraction of the pressure wave occurs, whereas at frequencies greater than that at which the wavelength matches the tunnel diameter, pressure-wave diffraction dominates the response.

Figure 4.16 presents the displacement-magnitude insertion gains at 20Hz and 60Hz, calculated as a function of the angle α, where α is the angle of tunnel 2 measured from tunnel 1. The loading is again a unit, harmonic point load applied radially to the base of tunnel 1. A number of vertical lines of large insertion gain can be seen in this figure. For example, at 60Hz the vertical-displacement insertion gain (Figure 4.16(b)) has three such lines located at $x = -18m$, $x = -3m$, and $x = 3m$. By examining the displacement

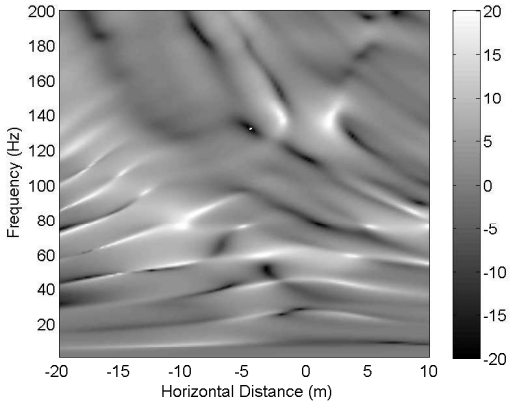

(a) Vertical displacement

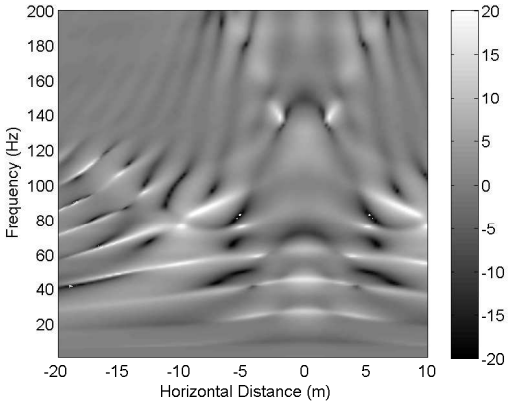

(b) Vertical displacement

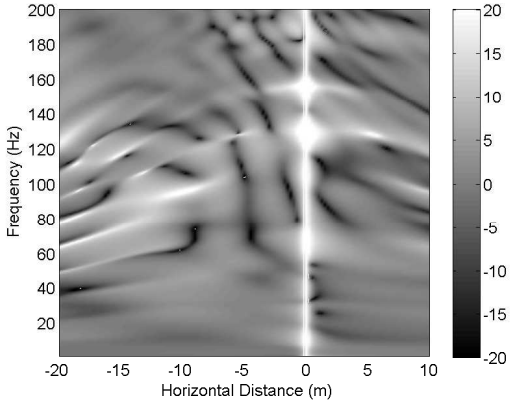

(c) Horizontal displacement

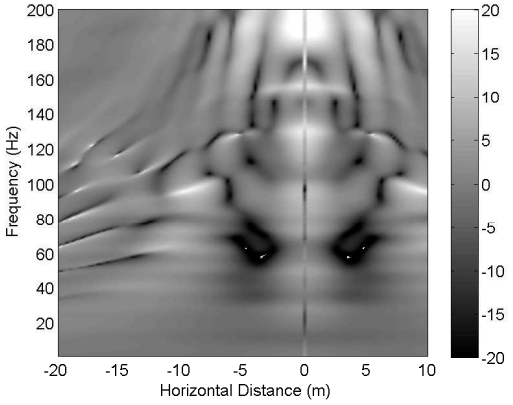

(d) Horizontal displacement

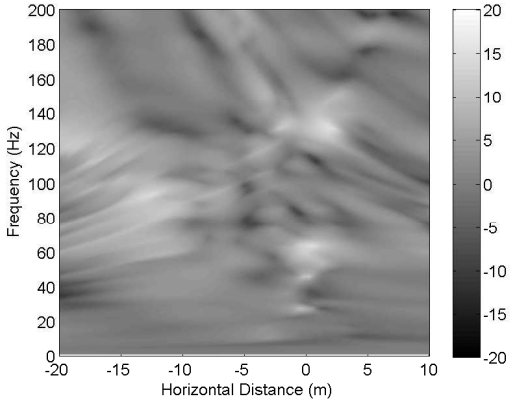

(e) Displacement magnitude

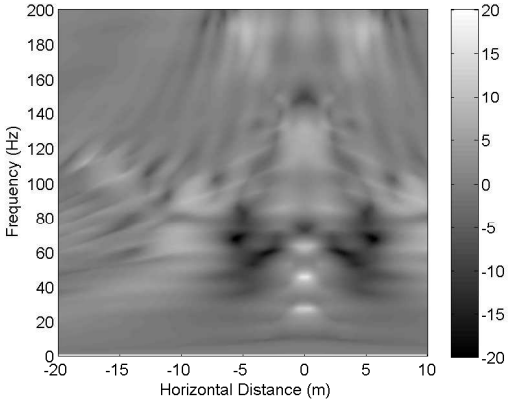

(f) Displacement magnitude

Fig. 4.15 Insertion gains as a function of frequency and position for side-by-side tunnels (left), and piggy-back tunnels (right)

fields of the single-tunnel model shown in Figure 4.17, the location of these lines can be seen to correspond with the troughs in the response calculated using the single-tunnel model. Thus the addition of the twin tunnel has effectively smoothed the single-tunnel displacement field to create a more uniform response. At both frequencies, the largest-negative insertion gains generally occur at angles greater than 100°. Three additional lines are plotted on these graphs: the solid line indicates the location of the measuring point lying on the line joining the centres of the two tunnels, while the dashed lines on either side indicate the locations of the measuring points lying on the lines joining the extreme edges of the two tunnels. Hence the region enclosed by the dashed lines indicates measuring points lying in the shadow of tunnel 2, as observed from tunnel 1. The overall trend in this region is large, negative insertion gains. Large, negative insertion gains are also observed on either side of this region, indicating that the second tunnel acts to shield nearby regions from vibrational energy. Apart from this trend, the insertion gains are again seen to be highly dependent on frequency and measurement position.

The final figure presented here, Figure 4.18, shows the vertical-displacement insertion gains for twin tunnels of varying invert thickness h. At low frequencies, such as at 20Hz shown in Figure 4.18(a), there is little separation between the insertion-gain curves and hence the tunnel thickness has little influence on the general shape of the insertion gain versus position plot. Although at the frequency of 20Hz the trend suggests that the thinner tunnel produces the lower insertion-gain level, this trend is not observed for all low frequencies. For example, at 10Hz it is the thicker tunnel that produces the lower insertion-gain level, and at 15Hz the tunnel thickness that produces the lower insertion-gain level varies with horizontal distance. At frequencies above approximately 40Hz, the tunnel thickness has a stronger influence on the general shape of the insertion gain versus position plot, and there is no consistent trend observed in the thickness of the tunnels and the level of insertion gain. For example, at 60Hz, shown in Figure 4.18(b), there is greater than 10dB variation in the insertion gains at given measurement positions. Hence it can be again concluded that the vibration response is highly dependent upon both frequency and position.

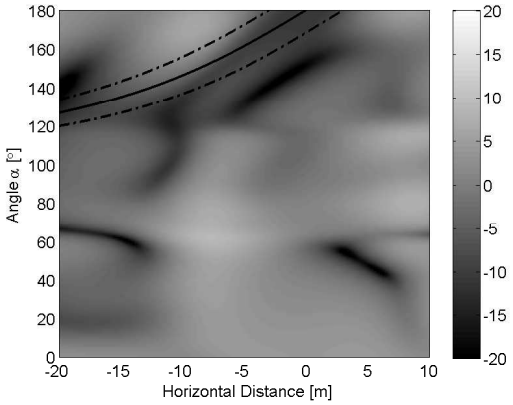

(a) 20Hz vertical displacement

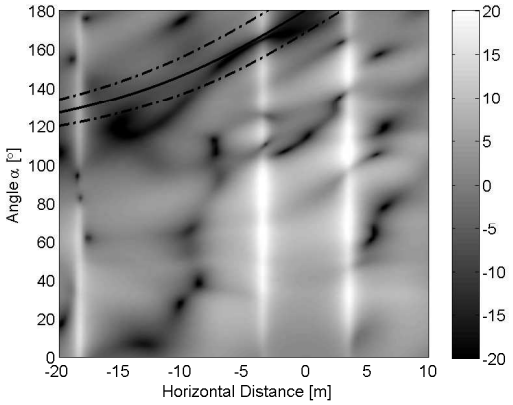

(b) 60Hz vertical displacement

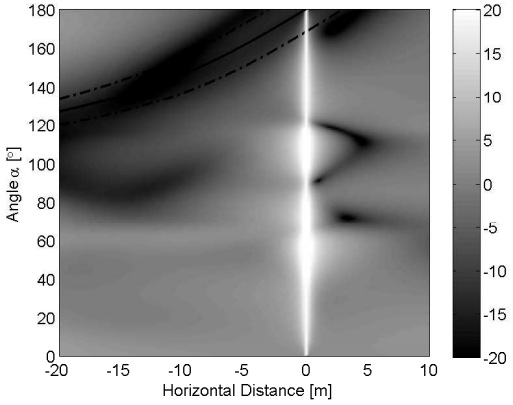

(c) 20Hz horizontal displacement

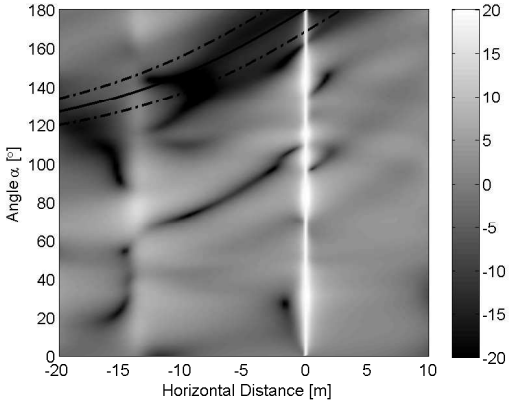

(d) 60Hz horizontal displacement

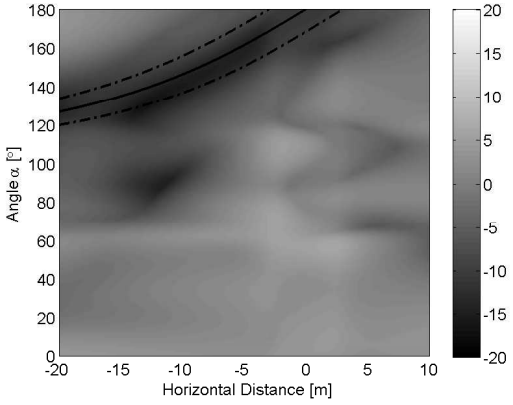

(e) 20Hz displacement magnitude

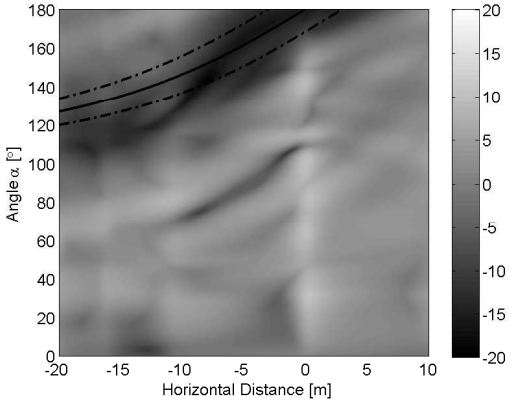

(f) 60Hz displacement magnitude

Fig. 4.16 Insertion gains as a function of angle α and position, calculated at 20Hz and 60Hz

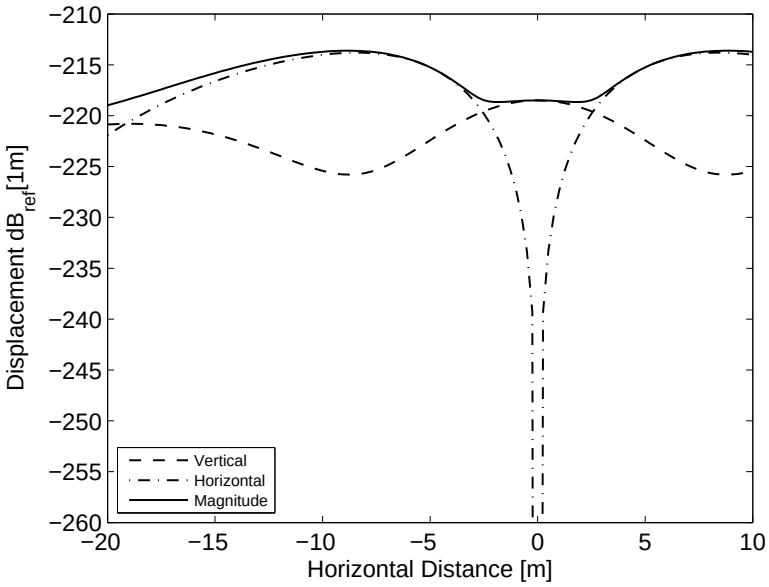

(a) 20Hz

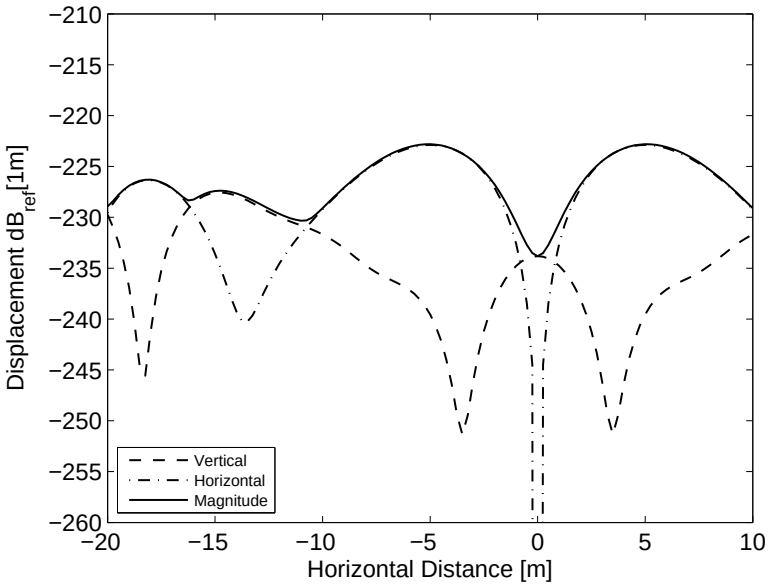

(b) 60Hz

Fig. 4.17 Single-tunnel displacements ($dB_{ref}[1m]$), calculated at 20Hz and 60Hz

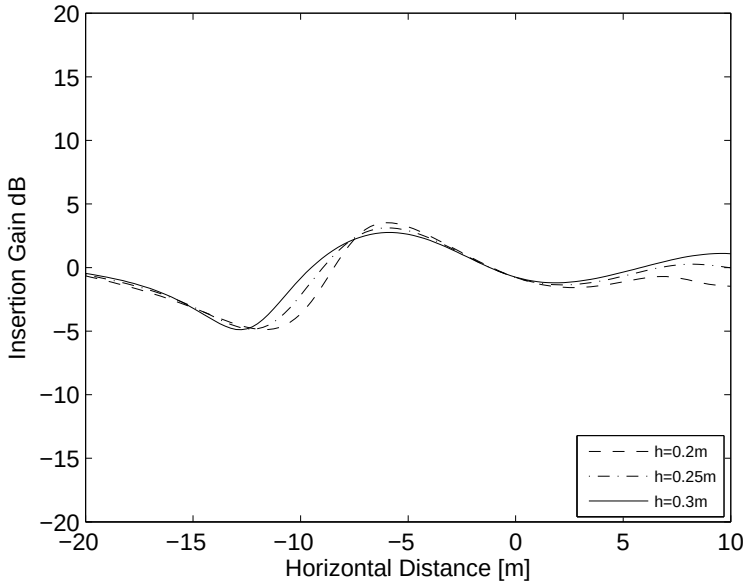

(a) 20Hz vertical displacement

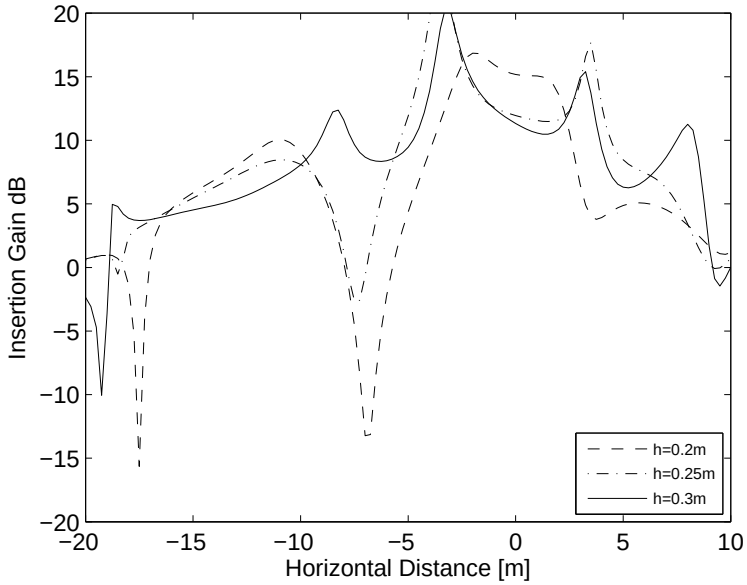

(b) 60Hz vertical displacement

Fig. 4.18 Insertion gains as a function of position and tunnel thickness, calculated at 20Hz and 60Hz

4.4 Conclusions

This chapter presents the formulation of a unique model for underground-railway vibration that includes the interaction between neighbouring tunnels. Each of these tunnels is subject to both known, dynamic train forces and dynamic cavity forces. The net forces acting on the tunnels are written as the sum of those tractions acting on the invert of a single tunnel, and those tractions that represent the motion induced by the neighbouring tunnel. By apportioning the tractions in this way, the vibration response of a two-tunnel system is written as a linear combination of displacement fields produced by a single-tunnel system. Using Fourier decomposition, forces are partitioned into symmetric and antisymmetric modenumber components to minimise computation times.

Analysis of the vibration fields produced over a range of frequencies, tunnel orientations and tunnel geometries is conducted. It is observed that the interaction between neighbouring tunnels is highly significant, at times in the order of 20dB. This demonstrates that a high degree of inaccuracy exists in any surface vibration-prediction model that includes only one of the two tunnels present. The results of this modelling also indicate that the presence of other underground inclusions, such as buried services, can have a significant effect on the ground-borne vibration field. It is recommended that all future models predicting vibration levels from underground railways include the interaction between neighbouring tunnels.

Chapter 5

Conclusions

This dissertation details the formulation of a number of mathematical models that can be used to assess the behaviour of two types of embedded structures: piled foundations; and twin tunnels, when subject to ground-borne vibration generated by an underground railway. In this chapter, the main findings of this research are summarised and general conclusions on the use and applicability of the mathematical models are drawn. Based on this and the experience gained by the author during the course of this research, a number of topics for further research are proposed.

5.1 Introduction

In Chapter 1, two important areas of research are identified: the effect of piled foundations; and the effect of neighbouring tunnels, on ground-borne vibrations generated by an underground railway. Neither area receives proper attention in the literature. For example, extensive research is conducted on the response of piled foundations to earthquake loadings, but only a few models of an above-ground railway seated on a pile row exist. For the case of twin tunnels, much research focuses on determining the static stresses and strains encountered during and post- construction, but only one dynamic model comparing the behaviour of a twin-tunnel model and a double-track, single-tunnel model exists.

The primary aim of the research presented in this dissertation, as stated in Section 1.8.1, is to develop computational models for the vibration response of piled foundations and neighbouring tunnels. The main applications of these models are: to determine the effect of piled foundations and twin tunnels on ground-borne vibration; to evaluate objectively the vibration performance of piled foundation and twin-tunnel designs; and to establish the best design practice. Each of these applications are reviewed here in turn, and the contribution of this research toward the fulfilment of these aims is assessed.

5.1.1 The Effect of Piled Foundations and Twin Tunnels on Ground-Borne Vibration

Chapter 2 addresses the development of a single-pile model, the starting point for any pile-group model. Two approaches are considered. Firstly, an existing plane-strain model by Novak [130, 134] is modified to include an incident wavefield and allow for calculation of farfield displacements. Secondly, the elastic-continuum equations used in the PiP model are coupled to the equations for an infinite column or an Euler beam to obtain a model for an infinitely long pile in the wavenumber domain. Using mirror-image techniques, a method for adapting this model to simulate a finite-length pile embedded in a halfspace is developed, and a computationally efficient approach to incorporating the incident wavefield from an underground railway is established.

Validation of the plane-strain and three-dimensional single-pile models is achieved by comparing the pile-head, driving-point response generated by these models against the response calculated by an existing boundary-element (BE) model. Whilst the agreement in axial vibration is good, the plane-strain assumption is shown to be invalid for lateral vibration in the frequency range of interest: 1-80Hz.

The response of a single pile to underground-railway vibration is calculated. In axial vibration, the single pile has a significant stiffening effect on the soil, resulting in reduced surface-displacement levels. The amount of vibration attenuation is observed to increase with increasing frequency. However, for the case of lateral vibration, the single pile marginally increases the vibration level at higher frequencies. Analysis of the power flows through the pile skin indicate that the power entering a pile by a vertical loading is dissipated along the whole length of the pile, whereas the power entering the pile by a lateral loading is dissipated in a highly localised region near the location of power inflow. This behaviour is expected for a slender cylinder like a pile, because the stiffness of the cylinder is higher in axial compression than in bending.

The pile models are extended in Chapter 3 to consider pile-soil-pile interactions within a pile group. The superposition method is chosen as an efficient means of calculating the direct-field component of the PSPI, and a model for calculating the interaction between two neighbouring piles is formulated based on the method of joining subsystems. The inertial interaction factors generated using the two-pile models are validated against a BE model and a dynamic stiffness matrix formulation by Kaynia [88]. The Novak model does not accurately represent pile-soil-pile interactions, however, the three-dimensional model compares well with the results obtained using the numerical methods. A model for evaluating the response of a pile group subject to an incident wavefield is developed, and comparison of the results with the three-dimensional and BE models

again shows good agreement. The kinematic interaction effects in the pile group subject to an incident wavefield are small, and it is concluded that the superposition method does not provide a comprehensive representation of the interactions occurring in this particular pile group. The chapter concludes with the development of a model for a piled building, and a case study to demonstrate how this model can be used together with power-flow techniques to evaluate the dynamic response of different foundation designs.

The effect of twin tunnels on ground-borne vibration is addressed in Chapter 4. The superposition of two displacement fields, the direct field and the scattered field, is used to formulate a fully-coupled model for two infinitely long tunnels in a fullspace. Comparison of this twin-tunnel model with the single-tunnel model reveals the effect of the neighbouring tunnel on the propagated vibrations. The second tunnel deflects the vibration field from the first tunnel, creating a shadow region behind the second tunnel and regions of significant insertion gain in the farfield. Whilst these trends are observed over a range of frequencies, tunnel orientations and tunnel thickness, the location of the maximum insertion gains are highly variable and dependent on all the aforementioned factors. The maximum insertion gains are commonly in the order of 20dB, indicating that a high degree of inaccuracy exists in any vibration-prediction model that considers the presence of only one tunnel.

5.1.2 The Vibration Performance of Embedded-Structure Designs

The mathematical models developed in this dissertation provide a means of evaluating the vibration performance of embedded structures. For both piled foundations and twin tunnels, the vibration performance of the system has been shown to be highly dependent on factors such as frequency, soil parameters and system geometry. For this reason, no generalisations on system design are offered here, but instead, the engineering practitioner is recommended to use these mathematical models to evaluate specific design cases.

The model of a piled building subject to a wavefield generated by an underground railway provides a useful means of evaluating the dynamic behaviour of piled foundation designs. More generally, the piled-building model may also be used to evaluate the dynamic behaviour of a foundation with some form of excitation at the pile heads, for example, a piled building with rotating equipment mounted in the basement. The models of piled foundations developed in this dissertation are shown to be both accurate and computationally efficient.

The twin-tunnel model is not specifically a vibration-prediction model due to the

fullspace formulation and the lack of consideration of other underground features. However, it provides useful insights into the deflection of a wavefield by a second tunnel. This model can therefore be used to evaluate various features of the tunnel design and approximate the magnitude of the error present in a single-tunnel model.

One of the difficulties involved in evaluating the vibration performance of these embedded structures is the choice of an appropriate vibration-performance measure. For piled foundations, displacement magnitude at the pile heads provides a measure of how the vibration level differs from that of greenfield conditions. Whilst this is useful for observing trends in pile behaviour, the frequency, direction and position dependence of displacement magnitudes does not provide a clear quantification of the vibration performance of various foundation designs. For this reason, power-flow techniques are recommended. Mean power flow provides a single measure to represent the vibrational-energy contributions from all piles and all vibration directions. Should the engineering practitioner wish to eliminate the frequency variation in the response, RMS power flow can be used to provide a single, real number to represent the foundation response.

The use of insertion gain provides an excellent measure for comparing the results of the twin-tunnel model with the single-tunnel model. However, some anomalous results are shown to be present due to lines of symmetry in the single-tunnel model.

5.1.3 The Best Design Practice

Retrofits involving the most effective vibration-isolation measures, such as floating slab track or base isolation, are expensive undertakings. The preferred practice is to assess the need for these isolation measures during the design stage. This requires the availability of well-validated, accurate and computationally efficient vibration-prediction tools. At present, the available prediction tools are only in the early stages of fulfilling this requirement. This dissertation represents a contribution towards improved model validation, accuracy and efficiency.

The twin-tunnel model has highlighted the scope for inaccuracies in prediction models. Simplifying assumptions about the underground and above-ground environment cannot be made without some recognition of an associated error, and efforts should be made to quantify the magnitude of this error before presenting final vibration predictions. An increased awareness of the sources of uncertainty in vibration-prediction models and the vibration-related consequences of design choices would benefit both engineering practitioners (particularly railway and building designers) and the affected public. This would contribute towards the establishment of better design practices and continued dialogue throughout all stages of the design procedure.

5.2 Recommendations for Future Work

The models outlined in this dissertation provide a useful and efficient means of assessing the vibration performance of piled foundations and twin tunnels. These models represent a valuable contribution towards the field of underground-railway research, as they provide a much-needed method for assessing generic design situations. There are several specific design situations that could be assessed by extending these models, and scope exists for further investigation of the main assumptions used in the modelling presented in this dissertation. Possible future developments are outlined below.

Further investigation of the errors introduced by the mirror-image method could be achieved by calculating the displacements at varying depths within the soil. The method for calculating these displacements using the three-dimensional model is straightforward. However, to obtain comparative results using the BE model requires meshing of the relevant region. Investigation of other pile-to-soil stiffness ratios would also further evaluate the robustness of the three-dimensional pile model.

One of the main assumptions implicit in the use of the method of joining subsystems is the uncoupling of the source and receiver. The validity of this assumption is evaluated for the joining of the piles to the incident wavefield and the pile-soil-pile interactions by comparison with the fully-coupled BE and DSM models. Good agreement is seen when the piles are joined to the incident wavefield, but this method does not provide a comprehensive representation of PSPI. The validity of this assumption in relation to the joining of the pile cap and the building to the pile group has not been assessed. Further investigation of uncoupled/coupled source-receiver models could provide useful insight not only for the modelling of the underground-railway environment, but also for other complex vibration systems.

As mentioned in Section 4.3.1, methods exist for adapting the twin-tunnel model to simulate twin tunnels embedded in a homogeneous or layered halfspace. The implementation of these methods is not expected to significantly alter the conclusions obtained using the twin-tunnel model presented in this dissertation. However, it is recognised that engineering practitioners may prefer to use a halfspace model rather than a fullspace model. For this reason, a model of twin tunnels embedded in a halfspace would be a useful tool.

In a congested underground environment, railway lines frequently cross over, which can result in two twin-tunnel systems in close proximity. It is proposed that the twin-tunnel model described in this dissertation may be extended to include additional neighbouring tunnels. Through the use of a transformation of the wavenumber components, non-parallel tunnels may also be accounted for. This extension of the twin-tunnel model

would also allow the incorporation of buried services near the tunnels.

Further developments of the foundation model presented in this dissertation include: the incorporation of base-isolation bearings between the piles and the building; the formulation of a more-detailed finite building model that may be attached to a finite pile group; and the investigation of other types of foundation, such as raft or strip foundations. Furthermore, the incorporation of varying soil properties, such as soil layers, anisotropic soil stiffness and pore pressures, into the piled-foundation and two-tunnel models would further improve the robustness of a prediction model.

Although this dissertation and much other research on the vibration from underground railways solely consider the modelling of the system, experimental measurements taken both below- and above- ground would be beneficial in validating these models and obtaining further insights into underground-railway vibration. Field-testing opportunities should be explored wherever possible, and the use of scale models or centrifuge testing could also provide a useful route for validation.

On a final note, it is recommended that underground-railway researchers and practitioners continue to collaborate by publishing their findings and allowing their models and data to be available for use in cross-validation.

References

[1] G. M. Aasvang, B. Engdahl, and K. Rothschild. Annoyance and self-reported sleep disturbances due to structurally radiated noise from railway tunnels. *Applied Acoustics*, 68(9):970–981, 2007.

[2] A. Abebe and I.G.N. Smith. Pile foundation design: a student guide, 2005.

[3] T. I. Addenbrooke and D. M. Potts. Twin tunnel construction - ground movements and lining behaviour. In R. J. Mair and R. N. Taylor, editors, *Geotechnical Aspects of Underground Construction in Soft Ground*, pages 441–446, London, 1996. Taylor and Francis.

[4] R. D. Ambrosini. Material damping vs. radiation damping in soil-structure interaction analysis. *Computers and Geotechnics*, 33(2):86–92, 2006.

[5] L. Andersen and C. J. C. Jones. Coupled boundary and finite element analysis of vibration from railway tunnels - a comparison of two- and three-dimensional models. *Journal of Sound and Vibration*, 293(3-5):611–625, 2006.

[6] L. Auersch. The excitation of ground vibration by rail traffic: theory of vehicle-track-soil interaction and measurements on high-speed lines. *Journal of Sound and Vibration*, 284(1-2):103–132, 2005.

[7] T. Balendra. Dynamic interaction of twin tunnels. In A.P. Boresi and K.P. Chong, editors, *Engineering Mechanics in Civil Engineering: Proceedings of the Fifth Engineering Mechanics Division Specialty Conference*, volume 1, pages 368–371, Laramie, 1984. American Society of Civil Engineers.

[8] P. K. Banerjee and S. M. Mamoon. A fundamental solution due to a periodic point force in the interior of an elastic half-space. *Earthquake Engineering and Structural Dynamics*, 19(1):91–105, 1990.

[9] V. A. Baranov. On the calculation of excited vibrations of an embedded foundation. *Voprosy Dynamiki Prochnocti*, 14:195–209, 1967.

[10] M. Beckers. Incorporating geometric features into the PiP model for subway induced vibrations. Master's thesis, Katholieke Universiteit Leuven, 2010.

[11] K. J. Bentley and M. H. El Naggar. Numerical analysis of kinematic response of single piles. *Canadian Geotechnical Journal*, 37(6):1368–1382, 2000.

[12] Y. Beredugo and M. Novak. Coupled horizontal and rocking vibration of embedded footings. *Canadian Geotechnical Journal*, 9(4):477–497, 1972.

[13] M. A. Biot. Dynamics of viscoelastic anisotropic media. In *Proceedings of the Fourth Midwestern Conference on Solid Mechanics, Publication No. 129*. Engineering Experiment Station, Purdue University, Lafayette, 1955.

[14] A. Boominathan and R. Ayothiraman. Dynamic behaviour of laterally loaded model piles in clay. *Proceedings of the Institution of Civil Engineers-Geotechnical Engineering*, 158(4):207–215, 2005.

[15] H. Bretz. Challenges in tunnel engineering in southeast asia. *Tunnel Construction*, 1998.

[16] G. N. Bycroft. Forced vibrations of a rigid circular plate on a semi-infinite elastic space and on an elastic stratum. *Philosophical Transactions of the Royal Society of London A - Mathematical and Physical Sciences*, 248(948):327–368, 1956.

[17] R. Cairo, E. Conte, and G. Dente. Analysis of pile groups under vertical harmonic vibration. *Computers and Geotechnics*, 32(7):545–554, 2005.

[18] R. Cairo, E. Conte, and G. Dente. Interaction factors for the analysis of pile groups in layered soils. *Journal of Geotechnical and Geoenvironmental Engineering*, 131(4):525–528, 2005.

[19] F. H. Chehade and I. Shahrour. Numerical analysis of the interaction between twin-tunnels: Influence of the relative position and construction procedure. *Tunnelling and Underground Space Technology*, 23(2):210–214, 2008.

[20] Y. K. Chow. Analysis of dynamic behavior of piles. *International Journal for Numerical and Analytical Methods in Geomechanics*, 9(4):383–390, 1985.

[21] B. L. Chu, S. C. Hsu, Y. L. Chang, and Y. S. Lin. Mechanical behavior of a twin-tunnel in multi-layered formations. *Tunnelling and Underground Space Technology*, 22(3):351–362, 2007.

[22] D. Clouteau, M. Arnst, T. M. Al-Hussaini, and G. Degrande. Freefield vibrations due to dynamic loading on a tunnel embedded in a stratified medium. *Journal of Sound and Vibration*, 283(1-2):173–199, 2005.

[23] D. Clouteau, G. Degrande, and G. Lombaert. Numerical modelling of traffic induced vibrations. *Meccanica*, 36(4):401–420, 2001.

[24] M. L. Cooper, D. N. Chapman, and C. D. F. Rogers. Prediction of settlement in existing tunnel caused by the second of twin tunnels. *Transportation Research Record: Journal of the Transportation Research Board*, 1814:103–112, 2002.

[25] P. Coulier. The vibration response of piled foundations to inertial and underground railway induced loadings. Master's thesis, Katholieke Universiteit Leuven, 2010.

[26] M. Crocker, editor. *Handbook of noise and vibration control*. Wiley, Hoboken, 2007.

[27] D. Cryer. *Modeling of vibration in buildings with application to base isolation*. PhD thesis, University of Cambridge, 1994.

[28] T. M. Dawn. Ground vibrations from heavy freight trains. *Journal of Sound and Vibration*, 87(2):351–356, 1983.

[29] T. M. Dawn and C. G. Stanworth. Ground vibrations from passing trains. *Journal of Sound and Vibration*, 66(3):355–362, 1979.

[30] F. C. P. De Barros and J. Luco. Discrete models for vertical vibrations of surface and embedded foundations. *Earthquake Engineering and Structural Dynamics*, 19:289–303, 1990.

[31] G. Degrande, M. Schevenels, P. Chatterjee, W. Van de Velde, P. Holscher, V. Hopman, A. Wang, and N. Dadkah. Vibrations due to a test train at variable speeds in a deep bored tunnel embedded in London clay. *Journal of Sound and Vibration*, 293(3-5):626–644, 2006.

[32] F. Dezi, S. Carbonari, and G. Leoni. A model for the 3D kinematic interaction analysis of pile groups in layered soils. *Earthquake Engineering and Structural Dynamics*, 38:1281–1305, 2009.

[33] G. Di Mino, M. Giunta, and C. Di Liberto. Assessing the open trenches in screening railway ground-borne vibrations by means of an artificial neural network. *Advances in Acoustics and Vibration*, 2009:1–12, 2009.

[34] R Dobry and G. Gazetas. Simple method for dynamic stiffness and damping of floating pile groups. *Geotechnique*, 38(4):557–574, 1988.

[35] H. R. Dou and P. M. Byrne. Dynamic response of single piles and soil pile interaction. *Canadian Geotechnical Journal*, 33(1):80–96, 1996.

[36] T. Ekevid, M. X. D. Li, and N. E. Wiberg. Adaptive FEA of wave propagation induced by high-speed trains. *Computers and Structures*, 79(29-30):2693–2704, 2001.

[37] M. H. El Naggar and K. J. Bentley. Dynamic analysis for laterally loaded piles and dynamic p-y curves. *Canadian Geotechnical Journal*, 37(6):1166–1183, 2000.

[38] B. Elsharnouby and M. Novak. Dynamic experiments with group of piles. *Journal of Geotechnical Engineering, Proceedings of the American Society of Civil Engineers*, 110(6):719–737, 1984.

[39] Institute of Civil Engineers. *Sprayed concrete linings (NATM) for tunnels in soft ground*. ICE design and practice guides. Thomas Telford, 1996.

[40] R. Flores-Berrones and R. Whitman. Seismic response of end-bearing piles. *Journal of the Geotechnical Engineering Division, Proceedings of the American Society of Civil Engineers*, 108(GT4):554–569, 1982.

[41] J. A. Forrest. *Modelling of ground vibration from underground railways*. PhD thesis, University of Cambridge, 1999.

[42] J. A. Forrest and H. E. M. Hunt. Ground vibration due to trains in underground railway tunnels. In *Proceedings of the 6th International Congress on Sound and Vibration*, Copenhagen, Denmark, 1999.

[43] J. A. Forrest and H. E. M. Hunt. Ground vibration generated by trains in underground tunnels. *Journal of Sound and Vibration*, 294(4-5):706–736, 2006.

[44] J. A. Forrest and H. E. M. Hunt. A three-dimensional tunnel model for calculation of train-induced ground vibration. *Journal of Sound and Vibration*, 294(4-5):678–705, 2006.

[45] N.N. Fotieva. Calculation of the linings of two closely spaced circular tunnels for seismic effects. *Soil Mechanics and Foundation Engineering*, 15(3):186–193, 1978.

[46] G. Y. Gao, Z. Y. Li, C. Qiu, and Z. Q. Yue. Three-dimensional analysis of rows of piles as passive barriers for ground vibration isolation. *Soil Dynamics and Earthquake Engineering*, 26(11):1015–1027, 2006.

[47] G. Gazetas. Soil dynamics: an overview. In P. K. Banerjee and R. Butterfield, editors, *Dynamic behaviour of foundations and buried structures*, volume 3. Elsevier Applied Science, London, 1987.

[48] H. G. D. Goyder and R. G. White. Vibrational power flow from machines into built-up structures. 1. Introduction and approximate analyses of beam and plate-like foundations. *Journal of Sound and Vibration*, 68(1):59–75, 1980.

[49] H. G. D. Goyder and R. G. White. Vibrational power flow from machines into built-up structures. 2. Wave-propagation and power flow in beam-stiffened plates. *Journal of Sound and Vibration*, 68(1):77–96, 1980.

[50] H. G. D. Goyder and R. G. White. Vibrational power flow from machines into built-up structures. 3. Power flow through isolation systems. *Journal of Sound and Vibration*, 68(1):97–117, 1980.

[51] S. Gupta, M. F. M. Hussein, G. Degrande, H. E. M. Hunt, and D. Clouteau. A comparison of two numerical models for the prediction of vibrations from underground railway traffic. *Soil Dynamics and Earthquake Engineering*, 27(7):608–624, 2007.

[52] T. G. Gutowski and C. L. Dym. Propagation of ground vibration - review. *Journal of Sound and Vibration*, 49(2):179–193, 1976.

[53] Y. C. Han and M. Novak. Dynamic behavior of single piles under strong harmonic excitation. *Canadian Geotechnical Journal*, 25(3):523–534, 1988.

[54] S. M. Hasheminejad and R. Avazmohammadi. Dynamic stress concentrations in lined twin tunnels within fluid-saturated soil. *Journal of Engineering Mechanics, Proceedings of the American Society of Civil Engineers*, 134(7):542–554, 2008.

[55] H. M. Hawari and M. H. Murray. Effects of train characteristics on the rate of deterioration of track roughness. *Journal of Engineering Mechanics, Proceedings of the American Society of Civil Engineers*, 134(3):234–239, 2008.

[56] M. Heckl, G. Hauck, and R. Wettschureck. Structure-borne sound and vibration from rail traffic. *Journal of Sound and Vibration*, 193(1):175–184, 1996.

[57] R. Hildebrand. *Countermeasures against railway ground and track vibrations*. PhD thesis, Royal Institute of Technology, 2001.

[58] R. Hildebrand. Asymptotic analysis of hard wave barriers in soil. *Soil Dynamics and Earthquake Engineering*, 23(2):143–158, 2003.

[59] D. M. Hiller and V. S. Hope. Groundborne vibration generated by mechanized construction activities. *Proceedings of the Institution of Civil Engineers-Geotechnical Engineering*, 131(4):223–232, 1998.

[60] R. A. Hood, R. J. Greer, M. Breslin, and P. R. Williams. The calculation and assessment of ground-borne noise and perceptible vibration from trains in tunnels. *Journal of Sound and Vibration*, 193(1):215–225, 1996.

[61] H. V. C. Howarth and M. J. Griffin. Human response to simulated intermittent railway-induced building vibration. *Journal of Sound and Vibration*, 120(2):413–420, 1988.

[62] H. H. Hung, Y. B. Yang, and D. W. Chang. Wave barriers for reduction of train-induced vibrations in soils. *Journal of Geotechnical and Geoenvironmental Engineering*, 130(12):1283–1291, 2004.

[63] H. E. M. Hunt. *Measurement and modelling of traffic-induced ground vibration.* PhD thesis, University of Cambridge, 1988.

[64] H. E. M. Hunt and J. E. May. Vibration generated by underground railway trains. In *Proceedings of the 5th International Congress on Sound and Vibration*, Adelaide, Australia, 1997.

[65] M. F. M. Hussein. *Vibration from underground railways.* PhD thesis, University of Cambridge, 2004.

[66] M. F. M. Hussein, S. Gupta, H. E. M. Hunt, G. Degrande, and J. P. Talbot. A computationally efficient model for calculating vibration from a railway tunnel embedded in a half space [in press]. *Journal of Sound and Vibration*, 2010.

[67] M. F. M. Hussein, S. Gupta, H. E. M. Hunt, G. Degrande, and J.P. Talbot. An efficient model for calculating vibration from a railway tunnel buried in a half-space. In *Proceedings of the 14th International Confress on Sound and Vibration*, Cairns, Australia, 2006.

[68] M. F. M. Hussein and H. E. M. Hunt. Modelling of floating-slab tracks with continuous slabs under oscillating moving loads. *Journal of Sound and Vibration*, 297(1-2):37–54, 2006.

[69] M. F. M. Hussein and H. E. M. Hunt. A power flow method for evaluating vibration from underground railways. *Journal of Sound and Vibration*, 293(3-5):667–679, 2006.

[70] M. F. M. Hussein and H. E. M. Hunt. A numerical model for calculating vibration from a railway tunnel embedded in a full-space. *Journal of Sound and Vibration*, 305(3):401–431, 2007.

[71] M. F. M. Hussein and H. E. M. Hunt. A numerical model for calculating vibration due to a harmonic moving load on a floating-slab track with discontinuous slabs in an underground railway tunnel. *Journal of Sound and Vibration*, 321(1-2):363–374, 2009.

[72] M. F. M. Hussein, H. E. M. Hunt, L. Rikse, S. Gupta, G. Degrande, J. P. Talbot, S. Francois, and M. Schevenels. Using the PiP model for fast calculation of vibration from a railway tunnel in a multi-layered half-space. In *9th International Workshop on Railway Noise*, volume 1, pages 136–142, Munich, Germany, 2007. Springer.

[73] British Standards Institution. Evaluation and measurement for vibration in buildings, 1990.

[74] British Standards Institution. Evaluation and measurement for vibration in buildings, 1993.

[75] British Standards Institution. Eurocode 7. Geotechnical design, 1997.

[76] M. R. M. Javan, A. Noorzad, and M. L. Namin. Three-dimensional nonlinear finite element analysis of pile groups in saturated porous media using a new transmitting boundary. *International Journal for Numerical and Analytical Methods in Geomechanics*, 32(6):681–699, 2008.

[77] K. P. Jaya and A. M. Prasad. Dynamic behaviour of pile foundations in layered soil medium using cone frustums. *Geotechnique*, 54(6):399–414, 2004.

[78] L. Jianwen, Z. Hao, and V. W. Lee. A series solution for surface motion amplification due to underground twin tunnels: incident SV waves. *Earthquake Engineering and Engineering Vibration*, 2(2):289–298, 2003.

[79] S. Jones and H. E. M. Hunt. Effect of inclined soil layers on vibration from underground railways. In *Proceedings of the International Conference on Noise and Vibration Engineering*, Leuven, 2008.

[80] S. Jones, M. F. M. Hussein, and H. E. M. Hunt. Use of PiP to investigate the effect of a free surface on ground vibration produced by underground railways. *Acoustics Australia*, 38(1):20–24, 2010.

[81] S. H. Ju. Finite element analysis of structure-borne vibration from high-speed train. *Soil Dynamics and Earthquake Engineering*, 27:259–273, 2007.

[82] M. Karakus, A. Ozsan, and H. Basarir. Finite element analysis for the twin metro tunnel constructed in Ankara Clay, Turkey. *Bulletin of Engineering Geology and the Environment*, 66(1):71–79, 2007.

[83] S. E. Kattis, D. Polyzos, and D. E. Beskos. Modelling of pile wave barriers by effective trenches and their screening effectiveness. *Soil Dynamics and Earthquake Engineering*, 18(1):1–10, 1999.

[84] S. E. Kattis, D. Polyzos, and D. E. Beskos. Vibration isolation by a row of piles using a 3-D frequency domain BEM. *International Journal for Numerical Methods in Engineering*, 46(5):713–728, 1999.

[85] E. Kausel and R. Peek. Dynamic loads in the interior of a layered stratum - an explicit solution. *Bulletin of the Seismological Society of America*, 72(5):1459–1481, 1982.

[86] E. Kausel and J. M. Roesset. Stiffness matrices for layered soils. *Bulletin of the Seismological Society of America*, 71(6):1743–1761, 1981.

[87] F. Kawakami, T. Kobayashi, C. Jaffe, M. Holden, and R. Cooper. Sound and vibration control for the Tokyo International Forum. *Journal of the Acoustical Society of America*, 103(5):2994, 1998.

[88] A. M. Kaynia. *Dynamic stiffness and seismic response of pile groups*. PhD thesis, Massachusetts Institute of Technology, 1982.

[89] A. M. Kaynia and E Kausel. Dynamic behaviour of pile groups. In *Proceedings of the 2nd International Conference on Numerical Methods in Offshore Piling*, pages 509–532, Austin, 1982.

[90] A. M. Kaynia and E Kausel. Dynamics of piles and pile groups in layered soil media. *Soil Dynamics and Earthquake Engineering*, 10(8):386–401, 1991.

[91] A. M. Kaynia, C. Madshus, and P. Zackrisson. Ground vibration from high-speed trains: prediction and countermeasure. *Journal of Geotechnical and Geoenvironmental Engineering*, 126(6):531–537, 2000.

[92] A. M. Kaynia and M Novak. Response of piles and pile groups to travelling SH waves. *Earthquake Engineering and Structural Dynamics*, 21:303–318, 1992.

[93] V. Knall. Railway noise and vibration: effects and criteria. *Journal of Sound and Vibration*, 193(1):9–20, 1996.

[94] U. Köpke. Transverse vibration of buried pipelines due to internal excitation at a point. *Journal of Process Mechanical Engineering, Proceedings of the Institution of Mechanical Engineers*, 207(E1):41–58, 1993.

[95] R. Krishnan, G. Gazetas, and A. Velez. Static and dynamic lateral deflection of piles in non-homogeneous soil stratum. *Geotechnique*, 33(3):307–325, 1983.

[96] R. Kuhlemeyer. Static and dynamic laterally loaded floating piles. *Journal of the Geotechnical Engineering Division, Proceedings of the American Society of Civil Engineers*, 105(GT2):289–304, 1979.

[97] R. Kuhlemeyer. Vertical vibration of piles. *Journal of the Geotechnical Engineering Division, Proceedings of the American Society of Civil Engineers*, 105(GT2):273–287, 1979.

[98] L. G. Kurzweil. Ground-born noise and vibration from underground rail systems. *Journal of Sound and Vibration*, 66(3):363–370, 1979.

[99] H. Lane, S. Berg, and M. Larsson. Finite element calculations of rail vibration countermeasures. *Vehicle System Dynamics*, 45(6):565–581, 2007.

[100] R. S. Langley. Analysis of power flow in beams and frameworks using the direct-dynamic stiffness method. *Journal of Sound and Vibration*, 136(3):439–452, 1990.

[101] S. Liao and D. A. Sangrey. Use of piles as isolation barriers. *Journal of the Geotechnical Engineering Division, Proceedings of the American Society of Civil Engineers*, 104(9):1139–1152, 1978.

[102] G. Lombaert and G. Degrande. Experimental validation of a numerical prediction model for free field traffic induced vibrations by in situ experiments. *Soil Dynamics and Earthquake Engineering*, 21(6):485–497, 2001.

[103] G. Lombaert, G. Degrande, and D. Clouteau. Numerical modelling of free field traffic-induced vibrations. *Soil Dynamics and Earthquake Engineering*, 19(7):473–488, 2000.

[104] G. Lombaert, G. Degrande, J. Kogut, and S. Francois. The experimental validation of a numerical model for the prediction of railway induced vibrations. *Journal of Sound and Vibration*, 297(3-5):512–535, 2006.

[105] F. Lopez-Caballero, A. Modaressi, F. Razavi, and H. Modaressi. Nonlinear numerical method for earthquake site response analysis i - elastoplastic cyclic model and parameter identification strategy. *Bulletin of Earthquake Engineering*, 5(3):303–323, 2007.

[106] J. F. Lu, D. S. Jeng, and W. D. Nie. Dynamic response of a pile embedded in a porous medium subjected to plane SH waves. *Computers and Geotechnics*, 33(8):404–418, 2006.

[107] J. F. Lu, B. Xu, and J. H. Wang. Numerical analysis of isolation of the vibration due to moving loads using pile rows. *Journal of Sound and Vibration*, 2008 (In Press).

[108] J. Luco and R. Westmann. Dynamic response of circular footings. *Journal of the Engineering Mechanics Division, Proceedings of the American Society of Civil Engineers*, 97(EM5):1381–1395, 1971.

[109] C. Madshus, B. Bessason, and L. Harvik. Prediction model for low frequency vibration from high speed railways on soft ground. *Journal of Sound and Vibration*, 193(1):195–203, 1996.

[110] C. Madshus and A. M. Kaynia. High-speed railway lines on soft ground: Dynamic behaviour at critical train speed. *Journal of Sound and Vibration*, 231(3):689–701, 2000.

[111] O. Maeso, J. J. Aznarez, and F. Garcia. Dynamic impedances of piles and groups of piles in saturated soils. *Computers and Structures*, 83(10-11):769–782, 2005.

[112] B. K. Maheshwari and H. Watanabe. Nonlinear dynamic behavior of pile foundations: Effects of separation at the soil-pile interface. *Soils and Foundations*, 46(4):437–448, 2006.

[113] N. Makris and D. Badoni. Seismic response of pile groups under oblique-shear and Rayleigh waves. *Earthquake Engineering and Structural Dynamics*, 24:517–532, 1995.

[114] N. Makris and G. Gazetas. Dynamic pile-soil-pile interaction. part ii: lateral and seismic response. *Earthquake Engineering and Structural Dynamics*, 21:145–162, 1992.

[115] S. M. Mamoon and S. Ahmad. Seismic response of piles to obliquely incident SH-waves, SV-waves, and P-waves. *Journal of Geotechnical Engineering, Proceedings of the American Society of Civil Engineers*, 116(2):186–204, 1990.

[116] S. M. Mamoon and P. K. Banerjee. Response of piles and pile groups to traveling SH-waves. *Earthquake Engineering and Structural Dynamics*, 19(4):597–610, 1990.

[117] MathWorks. Matlab, 2007.

[118] G. F. Miller and H. Pursey. On the partition of energy between elastic waves in a semi-infinite solid. *Proceedings of the Royal Society of London A - Mathematical and Physical Sciences*, 233:55–59, 1955.

[119] K. Miura, A. M. Kaynia, K. Masuda, E. Kitamura, and Y. Seto. Dynamic behavior of pile foundations in homogeneous and nonhomogeneous media. *Earthquake Engineering and Structural Dynamics*, 23(2):183–192, 1994.

[120] I. D. Moore and F. Guan. Three-dimensional dynamic response of lined tunnels due to incident seismic waves. *Earthquake Engineering and Structural Dynamics*, 25(4):357–369, 1996.

[121] G. Mylonakis and G. Gazetas. Vertical vibration and additional distress of grouped piles in layered soil. *Soils and Foundations*, 38(1):1–14, 1998.

[122] G. Mylonakis, A. Nikolaou, and G. Gazetas. Soil-pile-bridge seismic interaction: kinematic and inertial effects. part i: soft soil. *Earthquake Engineering and Structural Dynamics*, 26(3):337–359, 1997.

[123] D. E. Newland. *Mechanical vibration analysis and computation*. Dover, Harlow, 2006.

[124] C. W. W. Ng, K. M. Lee, and D. K. W. Tang. Three-dimensional numerical investigations of new Austrian tunnelling method (NATM) twin tunnel interactions. *Canadian Geotechnical Journal*, 41(3):523–539, 2004.

[125] J. C. O. Nielsen, R. Lunden, A. Johansson, and T. Vernersson. Train-track interaction and mechanisms of irregular wear on wheel and rail surfaces. *Vehicle System Dynamics*, 40(1-3):3–54, 2003.

[126] T. Nogami. Dynamic group effect of multiple piles under vertical vibration. In *Proceedings of the American Society of Civil Engineers Engineering Mechanics Division Specialty Conference*, pages 750–754, Austin, Texas, 1979.

[127] T. Nogami. Flexural responses of grouped piles under dynamic loading. *Earthquake Engineering and Structural Dynamics*, 13(3):321–336, 1985.

[128] T. Nogami and M. Novak. Soil-pile interaction in vertical vibration. *Earthquake Engineering and Structural Dynamics*, 4(3):277–293, 1976.

[129] T. Nogami and M. Novak. Resistance of soil to a horizontally vibrating pile. *Earthquake Engineering and Structural Dynamics*, 5(3):249–261, 1977.

[130] M. Novak. Dynamic stiffness and damping of piles. *Canadian Geotechnical Journal*, 11:574–598, 1974.

[131] M. Novak. Vertical vibration of floating piles. *Journal of the Engineering Mechanics Division, Proceedings of the American Society of Civil Engineers*, 103(EM1):153–168, 1977.

[132] M. Novak. Foundations for shock-producing machines. *Canadian Geotechnical Journal*, 20(1):141–158, 1983.

[133] M. Novak and F. Aboul-Ella. Impedence functions of piles in layered media. *Journal of the Engineering Mechanics Division, Proceedings of the American Society of Civil Engineers*, 104(EM6):643–661, 1978.

[134] M. Novak and Y. Beredugo. Vertical vibration of embedded footings. *Journal of the Soil Mechanics and Foundations Division, Proceedings of the American Society of Civil Engineers*, 98(SM12):1291–1310, 1972.

[135] M. Novak and B. El Sharnouby. Stiffness constants of single piles. *Journal of Geotechnical Engineering, Proceedings of the American Society of Civil Engineers*, 109(7):961–974, 1983.

[136] M. Novak and B. El Sharnouby. Evaluation of dynamic experiments on pile group. *Journal of Geotechnical Engineering, Proceedings of the American Society of Civil Engineers*, 110(6):738–756, 1984.

[137] M. Novak and R. Grigg. Dynamic experiments with small pile foundations. *Canadian Geotechnical Journal*, 13:372–385, 1976.

[138] M. Novak and T. Nogami. Soil-pile interaction in horizontal vibration. *Earthquake Engineering and Structural Dynamics*, 5(3):263–281, 1977.

[139] M. Novak, T. Nogami, and F. Aboul-Ella. Dynamic soil reactions for plane strain case. *Journal of the Engineering Mechanics Division, Proceedings of the American Society of Civil Engineers*, 104(EM4):953–959, 1978.

[140] E. Öhrström. Effects of exposure to railway noise - a comparison between areas with and without vibration. *Journal of Sound and Vibration*, 205(4):555–560, 1997.

[141] T. Okumura, N. Takewaki, K. Shimizu, and K. Fukutake. Dynamic response of twin circular tunnels during earthquakes. Technical Report 840, National Institute of Standards and Technology, US Department of Commerce, 1992.

[142] L. A. Padron, J. J. Aznarez, and O. Maeso. BEM-FEM coupling model for the dynamic analysis of piles and pile groups. *Engineering Analysis with Boundary Elements*, 31(6):473–484, 2007.

[143] E. A. Palma, A. C. Zingano, J. C. Koppe, and J. Costa. Displacements estimate due to twin tunnel excavation under low overburden. In J. Bartak, I. Hrdina, G. Romancov, and J. Zlamal, editors, *Underground Space - the 4th Dimension of Metropolises, Vols 1-3*, Proceedings and Monographs in Engineering, Water and Earth Sciences, pages 635–638. Taylor and Francis, London, 2007.

[144] Y-H. Pao and C-C. Mow. *Diffraction of elastic waves and dynamic stress concentrations*. Rand Corporation research study. Crane, New York, 1973.

[145] Kings Place. Kings place. http://www.kingsplace.co.uk/, 2008.

[146] H. Poulos. Behavior of laterally loaded piles: II-pile groups. *Journal of the Soil Mechanics and Foundations Division, Proceedings of the American Society of Civil Engineers*, 97(SM5):733–751, 1971.

[147] H. Poulos. Lateral load deflection prediction for pile groups. *Journal of the Geotechnical Engineering Division, Proceedings of the American Society of Civil Engineers*, GT1:19–34, 1975.

[148] H. Poulos. Group factors for pile-deflection estimation. *Journal of the Geotechnical Engineering Division, Proceedings of the American Society of Civil Engineers*, GT12:1489–1509, 1979.

[149] H. Poulos and E. H. Davis. *Pile foundation analysis and design*. John Wiley and sons, New York, 1980.

[150] B. Prange. Parameters affecting damping properties. In B. Prange, editor, *Proceedings of Dynamical Methods in Soil and Rock Mechanics 1: Dynamic Response and Wave Propagation in Soils*, volume 1, pages 61–78, Karlsruhe, 1977. Balkema.

[151] R. K. N. D. Rajapakse and A. H. Shah. On the lateral harmonic motion of an elastic bar embedded in an elastic half-space. *International Journal of Solids and Structures*, 23(2):287–303, 1987.

[152] R. K. N. D. Rajapakse and A. H. Shah. On the longitudinal harmonic motion of an elastic bar embedded in an elastic half-space. *International Journal of Solids and Structures*, 23(2):267–285, 1987.

[153] R. K. N. D. Rajapakse, A. H. Shah, and S. K. Datta. Torsional vibrations of elastic foundations embedded in an elastic half-space. *Earthquake Engineering and Structural Dynamics*, 15(3):279–297, 1987.

[154] L. Rikse. Modelling of subway induced vibrations using the pipe-in-pipe model. Master's thesis, Katholieke Universiteit Leuven, 2007.

[155] J. Roesset. Dynamic stiffness of pile groups. In *Pile Foundations*, pages 263–286. ASCE, New York, 1984.

[156] M. Schevenels, S. Francois, and G. Degrande. EDT: Elastodynamic toolbox for Matlab. http://www.kuleuven.be/bwm/edt/index.html, 2008.

[157] R. Sen, T. G. Davies, and P. K. Banerjee. Dynamic analysis of piles and pile groups embedded in homogeneous soils. *Earthquake Engineering and Structural Dynamics*, 13(1):53–65, 1985.

[158] R. Sen, E. Kausel, and P. K. Banerjee. Dynamic analysis of piles and pile groups embedded in non-homogenous soils. *International Journal for Numerical and Analytical Methods in Geomechanics*, 9(6):507–524, 1985.

[159] A. Seryi, F. Asiri, F. Le Pimpec, T. Tauchi, K. Fujii, and H. Yamaoka. Vibrational stability of GLC/NLC linear collider: status and R&D plans, 2004.

[160] X. Sheng, C. J. C. Jones, and D. J. Thompson. Modelling ground vibration from railways using wavenumber finite- and boundary-element methods. *Proceedings of the Royal Society A - Mathematical Physical and Engineering Sciences*, 461(2059):2043–2070, 2005.

[161] X. Sheng, C. J. C. Jones, and D. J. Thompson. Prediction of ground vibration from trains using the wavenumber finite and boundary element methods. *Journal of Sound and Vibration*, 293(3-5):575–586, 2006.

[162] M. Sheta and M. Novak. Vertical vibration of pile groups. *Journal of the Geotechnical Engineering Division, Proceedings of the American Society of Civil Engineers*, 108(GT4):570–590, 1982.

[163] Grand Central Sound Studios. Personal communication, 2008.

[164] A. Tadeu, J. Antonio, and L. Godinho. Green's function for two-and-a-half dimensional elastodynamic problems in a half-space. *Computational Mechanics*, 27:484–491, 2001.

[165] R. Taherzadeh, D. Clouteau, and R. Cottereau. Simple formulas for the dynamic stiffness of pile groups. *Earthquake Engineering and Structural Dynamics*, 38:1665–1685, 2009.

[166] J. P. Talbot. *On the performance of base-isolated buildings: a generic model*. PhD thesis, University of Cambridge, 2001.

[167] V.R. Thiruvenkatachar and K. Viswanathan. Dynamic response of an elastic half-space to time-dependent surface tractions over an embedded spherical cavity. *Proceedings of the Royal Society A - Mathematical Physical and Engineering Sciences*, 287(1411):549–567, 1965.

[168] D. J. Thompson and C. J. C. Jones. A review of the modelling of wheel/rail noise generation. *Journal of Sound and Vibration*, 231(3):519–536, 2000.

[169] M. J. Tomlinson. *Foundation design and construction*. Prentice Hall, Harlow, 7th edition, 2001.

[170] P. H. Tsai, Z. Y. Feng, and T. L. Jen. Three-dimensional analysis of the screening effectiveness of hollow pile barriers for foundation-induced vertical vibration. *Computers and Geotechnics*, 35(3):489–499, 2008.

[171] E. G. Vadillo, J. Herreros, and J. G. Walker. Subjective reaction to structurally radiated sound from underground railways: field results. *Journal of Sound and Vibration*, 193(1):65–74, 1996.

[172] A. Veletsos and Y. Wei. Lateral and rocking vibration of footings. *Journal of the Soil Mechanics and Foundations Division, Proceedings of the American Society of Civil Engineers*, 97(SM9):1227–1248, 1971.

[173] G. Waas. *Analysis method for footing vibrations through layered media*. PhD thesis, University of California, 1972.

[174] G. Waas and H. G. Hartmann. Analysis of pile foundations under dynamic loads. In *Structural Mechanics Reactor Technology*, Paris, 1981.

[175] J. H. Wang, X. L. Zhou, and J. F. Lu. Dynamic response of pile groups embedded in a poroelastic medium. *Soil Dynamics and Earthquake Engineering*, 23(3):235–242, 2003.

[176] G. R. Watts. The generation and propagation of vibration in various soils produced by the dynamic loading of road pavements. *Journal of Sound and Vibration*, 156(2):191–206, 1992.

[177] G. R. Watts and V. V. Krylov. Ground-borne vibration generated by vehicles crossing road humps and speed control cushions. *Applied Acoustics*, 59(3):221–236, 2000.

[178] G. P. Wilson, H. J. Saurenman, and J. T. Nelson. Control of ground-borne noise and vibration. *Journal of Sound and Vibration*, 87(2):339–350, 1983.

[179] E. Winkler. *Die Lehre von der Elasticitaet und Festigkeit.* Dominicus, Prague, 1867.

[180] J. P. Wolf. *Foundation vibration analysis using simple physical models.* Prentice-Hall, London, 1994.

[181] J. P. Wolf, J. W. Meek, and C. Song, editors. *Cone models for a pile foundation.* Piles under dynamic loads. GT Div. ASCE, New York, 1992.

[182] J. P. Wolf and G. A. Von Arx. Horizontally traveling waves in a group of piles taking pile-soil-pile interaction into account. *Earthquake Engineering and Structural Dynamics*, 10:225–237, 1978.

[183] J. P. Wolf and G. A. Von Arx. Impedance functions of a group of vertical piles. In *Proceedings of the American Society of Civil Engineers Specialty Conference on Earthquake Engineering and Soil Dynamics*, volume 2, pages 1024–1041, Pasadena, CA, 1978.

[184] J. P. Wolf, G. A. Von Arx, F. C. P. de Barros, and M. Kakubo. Seismic analysis of the pile foundation of the reactor building of the NPP Angra 2. *Nuclear Engineering Design*, 65:329–341, 1981.

[185] J. Wongsaroj, K. Soga, and R. J. Mair. Modelling of long-term ground response to tunnelling under St James's Park, London. *Geotechnique*, 57(1):75–90, 2007.

[186] R. Woods. Screening of surface waves in soils. *Journal of the Soil Mechanics and Foundations Division, Proceedings of the American Society of Civil Engineers*, SM4:951–979, 1968.

[187] Y-S. Wu and Y-B. Yang. A semi-analytical appproach for analyzing ground vibrations caused by trains moving over elevated bridges. *Soil Dynamics and Earthquake Engineering*, 24:949–962, 2004.

[188] Y. B. Yang and H. H. Hung. A parametric study of wave barriers for reduction of train-induced vibrations. *International Journal for Numerical Methods in Engineering*, 40(20):3729–3747, 1997.

[189] Y. B. Yang and H. H. Hung. A 2.5D finite/infinite element approach for modelling visco-elastic bodies subjected to moving loads. *International Journal for Numerical Methods in Engineering*, 51:1317–1336, 2001.

[190] Y. B. Yang and H. H. Hung. Soil vibrations caused by underground moving trains. *Journal of Geotechnical and Geoenvironmental Engineering*, 134(11):1633–1644, 2008.

Appendix A

Method of Joining Subsystems

The following explanation has been adapted from Newland [123]. The composite system produced using this method represents an uncoupled source-receiver model. This gives a good approximation of the dynamic behaviour of the system when the distance separating the source and the receiver is large compared to the longest wavelength in the soil.

Consider the two subsystems A and B, shown in Figure A.1(a), which are to be joined together as shown in Figure A.1(b). The subsystem A is subject to a force input $x_1(t)$ at position 1, and the displacement output $y_2(t)$ is to be calculated at position 2. The two subsystems are to be coupled together at point 3, and at this point there exists the input forces $x_{3A}(t)$ and $x_{3B}(t)$, both acting in the same direction, and the output displacements $y_{3A}(t)$ and $y_{3B}(t)$, both acting in the same direction. The deflection of subsystem B results in a force on subsystem A in the reference direction, and vice versa.

The frequency-response functions of subsystem A are given by

$$\left\{ \begin{array}{c} Y_2(\omega) \\ Y_{3A}(\omega) \end{array} \right\} = \left[\begin{array}{cc} A_{21}(\omega) & A_{23}(\omega) \\ A_{31}(\omega) & A_{33}(\omega) \end{array} \right] \left\{ \begin{array}{c} X_1(\omega) \\ X_{3A}(\omega) \end{array} \right\}, \tag{A.1}$$

and the frequency-response function of subsystem B is given by

$$Y_{3B}(\omega) = B_{33}(\omega) X_{3B}(\omega). \tag{A.2}$$

After the subsystems have been coupled together, the input and output of the composite system are denoted by $x_3(t)$ and $y_3(t)$, respectively. To satisfy geometric compatibility conditions, the displacement of the subsystems at position 3 are equal. This can be written as

$$y_3(t) = y_{3A}(t) = y_{3B}(t). \tag{A.3}$$

To satisfy force equilibrium conditions, the forces acting on the subsystems sum to the force acting on the composite system, written as

$$x_3(t) = x_{3A}(t) + x_{3B}(t). \tag{A.4}$$

Substitution of these conditions results in the governing equations of the composite system:

$$\left\{ \begin{array}{c} Y_2(\omega) \\ Y_3(\omega) \end{array} \right\} = \left[\begin{array}{cc} \frac{A_{21}A_{33}-A_{23}A_{31}+A_{21}B_{33}}{A_{33}+B_{33}} & \frac{A_{23}B_{33}}{A_{33}+B_{33}} \\ \frac{A_{31}B_{33}}{A_{33}+B_{33}} & \frac{A_{33}B_{33}}{A_{33}+B_{33}} \end{array} \right] \left\{ \begin{array}{c} X_1(\omega) \\ X_3(\omega) \end{array} \right\}. \tag{A.5}$$

In many cases there is no net force acting on the composite system at position 3. This means that $x_3(t) = 0$, and therefore x_{3A} and x_{3B} are equal and opposite. In this case the governing equation of the system is

$$\left\{ \begin{array}{c} Y_2(\omega) \\ Y_3(\omega) \end{array} \right\} = \left[\begin{array}{c} \frac{A_{21}A_{33}-A_{23}A_{31}+A_{21}B_{33}}{A_{33}+B_{33}} \\ \frac{A_{31}B_{33}}{A_{33}+B_{33}} \end{array} \right] \left\{ X_1(\omega) \right\}. \tag{A.6}$$

Furthermore, in some instances there is no net force acting on the composite system at position 3, and the displacement output $y_2(t)$ is located at position 3. In this case the governing equation of the system is

$$Y_2(\omega) = \frac{A_{31}B_{33}}{A_{33} + B_{33}} X_1(\omega), \tag{A.7}$$

which can also be written as

$$Y_2(\omega) = \left[I + A_{33}B_{33}^{-1} \right]^{-1} A_{31} X_1(\omega), \tag{A.8}$$

where I is the identity element.

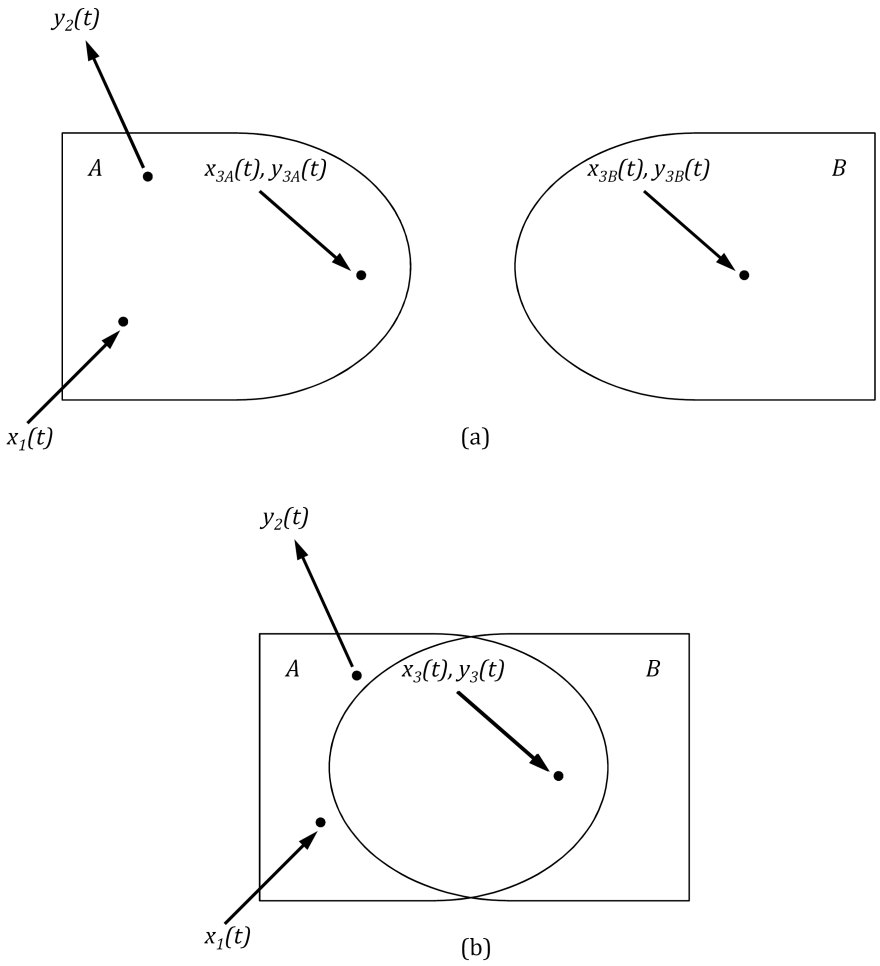

Fig. A.1 Diagrammatic representation of the method of joining subsystems: (a) two separate subsystems which are joined together to form the composite system (b)

Appendix B

Coefficient Matrices for a Cylindrical Shell and an Elastic Continuum

In the equations below, $\alpha^2 = \xi^2 - \frac{\omega^2}{c_P^2}$, $\beta^2 = \xi^2 - \frac{\omega^2}{c_S^2}$, and I_n and K_n are modified Bessel functions of the first and second kinds, respectively, of order n. Lamé's elastic constants are λ and μ. The speed of the pressure and shear waves in the medium are c_P and c_S, respectively. The angular frequency is ω, and ξ is the longitudinal wavenumber.

The matrix $[\mathbf{A}_E]$, used to determine the displacement components of the thin-walled cylinder, can be written as

$$[\mathbf{A}_E] = \frac{Eh}{-r(1-\nu^2)}\,[\mathbf{A}]\,, \tag{B.1}$$

where r is the radius of the cylinder and h is its thickness. The cylinder material is defined by Young's modulus E, Poisson's ratio ν and density ρ. The elements used to construct the matrix $[\mathbf{A}]$ are:

$$\begin{aligned}
a_{11} &= \tfrac{\rho r(1-\nu^2)}{E}\omega^2 - r\xi^2 - \tfrac{(1-\nu)}{2r}n^2 - \tfrac{(1-\nu)}{2r}\tfrac{h^2}{12r^2}n^2 \\
a_{12} &= \tfrac{(1+\nu)}{2}i\xi n \\
a_{13} &= -\nu i\xi + \tfrac{h^2}{12}(i\xi)^3 + \tfrac{h^2}{12r^2}\tfrac{(1-\nu)}{2}i\xi n^2 \\
a_{21} &= -\tfrac{(1+\nu)}{2}i\xi n \\
a_{22} &= \tfrac{\rho r(1-\nu^2)}{E}\omega^2 - \tfrac{r(1-\nu)}{2}\xi^2 - \tfrac{1}{r}n^2 - \tfrac{r(1-\nu)}{2}\tfrac{h^2}{4r^2}\xi^2 \\
a_{23} &= \tfrac{1}{r}n + \tfrac{h^2}{12}\tfrac{(3-\nu)}{2r}\xi^2 n \\
a_{31} &= \nu i\xi - \tfrac{h^2}{12}(i\xi)^3 - \tfrac{h^2}{12r^2}\tfrac{(1-\nu)}{2}i\xi n^2 \\
a_{32} &= \tfrac{1}{r}n + \tfrac{h^2}{12r}\tfrac{(3-\nu)}{2}\xi^2 n \\
a_{33} &= \tfrac{\rho r(1-\nu^2)}{E}\omega^2 - \tfrac{h^2}{12}\left(r\xi^4 + \tfrac{2}{r}\xi^2 n^2 + \tfrac{1}{r^3}n^4\right) - \tfrac{1}{r} + \tfrac{h^2}{6r^3}n^2 - \tfrac{h^2}{12r^3}.
\end{aligned} \tag{B.2}$$

For a symmetric loading, the matrix [**A**] is given by

$$[\mathbf{A}] = \begin{bmatrix} -a_{33} & a_{32} & a_{31} \\ a_{23} & -a_{22} & -a_{21} \\ a_{13} & -a_{12} & -a_{11} \end{bmatrix}. \tag{B.3}$$

For an antisymmetric loading, the matrix [**A**] is given by

$$[\mathbf{A}] = \begin{bmatrix} -a_{33} & -a_{32} & a_{31} \\ -a_{23} & -a_{22} & a_{21} \\ a_{13} & a_{12} & -a_{11} \end{bmatrix}. \tag{B.4}$$

The elements used to construct the matrix [**U**] are:

$$\begin{aligned} u_{12} &= \tfrac{n}{r}K_n(\alpha r) - \alpha K_{n+1}(\alpha r) \\ u_{14} &= i\xi K_{n+1}(\beta r) \\ u_{16} &= \tfrac{n}{r}K_n(\beta r) \\ u_{22} &= -\tfrac{n}{r}K_n(\alpha r) \\ u_{24} &= i\xi K_{n+1}(\beta r) \\ u_{26} &= -\tfrac{n}{r}K_n(\beta r) + \beta K_{n+1}(\beta r) \\ u_{32} &= i\xi K_n(\alpha r) \\ u_{34} &= \beta K_n(\beta r) \\ u_{36} &= 0. \end{aligned} \tag{B.5}$$

For a symmetric loading, the matrix [**U**] is given by

$$[\mathbf{U}] = \begin{bmatrix} u_{12} & u_{14} & u_{16} \\ u_{22} & u_{24} & u_{26} \\ u_{32} & u_{34} & u_{36} \end{bmatrix}. \tag{B.6}$$

For an antisymmetric loading, the matrix [**U**] is given by

$$[\mathbf{U}] = \begin{bmatrix} u_{12} & -u_{14} & -u_{16} \\ -u_{22} & u_{24} & u_{26} \\ u_{32} & -u_{34} & u_{36} \end{bmatrix}. \tag{B.7}$$

The elements used to construct the matrix $[\mathbf{T}]$ are:

$$
\begin{aligned}
t_{12} &= \left(2\mu\tfrac{n^2-n}{r^2} - \lambda\xi^2 + (\lambda+2\mu)\alpha^2\right) K_n(\alpha r) + 2\mu\tfrac{\alpha}{r}K_{n+1}(\alpha r) \\
t_{14} &= -2\mu i\xi\beta K_n(\beta r) - 2\mu i\xi\tfrac{n+1}{r}K_{n+1}(\beta r) \\
t_{16} &= 2\mu\tfrac{n^2-n}{r^2}K_n(\beta r) - 2\mu\tfrac{n}{r}\beta K_{n+1}(\beta r) \\
t_{22} &= -2\mu\tfrac{n^2-n}{r^2}K_n(\alpha r) + 2\mu\tfrac{n}{r}\alpha K_{n+1}(\alpha r) \\
t_{24} &= -\mu i\xi\beta K_n(\beta r) - 2\mu i\xi\tfrac{n+1}{r}K_{n+1}(\beta r) \\
t_{26} &= \left(-2\mu\tfrac{n^2-n}{r^2} - \mu\beta^2\right) K_n(\beta r) - 2\mu\tfrac{\beta}{r}K_{n+1}(\beta r) \\
t_{32} &= 2\mu i\xi\tfrac{n}{r}K_n(\alpha r) - 2\mu i\xi\alpha K_{n+1}(\alpha r) \\
t_{34} &= \mu\tfrac{n}{r}\beta K_n(\beta r) - \mu(\xi^2+\beta^2)K_{n+1}(\beta r) \\
t_{36} &= \mu i\xi\tfrac{n}{r}K_n(\beta r) \\
t_{42} &= \left(-2\mu\tfrac{n^2-n}{r^2} + \lambda(\alpha^2-\xi^2)\right) K_n(\alpha r) - 2\mu\tfrac{\alpha}{r}K_{n+1}(\alpha r) \\
t_{44} &= 2\mu i\xi\tfrac{n+1}{r}K_{n+1}(\beta r) \\
t_{46} &= -2\mu\tfrac{n^2-n}{r^2}K_n(\beta r) + 2\mu\tfrac{n}{r}\beta K_{n+1}(\beta r) \\
t_{52} &= -2\mu i\xi\tfrac{n}{r}K_n(\alpha r) \\
t_{54} &= -\mu\tfrac{n}{r}\beta K_n(\beta r) - \mu\xi^2 K_{n+1}(\beta r) \\
t_{56} &= -\mu i\xi\tfrac{n}{r}K_n(\beta r) + \mu i\xi\beta K_{n+1}(\beta r) \\
t_{62} &= (\lambda\alpha^2 - (\lambda+2\mu)\xi^2)K_n(\alpha r) \\
t_{64} &= 2\mu i\xi\beta K_n(\beta r) \\
t_{66} &= 0.
\end{aligned}
\tag{B.8}
$$

For a symmetric loading, the matrix $[\mathbf{T}]$ is given by

$$
[\mathbf{T}] = \begin{bmatrix} t_{12} & t_{14} & t_{16} \\ t_{22} & t_{24} & t_{26} \\ t_{32} & t_{34} & t_{36} \\ t_{42} & t_{44} & t_{46} \\ t_{52} & t_{54} & t_{56} \\ t_{62} & t_{64} & t_{66} \end{bmatrix}. \tag{B.9}
$$

For an antisymmetric loading, the matrix $[\mathbf{T}]$ is given by

$$[\mathbf{T}] = \begin{bmatrix} t_{12} & -t_{14} & -t_{16} \\ -t_{22} & t_{24} & t_{26} \\ t_{32} & -t_{34} & -t_{36} \\ t_{42} & -t_{44} & -t_{46} \\ -t_{52} & t_{54} & t_{56} \\ t_{62} & -t_{64} & -t_{66} \end{bmatrix}. \tag{B.10}$$

Appendix C

The Mirror-Image Method

The mirror-image method is used by Wolf [180] and Rikse [154] to introduce a boundary into a system. This boundary can be one of two types: a free surface (normal stresses are zero); or a fixed surface (normal displacements are zero). The type of boundary is determined by the direction of the mirror-image force, as will be demonstrated below.

The mirror-image method is best illustrated through example: consider a fixed-free column of length L, cross-sectional area A, density ρ and Young's modulus E, experiencing harmonic excitation P at its free end, as illustrated in Figure C.1(a). The equation of motion $Y_1(z)$ for this column is

$$Y_1(z) = \frac{P\left(e^{i\alpha z} + e^{-i\alpha z}e^{i\alpha 2L}\right)}{iEA\alpha\left(e^{i\alpha 2L}+1\right)}, \tag{C.1}$$

where

$$\alpha^2 = \frac{\rho\omega^2}{E}. \tag{C.2}$$

The displacements of this system can be calculated using the system shown in Figure C.1(b): the column and the applied load are mirrored about the clamped end. The equation of motion $Y_2(z)$ for the free-free column of length $2L$ loaded with harmonic force P at the left end is

$$Y_2(z) = \frac{-P\left(e^{-i\alpha 4L}e^{i\alpha z} + e^{-i\alpha z}\right)}{iEA\alpha\left(e^{-i\alpha 4L}-1\right)}. \tag{C.3}$$

The equation of motion $Y_3(z)$ for the free-free column of length $2L$ loaded with harmonic force $-P$ at the right end is

$$Y_3(z) = \frac{-P\left(e^{i\alpha z} + e^{-i\alpha z}\right)}{iEA\alpha\left(e^{i\alpha 2L}-e^{-i\alpha 2L}\right)}. \tag{C.4}$$

The superposition of these two equations of motion gives the equation of motion, Equation C.1, for the fixed-free column shown in Figure C.1(a). For this simple system it is instinctive that the displacement at the mirror surface produced by the original force is equal and opposite to that produced by the mirror-image force, thus the net displacement from the superposition of these two forces is zero.

Similarly, the displacements of a free-free column undergoing harmonic excitation P at one end (shown in Figure C.1(c)) are simulated by the system shown in Figure C.1(d): the column is mirrored about the far end, and the mirror-image force is in the same direction as the original force. The equation of motion $Y_4(z)$ for the free-free column of length L is

$$Y_4(z) = \frac{-P\left(e^{-i\alpha z} + e^{i\alpha z}e^{-i\alpha 2L}\right)}{iEA\alpha\left(e^{-i\alpha 2L} - 1\right)}. \tag{C.5}$$

The equation of motion $Y_2(z)$ for the free-free column of length $2L$, loaded with harmonic force P at the left end, is given in Equation C.3 above, and the equation of motion for the free-free column of length $2L$, loaded with harmonic force P at the right end, $Y_5(z)$, is

$$Y_5(z) = \frac{P\left(e^{i\alpha z} + e^{-i\alpha z}\right)}{iEA\alpha\left(e^{i\alpha 2L} - e^{-i\alpha 2L}\right)}. \tag{C.6}$$

The superposition of $Y_2(z)$ and $Y_5(z)$ gives the equation of motion, Equation C.5, for the fixed-free column shown in Figure C.1(c). Again, for this simple system it is instinctive that the stress produced at the mirror surface by the force on the left is equal and opposite to that produced by the mirror-image force, thus the net stress from the superposition of these two forces is zero at the mirror surface.

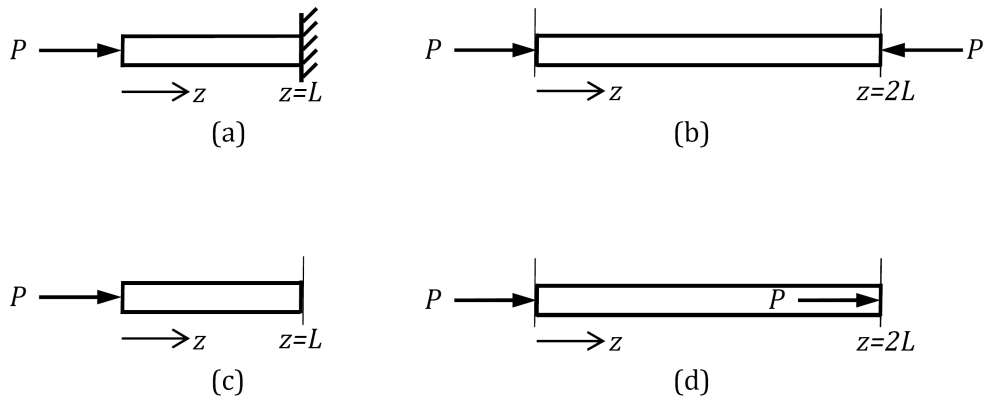

Fig. C.1 (a) Fixed-free column of length L; (b) free-free column of length $2L$, loaded to create a zero-displacement boundary condition; (c) free-free column of length L; and (d) free-free column of length $2L$, loaded to create a zero-stress boundary condition

Appendix D

Method for Calculating Maximum Displacement Magnitude

The displacements in the vertical and horizontal directions, u and w respectively, are harmonic with respect to time and represented by complex numbers. These displacements can therefore be written as

$$\begin{aligned} u &= u_x \sin(\omega t + \phi_x) \\ w &= w_y \sin(\omega t + \phi_y), \end{aligned} \tag{D.1}$$

where $u_x = |u|$, $w_y = |w|$, $\phi_x = \arctan(\frac{\Im(u)}{\Re(u)})$ and $\phi_y = \arctan(\frac{\Im(w)}{\Re(w)})$. The displacement magnitude u_R can be calculated using:

$$\begin{aligned} u_R^2 &= u^2 + w^2 \\ &= u_x^2 \sin^2(\omega t + \phi_x) + w_y^2 \sin^2(\omega t + \phi_y) \\ &= u_x^2 \left[\sin(\omega t) cos\phi_x + \cos(\omega t) \sin\phi_x\right]^2 + w_y^2 \left[\sin(\omega t)\cos\phi_y + \cos(\omega t)\sin\phi_y\right]^2 \\ &= \left[u_x^2 \cos^2\phi_x + w_y^2 \cos^2\phi_y\right] \sin^2(\omega t) + \left[u_x^2 \sin^2\phi_x + w_y^2 \sin^2\phi_y\right] \cos^2(\omega t) + \ldots \\ &\quad \left[\tfrac{u_x^2}{2} \sin(2\phi_x) + \tfrac{w_y^2}{2} \sin(2\phi_y)\right] \sin(2\omega t) \\ &= \left[u_x^2 \cos^2\phi_x + w_y^2 \cos^2\phi_y\right] \left[\tfrac{1}{2} - \tfrac{1}{2}\cos(2\omega t)\right] + \ldots \\ &\quad \left[u_x^2 \sin^2\phi_x + w_y^2 \sin^2\phi_y\right] \left[\tfrac{1}{2} + \tfrac{1}{2}\cos(2\omega t)\right] + \ldots \\ &\quad \left[\tfrac{u_x^2}{2} \sin(2\phi_x) + \tfrac{w_y^2}{2} \sin(2\phi_y)\right] \sin(2\omega t) \\ &= \tfrac{1}{2}\left[u_x^2 \sin(2\phi_x) + w_y^2 \sin(2\phi_y)\right] sin(2\omega t) - \ldots \\ &\quad \tfrac{1}{2}\left[u_x^2 \cos(2\phi_x) + w_y^2 \cos(2\phi_y)\right] cos(2\omega t) + \tfrac{u_x^2}{2} + \tfrac{w_y^2}{2} \end{aligned} \tag{D.2}$$

The maximum value of the displacement magnitude, u_{Rmax}, is then given by:

$$u_{Rmax}^2 = \tfrac{1}{2}\sqrt{u_x^4 + w_y^4 + 2u_x^2 w_y^2 \cos(2\phi_y - 2\phi_x)} + \tfrac{u_x^2}{2} + \tfrac{w_y^2}{2}. \tag{D.3}$$

In the case that $\phi_x = \phi_y$, that is, the horizontal and vertical displacement vectors are perpendicular, this expression simplifies to

$$u_{Rmax}^2 = u_x^2 + w_y^2, \tag{D.4}$$

which is consistent with Pythagorus' theorem.